8-11-2017

Experimental Studies and Finite Element Modeling Of Lightning Damage to Carbon/Epoxy Laminated and Stitched Composites

Juhyeong Lee

Recommended Citation

Lee, Juhyeong, "Experimental Studies and Finite Element Modeling Of Lightning Damage to Carbon/Epoxy Laminated and Stitched Composites" (2017). *Theses and Dissertations*. 2148.
https://scholarsjunction.msstate.edu/td/2148

Experimental studies and finite element modeling of lightning damage to carbon/epoxy laminated and stitched composites

By

Juhyeong Lee

A Dissertation
Submitted to the Faculty of
Mississippi State University
in Partial Fulfillment of the Requirements
for the Degree of Doctor of Philosophy
in Aerospace Engineering
in the Department of Aerospace Engineering

Mississippi State, Mississippi

August 2017

Experimental studies and finite element modeling of lightning damage to carbon/epoxy laminated and stitched composites

By

Juhyeong Lee

Approved:

Thomas E. Lacy Jr.
(Major Professor)

Michael Mazzola
(Co-Major Professor)

Charles U. Pittman Jr.
(Committee Member)

James C. Newman Jr.
(Committee Member)

Rani W. Sullivan
(Committee Member)

Scott M. Thompson
(Committee Member)

J. Mark Janus
(Graduate Coordinator)

Jason M. Keith
Dean
Bagley College of Engineering

Name: Juhyeong Lee

Date of Degree: August 11, 2017

Institution: Mississippi State University

Major Field: Aerospace Engineering

Major Professor: Dr. Thomas E. Lacy Jr.

Title of Study: Experimental studies and finite element modeling of lightning damage to carbon/epoxy laminated and stitched composites

Pages in Study: 197

Candidate for Degree of Doctor of Philosophy

Lightning damage resistance of unstitched carbon/epoxy laminates and a Pultruded Rod Stitched Efficient Unitized Structure (PRSEUS) panel were characterized by laboratory-scale lightning strike tests and multiphysics-based lightning strike finite element (FE) models. This dissertation combines three related research topics: (1) a three-dimensional (3D) heat transfer problem, (2) lightning damage resistance assessments of carbon/epoxy laminates, and (3) lightning damage resistance of PRSEUS panel. The *first* project deals with a 3D analytical heat transfer problem as a solid foundation for understanding the steady-state temperature distribution in an anisotropic composite heat spreader. The *second* project characterizes lightning damage to unprotected carbon/epoxy laminates and laminates with either copper mesh (CM) or pitch carbon fiber paper (PCFP) protection layers subjected to standard impulse current waveforms, consistent with actual lightning waveforms, with 50, 125, and 200 kA nominal peak currents. Multiphysics-based FE models were developed to predict matrix thermal decomposition (a primary form of lightning damage) in unprotected, CM-protected, and PCFP-protected carbon/epoxy laminates. The predicted matrix

decomposition domains in the damaged laminates showed good agreement with experimental results available in the literature. Both the CM and the PCFP lightning protection layers successfully mitigated lightning damage development in the underlying composites. The *third* project includes lightning damage characterization of a PRSEUS panel. Laboratory-scale lightning strike tests with nominal 50, 125, and 200 kA peak currents were performed at the mid-bay, stringer, frame, and frame/stringer intersection locations of the PRSEUS panel. The elliptical regions of intense local damage were elongated along the outermost lamina's carbon fiber direction, consistent with observations from the unstitched carbon/epoxy laminates. However, the damaged PRSEUS panel exhibited unique damage features due to use of warp-knitted fabrics and through-thickness Vectran™ stitches. The polyester threads used to weave the warp-knitted laminates locally confined small-scale fiber damage. This resulted in somewhat periodic and scattered small tufts of carbon fibers near the lightning attachments. Through-thickness Vectran™ stitches also confined intense local damage development at the stringer and frame locations. The polyester warp-knit fabric skins and through-thickness Vectran™ stitches have a significant beneficial effect on lightning damage development on a PRSEUS panel.

DEDICATION

To My Lovely Wife

Han, SongYi
한송이

ACKNOWLEDGEMENTS

First of all, I wish to express my profound appreciation and respect to my mentor, Dr. Thomas E. Lacy Jr. for his support and guidance through this research. I am highly indebted to him for the countless opportunities and exciting challenges that have significantly improved my knowledge.

I also thank my committee members for their valuable advice and comments on this work. I am grateful to Dr. Michael S. Mazzola and Dr. Charles U. Pittman Jr. for their guidance and constructive discussions. I am also very thankful to Dr. James C. Newman Jr., Dr. Rani W. Sullivan, and Dr. Scott M. Thompson for their continuous support and encouragement to achieve this work.

Special thanks to all industry collaborators for their valuable support: Alex Velicki and Patrick Thrash (Boeing Research and Technology Center), Greg Stewart and Christopher Sangster (Aurora Flight Sciences). Many thanks to research colleagues for their help in providing useful suggestions: Pedram Gharghabi, Dounia Boushab, James Gafford, Trenton M. Ricks, Kalyan Raj Kota, Brian Cerovsky, and Patrick Irizarry.

Lastly, I would like to thank my parents and parents-in-law for their endless support during my education at Mississippi State University.

TABLE OF CONTENTS

DEDICATION ii

ACKNOWLEDGEMENTS iii

LIST OF TABLES vii

LIST OF FIGURES ix

I. INTRODUCTION 1

1.1 Motivation 1
1.2 Lightning Threat to Aircraft Composite Structures 4
1.3 References 12

II. THERMAL SPREADING ANALYSIS OF A TRANSVERSELY ISOTROPIC HEAT SPREADER 15

2.1 Abstract 15
2.2 Introduction 16
2.3 Literature Review 20
2.4 Analytical Solutions 22
  2.4.1 Dimensionless Temperature Distribution 26
  2.4.2 Dimensionless Thermal Spreading Resistance 27
2.5 ABAQUS FE Solutions 29
2.6 Results and Discussion 30
  2.6.1 Dimensionless Temperature Distribution 30
  2.6.2 Dimensionless Thermal Spreading Resistance 41
2.7 Conclusions 44
2.8 References 47

III. ARTIFICIAL LIGHTNING STRIKE TESTING OF AS4/8552 CARBON/EPOXY COMPOSITES PROTECTED WITH EITHER COPPER MESH OR PITCH CARBON FIBER PAPER LAYERS 49

3.1 Abstract 49
3.2 Introduction 50
3.3 Laboratory-Scale Lightning Strike Test 51
  3.3.1 AS4/8552 Laminated Test Coupon Preparation 51
  3.3.2 High Impulse Current Generator 52

3.3.3 Grounding Conditions 53
3.3.4 Impulse Current Waveforms 55
3.4 Results and Discussion 57
3.4.1 Unprotected AS4/8552 Carbon/Epoxy Laminates 58
3.4.2 CM and PCFP-Protected AS4/8552 Carbon/Epoxy Laminates 61
3.5 Conclusions and Recommendations 65
3.6 References 67

IV. THERMAL RESPONSE OF SIMULATED LIGHTNING CURRENTS OF CARBON/EPOXY COMPOSITES WITH METALLIC AND NON-METALLIC PROTECTION LAYERS 70

4.1 Abstract 70
4.2 Introduction 71
4.3 Literature Review 73
4.3.1 Lightning Damage 73
4.3.2 Lightning Strike Test Parameters 76
4.4 Theoretical Background 78
4.5 FE Model Development for Predicting Thermal Damage 80
4.5.1 Carbon/Epoxy Composite Material Properties 80
4.5.2 Copper Mesh (CM) Material Properties 85
4.5.3 Pitch-based Carbon Fiber Paper (PCFP) Material Properties 88
4.5.4 FE Model Discretization and Boundary Conditions 90
4.5.5 Simulated Ablation of Lightning Protection Layers 93
4.5.6 Special-Purpose User Subroutines 95
4.6 Matrix Thermal Decomposition Prediction 98
4.6.1 Electrical Response of Unprotected and Protected Composites 98
4.6.2 Matrix Thermal Decomposition in Unprotected and Protected Composites 99
4.7 Conclusions and Recommendations 107
4.8 References 110

V. TEMPERATURE-DEPENDENT THERMAL DECOMPOSITION OF CARBON/EPOXY LAMINATES SUBJECTED TO HIGH IMPULSE CURRENTS 114

5.1 Abstract 114
5.2 Introduction 115
5.3 Literature Review 117
5.3.1 Lightning Strike Damage 117
5.3.2 Lightning Strike Test Parameters 123
5.4 Theoretical Background 124
5.5 FE Model Development for Predicting Matrix Thermal Damage 127
5.5.1 Carbon/Epoxy Composite Material Properties 127
5.5.2 FE Model Discretization and Boundary Conditions 129
5.5.3 Special-Purpose User Subroutines 130

5.6 Predicted Matrix Thermal Decomposition 134
5.7 Conclusions and Recommendations...146
5.8 References 149

VI. LIGHTNING STRIKE TESTS ON A SANDED PRSEUS PANEL 153

6.1 Abstract..153
6.2 Introduction 154
6.3 PRSEUS Structures 156
6.4 Laboratory-scale Lightning Strike Testing Conditions 162
  6.4.1 High Impulse Current Generator 162
  6.4.2 Electrical Grounding Condition 163
  6.4.3 Artificial Lightning Current Waveform 164
  6.4.4 Lightning Strike Locations on the PRSEUS Panel..........................167
6.5 Results and Discussion 169
  6.5.1 Lightning Damage Characterization...169
  6.5.2 Effect of Peak Current and Attachment Point on Lightning Damage Formation 173
6.6 Conclusions and Recommendations...181
6.7 References 184

VII. CONCLUDING REMARKS AND FUTURE WORK 188

7.1 Concluding Remarks 188
7.2 Future Work..191

A. FOURIER COEFFICIENTS 193

B. COMPARISON OF DIMENSIONLESS TEMPERATURES FROM ANALYTICAL AND FE SOLUTIONS 195

LIST OF TABLES

1.1 Frequency of lightning strike on US commercial aircraft [12, 24, 25] 5

1.2 Initial lightning attachment locations (adopted from [29]) 8

2.1 Material properties of aluminum heat spreader used for FE model evaluation [22] 30

2.2 Maximum, dimensionless temperature at the heat source center (0, 0, 1) 32

3.1 Dimensions and layup of the unprotected, CM-protected, and PCFP-protected AS4/8552 carbon/epoxy laminates 52

3.2 Charging voltage and corresponding peak currents with the trigatron spark gap spacing 53

3.3 Lightning waveform characteristics 56

4.1 Material properties of AS4/3506^{a} carbon/epoxy plies [7, 8, 12, 15, 23] 82

4.2 Material properties of pure copper [26, 28, 29]...87

4.3 Material properties of a PCFP protection layer [31-33]................................89

4.4 Material properties used for developing the H-K model [26, 28, 29, 32, 33, 40]...94

5.1 Material properties of AS4/3506^{a} carbon/epoxy plies [29-33] 128

5.2 Comparison of predicted matrix decomposition domains for 40 kA peak current with the experimental result [13] 138

6.1 Material, thickness, and layup of LaRC PRSEUS sub-components [2, 21]...158

6.2 Charging voltage and corresponding peak currents with the trigatron spark gap spacing 163

6.3 Lightning waveform characteristics 166

A.1 Fourier coefficients for Eq. 2.10 194

B.1 Dimensionless maximum temperatures for isotropic and TI heat spreaders with the dimensionless heat spreader thickness (τ) for various Biot numbers (Bi), source-to-spreader area ratios (A^*), and thermal conductivity ratios (κ^2) 196

LIST OF FIGURES

1.1 Percentage of composite structural weight used in commercial airplanes over the last five decades [2] 2

1.2 Various lightning-induced damage sources at the attachment [26] 7

1.3 Lightning damage to the composite radome of Beechcraft Model 99 [30]. 9

1.4 Typical lightning damage to Bombardier DHC 8-102. 10

1.5 Typical lightning damage to Bombardier RJ 100 10

2.1 A fiber-reinforced, rectangular composite with anisotropic bulk thermal conductivity and uniformly-distributed, unidirectional reinforcements. 19

2.2 A rectangular, transversely isotropic heat spreader with square heat source centered on its top surface ($z = t$) opposite of uniform, Newtonian free convection. 23

2.3 FE model and boundary conditions used for numerically determining the steady-state temperature distribution in a square heat spreader with a centrally-applied, square heat source. 30

2.4 Dimensionless temperature distribution along the heat spreader's top surface ($Z = 1$) for various A^* and κ^2 at $\mathrm{Bi} = 10^{-4}$ and $\tau = 10^{-2}$ calculated using the analytical model. 32

2.5 Dimensionless maximum temperature (θ_R) along the half length of the spreader ($X = x/L$) for various Bi and κ^2 at $A^* = 10^{-4}$ and $\tau = 10^{-2}$. 33

2.6 Comparison of dimensionless temperature along the half-length of the heated surface of an isotropic ($\kappa^2 = 1$) heat spreader for $A^* = 10^{-4}$ and $\tau = 10^{-2}$ with various Biot numbers from analytical and FE solutions. 35

2.7 Comparison of dimensionless temperature along the half-length of the heated surface of an isotropic ($\kappa^2 = 1$) heat spreader for $A^* = 10^{-3}$ and $\tau = 10^{-2}$ with various Biot numbers from analytical and FE solutions. 36

2.8 Comparison of dimensionless temperature along the half-length of heated surface of an isotropic ($\kappa^2 = 1$) heat spreader for $A^* = 10^{-2}$ and $\tau = 10^{-2}$ with various Biot numbers from analytical and FE solutions. 36

2.9 Comparison of dimensionless temperature along the half-length of heated surface of a transversely isotropic heat spreader ($\kappa^2 = 0.1$) for $A^* = 10^{-4}$ and $\tau = 10^{-2}$ with various Biot numbers from analytical and FE solutions. 38

2.10 Comparison of dimensionless temperature along the half-length of heated surface of a transversely isotropic heat spreader ($\kappa^2 = 0.1$) for $A^* = 10^{-3}$ and $\tau = 10^{-2}$ with various Biot numbers from analytical and FE solutions. 38

2.11 Comparison of dimensionless temperature along the half-length of heated surface of a transversely isotropic heat spreader ($\kappa^2 = 0.1$) for $A^* = 10^{-2}$ and $\tau = 10^{-2}$ with various Biot numbers from analytical and FE solutions. 39

2.12 Comparison of dimensionless temperature along the half-length of heated surface of a transversely isotropic heat spreader ($\kappa^2 = 10$) for $A^* = 10^{-4}$ and $\tau = 10^{-2}$ with various Biot numbers from analytical and FE solutions. 40

2.13 Comparison of dimensionless temperature along the half-length of heated surface of a transversely isotropic heat spreader ($\kappa^2 = 10$) for $A^* = 10^{-3}$ and $\tau = 10^{-2}$ with various Biot numbers from analytical and FE solutions. 40

2.14 Comparison of dimensionless temperature along the half-length of heated surface of a transversely isotropic heat spreader ($\kappa^2 = 10$) for $A^* = 10^{-2}$ and $\tau = 10^{-2}$ with various Biot numbers from analytical and FE solutions. 41

2.15 Dimensionless thermal spreading resistances versus area ratio (A^*) for various dimensionless heat spreader thicknesses (τ) and thermal conductivity ratios (κ^2) at $\mathrm{Bi} = 10^{-4}$. 43

2.16 Dimensionless thermal spreading resistances versus thermal conductivity ratio (κ^2) for various area ratios (A^*), dimensionless heat spreader thicknesses (τ) and Biot numbers (Bi). 44

3.1 MSU-HVL impulse current generator: (a) edge and (b) top views. 53

3.2 (a) Schematic and (b) photograph of the grounding condition. 54

3.3 SAE component A [24] and MSU-HVL impulse current waveform (200 kA nominal peak current)......56

3.4 MSU-HVL impulse current waveforms with 50, 125, and 200 kA nominal peak currents......57

3.5 Typical lightning damage in unprotected AS4/8552 carbon/epoxy laminates after they are subjected to (a) 51 kA, (b) 126 kA, and (c) 189 kA peak currents......59

3.6 Lightning damage to (a-b) unprotected, (c-d) CM-protected, and (e-f) PCFP-protected AS4/8552 carbon/epoxy laminates subjected to 50 and 125 kA peak currents......64

4.1 Standard current waveforms and their associated criteria (adopted from [10])......76

4.2 FE idealization of (a) the copper mesh (CM) and (b) the PCFP outer layers......91

4.3 Electrical and thermal boundary conditions imposed in lightning strike FE simulations: (a) in coupled thermal-electrical analyses and (b) in subsequent heat transfer analyses......92

4.4 Electrical current density and electrical potential distributions in the top lamina of a) unprotected, b) CM-protected, and c) PCFP-protected 32-ply AS4/3506 carbon/epoxy laminates at the end of coupled thermal-electrical analyses ($t = 30\mu s$)......99

4.5 Matrix thermal decomposition in the top four lamina of the a) unprotected, b) CM-protected, and c) PCFP-protected 32-ply AS4/3506 carbon/epoxy laminates at the end of heat transfer analyses ($t = 10$ s)......101

4.6 Lightning-induced thermal damage in typical carbon/epoxy laminate subjected to a simulated 40 kA peak lightning current: (a) photograph from Ref. [1], (b) ultrasonic C-scan from Ref. [4], (3) predicted matrix decomposition domain by the current FE model, and (d) temperature distribution after lightning strike from Ref. [42]......102

4.7 Thermal damage penetration from 40 kA peak current of a) unprotected and b) CM-protected, c) PCFP-protected, and d) PCFP-protected (with both the in-plane and through-thickness electrical conductivities 100 times greater the values defined in Table 3) 32-ply AS4/3506 carbon/epoxy composites at the end of heat transfer analyses ($t = 10$s)......105

5.1 Standard current waveforms associated with peak current magnitudes, time durations, electrical charges and action integrals adopted from [6]. 124

5.2 Electrical and thermal boundary conditions imposed in lightning strike FE simulations: (a) in coupled thermal-electrical analyses and (b) in subsequent heat transfer analyses [1]. 130

5.3 Lightning current waveform (I_0 = 43,762 A, α = 22,708 1/s, and β = 1,294,530 1/s) for a 40 kA peak current, these parameters were those defined in the current waveform D [6]. 131

5.4 Predicted matrix thermal decomposition profiles defined by using a linear (m = 1) or quadratic (m = 2) approximation (Eq. 5.5) in the temperature ranges of 300-500˚C and 300-600˚C. 133

5.5 Lightning-induced damage in an IM600/133 carbon/epoxy composite subjected to a simulated 40 kA peak lightning current: (a) photograph, (b) ultrasonic C-scan, and (c) projected regions with predicted temperature distributions in the range of 300-500˚C (adopted from [20]). 135

5.6 Predicted extent of matrix thermal decomposition obtained using a linear (m = 1) or quadratic (m = 2) approximation (Eq. 5.5) in the top AS4/3506 lamina subjected to a 40 kA peak lightning current: (a) linear (m = 1, 300-500˚C), (b) quadratic (m = 2, 300-500˚C), (c) linear (m = 1, 300-600˚C), (d) quadratic (m = 2, 300-600˚C), and (e) quadratic Arrhenius (m = 2, 380-490˚C). 137

5.7 Predicted extent of thermal damage penetration using a linear (m = 1) or quadratic (m = 2) approximation (Eq. 5.5) in the top 16 AS4/3506 lamina subjected to a 40 kA peak lightning current: (a) linear (m = 1, 300-500˚C), (b) quadratic (m = 2, 300-500˚C), (c) linear (m = 1, 300-600˚C), (d) quadratic (m = 2, 300-600˚C), and (e) quadratic Arrhenius (m = 2, 380-490˚C). 141

5.8 Photographs and ultrasonic C-scan images of lightning-induced damage to IM600/133 carbon/epoxy laminates subjected to 20, 30, and 40 kA peak lightning currents (adopted from [13]). 143

5.9 Comparison of (a-c) actual lightning damage morphology with (d-f) predicted extent of matrix thermal decomposition obtained using a linear (m = 1) approximation (Eq. 5.5) in the top AS4/3506 lamina subjected to 20, 30, and 40 kA peak lightning currents. 144

5.10 (a) Lightning damage morphology of the AS4/8552 carbon/epoxy composite subjected to 50 kA nominal peak current and (b) the predicted matrix thermal decomposition domain using the present lightning strike FE model. 146

6.1 Schematic of PRSEUS concept [3]. 155

6.2 (a) Schematic of multiaxial warp-knitted fabric [17] and (b) photograph of SAERTEX multiaxial warp-knitted dry carbon fiber fabric [18]. 157

6.3 Single-sided stitching for the PRSEUS concept: (a) frame/stringer intersection (adapted from [21]), (b) flange-to-skin stiches [21], (c) single-sided stitch seam (adapted from [4]), and (d) a complete flat PRSEUS panel preform after stitching (adapted from [4]). 160

6.4 PRSEUS panel delivered to MSU: (a) photograph of IML surface, (b) schematics of IML surface, (c) rod-stiffened stringer, and (d) foam core-reinforced frame. 161

6.5 MSU-HVL impulse current generator: (a) edge view and (b) top View. 163

6.6 Electrical grounding condition along the edges PRSEUS panel: (a) IML view and (b) OML view. 164

6.7 SAE component A [16] and MSU-HVL impulse current waveform (200 kA nominal peak current)....................166

6.8 MSU-HVL impulse current waveforms with 50, 125, and 200 kA nominal peak currents....................167

6.9 Simulated lightning strike locations on the PRSEUS panel that include the (a) target and (b) measured peak currents (in kA). 169

6.10 Damaged PRSEUS panel after being subjected to artificial lightning waveforms. 171

6.11 Two lightning damage categories observed at the PRSEUS mid-bay location subjected to 200 kA nominal peak current. 172

6.12 Typical lightning damage at the mid-bay locations subjected to (a) 50 kA, (b) 125 kA, and (c) 200 kA nominal peak currents. 175

6.13 Typical lightning damage at the stringer locations subjected to (a) 50 kA, (b) 125 kA, and (c) 200 kA nominal peak currents. 177

6.14 Typical lightning damage at the PRSEUS panel subjected to 50 kA nominal peak currents: (a) frame location (50.6 kA) and (b) frame/stringer intersection location (54.2 kA). 179

6.15 Photographs and TTU C-scan images of lightning damage at the mid-bay locations subjected to: (a) 50 kA, (b) 125 kA, and (c) 200 kA nominal peak currents...181

CHAPTER I

INTRODUCTION

1.1 Motivation

Carbon fiber-reinforced polymer (CFRP) composites are becoming more popular in high-performance aerospace applications that require high specific modulus and strength. Recent generation aircraft have been designed with composites for airframe structures (*i.e.*, fuselage and wings), secondary structures (*i.e.*, floor beams), and control surfaces. Airbus introduced the A310 in 1983 with a composite fin box, the A320 in 1988 with an all-composite tail section, and the A380 in 2005 with a CFRP composite central wing box [1-5]. Similarly, the Boeing Company introduced the Boeing 777 in 1995 with composite vertical fins, horizontal stabilizers, and passenger-floor beams [6, 7], and the Boeing 787 in 2011 which used composites in most airframe components [8, 9]. Figure 1.1 shows the percentage of composite structural weight used in commercial airplanes over the last five decades [2]. Prior to the mid-1960s, composite materials were rarely used in the aircraft industry. The use of composite materials has increased gradually since 1985. Since 2010, more than half of the structural weight of the Airbus A350 and the Boeing 787 is from composite materials. The vast expansion of composite materials for aircraft applications can be attributed to (1) excellent strength-to-weight ratio creating higher fuel efficiency, (2) design flexibility leading to easier fabrication of complex geometry parts, and (3) high corrosion resistance for composites that can withstand harsher environments compared to traditional aerospace-grade metal alloys [10].

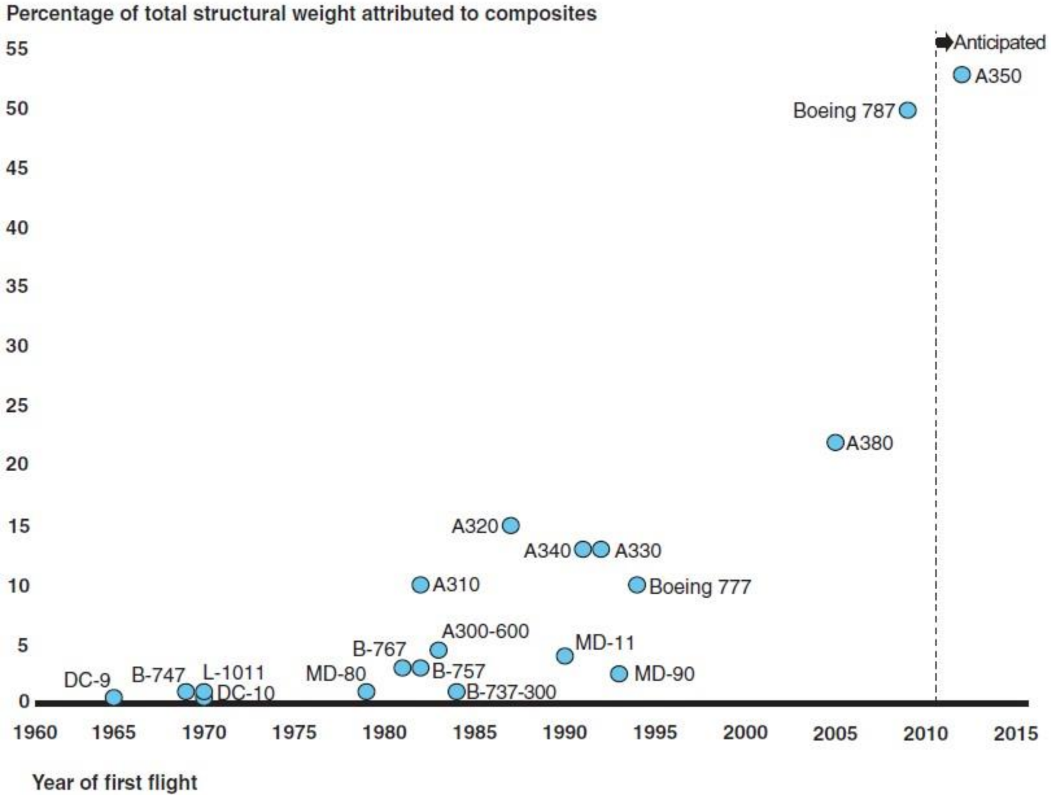

Figure 1.1 Percentage of composite structural weight used in commercial airplanes over the last five decades [2].

A lightning strike can induce severe damage to the structural components, essential electrical systems, and fuel tanks of any aircraft [11-14]. Older aircraft were designed and built with traditional aerospace-grade metal alloys that could conduct electrical current over their exterior skin. By distributing electrical current over their surfaces, these metal alloys protect aircraft from a lightning strike. However, CFRP composites exhibit much lower electrical conductivity than traditional aircraft metals (*i.e.*, aluminum, titanium, and magnesium alloys). CFRP composites cannot efficiently distribute electrical lightning currents, thus lightning strikes can inflict severe damage to composite aircraft components. The severity of lightning damage generally decreases as a given material's electrical conductivity increases. Any material having lower electrical conductivity absorbs more electrical energy from the lightning. This lightning-induced electrical energy is converted into thermal energy due to Joule (or resistive) heating. Thus, more electrical energy is dissipated as heat in CFRP composites than traditional aerospace-grade metal alloys. This raises serious concerns about using CFRP composites at critical locations of the aircraft.

The primary goal of this study is to understand lightning damage mechanisms for both carbon/epoxy laminated composites and Pultruded Rod Stitched Efficient Unitized Structure (PRSEUS) structure, an integrated stitched composite structural concept developed by the Boeing Company [15-18]. First, a number of laboratory-scale lightning strike tests with nominal 50, 125, and 200 kA peak currents were performed on AS4/3506 carbon/epoxy laminates. Lightning damage in these *unprotected* composites was then compared with those in *protected* composites with either copper mesh (CM) or pitch carbon fiber paper (PCFP) protection layers. Multiphysics-based finite element (FE) models were developed to predict lightning thermal damage in unprotected, CM-protected, and PCFP-protected carbon/epoxy laminated composites. In the FE models, matrix thermal decomposition was predicted as a primary form of lightning damage to the composites. The predicted matrix decomposition domains agreed well with surface examinations and damage penetration of actual lightning damage to similar IM600/133 carbon/epoxy laminates from the literature [19]. Based upon a fundamental understanding of lightning damage mechanisms, a series of laboratory-scale lightning strike tests were conducted at each of four representative locations on the outer mold line (OML) skin of a PRSEUS panel (*i.e.*, the mid-bay, the stringer, the frame, and the frame/stringer intersection locations). The OML skin of the panel was lightly sanded prior to lightning strike testing to remove a thin layer of primer. Each location of the PRSEUS panel was subjected to standard impulse current waveforms with 50, 125, and 200 kA nominal peak currents. Lightning-damaged regions gradually increased as the peak current increased. The regions of both intense local damage and widespread small tufts of local fiber damage were elliptical in shape and elongated along the top lamina's fiber direction. This is consistent with observations from unstitched carbon/epoxy laminates. The domains with small-scale fiber damage were somewhat periodic due to polyester knitting threads that are used weave the PRSEUS warp-knitted fabric skins. Through-thickness Vectran™ stitches confined intense local damage at the stringer, frame, and frame/stringer intersection locations between the stitching lines. The PRSEUS panel made of warp-knitted fabrics and through-thickness Vectran™ stitches exhibited profoundly different lightning damage characteristics, compared to traditional laminated composites.

1.2 Lightning Threat to Aircraft Composite Structures

Lightning is a naturally occurring, high voltage, high current, transient electrical discharge between two charged regions with opposite polarities. Lightning creates highly conductive ionized channels for the flow of electric current between the charged regions; the peak local temperature of a lightning arc channel is about 30,000 K. The frequency of lightning strikes to aircraft is affected by geographic location, environmental conditions (*i.e.*, rain, hail, snow, and thunderstorm), and cruising conditions (*i.e.*, altitude, temperature) [11-14, 20, 21]. Uman and Rakov [22] reported that lightning strikes to US commercial airlines mostly occur either in climbing to a cruising altitude near 30,000 ft (9,000 m) or during landing. A more recent study [23] showed that US commercial jets experienced lightning strikes at altitudes between 5,000-15,000 ft (1,524-4,572 m). Table 1.1 shows the frequency of lightning strikes on US commercial aircraft between 1950 and 1974 [24, 25]. A typical commercial aircraft is struck once every 3,000 flight hours, or about once a year [22]. Similarly, general aviation (GA) aircraft experienced lightning strikes every 1,000-3,000 flight hours [14]. Special-purpose military aircraft may be more susceptible to lightning strikes than commercial/GA aircraft since they typically operated under more severe environmental conditions.

Table 1.1 Frequency of lightning strike on US commercial aircraft [12, 24, 25]

Aircraft engine type	Newman *et al.* [24] (1950–1961)		Plumer and Perry [25] (1959–1974)		All data combined [12]		
	Strikes	Flight hours	Strikes	Flight hours	Strikes	Hours	No. hours per strike
Piston	808	2,000,000	-	-	808	2,000,000	2,475
Turboprop	109	415,000	280	876,000	389	1,291,000	3,320
Pure jet	41	427,000	480	1,314,000	521	1,741,000	3,340
All	958	2,842,000	760	2,190,000	1,718	5,032,000	2,930

Effects of lightning strikes on aircraft composites can be categorized based upon the severity of damage: (1) direct (or thermo-mechanical) effects and (2) indirect (or electromagnetic) effects. Lightning direct effects on aircraft components induce various types of physical damage. For instance, lightning-induced physical damage to CFRP composites includes carbon fiber rupture/ablation, matrix burn/scorching/decomposition, local puncture, and delamination failures. Lightning direct effects can lead to different thermo-mechanical damage types, as shown in Fig. 1.2 (from [26]). Direct plasma heat flux (*i.e.*, conduction, convection, and radiation flux) and Joule heating emanating from the lightning attachment location are two major thermal damage sources, while acoustic and electromagnetic forces resulting from the explosion of the lightning channel are two mechanical damage sources [26]. In general, thermal damage is considered more significant than mechanical damage since lightning creates only small-scale mechanical loading [26-28]. For instance, the estimated acoustic overpressure induced by actual lightning strike was only 10 MPa [28] and the predicted electromagnetic pressure at a 100 kA lightning attachment location varied from 0.5 to 50 MPa [26]. In contrast, lightning indirect effects induce electromagnetic interference on essential onboard electronic systems, leading to malfunction in control systems or failure of electrical components. Lightning indirect effects can cause non-structural damage to an aircraft, thus it may have a significant impact on the normal flight operations. A primary concern of this work is to only assess and characterize lightning-induced structural damage to aerospace-grade carbon/epoxy composites, thus lightning indirect effects were not considered.

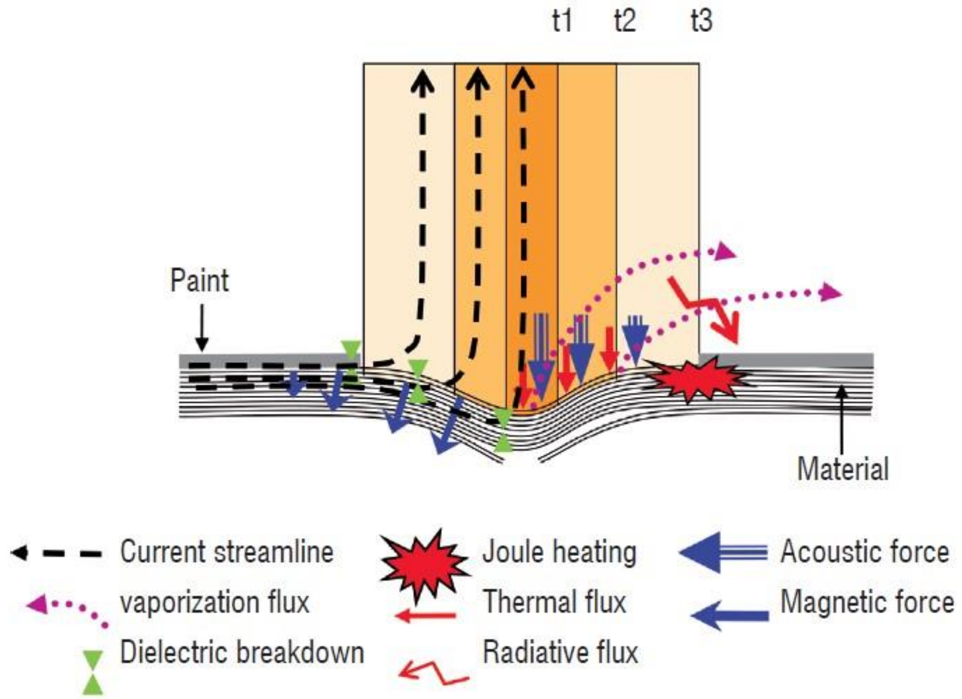

Figure 1.2 Various lightning-induced damage sources at the attachment [26].

Due to the complex physics and the probabilistic nature of lightning, the exterior skin surface of any aircraft may be susceptible to a lightning strike. In fact, a lightning strike usually hits an airplane extremity (such as radome, forward fuselage, nacelle, or empennage), travels through the airplane skin, and then exits through another extremity (such as, wing tips). Table 1.2 shows the predicted initial lightning attachment locations in comparison with flight test results obtained from the F-4 Phantom II [29]. The predicted initial lightning attachment locations showed good agreement with the flight test results. The radome and wings are the most vulnerable to lightning strikes: more than 30% of the initial lightning attachments were observed in each of these locations.

Table 1.2 Initial lightning attachment locations (adopted from [29])

Lightning attachment location	Numerical Prediction		Actual flight tests* (%)
	# of lightning strikes	(%)	
Radom (or nose cone)	194	29.8	33.0
Wing	203	31.2	32.0
Horizontal Stabilizer	99	15.2	14.4
Vertical Stabilizer	84	12.9	11.3
Other	71	10.9	9.3
Total	651	100.0	100.0

*McDonnell Douglas F-4 Phantom II

Figure 1.3 shows typical lightning damage to a composite radome of the Beechcraft Model 99 [30]. A radome is typically protected against lightning strikes with multiple metallic strips that are electrically connected to the fuselage structure. However, the Beechcraft Model 99 does not have enough lightning diverters integrated into its composite radome [30], thus is very susceptible to lightning damage.

Figure 1.3 Lightning damage to the composite radome of Beechcraft Model 99 [30].

Figure 1.4 shows a picture of typical lightning-related local puncture to a metallic wing skin panel observed in the lower aft fuselage of Bombardier DHC 8-102 [31]. As shown in the figure, highly localized damage develops near the lightning attachment location. Figure 1.5 show representative lightning damage to an Bombardier CRJ 100 wing components made of CFRP composites [32]. Evidence of lightning damage was observed in the left winglet lower static discharger and fairing composite components. As previously explained, CFRP composites are more vulnerable to lightning strikes than aerospace-grade metal alloys due to their low electrical conductivities. Thus, repair assessment of lightning-damaged CFRP composites is a crucial element in maintaining "normal" flight operations.

Figure 1.4 Typical lightning damage to Bombardier DHC 8-102.

Lightning strike created a local puncture hole in a metallic wing skin panel [31].

Figure 1.5 Typical lightning damage to Bombardier RJ 100.

The left winglet lower static discharger and fairing composite components were damaged [32].

Conventional lightning strike protection systems are fabricated primarily from aluminum or copper [23, 33-35] due to their high electrical conductivities. Protection systems include thin metallic meshes, expanded foils, aluminum flame spray coatings, embedded metallic wires, diverter strips, metallic foil liners, coated glass fabrics, and bonded aluminum foils. Although metallic protection systems are convenient in terms of maintenance and repair, they introduce the risk of galvanic corrosion when in contact with CFRP composites. Moreover, the higher density of the metallic systems can increase overall aircraft structural weight. Thus, metallic protection systems can offset some benefits of using lightweight CFRP composites. Lightning strikes carry large transient electrical currents and electromagnetic forces. In order to prevent lightning-induced structural damage, CFRP composites should be designed with high electrical surface conductivities that enable them to withstand lightning currents [34]. Thus, aircraft structural CFRP composites should possess electrical conductivities comparable to those of aerospace-grade metal alloys. This can be achieved by either attaching a highly conductive outer layer on the composite structure or making CFRP composites more conductive.

1.3 References

[1] Jerome, P., "Composite Materials in the Airbus A380 from History to Future," 2001.

[2] US Government Accountability Office, "Status of FAA's Actions to Oversee the Safety of Composite Airplanes," *AVIATION SAFETY*, 2011.

[3] Katnam, K., L. Da Silva, and T. Young, "Bonded repair of composite aircraft structures: A review of scientific challenges and opportunities," *Progress in Aerospace Sciences*, 2013, **61**: p. 26-42.

[4] Hinrichsen, J. "A380: Advanced Composite Structures Designed for the Flagship of the 21st Century," in the *Proceedings of the Japan International SAMPE Symposium*, 2001, Tokyo, Japan.

[5] Gellard, G., "A380 Composite in Airbus, Global Investor Forum." 2008.

[6] Roeseler, W.G., B. Sarh, M. Kismarton, J. Quinlivan, J. Sutter, and D. Roberts. "Composite structures: the first 100 years," in the *Proceedings of the 16th International Conference on Composite Materials*, 2007, Kyoto, Japan.

[7] Soutis, C., "Fibre Reinforced Composites in Aircraft Construction," *Progress in Aerospace Sciences*, 2005, **41**(2): p. 143-151.

[8] Brosius, D., "Boeing 787 update: Approaching rollout and first flight, the 787 relies on innovations in composite materials and processes to hit its targets," *High Performance Composites*, 2007, **15**(3): p. 56.

[9] Chawla, K.K., Composite materials: science and engineering. 2012: Springer Science & Business Media.

[10] Baker, A.A.B., Composite materials for aircraft structures. 2004: AIAA.

[11] Plumer, J. and B. Hourihan. "Data from the Airlines Lightning Strike Reporting Project," in the *Proceedings of the Lightning and Static Electricity Conference*, 1972, Air Force Avionics Laboratory.

[12] Fisher, F.A. and J.A. Plumer, Lightning Protection of Aircraft. 1977: NASA.

[13] McDowall, R.L., J.A. Plumer, and M.S. Glynn. "Lightning Data Acquisition," in the *Proceedings of the 15th International Aerospace and Ground Conference on Lightning and Static Electricit*, 1992, Atlantic City, NJ.

[14] O'Loughlin, J. and S. Skinner, "General Aviation Lightning Strike Report and Protection Level Study." 2004, DOT/FAA/AR-04/13, FAA.

[15] Velicki, A. and P. Thrash. "Advanced Structural Concept Development Using Stitched Composites," in the *Proceedings of the 49th AIAA/ASME/ASCE/ASC Structures, Structural Dynamics, and Materials Conference*, 2008, Schaumburg, IL.

[16] Velicki, A., N. Yovanof, J. Baraja, K. Linton, V. Li, A. Hawley, P. Thrash, S. DeCoux, and R. Pickell, "Damage Arresting Composites for Shaped Vehicles-Phase I Final Report." 2009, NASA/CR-2009-215932, NASA.

[17] Velicki, A., N. Yovanof, J. Baraja, K. Linton, V. Li, A. Hawley, P. Thrash, S. DeCoux, and R. Pickell, "Damage Arresting Composites for Shaped Vehicles-Phase II Final Report." 2011, NASA/CR-2011-216880, NASA.

[18] Velicki, A. and D. Jegley. "PRSEUS Development for the Hybrid Wing Body Aircraft," in the *Proceedings of the 11th AIAA Aviation Technology, Integration, and Operation*, 2011, Virginia Beach, VA.

[19] Ogasawara, T., Y. Hirano, and A. Yoshimura, "Coupled Thermal–Electrical Analysis for Carbon Fiber/Epoxy Composites Exposed to Simulated Lightning Current," *Composites Part A: Applied Science and Manufacturing*, 2010, **41**(8): p. 973-981.

[20] Rakov, V.A. and M.A. Uman, Lightning: Physics and Effects. 2003: Cambridge University Press.

[21] Thottappillil, R. and M.A. Uman, "Comparison of Lightning Return-Stroke Models," *Journal of Geophysical Research: Atmospheres*, 1993, **98**(D12): p. 22903-22914.

[22] Uman, M. and V. Rakov, "The Interaction of Lightning with Airborne Vehicles," *Progress in Aerospace Sciences*, 2003, **39**(1): p. 61-81.

[23] Sweers, G., B. Birch, and J. Gokcen, "Lightning Strikes: Protection, Inspection, and Repair," *AERO Quarterly. GTR*, 2004, **12**: p. 19-28.

[24] Newman, M., J. Robb, and E. Yonkers, Aircraft Protection from Thunderstorm Electromagnetic Effects-I. 1962: Lightning & Transients Research Institute.

[25] Plumer, J. and B. Perry. "An Analysis of Lightning Strikes in Airline Operation in the USA and Europe," in the *Proceedings of the Conference on Lightning and Static Electricity*, 1975, Culham Laboratory, UK.

[26] Chemartin, L., P. Lalande, B. Peyrou, A. Chazottes, P. Elias, C. Delalondre, B. Cheron, and F. Lago, "Direct Effects of Lightning on Aircraft Structure: Analysis of the Thermal, Electrical and Mechanical Constraints," *AerospaceLab*, 2012, (5): p. 1-15.

[27] Reid, G. "Mechanical Damage to Aircraft Structures from Lightning Strikes," in the *Proceedings of the Institution of Mechanical Engineers, Part G: Journal of Aerospace Engineering*, 1993.

[28] Aérospatiale-Matra, AEA Technology, BAE Systems, CEAT, DaimlerChrysler Dornier, Ericsson Saab Avionics, Eurocopter, and ONERA, *European FULMEN project*, 2002; Available from: http://www.transport-research.info/sites/default/files/project/documents/fulmen_frep.pdf.

[29] Zhao, X., K. Sun, H. Zang, G. Zhang, and D. Su, "Method for Generating Aircraft Initial Lightening Stroke Attachment Points " in *CN 103293397*. 2013.

[30] WXGuard, *Lightning Puts Hole in Beechcraft Radome*, 2012; Available from: http://wxguard.com/lightning-news/lightning-puts-hole-in-beechcraft-radome/.

[31] 510020330, A.S.D.R., *Lightning Damage to Bombardier DHC8-102*, 2014; Available from: http://www.flightsafetyaustralia.com/2015/03/17-november-2014-19-january-2015-3/.

[32] 20110822011, C.S.D.R., *Lightning Damage to Bombardier RJ 100*, 2011; Available from: https://www.tc.gc.ca/eng/civilaviation/certification/continuing-feedback-fixed-wing-1697.htm.

[33] Bazelyan, E.M. and Y.P. Raizer, Lightning Physics and Lightning Protection. 2000: CRC Press.

[34] Gagné, M. and D. Therriault, "Lightning Strike Protection of Composites," *Progress in Aerospace Sciences*, 2014, **64**: p. 1-16.

[35] Wang, F., Y. Ji, X. Yu, H. Chen, and Z. Yue, "Ablation Damage Assessment of Aircraft Carbon Fiber/Epoxy Composite and its Protection Structures Suffered from Lightning Strike," *Composite Structures*, 2016, **145**: p. 226-241.

CHAPTER II

THERMAL SPREADING ANALYSIS OF A TRANSVERSELY ISOTROPIC HEAT SPREADER

2.1 Abstract

An analytical solution for the steady-state temperature distribution in a transversely isotropic (TI) heat spreader with transversely isotropic thermal conductivity is provided and validated using three-dimensional finite element (FE) analysis. The dimensionless maximum temperature and corresponding thermal spreading resistance were determined for various Biot numbers, dimensionless heat spreader thicknesses, source-to-spreader area ratios and thermal conductivity ratios (ratio of out-of-plane to in-plane thermal conductivities). The heat spreader considered involves uniformly-distributed fibers/channels aligned in the heat spreader's thickness direction. Solutions are presented graphically for various geometric, material and operating mode combinations. The analytical solutions differ by less than 1% from the FE solutions, indicating that the analytical solution, with cosine solution form, is both effective and accurate in predicting the thermal spreading resistance of a TI heat spreader for many parameter combinations. These results can aid the design or analysis of non-traditional media for thermal spreading, including polymer composites, metal matrix composites, nanocomposites, heat pipes and electronics packaging materials with uniformly-distributed thermal vias.

2.2 Introduction

Composite materials are attractive to many industries due to their tailorable properties for a variety of design constraints. Composites generally consist of least one *reinforcement* phase surrounded by a binder or *matrix* phase. The *reinforcement* is typically stiffer, stronger, or more conductive than the *matrix* phase. The *matrix* holds each *reinforcement* in an orderly pattern while retaining its intrinsic properties [1]. Reinforcements (short and long fibers, particles, etc.) may be integrated into ceramic, metal, or polymer matrices for achieving more desirable bulk properties than that of the matrix material alone. A carbon fiber reinforced polymer (CFRP) composite is a common type of composite. Relative to traditional, single-phase metals, CFRP composites can be more lightweight, corrosion resistant, tailorable, and formable to complex shapes [2]. For these reasons, CFRP composites have been used as construction materials for assembling critical aerospace components such as airframes, fuselages, central wing boxes, and other wing components (*i.e.*, skins, stringers/ribs, and ailerons) [3, 4].

Heat spreaders are single-phase or multi-phase media used for diffusing concentrated heat fluxes, from sources such as central processing units (CPUs) or light emitting diodes (LEDs), to a heat sink for subsequent convection and/or radiation with surroundings. They are used to manage temperature, heat transfer rates, temperature gradients and interfacial thermal stresses in a variety of applications in which the performance, reliability, and safety of a heat dissipating source are of interest. Heat spreaders have been used with success for avionics thermal management, in which heat fluxes are relatively high and the assembly volume is constrained [5-11]. Single-phase heat spreaders are fabricated using a single, solid material and are typically metallic (copper, aluminum, etc.). Multi-phase heat spreaders can consist of (1) composites with multiple solid constituents or (2) a solid encapsulating liquid and vapor, *i.e.*, heat pipes or "thermal ground planes" [12]. During heat pipe operation, encapsulated liquid and vapor repeatedly evaporates and condenses, respectively, allowing for enhanced heat transfer. An ideal heat spreader possesses minimal volume and a near-isothermal temperature distribution (*i.e.*, reduced temperature gradients) at its heat sink interface during operation. Multi-phase heat spreaders can be designed to have high in-plane thermal conductivity for promoting heat transfer along the heated and/or cooled surface [13, 14]. In general, *c*omposites can be designed to possess preferentially arranged thermally conductive reinforcements in order to achieve heat transfer in a specific direction [15, 16]. In this work, conductive fibers are arranged to provide enhanced through-thickness conductivity.

Composites can possess anisotropic (*i.e.*, directionally dependent) thermal conductivities represented by the second-order thermal conductivity tensor, $\bar{\boldsymbol{k}}$. This tensor for an anisotropic composite depends on matrix and reinforcement thermal conductivities, reinforcement orientation distribution, and volume fraction, cleanliness, and other factors. In many cases, the thermal conductivity tensor is nearly independent of temperature, and for an anisotropic rectangular heat spreader can be expressed as:

$$\bar{\boldsymbol{k}} = \begin{bmatrix} k_{xx} & k_{xy} & k_{xz} \\ k_{yx} & k_{yy} & k_{yz} \\ k_{zx} & k_{zy} & k_{zz} \end{bmatrix}$$

where the diagonal terms (k_{xx}, k_{yy}, and k_{zz}) are the thermal conductivities in the *x*-, *y*-, and *z*-directions, respectively. The off-diagonal terms (k_{xy}, k_{xz}, k_{yz}, etc.) denote thermal conductivities that couple heat fluxes in one direction with temperature gradients in orthogonal directions. These off-diagonal terms are very small so that they can be neglected in most cases. For this reason, an anisotropic heat spreader can be idealized as an orthotropic heat spreader. For an isotropic material, the thermal conductivity tensor reduces to a single scalar quantity (*i.e.*, $\overline{\boldsymbol{k}} = k_{\mathrm{xx}} = k_{\mathrm{yy}} = k_{\mathrm{zz}} = k$ with zero off-diagonal terms). In contrast, a unidirectional composite containing a square array of continuous fibers (Fig. 2.1) will display transversely isotropic (TI) bulk thermal conductivity behavior. This type of composite heat spreader exhibits in-plane, isotropic thermal conductivity, *i.e.*, $k_{xx} = k_{yy} = k$. The through-thickness thermal conductivity, k_{zz}, will be a strong function of the fibers' thermal conductivity and volume fraction. Depending on operating conditions and constraints, directionally-dependent thermal transport properties can be advantageous or detrimental for aerospace structural design, especially in the presence of high thermal gradients/loads.

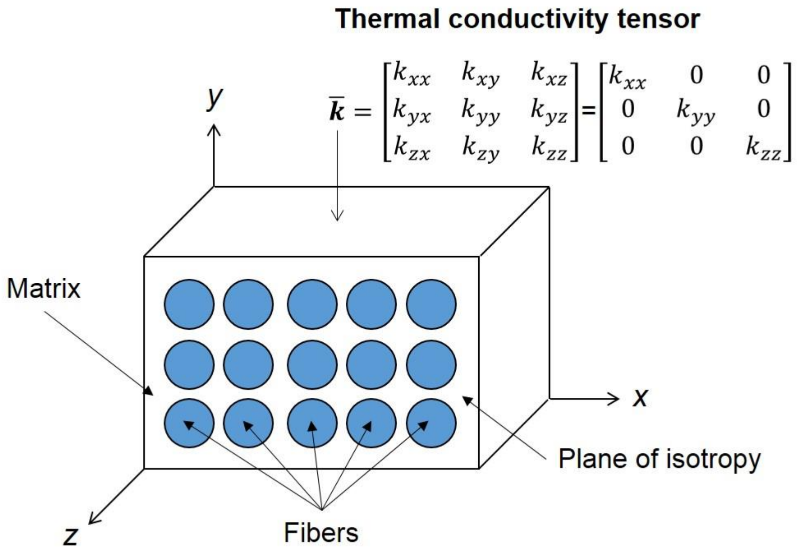

* For transversely isotropic composite, $k_{xx} = k_{yy}$

Figure 2.1 A fiber-reinforced, rectangular composite with anisotropic bulk thermal conductivity and uniformly-distributed, unidirectional reinforcements.

A special class of TI multi-phase heat spreaders consists of uniformly distributed encapsulated structures/fibers or fluid channels oriented perpendicular to the plane of the heat spreader. Such aligned structures/channels can be viewed as ‘thermal vias’ installed to promote or impede heat transfer and perhaps to provide mechanical stability. Unidirectional composites and heat pipes, when functioning as heat spreaders, can have such thermal vias, resulting in the structure possessing a TI thermal conductivity tensor with conduction bias in the fiber (spreader thickness) direction. Hence, the heat transfer along the ‘in-plane’ and ‘through-thickness’ directions are each tailorable. Here, the thermal vias are aligned parallel to the through-thickness direction.

The present study provides unique analytical solutions for the steady-state temperature distribution in TI heat spreaders with conduction bias in the thickness direction; such a heat spreader is representative of unidirectional composites or heat pipes with thermal vias (fibers, channels) aligned in the thickness direction. Unlike previous analytical solutions, both the dimensionless maximum temperature distribution and the thermal spreading resistance are developed as functions of various geometric (*i.e.*, source-to-spreader area ratio, heat spreader thickness) and thermal parameters (*i.e.*, out-of-plane to in-plane thermal conductivity ratio, Biot number). The analyzed heat spreader consists of rectangular geometry and a centrally-located, square heat source located opposite to a plane undergoing uniform free convection. The presented temperature solution is found via a Fourier cosine series expansion [11] and by defining/using an out-of-plane to in-plane thermal conductivity ratio. The accuracy of the analytical temperature solution is benchmarked using steady-state solutions predicted via the ABAQUS finite element (FE) software. Such a comparison is crucial since the FE model may be readily adapted to highly specialized cases involving non-uniform incident heat fluxes, functional gradations in heat spreader material morphologies, and highly tailored heat spreader geometries. The presented solution is intended to serve as a platform for optimizing composite materials or two-phase heat spreaders for various geometric and matrix/constituent combinations.

2.3 Literature Review

Kennedy [5] developed several analytical solutions for the steady-state temperature distribution in a single-phase cylindrical heat spreader with a centrally-applied cylindrical heat source while assuming adiabatic/isothermal boundary conditions. Using a control volume finite difference method, Nelson and Sayers [6] presented two- and three-dimensional thermal spreading resistance models for a rectangular heat spreader in Cartesian coordinates and a circular heat spreader in cylindrical coordinates. The two-dimensional rectangular solution agreed well with the three-dimensional rectangular solution for relatively thin heat spreaders. An axisymmetric solution in cylindrical coordinates was found to be insensitive to the heat spreader thickness and accurate (to within 10%) for all Biot numbers investigated. Lee *et al.* [7] presented an analytical model for the thermal spreading resistance in a rectangular heat spreader (with an axisymmetric cylindrical heat source) subjected to various thermal boundary conditions. The model was flexible enough to reliably predict the response for mixed boundary conditions ranging from isothermal to uniform heat-flux boundary conditions. The solutions agreed well with numerical solutions presented by Nelson and Sayers [6]. Using a Fourier series expansion and Green's functions, Ellison [9] derived an analytical solution for the three-dimensional Poisson's equation governing the temperature distribution of a rectangular heat spreader with various source-to-spreader aspect ratios and Biot numbers. For the special case of a square heat source, the dimensionless thermal spreading resistance was shown to agree reasonably well with results from Lee *et al.* [7] and Nelson and Sayers [6]. As first proposed by Feng and Xu [10], and later employed by Thompson and Ma [11], the analytical solution for the steady-state temperature distribution in an isotropic, rectangular heat spreader with a centrally-applied, rectangular heat source was derived by solving a modified form of Laplace's equation via a Fourier cosine series. Thompson and Ma [11] incorporated a source-to-spreader area ratio (ratio of the cross-sectional area of a heat source to that of a heat spreader) and derived a new analytical solution for the steady-state temperature distribution in a centrally heated, rectangular heat spreader.

A number of analytical solutions have been provided for the thermal spreading resistance of anisotropic heat spreaders consisting of (1) a single-layered medium with anisotropic thermal conductivity [13] or (2) multiple materials stacked parallel to each other in the thickness direction [17-20]. Gholami and Bahrami [13] developed a steady-state thermal resistance model for a single-layered rectangular heat spreader with multiple heat sources at arbitrary locations. Using the superposition principle, the solution corresponding to a single heat source was extended to one for multiple heat sources and then validated with numerical solutions. The dimensionless thermal resistance was obtained as a function of a thermal conductivity ratio for geometric parameters with the same heat source and sink areas. Using linear superposition and neglecting thermal contact (interface) resistance between stacked materials, Muzychka *et al.* [17, 18] extended their analytical solution for an isotropic heat spreader and determined a solution for a multi-layered anisotropic heat spreader with arbitrarily located heat sources. More recently, Muzychka [19] developed an analytical temperature solution based on arbitrarily located heat sources on a multi-layered orthotropic heat spreader with and without interfacial resistance between layers. This analytical solution was further extended by Bagnall *et al.* [20] by recursively solving a spreading function (ratio of the Fourier coefficients) with respect to each layer.

2.4 Analytical Solutions

A schematic of a TI, rectangular heat spreader with a square heat source centered in Cartesian coordinate space is provided in Fig. 2.2. The heat spreader has in-plane dimensions of $2L \times 2L$ and thickness t. At the top surface of the heat spreader ($z = t$), a uniform heat flux is applied over the region $2l \times 2l$. At the bottom surface ($z = 0$), the spreader undergoes uniform, Newtonian free convection with surroundings, quantifiable by a free stream temperature, T_∞, and a convective/total heat transfer coefficient, h. The side/lateral surfaces of the heat spreader are assumed to be adiabatic. The TI bulk thermal conductivity of the heat spreader is considered; the in-plane thermal conductivities, $k_{xx} = k_{yy}$, are distinct from the through-thickness value, k_{zz}. Hence, the two-phase heat spreader possesses a thickness-wise conduction bias and uniform bulk thermal conductivities, $k_{xx} = k_{yy} \neq k_{zz}$. Note these idealized boundary conditions are typical to heat spreader analyses, but error is introduced as the thickness of the heat spreader becomes exceedingly large, convection/heating uniformity decreases or the degree of orthotropy decreases.

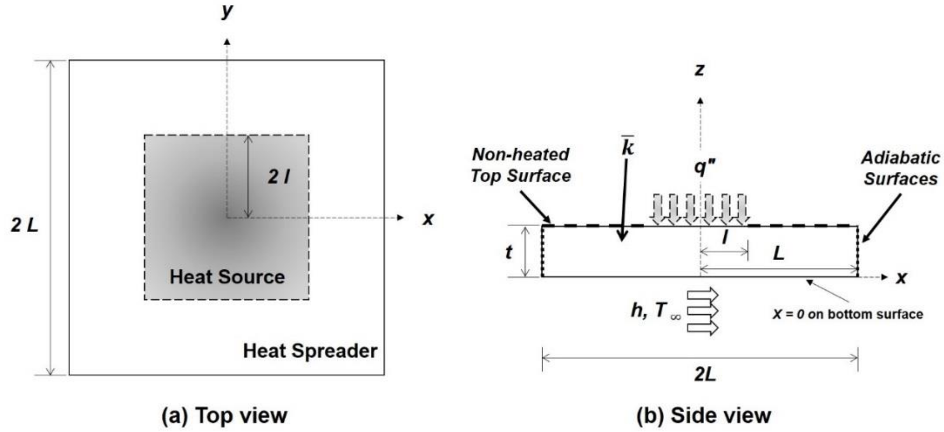

(a) Top view

(b) Side view

Figure 2.2 A rectangular, transversely isotropic heat spreader with square heat source centered on its top surface ($z = t$) opposite of uniform, Newtonian free convection.

The heat spreader temperature at steady-state, while assuming no internal heat generation, is sought. The energy equation governing the steady-state temperature distribution in the heat spreader with temperature-independent, in-plane and out-of-plane thermal conductivities, can be expressed as

$$\nabla^2\theta(x,y,z) = k_{xx}\left(\frac{\partial^2\theta}{\partial x^2}+\frac{\partial^2\theta}{\partial y^2}\right)+k_{zz}\frac{\partial^2\theta}{\partial z^2}=0 \tag{2.1}$$

where $k_{xx} = k_{yy}$ is the representative in-plane thermal conductivity, k_{zz} is the out-of-plane thermal conductivity, and $\theta(x,y,z) = T(x,y,z) - T_\infty$. The boundary conditions for Eq. 2.1 are defined as

$$\begin{aligned}
&\text{(a)} && \frac{\partial\theta(x,0,z)}{\partial x}=\frac{\partial\theta(x,L,z)}{\partial x}=\frac{\partial\theta(0,y,z)}{\partial y}=\frac{\partial\theta(L,y,z)}{\partial y}=0\\
&\text{(b)} && k_{zz}\frac{\partial\theta(x,y,t)}{\partial z}=\begin{cases} q", (x,y)\in[0,l]\\ 0, (x,y)\in(l,L]\end{cases}\\
&\text{(c)} && \frac{\partial\theta(x,y,0)}{\partial z}+\frac{h}{k_{zz}}\theta(x,y,0)=0
\end{aligned} \tag{2.2}$$

where $q"$ is an applied, uniform heat flux and *h* is the total heat transfer coefficient. In order to derive the general solution for Eq. 2.1, several dimensionless, geometric and thermal parameters are introduced, including the normalized dimensions (*X*, *Y*, and *Z*), dimensionless heat spreader thickness (τ), the Biot number (Bi), and the dimensionless, out-of-plane to in-plane thermal conductivity ratio (κ^2), respectively,

$$\begin{aligned}
&\text{(a)} && X=\frac{x}{L}\quad,\quad Y=\frac{y}{L}\quad,\quad Z=\frac{z}{t}\\
&\text{(b)} && \tau=\frac{t}{L}\\
&\text{(c)} && \mathrm{Bi}=\frac{h\,t}{k_{zz}}\\
&\text{(d)} && \kappa^2=\frac{k_{zz}}{k_{xx}}
\end{aligned} \tag{2.3}$$

where *L* is the heat spreader half-length and *t* is the heat spreader thickness.

Using the dimensionless parameters defined in Eqs. 2.3 (a-d), Eq. 2.1 can be transformed to Eq. 2.4, *i.e.*,

$$\nabla^2\theta^*(X,Y,Z) = \frac{\partial^2\theta^*}{\partial X^2} + \frac{\partial^2\theta^*}{\partial Y^2} + \left(\frac{\kappa^2}{\tau^2}\right)\frac{\partial^2\theta^*}{\partial Z^2} = 0 \tag{2.4}$$

where the transformed, dimensionless temperature, $\theta^*(X,Y,Z)$, may be expressed as [11]

$$\theta^*(X,Y,Z) = \frac{k_{ZZ}\mathrm{Bi}}{tq"A^*}\theta(X,Y,Z) = \frac{4hL^2}{Q}\theta(X,Y,Z) \tag{2.5}$$

and $q"$ and Q are the heat flux and heat transfer rate, respectively, related by

$$Q = q"A_s = q"(4l^2) \tag{2.6}$$

and A^* is the area ratio defined as the ratio of heat source planform area, A_s, to heat spreader planform area, A_b, *i.e.*, [11]

$$A^* = \frac{A_s}{A_b} = \frac{(2l)^2}{(2L)^2} = \frac{l^2}{L^2} \tag{2.7}$$

The boundary conditions defined in Eqs. 2.2 (a–c) then become

$$\begin{aligned}
&\text{(a)} \quad \frac{\partial\theta^*(X,0,Z)}{\partial X} = \frac{\partial\theta^*(X,1,Z)}{\partial X} = \frac{\partial\theta^*(0,Y,Z)}{\partial Y} = \frac{\partial\theta^*(1,Y,Z)}{\partial Y} = 0 \\
&\text{(b)} \quad \frac{\partial\theta^*(X,Y,1)}{\partial Z} = \frac{\mathrm{Bi}}{A^*}\varphi(X,Y) \\
&\text{(c)} \quad \frac{\partial\theta^*(X,Y,0)}{\partial Z} = \mathrm{Bi}\,\theta^*(X,Y,0)
\end{aligned} \tag{2.8}$$

where $\varphi(X,Y)$ is the unit piecewise function and may be expressed using the Heaviside step function, H

$$\varphi(X,Y) = \left[\mathrm{H}(X) - \mathrm{H}(X-\sqrt{A^*})\right]\left[\mathrm{H}(Y) - \mathrm{H}(Y-\sqrt{A^*})\right] \tag{2.9}$$

As first proposed by Feng and Xu [10], and later employed by Thompson and Ma [11], the dimensionless temperature distribution for the heat spreader is expanded using an Fourier cosine series, *i.e.*,

$$\theta^*(X,Y,Z) \cong A_{00}(Z) + \sum_{m=1}^{m=\infty} A_{m0}(Z)\cos(m\pi X) + \sum_{n=1}^{n=\infty} A_{0n}(Z)\cos(n\pi Y) + \sum_{n=1}^{n=\infty}\sum_{m=1}^{m=\infty} A_{mn}(Z)\cos(m\pi X)\cos(n\pi Y) \tag{2.10}$$

where A_{00}, A_{m0}, A_{0n}, A_{mn} are the Fourier series coefficients provided in APPENDIX A.

The analytical solution, *i.e.*, Eq. 2.10, was numerically evaluated and plotted using *Mathematica*® v. 12. The cosine series were truncated to $m = 100$ and $n = 100$ terms which were found to sufficiently minimize the L2 norm to less than 10^{-6}. The L2 norm of the solution was defined as:

$$\|\theta^*(X,Y,0)\|_2 = \sqrt{\left(\sum_{i=1}^{p} |\theta^*(X_i,Y_i,0)|^2\right)} \tag{2.11}$$

where X_i and Y_i are relative locations between $X_i = Y_i = 0$ and $X_p = Y_p = 1$.

2.4.1 Dimensionless Temperature Distribution

The thermal performance of a heat spreader can be evaluated, in part, by its temperature uniformity, or isothermality, along its heated and/or cooled surface. In general, a higher degree of isothermality along a surface indicates a heat spreader's ability to diffuse concentrated heat sources more efficiently. Lower out-of-plane thermal conductivities or faster convective heat transfer rates from the heated spreader surface result in higher Biot numbers, as prescribed by Eq. 2.3 (c). The analytical temperature distribution was normalized by the heat spreader maximum temperature (*i.e.*, at $X = Y = 0, Z = 1$). This dimensionless temperature distribution (θ_R) is defined as:

$$\theta_\mathrm{R}(X,Y,Z) = \frac{\theta^*(X,Y,Z)}{\theta^*_\mathrm{max}} = \frac{\theta^*(X,Y,Z)}{\theta^*(0,0,1)} \tag{2.12}$$

For validation, the dimensionless temperature distributions, Eq. 2.12, along the heated surface were evaluated for varying τ, Bi, A^*, and κ. These were compared with the solutions by Ellison [9] and Thompson and Ma [11] for an isotropic heat spreader and the solution by Gholami and Bahrami [13] for an anisotropic heat spreader. For an isotropic square heat spreader, the current analytical solution agrees well with Thompson and Ma's and Ellison's for any combination of Bi and A^*. Similarly, the present analytical solution for an anisotropic heat spreader shows fairly good agreements with Gholami and Bahrami's predictions for given thermal conductivity ratios (*i.e.*, $0.1 \le \kappa^2 \le 1$). Therefore, the current solution is applicable.

2.4.2 Dimensionless Thermal Spreading Resistance

The thermal spreading resistance of a heat spreader, ψ_{sp}, can be expressed as

$$\psi_{sp} = \psi_{max} - \psi_m - \psi_{conv} \tag{2.13}$$

where ψ_{max} is the total, maximum thermal resistance, ψ_m is the material (or conduction) thermal resistance, and ψ_{conv} is the convection (or environmental) thermal resistance. The total maximum and convection thermal resistances are found using Eqs. 2.14 (a-b), respectively, *i.e.*,

$$\text{(a)} \qquad \psi_{\max} = \frac{\theta(0,0,1)}{Q} = \frac{\theta^*_{max}}{4hL^2}$$

$$\text{(b)} \qquad \psi_{conv} = \frac{1}{hA_b} = \frac{1}{4hL^2} \tag{2.14}$$

In order to determine the material resistance, a TI heat spreader is assumed to behave as a two-layered heat spreader: (1) the first layer has an isotropic, in-plane thermal conductivity ($k_{xx} = k_{yy}$) and (2) the second layer has an isotropic, out-of-plane thermal conductivity (k_{zz}); each with magnitude representative of the TI heat spreader. The thickness of each isotropic layer is assumed to be governed by the thermal conductivity ratio defined as κ^2 in this study. The material resistance of a TI heat spreader is then defined as

$$\psi_m = \frac{t_{\text{xx}}}{k_{xx}A_b} + \frac{t_{\text{zz}}}{k_{zz}A_b} = \frac{1}{4L^2}\left(\frac{1}{k_{xx}} + \frac{1}{k_{zz}}\right) \tag{2.15}$$

where t_{xx} and t_{zz} are the isotropic layer thicknesses with in-plane and out-of-plane thermal conductivities, respectively. Since overall thickness is preserved, the summation of t_{xx} and t_{zz} is equal to t. Hence, the thermal spreading resistance is found by

$$\psi_{sp} = \frac{\theta^*_{max}}{4hL^2} - \frac{1}{4L^2}\left(\frac{1}{k_{xx}} + \frac{1}{k_{zz}}\right) - \frac{1}{4hL^2} \tag{2.16}$$

After some manipulation, a dimensionless thermal spreading resistance, ψ^*_{sp}, may be presented as a function of A^*, τ, and κ

$$\psi^*_{sp} = \frac{\tau\sqrt{A^*}}{2\text{Bi}}(\theta^*_{max} - 1) - \sqrt{A^*}\,\frac{\tau\,\kappa^2}{\kappa^2 + 1} \tag{2.17}$$

where θ^*_{max} is the dimensionless maximum temperature expressed as [11]

$$\theta^*_{max} = \theta^*(0,0,1) = \frac{4\,h\,L^2}{Q}\theta_{max} \tag{2.18}$$

2.5 ABAQUS FE Solutions

Figure 2.3 shows a 3D FE model of a TI heat spreader (with boundary conditions) developed for benchmarking the analytical model using ABAQUS 6.14 [21]. The simulated 20 × 20 × 1 mm^3 heat spreader was discretized using uniformly-sized, eight-node convection-diffusion brick elements. A series of preliminary FE simulations were performed to determine mesh size sensitivity. Element sizes were varied between 0.1-1.0 mm. A mesh-independent solution was found when using an element size smaller than 0.1 mm. Therefore, the simulated heat spreader was discretized using 400,000 (200 × 200 × 10) continuum brick elements with dimensions of 0.1 × 0.1 × 0.1 mm^3. The centrally-applied heat source was simulated by assigning a uniform surface heat flux to the heat spreader with magnitude of $q'' = 10^4$ W/m^2. The surface opposite of the heat source was assigned a uniform free convection boundary condition with air at $T_\infty = 25$ ºC. Buoyancy effects associated with the adjoining air were neglected. The total heat transfer coefficient was calculated using Eq. 2.3 (c) and was varied in order to achieve the desired Biot number. Numerical analyses were performed for three source-to-spreader area ratios, i.e., $A^* = 10^{-2}$, 10^{-3}, and 10^{-4}. Three thermal conductivity ratios, i.e., $\kappa^2 = 0.1$, 1, and 10, were considered for characterizing the heat spreader temperature distribution; with $\kappa^2 = 1$ corresponding to an isotropic heat spreader. The in-plane thermal conductivity was arbitrarily chosen to match that of conventional, pure aluminum. All properties used for the FE analysis are summarized in Table 2.1.

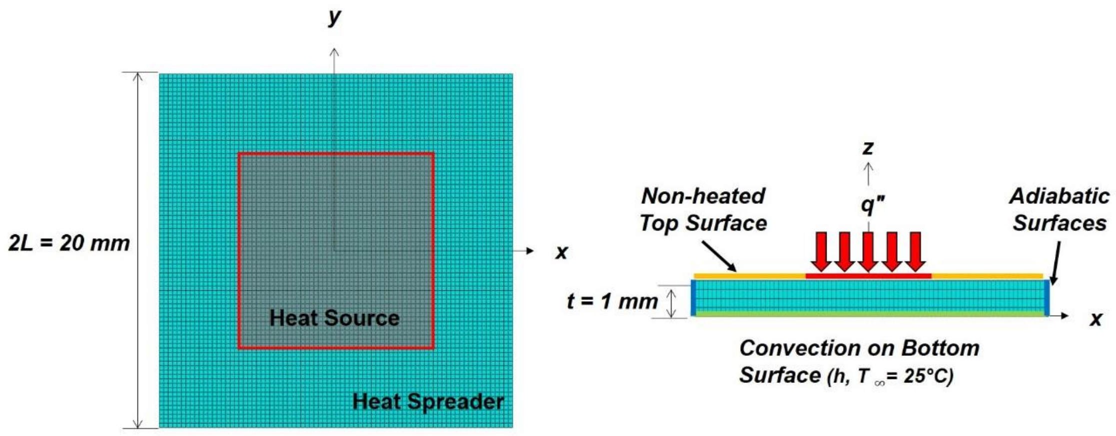

(a) Top view **(b) Side view**

Figure 2.3 FE model and boundary conditions used for numerically determining the steady-state temperature distribution in a square heat spreader with a centrally-applied, square heat source.

Table 2.1 Material properties of aluminum heat spreader used for FE model evaluation [22]

Case	Density (kg/m^3)	Thermal conductivity			Specific heat capacity (J/kg·K)	Isotropy
		In-plane, k_{xx} (W/m·K)	Out-of-plane, k_{zz} (W/m·K)	Ratio [b] (k_{zz}/k_{xx})		
0	2700	170	170	1	950	Isotropic
1	2700	170	1.7 [a]	0.1	950	Transversely Isotropic
2	2700	170	1700 [a]	10	950	Transversely Isotropic

[a] Out-of-plane thermal conductivity that satisfies a given thermal conductivity ratio

[b] The ratio of out-of-plane to in-plane thermal conductivities denoted as κ in Eq. 2.4 (b)

2.6 Results and Discussion

2.6.1 Dimensionless Temperature Distribution

Figure 2.4 shows the dimensionless temperature distribution (θ_R) along the heated surface (*i.e.*, $Z = 1$) for Biot number (Bi) of 10^{-4} and dimensionless heat spreader thicknesses (τ) of 10^{-2} for various source-to-area ratios ($A^* = 10^{-4}, 10^{-3}, 10^{-2}$, and 10^{-1}) and thermal conductivity ratios ($\kappa^2 = 0.1$, 1, and 10) over the range of $0 \leq \theta_R \leq 10$. As expected, the dimensionless temperature is found to be maximum at the heat source center for all parameter combinations. The magnitude of θ_R increases as A^* and κ^2 increase, resulting in lower through-thickness heat transfer rates. Steep dimensionless temperature gradients along the in-plane directions are more noticeable for lower A^* and higher κ^2. When compared to those of an isotropic heat spreader, the maximum dimensionless temperatures are 290-704% higher for TI heat spreaders with $\kappa^2 = 10$ and 34-68% lower for TI heat spreaders with $\kappa^2 = 0.1$, as shown in Table 2.2. This indicates that a higher degree of isothermality is achieved as A^* increases and κ^2 decreases. This is reasonable since lower A^* approximates more localized (point) heat sources. All dimensionless temperature fields are found to be symmetric regardless of κ^2 due to the heat spreader being TI.

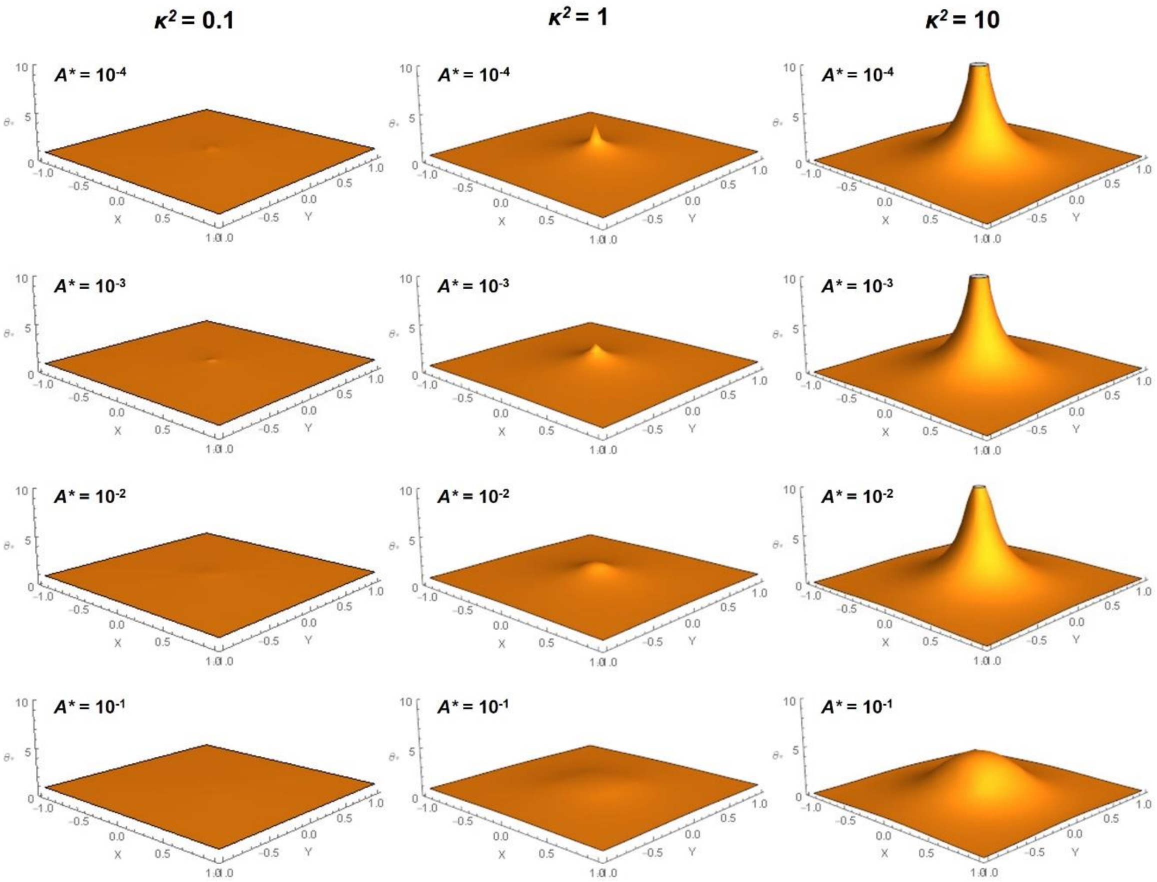

Figure 2.4 Dimensionless temperature distribution along the heat spreader's top surface ($Z = 1$) for various A^* and κ^2 at Bi = 10^{-4} and $\tau = 10^{-2}$ calculated using the analytical model.

Table 2.2 Maximum, dimensionless temperature at the heat source center (0, 0, 1)

A^*	$\kappa^2 = 0.1$ (RPD[*])	$\kappa^2 = 1$	$\kappa^2 = 10$ (RPD[*])
10^{-4}	1.21 (34 %)	3.57	25.1 (704 %)
10^{-3}	1.19 (40 %)	3.00	17.8 (594 %)
10^{-2}	1.13 (50 %)	2.25	10.7 (474 %)
10^{-1}	1.06 (68 %)	1.55	4.5 (290 %)

[*] Relative Percent Difference to the maximum, dimensionless temperature of an isotropic heat spreader ($\kappa^2 = 1$).

The dimensionless temperature distribution along the half length of the heat spreader surface is plotted for various Biot numbers (Bi) and thermal conductivity ratios (κ^2) with source-to-area $A^* = 10^{-4}$ and dimensionless heat spreader thicknesses $\tau = 10^{-2}$ in Fig. 2.5. As shown in Fig. 2.5, a higher degree of isothermality is achieved along the heat spreader surface as Bi and κ^2 decrease. As Bi decreases, the dimensionless temperature distribution becomes more dependent on κ^2. For all κ^2 investigated, the dimensionless temperature distributions corresponding to higher Bi were found to decrease sharply toward regions further from the heat source. From Figs. 2.4-2.5, it may be seen that dimensionless temperature distributions in an isotropic heat spreader ($\kappa^2 = 1$) are distinct from those of TI heat spreaders. TI heat spreaders ($\kappa^2 < 1$) can provide better heat spreading ability than an isotropic heat spreader, as evidenced by a higher degree of isothermality along their heated surface, while TI heat spreaders ($\kappa^2 > 1$) possesses higher Z-wise (through thickness) heat transfer rates and lower overall temperatures.

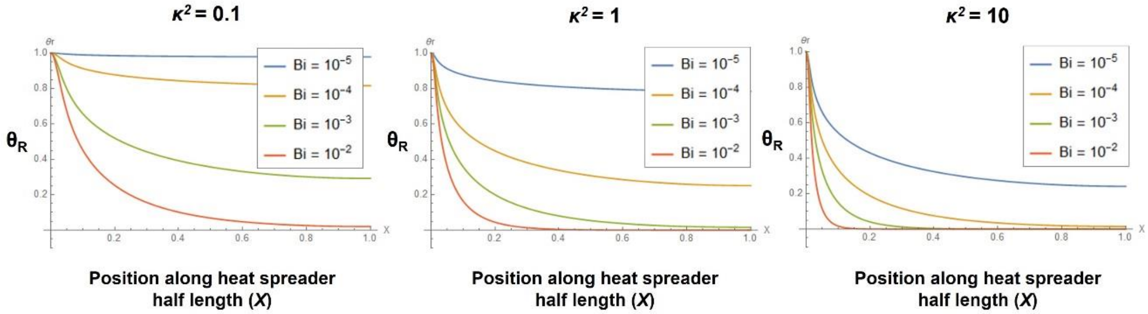

Figure 2.5 Dimensionless maximum temperature (θ_R) along the half length of the spreader ($X = x/L$) for various Bi and κ^2 at $A^* = 10^{-4}$ and $\tau = 10^{-2}$.

A TI composite can possess a lower out-of-plane thermal conductivity relative to its in-plane thermal conductivity by having uniformly distributed (1) relatively *insulating* fibers/vias aligned in the thickness direction or (2) relatively *conductive* randomly oriented fibers/vias aligned in the in-plane direction perpendicular to the thickness direction. Once centrally-heated and uniformly-cooled following the configuration of Fig. 2.2, these composites will have higher heat transfer along the XY plane and thermal conductivity ratios (κ^2) of < 1. Such composites are certainly capable of 'spreading' concentrated heat sources, but at the price of increased operating temperatures. For TI composites, the use of *insulating* Z-aligned fibers is not beneficial for enhancing thermal spreading performance since the matrix thermal conductivity becomes dominant. TI composites with $\kappa^2 > 1$ will possess less temperature uniformity along the XY planes/surfaces; the magnitude of the temperature distribution, however, is generally reduced. Temperature uniformity can be an issue for applications/scenarios in which temperature gradients are of importance, such as thermal shock and deformation.

For an isotropic heat spreader ($\kappa^2 = 1$), the dimensionless temperature distributions, plotted along dimensionless half-length of a heated spreader surface, at source-to-area ratios (A^*) of 10^{-4}, 10^{-3}, and 10^{-2} for various Biot numbers (Bi) are shown in Figs. 2.6-2.8. For relatively thin heat spreaders, *i.e.*, $\tau < 10^{-2}$, the maximum, dimensionless temperature is more sensitive to A^* [11]. It is for this reason that the analytical dimensionless temperature distributions (along the heated surface) were compared with results from the FE model while employing a dimensionless heat spreader thickness, $\tau = 10^{-2}$. From Figs. 2.6-2.8, it may be seen that for all Bi and A^* investigated, the analytical solutions, Eq. 2.12 showed very good agreements with the FE solutions.

The maximum difference between the analytical and FE solutions obtained at half length of the heat spreader ($X = 1$, $Y = 0$, and $Z = 1$) is ≤ 1 %. For instance, at the lowest Bi (i.e., 10^{-5}) and the highest A^* (i.e., 10^{-2}) shown in Fig. 2.8, the difference between the analytical and FE solutions is 0.29 %. Comparison with the FE solution demonstrates that the proposed analytical solution for an isotropic heat spreader is accurate for all combinations of Bi and A^*.

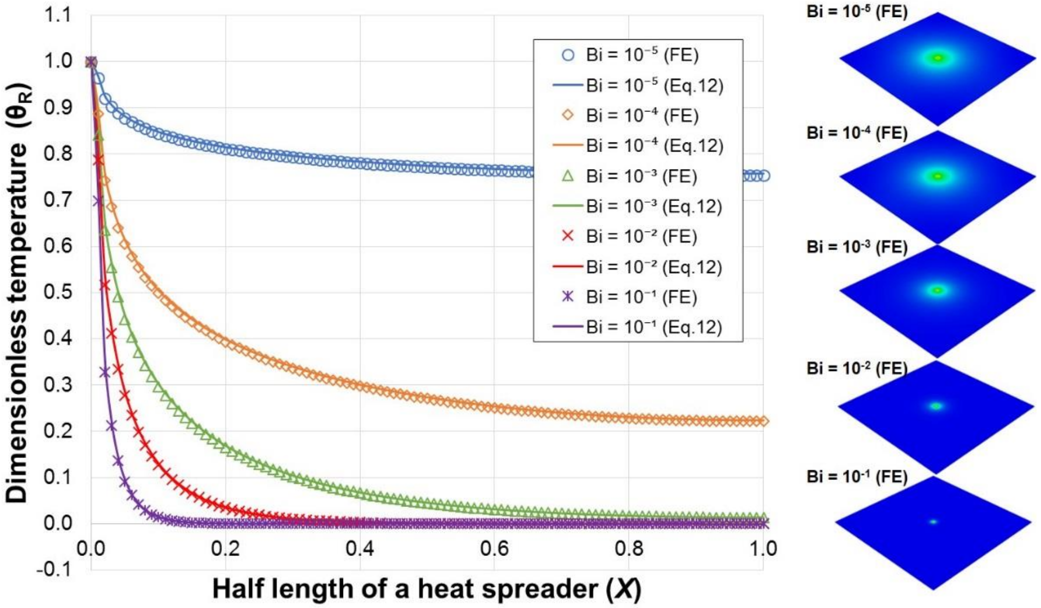

Figure 2.6 Comparison of dimensionless temperature along the half-length of the heated surface of an isotropic ($\kappa^2 = 1$) heat spreader for $A^* = 10^{-4}$ and $\tau = 10^{-2}$ with various Biot numbers from analytical and FE solutions.

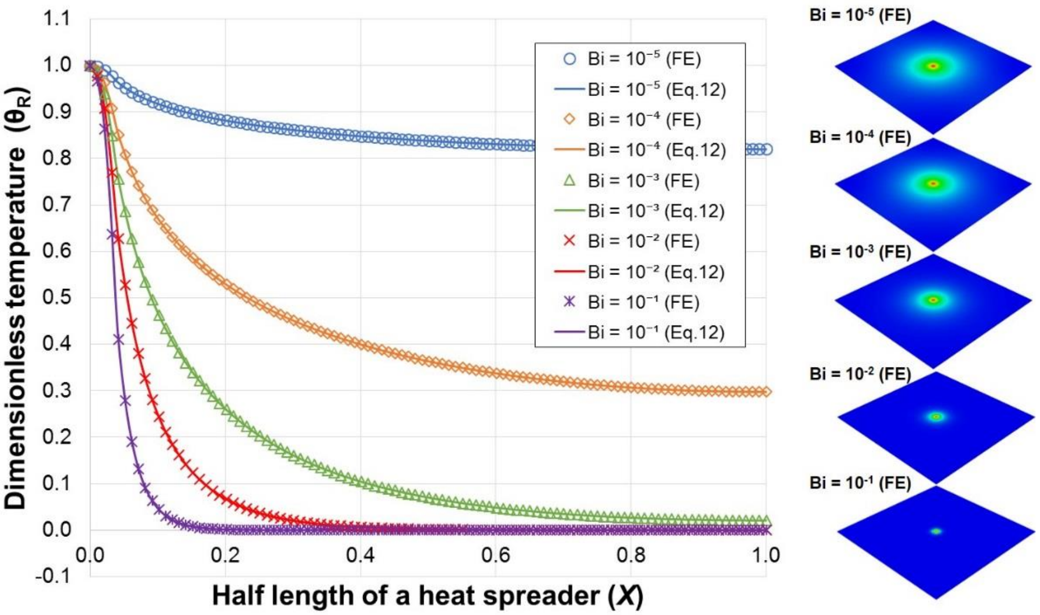

Figure 2.7 Comparison of dimensionless temperature along the half-length of the heated surface of an isotropic ($\kappa^2 = 1$) heat spreader for $A^* = 10^{-3}$ and $\tau = 10^{-2}$ with various Biot numbers from analytical and FE solutions.

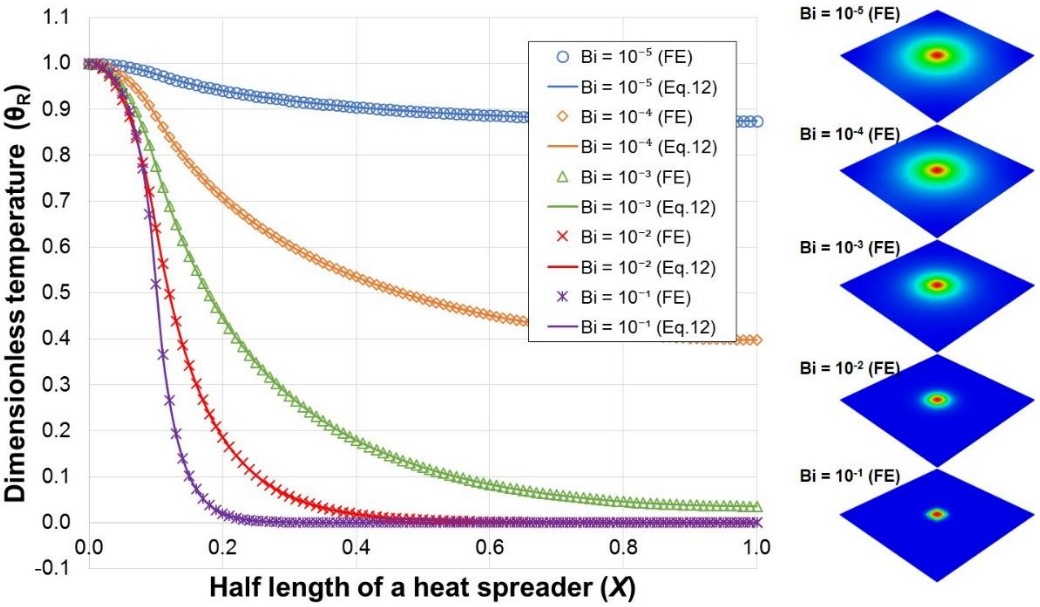

Figure 2.8 Comparison of dimensionless temperature along the half-length of heated surface of an isotropic ($\kappa^2 = 1$) heat spreader for $A^* = 10^{-2}$ and $\tau = 10^{-2}$ with various Biot numbers from analytical and FE solutions.

The dimensionless temperature distributions plotted along the dimensionless half-length of a heated surface of a TI heat spreader ($\kappa^2 = 0.1$) at source-to-area ratios $A^* = 10^{-4}$, 10^{-3}, and 10^{-2} for various Biot number (Bi) are provided in Figs. 2.9-2.11. In general, it may be seen that the analytical solution is reasonably accurate for a TI heat spreader and that a higher degree of isothermality is achieved for lower Biot numbers. Compared to an isotropic heat spreader ($\kappa^2 = 0.1$), a TI heat spreader with a relatively high in-plane thermal conductivity (*i.e.*, $\kappa^2 = 0.1$) shows higher isothermality, which can prove beneficial in many various thermal spreading applications.

Similar to an isotropic heat spreader (Figs. 2.6-2.9), the relative percent differences between the analytical and FE solutions of a TI heat spreader ($\kappa^2 = 0.1$) were also ≤ 1 %. At the lowest A^* investigated, the heat input is essentially a point source, resulting in steep dimensionless in-plane temperature gradients along the heated surface. Higher summation terms in analytical solutions and higher FE mesh resolution may be required to accommodate for point heat sources. The truncated, 200-term analytical solutions were sufficient and closely matched with the FE solutions in the case of the lowest A^*. [10]. One can conservatively state that the analytical solutions for a TI heat spreader with $\kappa^2 = 0.1$ have less than 10% relative difference (compared to FE solutions) for $A^* = 10^{-4}$, regardless of Bi. The difference between the analytical and FE solutions decreases negligible (≤ 1%) for all combinations of A^* and Bi.

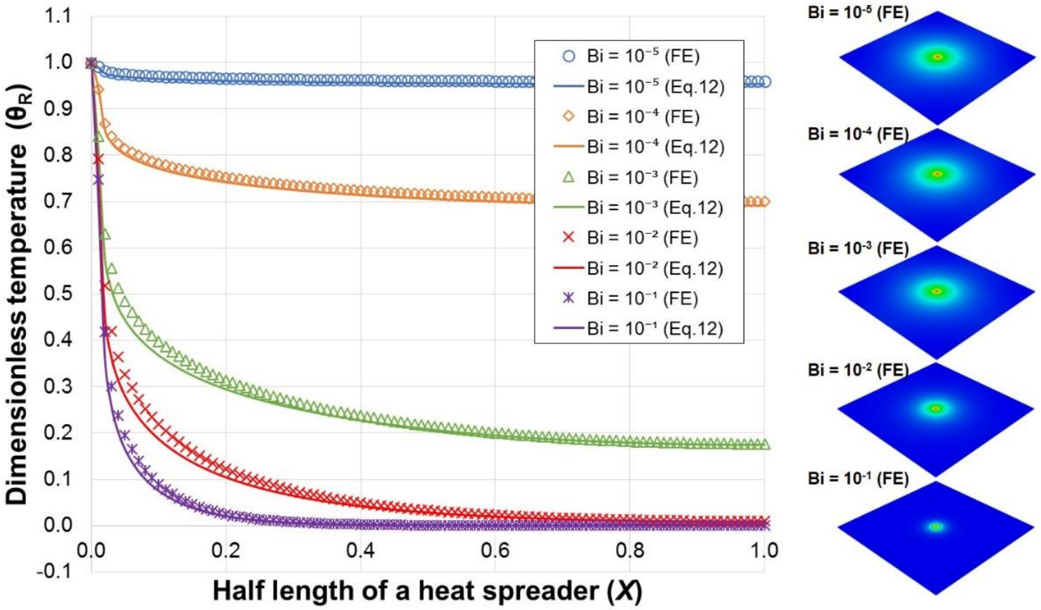

Figure 2.9 Comparison of dimensionless temperature along the half-length of heated surface of a transversely isotropic heat spreader ($\kappa^2 = 0.1$) for $A^* = 10^{-4}$ and $\tau = 10^{-2}$ with various Biot numbers from analytical and FE solutions.

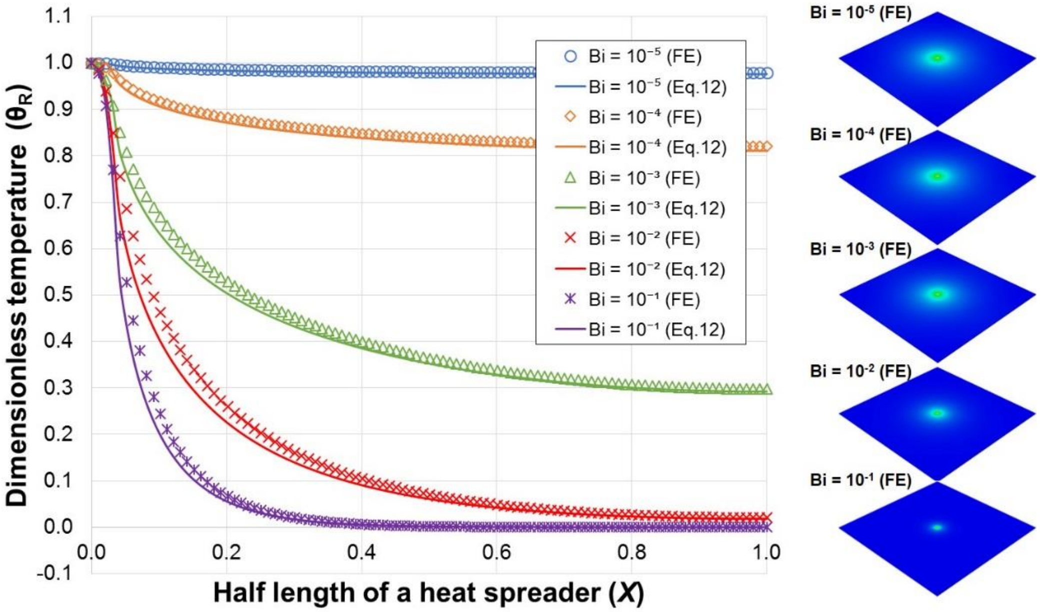

Figure 2.10 Comparison of dimensionless temperature along the half-length of heated surface of a transversely isotropic heat spreader ($\kappa^2 = 0.1$) for $A^* = 10^{-3}$ and $\tau = 10^{-2}$ with various Biot numbers from analytical and FE solutions.

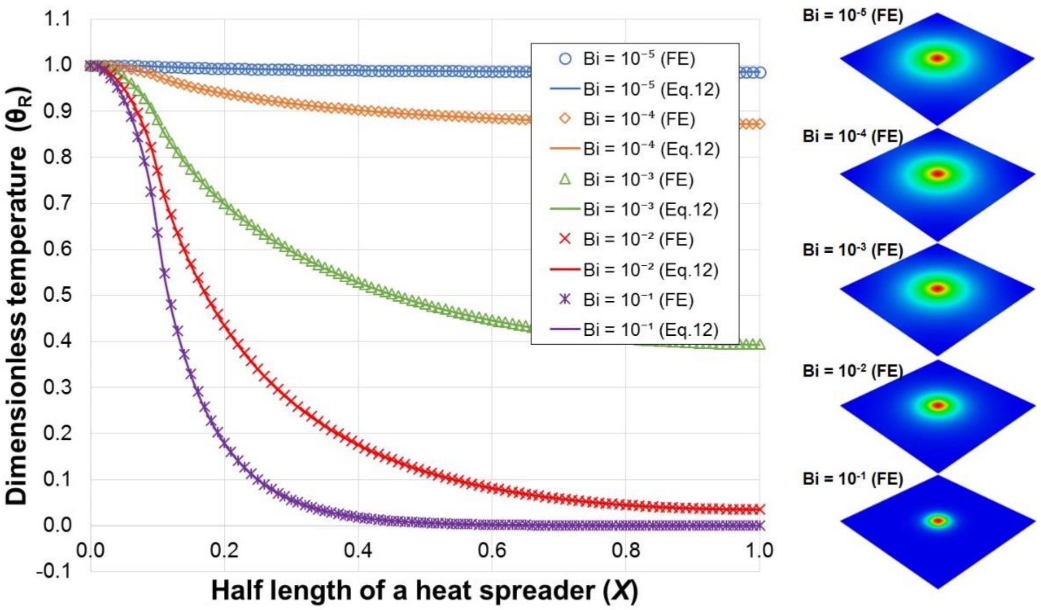

Figure 2.11 Comparison of dimensionless temperature along the half-length of heated surface of a transversely isotropic heat spreader ($\kappa^2 = 0.1$) for $A^* = 10^{-2}$ and $\tau = 10^{-2}$ with various Biot numbers from analytical and FE solutions.

The analytical dimensionless temperature distributions in a TI heat spreader with relatively high out-of-plane thermal conductivity ($\kappa^2 = 10$) at source-to-area ratios $A^* = 10^{-4}$, 10^{-3}, and 10^{-2} for various Biot numbers (Bi) are compared with FE solutions in Figs. 2.12-2.14. Similar to both the isotropic heat spreader ($\kappa^2 = 1$) and the TI heat spreader ($\kappa^2 = 0.1$), the analytical and FE solutions closely match each other as Bi decreases and A^* increases. A TI heat spreader with a higher out-of-plane thermal conductivity experiences more severe temperature gradients at the heated surface due to the dominance of heat transfer is in the thickness direction.

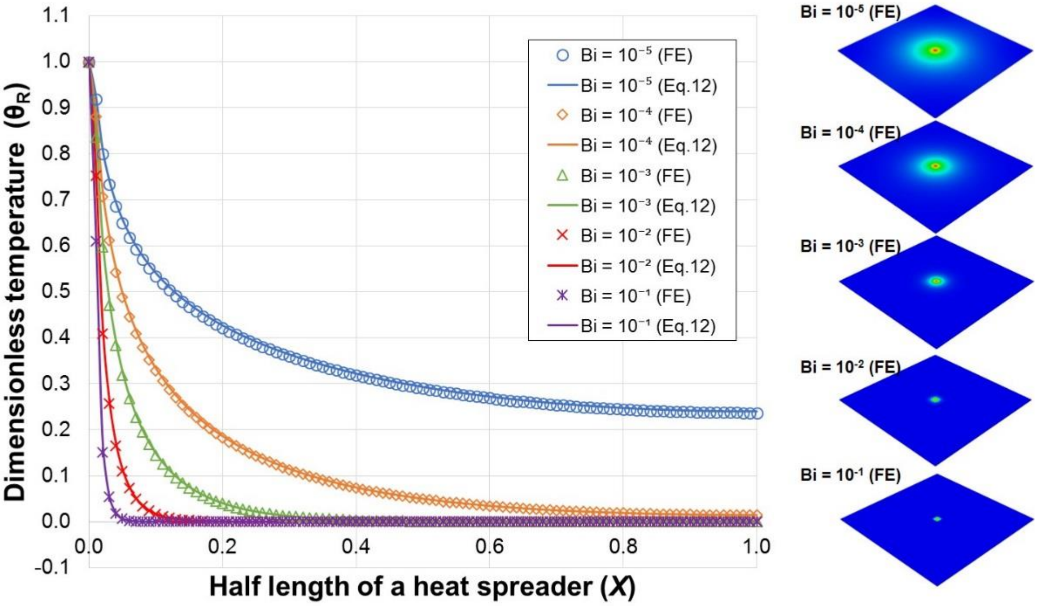

Figure 2.12 Comparison of dimensionless temperature along the half-length of heated surface of a transversely isotropic heat spreader ($\kappa^2 = 10$) for $A^* = 10^{-4}$ and $\tau = 10^{-2}$ with various Biot numbers from analytical and FE solutions.

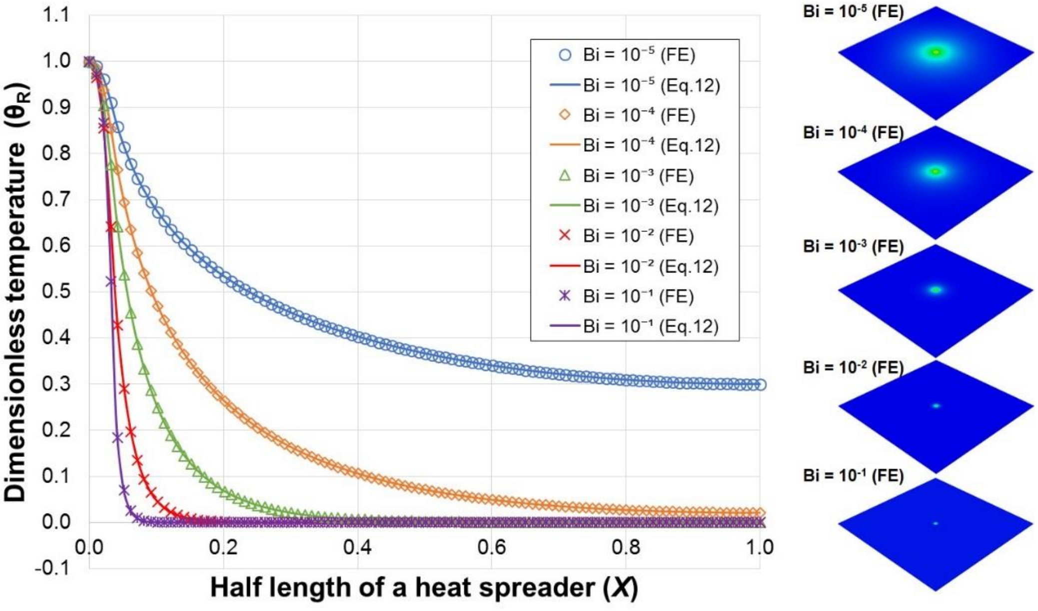

Figure 2.13 Comparison of dimensionless temperature along the half-length of heated surface of a transversely isotropic heat spreader ($\kappa^2 = 10$) for $A^* = 10^{-3}$ and $\tau = 10^{-2}$ with various Biot numbers from analytical and FE solutions.

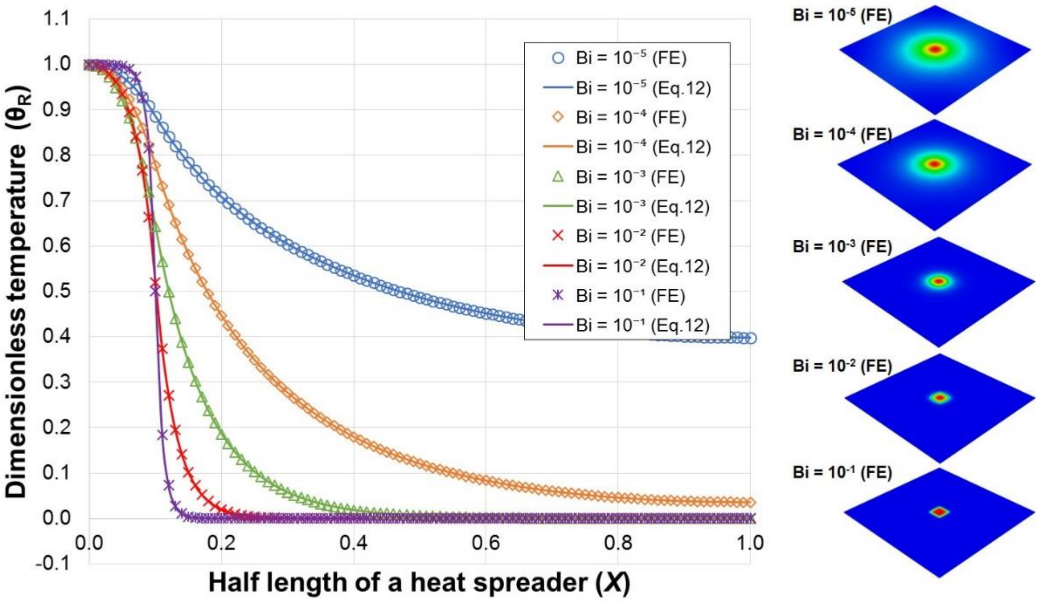

Figure 2.14 Comparison of dimensionless temperature along the half-length of heated surface of a transversely isotropic heat spreader ($\kappa^2 = 10$) for $A^* = 10^{-2}$ and $\tau = 10^{-2}$ with various Biot numbers from analytical and FE solutions.

The proposed analytical solutions for TI heat spreaders, regardless of κ^2, can accurately predict the dimensionless temperature distribution along the heated spreader surface. The accuracy of the truncated, 200-term analytical solutions was benchmarked with the FE solutions for many possible combinations of Bi, A^*, and κ^2. A summary of relative percentage differences between the analytical and FE solutions obtained at half length of the heat spreader ($X = 1$, $Y = 0$, and $Z = 1$) are provided in Appendix B.

2.6.2 Dimensionless Thermal Spreading Resistance

Figure 2.15 shows the dimensionless thermal spreading resistance (ψ^*_{sp}) plotted as a function of the source-to-spreader area ratio (A^*) for varying dimensionless heat spreader thicknesses (τ) for the thermal conductivity ratios $\kappa^2 = 0.1$, 1, 5 and 10. The magnitude of ψ_{sp}^{*} significantly increases as κ^2 increases. This is primarily due to ψ_{sp}^{*} being proportional to the maximum dimensionless temperature which is proportional to the out-of-plane thermal conductivity (*i.e.*, Fig. 2.3). Furthermore, ψ_{sp}^{*} becomes very sensitive to both A^* and τ as κ^2 increases. However, ψ_{sp}^{*} becomes nearly independent of A^* and κ^2 as τ increases. For all combinations of κ^2 and τ, ψ_{sp}^{*} is maximum at $A^* \approx 0.10$. The critical ψ_{sp}^{*} for each κ^2 is obtained by decreasing A^* (*i.e.*, a highly localized heat source) and increasing τ (*i.e.*, a very thick heat spreader). In the special case of $A^* < 10^{-4}$ and $\tau > 1.0$, the critical ψ_{sp}^{*} approaches ≈ 0.179, ≈ 0.563, ≈ 1.539, and ≈ 2.440 for $\kappa^2 = 0.1$, 1, 5 and 10, respectively. Especially for the isotropic heat spreader (*i.e.*, $\kappa^2 = 1$), this critical ψ_{sp}^{*} (≈ 0.563) agrees well with previously reported results [9, 11].

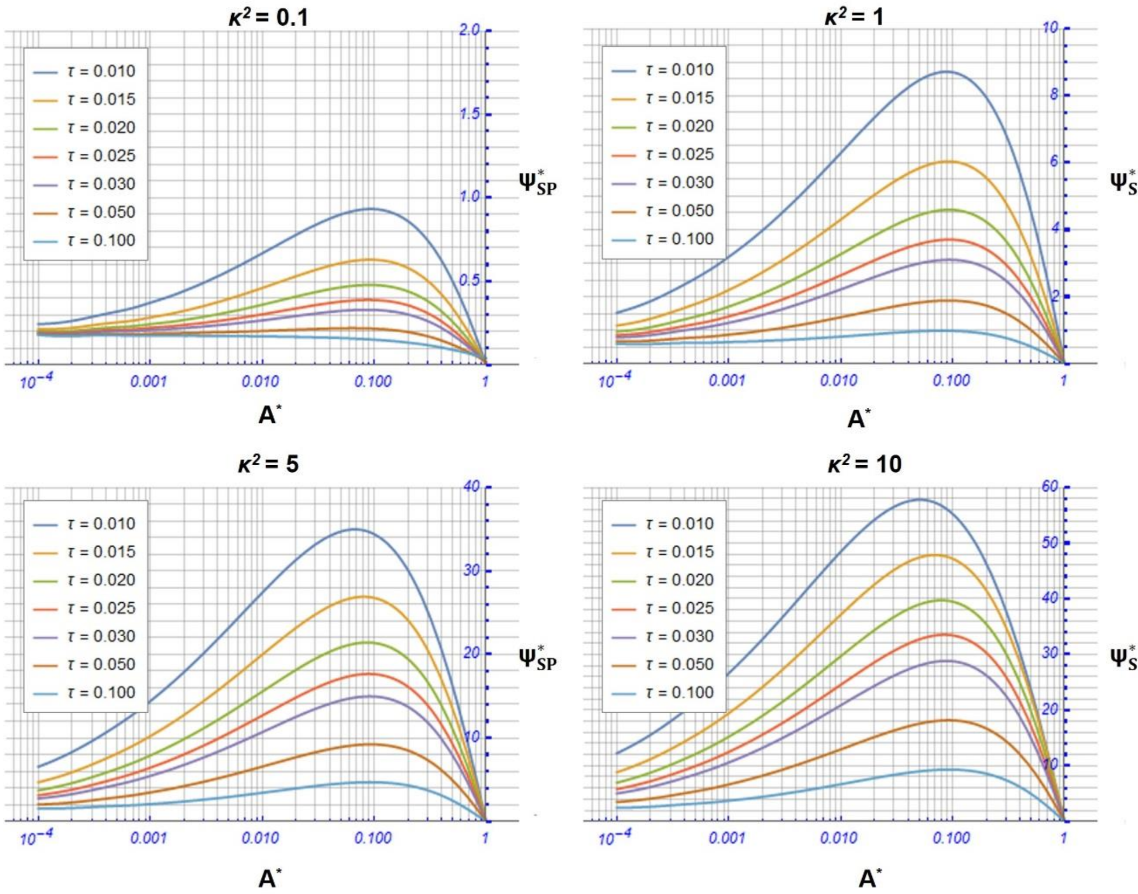

Figure 2.15 Dimensionless thermal spreading resistances versus area ratio (A^*) for various dimensionless heat spreader thicknesses (τ) and thermal conductivity ratios (κ^2) at Bi = 10^{-4}.

The dimensionless thermal spreading resistance can be plotted as a function of thermal conductivity ratios (κ^2), Biot number (Bi), and dimensionless heat spreader thicknesses (τ) for various source-to area ratios (A^*) (Fig 2.16). It may be seen that, for a given κ^2, the dimensionless thermal spreading resistance decreases as τ increases. The dimensionless thermal spreading resistance significantly increases as both κ^2 and A^* increase for any combination of Bi and τ, except for the special case of a thin TI heat spreader (*i.e.* $\tau \leq 0.10$ and $\kappa^2 > 1$) with $A^* \geq 0.01$.

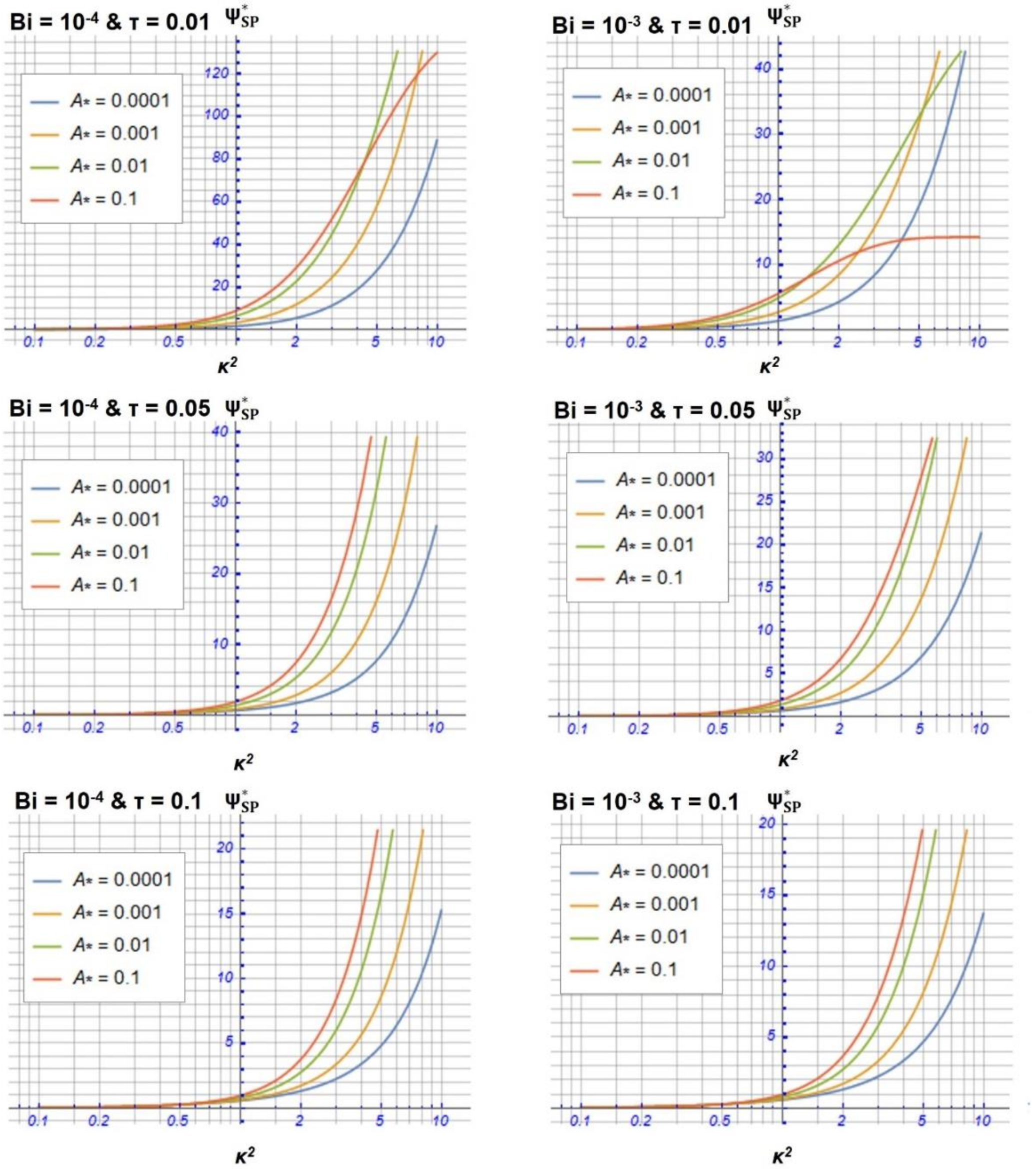

Figure 2.16 Dimensionless thermal spreading resistances versus thermal conductivity ratio (κ^2) for various area ratios (A^*), dimensionless heat spreader thicknesses (τ) and Biot numbers (Bi).

2.7 Conclusions

An analytical model for predicting the steady-state temperature distribution in a fiber-reinforced, transversely isotropic (TI) heat spreader with a square heat source applied at its center was developed and solved using an infinite Fourier cosine series expansion. The TI heat spreader corresponded to the case of uniformly-distributed fibers aligned in the heat spreader's thickness direction. The dimensionless maximum temperature distribution and corresponding thermal spreading resistance were determined for various combinations of the Biot number, dimensionless heat spreader thickness, source-to-spreader area ratio, and thermal conductivity ratio.

The results showed that the magnitude of the dimensionless temperature distribution increased as both the source-to-spreader area ratio and the thermal conductivity ratio increase, resulting in lower through-thickness heat transfer rates. Steep dimensionless temperature gradients along the in-plane directions were more noticeable for low source-to-spreader area ratios and high thermal conductivity ratios. Furthermore, the magnitude of the dimensionless thermal spreading resistance significantly increased as the thermal conductivity ratio increased. As the thermal conductivity ratio increased, the dimensionless thermal spreading resistance became very sensitive to both the source-to-spreader area ratio and the dimensionless heat spreader thickness. A critical, maximum dimensionless thermal spreading resistance was obtained for a given thermal conductivity ratio by decreasing the source-to-spreader area ratio (*i.e.*, a highly localized heat source) and increasing the heat spreader thickness (*i.e.*, a very thick heat spreader). For the isotropic heat spreader, the critical dimensionless thermal spreading resistance agreed well with that described in the literature [9, 11].

The accuracy of the presented analytical solutions was benchmarked with FE solutions. For many parameter combinations, the analytical solution possessed lower than 1% percent difference relative to the corresponding FE solution, indicating that using a

Fourier cosine series expansion is effective and accurate in predicting the temperature field and the thermal spreading resistance of both isotropic and TI heat spreaders. The accuracy of the analytical solutions may be enhanced by increasing the number of terms in the truncated Fourier series. Similarly, the FE solutions may be improved by increasing the mesh refinement in the vicinity of the point heat source.

The presented analytical solutions derived herein provide a useful means to visualize the TI heat spreader dimensionless temperature distribution, and corresponding thermal spreading resistance, as a function of various geometric and thermal parameters. This provides more flexibility to the engineer designing anisotropic heat spreaders for various electronics cooling or aerospace applications. These analytical solutions are relatively simple and practical to implement, computationally efficient, and helpful in understanding thermal issues in both isotropic and TI heat spreaders. They provide a platform for optimizing composite materials or two-phase heat spreaders for various geometric and matrix/constituent combinations.

2.8 References

[1] Vinson, J.R. and R.L. Sierakowski, The Behavior of Structures Composed of Composite Materials. Vol. 5. 2012: Springer Science & Business Media.

[2] Campbell, F.C., Lightweight Materials: Understanding the Basics. 2012: ASM International.

[3] Njuguna, J. and K. Pielichowski, "Polymer Nanocomposites for Aerospace Applications: Properties," *Advanced Engineering Materials*, 2003, **5**(11): p. 769-778.

[4] Kolesnikov, B., L. Herbeck, and A. Fink, "CFRP/Titanium Hybrid Material for Improving Composite Bolted Joints," *Composite Structures*, 2008, **83**(4): p. 368-380.

[5] Kennedy, D.P., "Spreading Resistance in Cylindrical Semiconductor Devices," *Journal of Applied Physics*, 1960, **31**(8): p. 1490-1497.

[6] Nelson, D. and W. Sayers. "A Comparison of Two-Dimensional Planar, Axisymmetric and Three-Dimensional Spreading Resistances," in the *Semiconductor Thermal Measurement and Management Symposium*, 1992: IEEE.

[7] Lee, S., V.A. Seaho Song, and K.P. Moran. "Constriction/Spreading Resistance Model for Electronics Packaging," in the *Proceedings of the 4th ASME/JSME Thermal Engineering Joint Conference*, 1995.

[8] Fisher, T.S., F. Zell, K.K. Sikka, and K.E. Torrance, "Efficient Heat Transfer Approximation for the Chip-on-Substrate Problem," *Journal of Electronic Packaging*, 1996, **118**(4): p. 271-279.

[9] Ellison, G.N., "Maximum Thermal Spreading Resistance for Rectangular Sources and Plates with Nonunity Aspect Ratios," *Components and Packaging Technologies*, 2003, **26**(2): p. 439-454.

[10] Feng, T. and J. Xu, "An Analytical Solution of Thermal Resistance of Cubic Heat Spreaders for Electronic Cooling," *Applied Thermal Engineering*, 2004, **24**(2): p. 323-337.

[11] Thompson, S.M. and H. Ma, "Thermal Spreading Analysis of Rectangular Heat Spreader," *Journal of Heat Transfer*, 2014, **136**(6): p. 064503.

[12] Thompson, S. and H. Ma, "Recent Advances in Two-Phase Thermal Ground Planes," *Annual Review of Heat Transfer*, 2015, **18**: p. 101-153.

[13] Gholami, A. and M. Bahrami, "Thermal Spreading Resistance inside Anisotropic Plates with Arbitrarily Located Hotspots," *Journal of Thermophysics and Heat Transfer*, 2014, **28**(4): p. 679-686.

[14] Ying, T. and K. Toh. "A Heat Spreading Resistance Model for Anisotropic Thermal Conductivity Materials in Electronic Packaging," in the *Proceeding of the 7th Intersociety Conference on Thermal and Thermomechanical Phenomena in Electronic Systems*, 2000: IEEE.

[15] Cho, S., K. Kikuchi, T. Miyazaki, K. Takagi, A. Kawasaki, and T. Tsukada, "Multiwalled Carbon Nanotubes as a Contributing Reinforcement Phase for the Improvement of Thermal Conductivity in Copper Matrix Composites," *Scripta Materialia*, 2010, **63**(4): p. 375-378.

[16] Sommers, A., Q. Wang, X. Han, C. T'Joen, Y. Park, and A. Jacobi, "Ceramics and Ceramic Matrix Composites for Heat Exchangers in Advanced Thermal Systems—A review," *Applied Thermal Engineering*, 2010, **30**(11): p. 1277-1291.

[17] Muzychka, Y., J. Culham, and M. Yovanovich, "Thermal Spreading Resistance of Eccentric Heat Sources on Rectangular Flux Channels," *Journal of Electronic packaging*, 2003, **125**(2): p. 178-185.

[18] Muzychka, Y., M. Yovanovich, and J. Culham, "Thermal Spreading Resistance in Compound and Orthotropic Systems," *Journal of Thermophysics and Heat Transfer*, 2004, **18**(1): p. 45-51.

[19] Muzychka, Y., "Spreading Resistance in Compound Orthotropic Flux Tubes and Channels with Interfacial Resistance," *Journal of Thermophysics and Heat Transfer*, 2014, **28**(2): p. 313-319.

[20] Bagnall, K.R., Y.S. Muzychka, and E.N. Wang, "Analytical Solution for Temperature Rise in Complex Multilayer Structures with Discrete Heat Sources," *IEEE Transactions on Components, Packaging and Manufacturing Technology*, 2014, **4**(5): p. 817-830.

[21] ABAQUS, "ABAQUS Documentation," *Dassault Systémes Simulia Corp.*, 2014.

[22] Azar, K., B. Tavassoli, and A. Koss, Qpedia Thermal Management eMagazine. Vol. 4. 2011: Advanced Thermal Solutions.

CHAPTER III

ARTIFICIAL LIGHTNING STRIKE TESTING OF AS4/8552 CARBON/EPOXY COMPOSITES PROTECTED WITH EITHER COPPER MESH OR PITCH CARBON FIBER PAPER LAYERS

3.1 Abstract

The lightning damage resistance of unprotected nine-ply AS4/8552 carbon/epoxy laminates with a [+45/-45/0/0/90/0/0/-45/+45] layup were characterized. The laminates were subjected to standard impulse current waveforms with nominal 50, 125, and 200 kA peak currents. The observed surface and through-thickness damage gradually increased as the peak current increased. Lightning damage to carbon/epoxy laminate includes fiber rupture, tow splitting, matrix decomposition, and localized delamination damage at the lightning attachment point. The regions of severe fiber damage were elongated along the outermost lamina's fiber orientation, indicating that such damage is due to local electrical conduction and instantaneous Joule heating occurring along the fiber orientation. In order to evaluate several potential lightning protection layers, copper mesh (CM)-protected and pitch carbon fiber paper (PCFP)-protected laminates were fabricated and then subjected to nominal 50 and 125 kA peak currents. Both the CM and the PCFP outer layers successfully mitigated lightning damage development. Lightning damage in the CM-protected and the PCFP-protected laminates was much smaller than those in the unprotected laminates. The CM layer showed better lightning protection ability than the

PCFP outer layer due to its relatively high electrical conductivity. The PCFP protection layer electrical conductivity, however, can be tailored to improve its lightning strike protection ability. Thus, PCFP or similar conductive carbon-based layers may be used to inhibit lightning damage development, and serving as an effective, lightweight non-metallic lightning protection layer.

3.2 Introduction

Lightning strikes are one of the major threats to composite aircraft structures. Lightning damage characterization in composites has been the focus of a number of experimental studies [1-10] and numerical modeling investigations [11-18]. While lightning damage to carbon/epoxy laminates induced by moderate (≤ 50 kA) peak currents has been reasonably well characterized, damage induced by intermediate (50-100 kA) or extremely high (≥ 100 kA) peak currents are not well understood. Higher peak lightning currents can induce greater surface damage and deeper damage through-thickness penetration since rapid temperature increases are due to Joule heating proportional to the peak lightning current [1, 3-5]. Lightning damage to carbon/epoxy laminates does not vary linearly with the peak lightning current. One of the goals of the present study is to understand lightning damage to traditional carbon/epoxy laminates subjected to a wide range of peak currents. Three peak currents were considered: (1) 50 kA (2) 125 kA, and 200 kA.

As discussed in Chapter 1, the use of metallic lightning protection layers somewhat offset the benefits of using lightweight CFRP composites for aircraft structural applications. Since lightning strikes carry large transient electrical currents and electromagnetic forces [13], CFRP composites should be designed with high electrical conductivities that enable them to withstand lightning currents with minimal damage [19]. One prevalent approach to mitigate lightning damage is to bond highly conductive outer protection layers to CFRP composites. Two representative lightning protection layers are evaluated in this study: (1) a copper mesh (CM) commonly used for aircraft lightning strike protection and (2) a highly conductive pitch carbon fiber paper (PCFP), consisting of two-dimensional, randomly oriented pitch-derived carbon fibers (PCFs).

3.3 Laboratory-Scale Lightning Strike Test

3.3.1 AS4/8552 Laminated Test Coupon Preparation

The carbon/epoxy laminates were fabricated using nine-ply Hexcel AS4/8552 unidirectional prepregs (ply thickness, 0.125 mm) with a [+45/-45/0/0/90/0/0/-45/+45] layup; this layup is identical to that commonly used in the outer skin of Pultruded Rod Stitched Efficient Unitized Structure (PRSEUS) concept (Chapter 6). The laminates had in-plane dimensions of 200×200 mm^2. “Protected” laminates were manufactured by co-curing a single CM or PCFP protection layer to a given baseline carbon/epoxy laminate using the manufacturer’s recommended epoxy cure schedule [20]. Hexcel Redux 330 MPCU expanded CM (nominal thickness, 0.1 mm from [21]) impregnated with toughened epoxy resin and Osaka Gas Chemical DONACARBO PCFP (nominal thickness, 0.5 mm from [22]) were used as protection layers in this study. A summary of dimensions and layup for the unprotected and protected carbon/epoxy laminates is included in Table 3.1.

Table 3.1 Dimensions and layup of the unprotected, CM-protected, and PCFP-protected AS4/8552 carbon/epoxy laminates

Test Coupons	Protection Layer	Nominal Dimensions (mm)			Layup
		Length	Width	Total Thickness	
Baseline Laminate	-	200	200	1.125	[+45/-45/0/0/90/0/0/-45/+45]
CM-protected Laminate	CM[a]	200	200	1.225	[CM+45/-45/0/0/90/0/0/-45/+45]
PCFP-protected Laminate	PCFP[b]	200	200	1.625	[PCFP+45/-45/0/0/90/0/0/-45/+45]

[a] Hexcel Redux 330 MPCU expanded copper mesh (CM) [21].
[b] Osaka Gas Chemical DONACARBO pitch carbon fiber paper (PCFP) [22].

3.3.2 High Impulse Current Generator

A one-stage impulse current generator was designed and assembled to produce standard impulse current waveforms consistent with actual lightning strikes [23]. The impulse current generator (Fig. 3.1) built at the Mississippi State University High-Voltage Lab (MSU-HVL) is able to produce double exponential current waveforms with up to 200 kA peak currents. The generator controls the electrical energy by adjusting the charging voltage for the unit's capacitors.

The trigatron spark gap switch (Fig. 3.1a) was constructed to initiate an impulse current discharge. This spark gap switch consisted of two separated electrodes operating in air at atmospheric pressure. The upper electrode was connected to a set of capacitors (Fig 3.1b) and the lower electrode was grounded. Electrical current was discharged across the gap between the two electrodes. The gap spacing was optimized to achieve reliable control over the generated current. Preliminary test results showed that (1) the peak current depended on the gap spacing and (2) a minimum gap spacing existed below which un-triggered (or self-triggered) current discharges would occur.

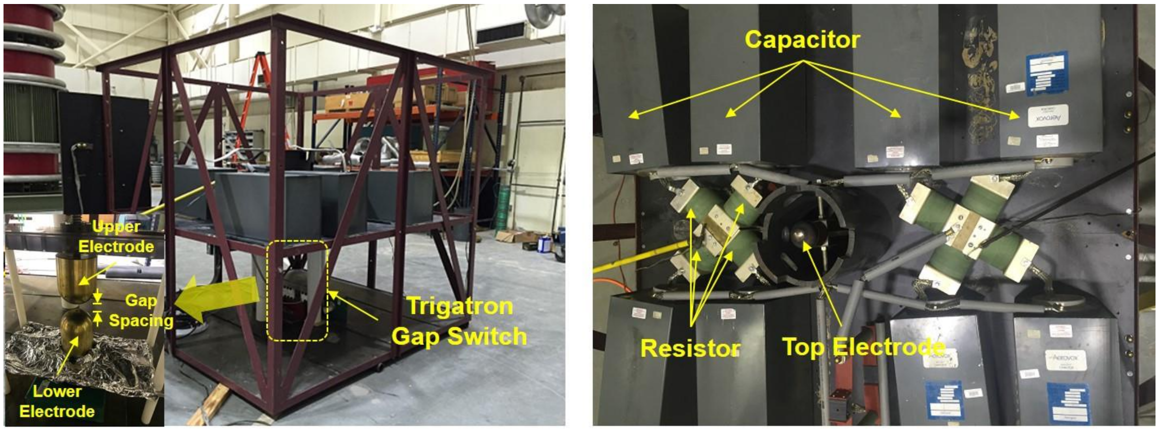

(a) (b)

Figure 3.1 MSU-HVL impulse current generator: (a) edge and (b) top views.

Table 3.2 contains the charging voltage and corresponding peak current with the optimized trigatron spark gap spacing. A more detailed description of the MSU-HVL impulse current generator will be discussed in as part of future work.

Table 3.2 Charging voltage and corresponding peak currents with the trigatron spark gap spacing

Charging Voltage (kV)	Peak Current Level (kA)	Nominal Spark Gap Spacing (mm)
10	50	9
24	125	15
38	200	25

3.3.3 Grounding Conditions

In traditional carbon/epoxy laminates, electrical current flow depends on both the optimal conduction path (*i.e.*, in the fiber direction) and grounding conditions. The shape and extent of lightning damage can vary depending on local grounding conditions. Figure 3.2 shows the grounding conditions of the carbon/epoxy laminates used in this study. All four edges of the laminates were smoothly sanded and then grounded using aluminum plates to permit evenly distributed electrical conduction throughout the laminates. Flexible braided copper straps were inserted between four aluminum strips overlapping the perimeter of the laminate and connected to an underlying steel base plate that grounded the contacting surface. To prevent through-thickness electrical current flow, a thin insulating acrylic plate was placed between the laminate and the steel base plate. This grounding condition promoted electrical current flow on the top lamina surface, thus reducing through-thickness damage penetration, consistent with an aircraft's natural grounding conditions.

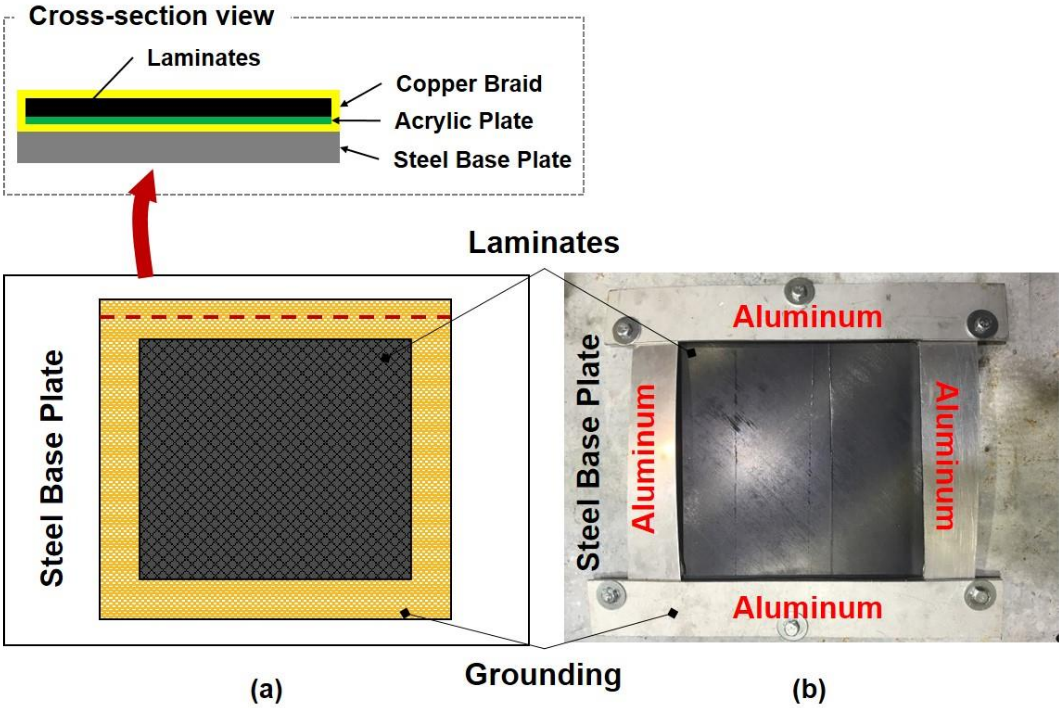

Figure 3.2 (a) Schematic and (b) photograph of the grounding condition.

3.3.4 Impulse Current Waveforms

Figure 3.3 compares the standard impulse current waveform component A defined in SAE ARP 5412 [24] with the measured MSU-HVL 200 kA peak current impulse current waveform. The standard SAE waveform [24] has 200 kA peak current, a rise time of 6.4 μs, and the decay time of 69 μs with a ±20% tolerance level for repeatability. The MSU-HVL 200 kA peak current waveform was consistent with the standard SAE component A waveform. The rise and decay time determined from the MSU-HVL current waveforms were 18 μs and 75 μs (*cf.* Table 3.3). The MSU-HVL 200 kA current waveform had a rise time slightly longer than that of the SAE component A waveform; the decay time was consistent. The difference in the rise time between the MSU-HVL lightning waveform and the SAE component A waveform is not significant because the rise time is typically less important than decay time in determining the time response of an impulse current waveform [25]. A significant variation in rise time will not lead to noticeable changes in lightning-induced damage since lightning damage is governed by the amount of electrical energy, defined as the action integral, injected into the composite (integral of the square of the time-varying current over its time duration [26]). Similar action integrals were observed for both the MSU-HVL 200 kA current waveform and the SAE component A waveform (*cf.* Table 3.3).

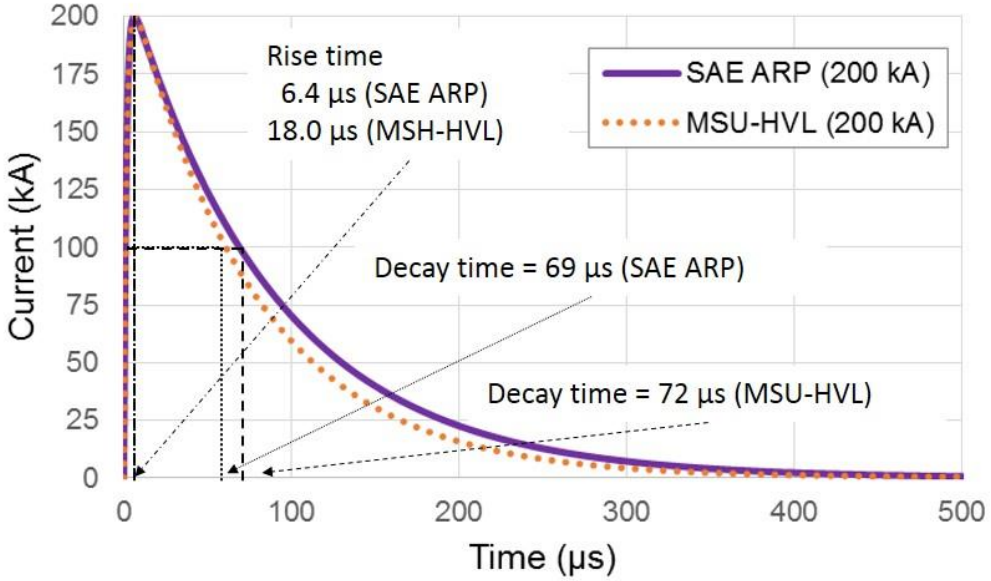

Figure 3.3 SAE component A [24] and MSU-HVL impulse current waveform (200 kA nominal peak current)

Table 3.3 Lightning waveform characteristics

Nominal Peak Current (kA)	Rise Time (µs)	Decay Time (µs)	Action Integral ($\times 10^5$ A^2s)	Source
50	18.0	75	1.3	MSU-HVL*
125	18.0	75	8.5	MSU-HVL*
200	18.0	75	21.5	MSU-HVL*
200	6.4 (±20%)	69 (±20%)	20.0 (±20%)	SAE ARP 5412 [24]

*Mississippi State University High Voltage Lab

Figure 3.4 shows the MSU-HVL impulse current waveforms with 50, 125, and 200 kA nominal peak currents. Note that rise and decay times of a current waveform strongly depend on the circuit parameters for the system (*i.e.*, resistance and inductance). These are independent of the charging voltage, peak current, and test specimen. An impulse current generator typically has a constant resistance and inductance. Thus, the resulting rise and decay times of a current waveform are relatively constant, regardless of the magnitude of the peak current. For this reason, all MSU-HVL lightning waveforms showed identical rise and decay times. However, the action integrals of MSU-HVL lightning waveforms varied depending on the peak current, as would be expected.

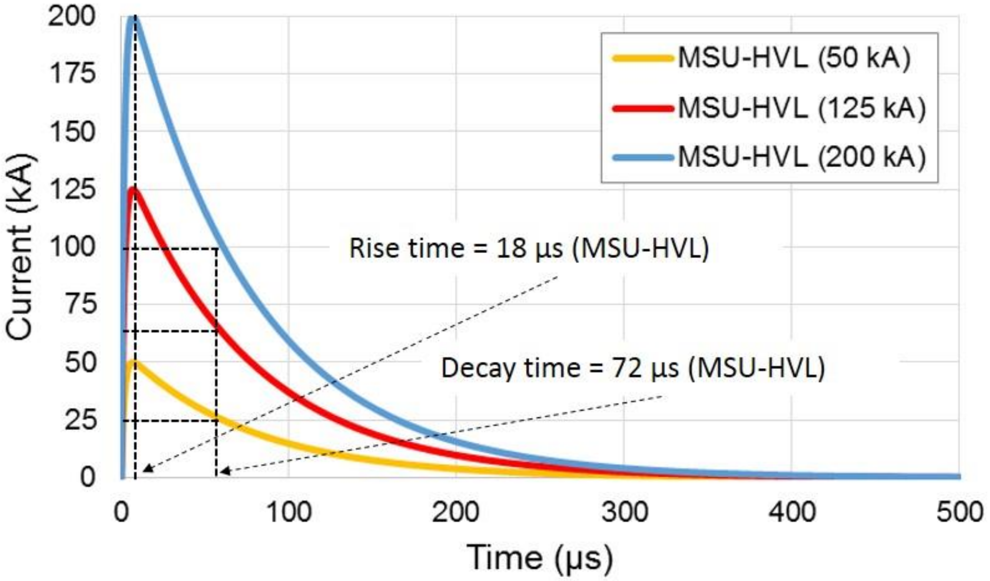

Figure 3.4 MSU-HVL impulse current waveforms with 50, 125, and 200 kA nominal peak currents.

3.4 Results and Discussion

Two 50 kA, one 125kA, and one 200 kA nominal peak current tests were performed on the unprotected laminates to investigate lightning damage characterization. Similarly, a single 50 kA, 125kA, and 200 kA nominal peak current test was performed on each CM-protected and PCFP-protected laminate to evaluate the effectiveness of lightning protection layers.

3.4.1 Unprotected AS4/8552 Carbon/Epoxy Laminates

Figure 3.5 shows typical lightning damage to unprotected AS4/8552 carbon/epoxy laminates after being subjected to nominal 50, 125, and 200 kA peak currents. The actual measured peak currents are included for clarity in the figure. Red and orange dotted lines denote severe fiber damage in the +45° outer plies and noticeable fiber damage in underlying -45° plies, respectively. In addition, the approximate domains with visible delaminations are presented in the figure. Intense carbon fiber damage (fiber rupture, tow splitting, etc.) occurred at the lightning attachment locations along with significant amounts of matrix decomposition and delaminations. Lightning damage formation is a consequence of a rapid temperature increase via Joule heating and mechanical pressure (*i.e.*, electromagnetic force and acoustic force). The local laminate temperature may reach as high as the carbon fiber sublimation temperature (3,316˚C from [27]) resulting in thermal ablation. The sudden temperature increase is due to the rapid expansion of the air surrounding and within the lightning arc channel [13]. Carbon fibers can also fracture due to dynamic thermal strains. Carbon fibers have a negative thermal expansion coefficient in the axial direction which induces contraction as the fiber temperature increases. The resulting significant thermal strains can lead to carbon fiber breakage/rupture, as well as tow splitting and fiber matrix decohesion.

(a) 51kA

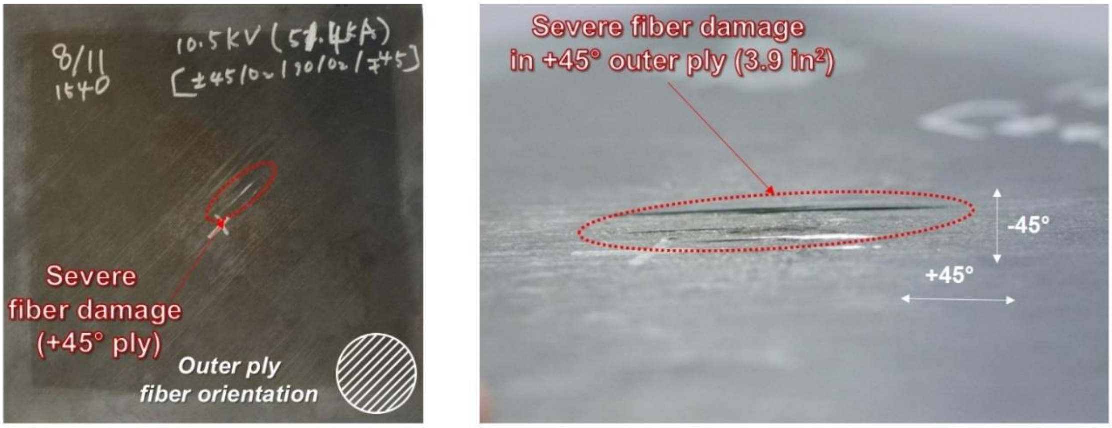

(b) 126kA

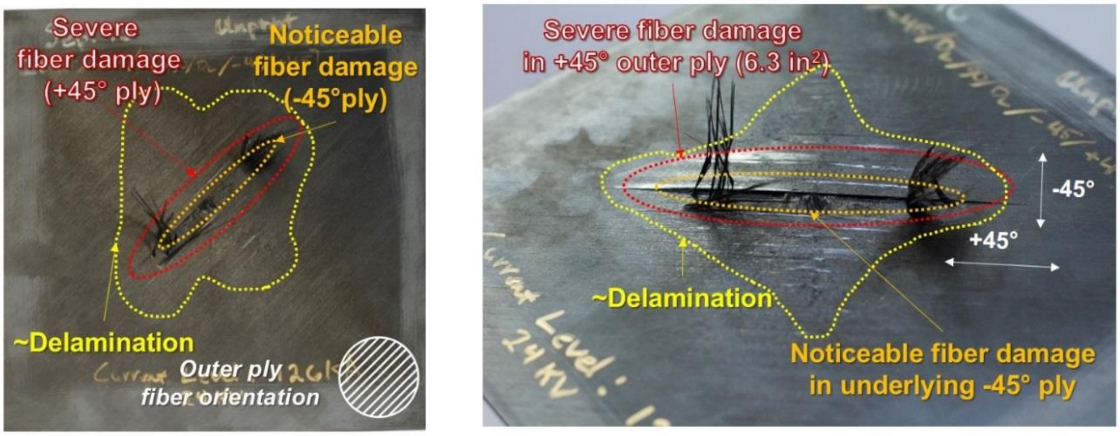

(c) 189kA

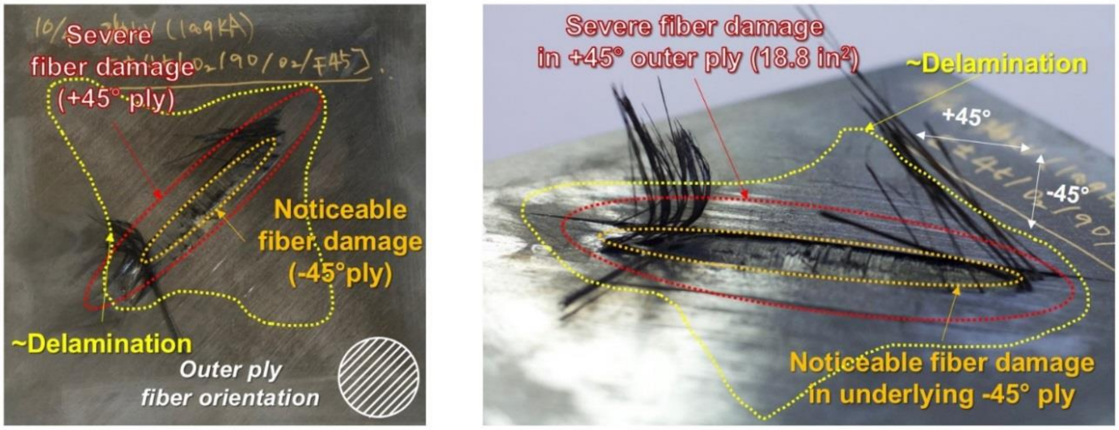

Top view Side view

Figure 3.5 Typical lightning damage in unprotected AS4/8552 carbon/epoxy laminates after they are subjected to (a) 51 kA, (b) 126 kA, and (c) 189 kA peak currents.

The damaged laminates displayed severe fiber breakage in the +45˚ outer ply, noticeable fiber breakage in underlying -45˚ ply, clear evidence of matrix decomposition/burning, and localized delamination (Fig. 3.5). Laminates subjected to 50 kA peak current exhibited relatively small domains of matrix decomposition and localized delamination at the lightning attachment location. The regions of fiber breakage in the +45˚ outer ply and in the underlying -45˚ ply drastically increased as the peak current increased. For instance, the measured regions of severe fiber damage in +45˚ outer plies increased from 3.9 in^2 (51 kA) to 6.3 in^2 (126 kA) to 18.8 in^2 (189 kA). Higher peak current leads to markedly greater lightning damage (carbon fiber damage, matrix decomposition, delamination, etc.) to the laminates. This makes sense since the degree of Joule heating is proportional to electrical energy which is also proportional to the square of the applied electrical current. Higher peak currents produce greater electrical energy at the same rise and decay time durations. Thus, higher peak currents lead to more Joule heating (*i.e.*, more thermal damage).

Typical carbon/epoxy composites experience matrix decomposition once the local composite temperature reaches 300-500˚C ([28, 29]), while carbon fibers remain undamaged in this temperature range. In the laminate tests, the matrix damage in regions surrounding the severe fiber damage domain was relatively minor, indicating the presence of a steep temperature gradient near the lightning attachment location. Moreover, large scale delaminations were easily visible in high-current specimens that extended well beyond the domain with extensive fiber damage (Fig. 3.5). Delamination is due to lightning-driven mechanical pressures that generate compressive through-the-thickness stress waves that reflect as tensile stresses at the innermost lamina [30].

Surface inspection of the damaged AS4/8552 laminates showed that higher peak currents led to more through-thickness damage (*i.e.*, noticeable fiber damage in inner plies, delamination). More fiber damage and localized delamination occurred in the underlying plies at higher peak currents. Destructive sectioning of the damaged laminates is ongoing. Preliminary destructive sectioning of damaged laminates subjected to nominal 125 kA peak current suggests that localized fiber rupture, tow splitting, and matrix decomposition occur in the top 2-3 plies. In addition, delamination between these outermost plies could extend well beyond the domain with visible extreme fiber surface damage. In general, the delamination would extend both parallel and orthogonal to the outer ply fiber orientation (Fig. 3.5). Specific details of through-thickness lightning damage morphology is currently being investigated.

3.4.2 CM and PCFP-Protected AS4/8552 Carbon/Epoxy Laminates

Lightning protection layers are sacrificial layers that aim to distribute electric current across their surfaces, thus reducing corresponding thermal damage. In a preliminary study, visible lightning damage to unprotected AS4/8552 carbon/epoxy laminates was compared to analogous “protected” laminates with either a CM or PCFP outer layer. CM and PCFP outer layers arguably better distribute electrical currents over their surfaces due to their relatively high electrical conductivities resulting in less in-plane and through-thickness damage development.

The unprotected and protected laminates were subjected to nominal 50 and 125 kA peak currents. Only one test was performed for each protection layer/peak current combination. As a reminder, the unprotected AS4/8552 laminate has a layup of

[+45/-45/0/0/90/0/0/-45/+45]; the protected carbon/epoxy laminates contained an outer layer of either CM or PCFP.

Figure 3.6 contains images of lightning damage in AS4/8552 laminates as well as identical laminates with either a CM or PCFP protection layer. Figures 4.3a and 4.3b contain images of unprotected laminates subjected to 50 or 125 kA nominal peak currents, respectively. Included in the figure is a description of the visible surface damage. For both peak currents, the unprotected laminates experienced intense fiber damage and matrix decomposition at the lightning attachment point. For a 50 kA nominal strike (Fig. 3.6a), the visible local damage was limited to the outermost +45˚ ply. For a 125 kA nominal peak current (Fig. 3.6b), however, the magnitude and severity of the intense local damage markedly increased. There was visible fiber rupture, tow splitting, and matrix decomposition in the underlying -45˚ ply, as well as widespread delamination that was easily visible than surface inspections. In contrast, CM-protected laminates subjected to 50 and 125 kA nominal peak currents displayed no visible damage to the underlying composite (Fig. 3.6c and 3.6d, respectively). The CM protection layers remained intact and undamaged. CM exhibits high, isotropic electrical conductivities that can effectively distribute electrical currents and Joule heating over its surface. This reduces through-thickness damage development. Instead, widespread minor surface scorching was observed due to epoxy adhesive decomposition in the Hexcel Redux 330 MPCU expanded CM. Such minor surface scorching is confined to the CM layer. Thus, the underlying laminates visually appeared remained undamaged. No visual evidence of underlying carbon fiber damage, matrix decomposition, and localized delamination occurred in the CM-protected laminates. The regions of surface scorching were somewhat circular due to isotropic CM electrical/thermal conductivities; these regions increased in size with increasing current (*cf.*, Fig. 3.6c and 3.6d).

The PCFP protection layer also effectively mitigated lightning damage development. Much smaller domains with carbon fiber damage were observed for the PCFP-protected laminates than for unprotected laminates. At the 50 kA peak current (Fig. 3.6e), there was no visual evidence of damage in the underlying laminate. Instead, a small pitch carbon fiber (PCF)-damage region was observed in the PCFP outer layer. At the 125 kA peak current (Fig. 3.6f), damage to the PCFP layer increased, but this was still much smaller than that of the unprotected laminates (Fig. 3.6b).

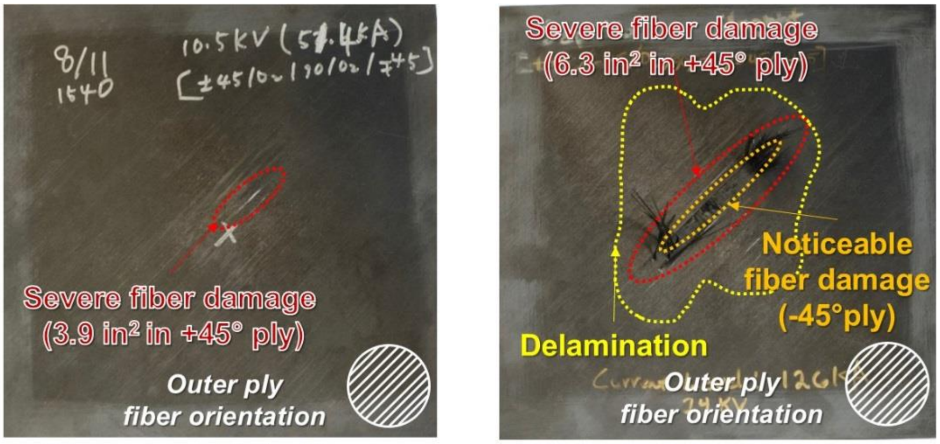

(a) Unprotected (51 kA)

(b) Unprotected (126 kA)

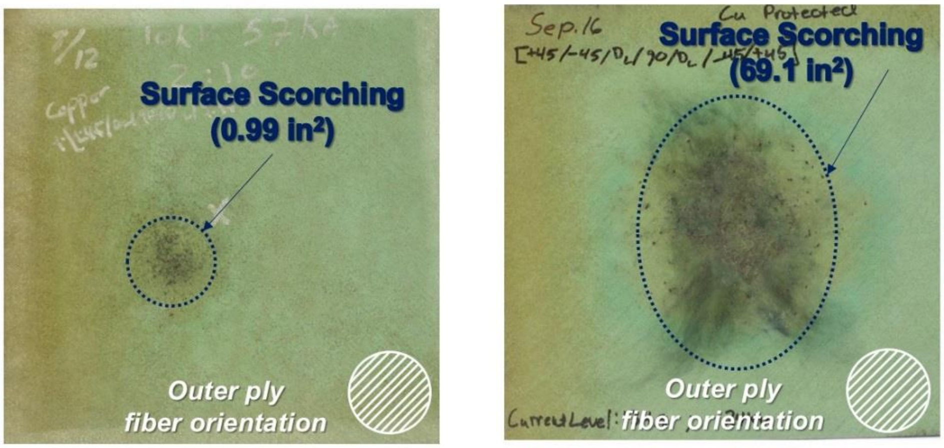

(c) CM-protected (57 kA)

(d) CM-protected (135 kA)

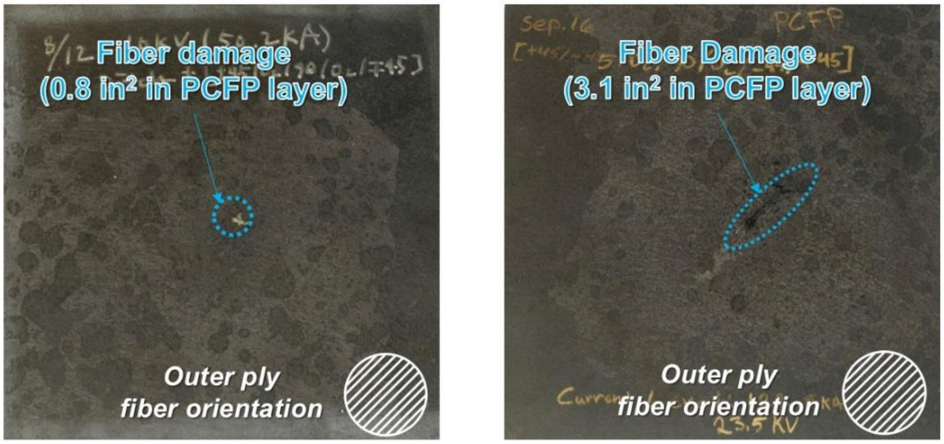

(e) PCFP-protected (50 kA)

(f) PCFP-protected (123 kA)

Figure 3.6 Lightning damage to (a-b) unprotected, (c-d) CM-protected, and (e-f) PCFP-protected AS4/8552 carbon/epoxy laminates subjected to 50 and 125 kA peak currents.

As an aside, PCFP protection layer in-plane and through-thickness electrical conductivities can be highly tailored to improve its lightning strike protection abilities by controlling PCF volume fraction and fiber orientation. Therefore, PCFP protection layers or similar conductive carbon-based layers may be used to inhibit through-thickness lightning damage development, thus serving as an effective, non-metallic lightning protection layer in future PRSEUS panels (see Chapter 6).

3.5 Conclusions and Recommendations

Laboratory-scale lightning strike tests were performed on nine-ply AS4/3506 carbon/epoxy laminates with a [+45/-45/0/0/90/0/0/-45/+45] layup to characterize lightning damage development. Three 50 kA, two 125 kA, and two 200 kA peak current tests were performed on unprotected laminates. The laminates were subjected to standard impulse current waveforms with nominal 50, 125, and 200 kA peak currents. Lightning damage includes severe localized fiber rupture, tow splitting, and matrix decomposition. Higher peak currents led to greater lightning damage. The regions of severe carbon fiber damage gradually increased as the peak current increased. Surface inspection of lightning damage at attachment locations showed higher peak current caused more through-thickness damage.

Two lightning protection layers were considered to evaluate lightning protection ability: (1) a copper mesh (CM) commonly used for aircraft lightning strike protection and (2) highly conductive pitch carbon fiber paper (PCFP). “Protected” laminates were manufactured by co-curing a single CM or PCFP protection layer to a given baseline carbon/epoxy laminate using the manufacturer’s recommended epoxy cure schedule. One 50kA and one 125 kA peak current tests were conducted on either CM-protected or

PCFP-protected laminates. Both the CM-protected and the PCFP-protected laminates exhibited much smaller lightning damaged-region than the unprotected laminates. The CM layer remained relatively undamaged after lightning strike tests and showed somewhat better lightning protection ability than the PCFP outer layer due to its relatively high in-plane electrical conductivity. The CM protected laminates displayed widespread small-scale surface scorching. Lightning damage in the PCFP-protected laminates was much smaller than those in the unprotected laminates. PCFP protection layer in-plane and through-thickness electrical conductivities can be tailored to improve its lightning strike protection abilities. Thus, PCFP protection layer or similar conductive carbon-based layers may be used to inhibit through-thickness lightning damage development, thus serving as an effective, lightweight non-metallic lightning protection layer.

Additional phased-array ultrasonic inspection coupled with destructive sectioning of the unprotected, CM-protected and PCFP-protected AS4/8552 carbon/epoxy laminates will be performed to characterize internal damage morphologies (*i.e.*, noticeable fiber damage in inner plies, delamination). Moreover, lightning strike protection layers can be designed for minimizing both surface and through-thickness damage. As expected, greater in-plane and through-thickness electrical conductivities of a protection layer reduce through-thickness damage. The significance of protection layer properties (*i.e.*, ratio of in-plane to through-thickness electrical/ thermal conductivities) and interfacial properties (*i.e.*, adhesive electrical/ thermal conductivities) on lightning damage to composites are also being evaluated. These issues will be addressed in a future manuscript.

3.6 References

[1] Feraboli, P. and M. Miller, "Damage Resistance and Tolerance of Carbon/Epoxy Composite Coupons Subjected to Simulated Lightning Strike," *Composites Part A: Applied Science and Manufacturing*, 2009, **40**(6): p. 954-967.

[2] Gou, J., Y. Tang, F. Liang, Z. Zhao, D. Firsich, and J. Fielding, "Carbon Nanofiber Paper for Lightning Strike Protection of Composite Materials," *Composites Part B: Engineering*, 2010, **41**(2): p. 192-198.

[3] Feraboli, P. and H. Kawakami, "Damage of Carbon/Epoxy Composite Plates Subjected to Mechanical Impact and Simulated Lightning," *Journal of Aircraft*, 2010, **47**(3): p. 999-1012.

[4] Hirano, Y., S. Katsumata, Y. Iwahori, and A. Todoroki, "Artificial Lightning Testing on Graphite/Epoxy Composite Laminate," *Composites Part A: Applied Science and Manufacturing*, 2010, **41**(10): p. 1461-1470.

[5] Kawakami, H., "Lightning Strike Induced Damage Mechanisms of Carbon Fiber Composites." 2011, PhD Dissertation, University of Washington.

[6] Chen, X., G. Liu, and H. Wang. "The Residual Strength Test and Analysis of Composite Rudder After Lightning Strike," in the *Proceedings of the 18th International Conference on Composite Materials*, 2011, Jeju, South Korea.

[7] Szatkowski, G.N., K.L. Dudley, S.V. Koppen, J.J. Ely, T.X. Nguyen, L.A. Ticatch, J.J. Mielnik, and P.A. Mcneill. "Common Practice Lightning Strike Protection Characterization Technique to Quantify Damage Mechanisms on Composite Substrates," in the *Proceedings of the International Conference on Lightning and Static Electricity*, 2013, Seattle, WA.

[8] Yamashta, S., I. Ohsawa, and J. Takahashi. "Structural Integrity of Carbon Fiber Reinforced Polyprophylene After Lightning Strike," in the *Proceedings of the SAMPE Europe's 35th International Conference*, 2014, Paris, France.

[9] Li, Y., R. Li, L. Huang, K. Wang, and X. Huang, "Effect of Hygrothermal Aging on the Damage Characteristics of Carbon Woven Fabric/Epoxy Laminates subjected to Simulated Lightning Strike," *Materials & Design*, 2016, **99**: p. 477-489.

[10] Hirano, Y., T. Yokozeki, Y. Ishida, T. Goto, T. Takahashi, D. Qian, S. Ito, T. Ogasawara, and M. Ishibashi, "Lightning Damage Suppression in a Carbon Fiber-Reinforced Polymer with a Polyaniline-based Conductive Thermoset Matrix," *Composites Science and Technology*, 2016, **127**: p. 1-7.

[11] Metwally, I., A. A-Rahim, F. Heidler, and W. Zischank, "Computation of transient-temperature profiles in objects exposed to simulated lightning currents," *International journal of thermal sciences*, 2006, **45**(7): p. 691-696.

[12] Ogasawara, T., Y. Hirano, and A. Yoshimura, "Coupled Thermal–Electrical Analysis for Carbon Fiber/Epoxy Composites Exposed to Simulated Lightning Current," *Composites Part A: Applied Science and Manufacturing*, 2010, **41**(8): p. 973-981.

[13] Chemartin, L., P. Lalande, B. Peyrou, A. Chazottes, P. Elias, C. Delalondre, B. Cheron, and F. Lago, "Direct Effects of Lightning on Aircraft Structure: Analysis of the Thermal, Electrical and Mechanical Constraints," *AerospaceLab*, 2012, (5): p. 1-15.

[14] Wang, F., N. Ding, Z. Liu, Y. Ji, and Z. Yue, "Ablation Damage Characteristic and Residual Strength Prediction of Carbon Fiber/Epoxy Composite Suffered from Lightning Strike," *Composite Structures*, 2014, **117**: p. 222-233.

[15] Liu, Z., Z. Yue, F. Wang, and Y. Ji, "Combining Analysis of Coupled Electrical-Thermal and Blow-off Impulse Effects on Composite Laminate Induced by Lightning Strike," *Applied Composite Materials*, 2015, **22**(2): p. 189-207.

[16] Dong, Q., Y. Guo, X. Sun, and Y. Jia, "Coupled Electrical-Thermal-Pyrolytic Analysis of Carbon Fiber/Epoxy Composites Subjected to Lightning Strike," *Polymer*, 2015, **56**: p. 385-394.

[17] Wang, Y. and O.I. Zhupanska. "Lightning-Strike-Induced Heat Transfer in Glass Fiber Polymer Matrix Composite Blades," in the *Proceeding of the American Society of Composites 30th Technical Conference*, 2015.

[18] Wang, F., Y. Ji, X. Yu, H. Chen, and Z. Yue, "Ablation Damage Assessment of Aircraft Carbon Fiber/Epoxy Composite and its Protection Structures Suffered from Lightning Strike," *Composite Structures*, 2016, **145**: p. 226-241.

[19] Gagné, M. and D. Therriault, "Lightning Strike Protection of Composites," *Progress in Aerospace Sciences*, 2014, **64**: p. 1-16.

[20] Hexcel, *8552 Epoxy Matrix Product Data*, 2010; Available from: http://www.niar.wichita.edu/coe/ncamp_documents/Hexcel%208552/Hexcel8552-ProcessingCharacterizationV1-0.pdf.

[21] Hexcel, R., "Redux 330 Epoxy Film Adhesives for the Bonding and Finishing of Composites." 2007.

[22] Osaka Gas Chemicals, *DONACARBO Paper Data Sheet*, [cited 2015 17 Jun]; Available from: http://www.ogc.co.jp/e/products/carbon-f/donacarbo_paper.html.

[23] Gharghabi, P., Lee, J., M. S. Mazzola, T. E. Lacy, Jr., C. U. Pittman, Jr., and James, G., "Carbon/Epoxy Laminates Protected with Copper Mesh and Pitch-Based Carbon Fiber Paper Subjected to Artificial Lightning Strikes " *manuscript in preparation*, 2016.

[24] SAE, "Aircraft Lightning Environment and Related Test Waveforms," *Aerospace Recommended Practice ARP 5412*, 1999.

[25] Schon, K., Characterisation and Generation of High Impulse Voltages and Currents, in *High Impulse Voltage and Current Measurement Techniques*. 2013, Springer. p. 5-38.

[26] Heidler, F., W. Zischank, Z. Flisowski, C. Bouquegneau, and C. Mazzetti. "Parameters of Lightning Current Given in IEC 62305-Background, Experience and Outlook," in the *Proceedings of the 29th International Conference on Lightning Protection*, 2008.

[27] Suzuki, Y., A. Todoroki, R. Matsuzaki, and Y. Mizutani, "Impact-damage Visualization in CFRP by Resistive Heating: Development of a New Detection Method for Indentations caused by Impact Loads," *Composites Part A: Applied Science and Manufacturing*, 2012, **43**(1): p. 53-64.

[28] Kanapitsas, A., C. Tsonos, H. Zois, C.G. Delides, and G.C. Psarras, "Thermal and Mechanical Characterization of Epoxy Resin Nanocomposites," *Journal of Advanced Physics*, 2013, **2**(1): p. 25-28.

[29] Lampman, S., Characterization and Failure Analysis of Plastics. 2003: ASM International.

[30] Muñoz, R., S. Delgado, C. González, B. López-Romano, D.-Y. Wang, and J. LLorca, "Modeling Lightning Impact Thermo-Mechanical Damage on Composite Materials," *Applied Composite Materials*, 2014, **21**(1): p. 149-164.

CHAPTER IV

THERMAL RESPONSE OF SIMULATED LIGHTNING CURRENTS OF CARBON/EPOXY COMPOSITES WITH METALLIC AND NON-METALLIC PROTECTION LAYERS

4.1 Abstract

Nonlinear finite element (FE) simulations to characterize lightning-induced thermal damage in AS4/3506 carbon/epoxy composites with metallic and non-metallic protection layers were performed and then compared with that of unprotected composites. In this study, we calculated matrix thermal decomposition as a primary form of lightning damage in the composites subjected to 40 kA peak currents. Two protection layers were considered: (1) a traditional copper mesh (CM) commonly used for aircraft lightning strike protection and (2) a single layer of highly conductive pitch carbon fiber paper (PCFP). Temperature-dependent material properties of each constituent were used to predict the matrix thermal decomposition induced by simulated lightning current waveforms. The lightning strike FE models suggest that both the CM and the PCFP lightning protection layers successfully mitigated thermal damage development in the underlying composites as a consequence of reduced through-thickness electrical current flow heat conduction. The CM provided excellent protection from thermal damage; the predicted matrix decomposition only penetrated the first AS4/3506 ply. Similarly, the PCFP outer layer limited thermal damage to the top three composite plies, while the

predicted matrix decomposition of the unprotected composite penetrated the sixth ply. Improved PCFP protection layers appear possible to design by making variations in the in-plane and through-thickness electrical conductivities and in the PCFP-to-first ply gap conductance. This suggests that PCFP outer layers or similar lightweight carbon-based layers may serve as efficient lightning protection layers.

4.2 Introduction

A considerable amount of research has been performed in order to characterize lightning strike-induced damage in composite aircraft structural components [1-6]. Such research has largely focused on determining and simulating the thermal damage mechanisms in continuous carbon fiber reinforced polymer (CFRP) composites. Lightning-induced damage to CFRP composites can be severe due to their orthotropic ply properties and laminated architectures [4, 5]. Such composites typically display material properties in the longitudinal (fiber) direction that are profoundly different from those in the transverse and through-thickness directions. In CFRP composites, the electrical conductivity in the thickness and in-plane transverse directions can be significantly lower than in the fiber direction. The electrical conductivity of a AS4/3506 carbon/epoxy composite in the fiber direction is approximately four and seven orders of magnitude higher than that for the in-plane and thickness directions, respectively [7, 8]. In order to minimize lightning strike-induced damage in a composite, it is desirable to increase the in-plane electrical conductivity of the outermost layer [4-6]. This more effectively distributes electric current across the outer lamina surface, thus reducing through-thickness heat transfer and corresponding internal thermal damage development.

Lightning strike is a substantial transient electric charge that is typically injected at the lightning attachment point over 50-200 μs time scales [9, 10]. In CFRP composites, electrical current flow depends on both the optimal conduction path (*i.e.*, in the fiber direction) and the boundary conditions far away from the attachment point. The composite electrical properties are governed by the intrinsic properties of each ply constituent: highly conductive carbon fibers and a far more insulating isotropic polymer matrix. The amount of electrical energy dissipated as heat in composites by a transient lightning electric discharge is proportional to each constituents' electrical resistance [11]. Thus, more Joule heating can occur in a relatively insulating polymer matrix than for a conductive fiber per unit of current passing through the matrix. Above the epoxy matrix thermal decomposition temperatures (*i.e.*, ≥ 300˚C), CFRP composites can be progressively and irreversibly damaged due to permanent pyrolytic matrix decomposition as a function of time at these temperatures. Simultaneously, some oxidation can occur on the carbon fiber surfaces if oxygen is available. Fiber-to-matrix adhesion may also be seriously damaged.

In the present study, a highly conductive pitch carbon fiber paper (PCFP), consisting of two-dimensional, randomly oriented pitch-derived carbon fibers (PCFs), was chosen as a low cost non-metallic lightning protection layer. PCFs have high carbon fiber conversion yields, making them less expensive than Rayon- and polyacrylonitrile (PAN)-based carbon fibers [12, 13]. Moreover, PCFs generally exhibit superior electrical and thermal properties due to a higher degree of graphitization and structural order than fibers derived from other precursors [14]. Therefore, a PCFP outer layer may potentially reduce through-thickness thermal damage in the underlying composites. Inclusion of a non-metallic lightning protection layer in composites has not been widely considered in the literature. In this study, the lightning strike-induced thermal damage development in both the unprotected and protected AS4/3506 carbon/epoxy composites were characterized using nonlinear transient ABAQUS finite element (FE) simulations. Lightning strike-induced mechanical damage was not considered in the current work.

4.3 Literature Review

4.3.1 Lightning Damage

Hirano *et al.* [1] measured the effects of lightning peak currents, electrical charges, and action integrals on the thermal damage induced in carbon/epoxy composites. Fiber breakage and thermal damage penetration were governed by the peak current. In contrast, lightning-induced surface (thermal) damage and delamination were related to the electrical charge (defined as integral of the time-varying current amplitude over its time duration) and the action integral (defined as integral of the square of the time-varying current over its time duration) associated with an electric current waveform [1].

Feraboli *et al.* [2] performed several laboratory-scale *artificial* lightning strike tests (peak currents ≤ 50 kA) to induce damage at the center of 8×8 in^2 16-ply carbon fiber/epoxy laminates with and without stainless steel fasteners. The axial moduli were relatively insensitive to the applied lightning strike current levels (10-50 kA). Composites subjected to the maximum lightning current (50 kA) displayed a ~20% reduction in tensile residual strength and a ~30% reduction in compressive residual strength. Moreover, the presence of a metallic fastener significantly decreased the compressive residual strength by 65% at 50 kA since the fastener provides a through-thickness electrical conduction path, leading to more local electrical energy absorption and damage than for the case where energy dissipation is mostly distributed over the composite surface.

Ogasawara *et al*. [4] performed coupled thermal-electrical FE analyses to evaluate lightning-induced thermal damage development in carbon/epoxy composites. Their simulation results were compared with the experiments of Hirano *et al.* [1]. Temperature-dependent composite *electrical* conductivities were used to estimate the dynamic temperature change during the analyses. The surface areas with predicted temperature distributions in the range of 300-500˚C (where thermal damage can occur in an epoxy matrix) showed good agreement with visual inspection, ultrasonic testing, micro X-ray inspection, and sectional observations of damage performed by Hirano *et al.* [1]. However, Ogasawara *et al.* [4] neglected to consider the strong effect of temperature on material *thermal* conductivities. Menousek *et al.* [12] and Mueller [15] noted that the specific heats, thermal conductivities, and densities of carbon/epoxy composites all increase as temperature increases. Thus, time/temperature-dependent thermal properties must be employed in order to accurately simulate thermal damage induced in carbon/epoxy composites. Moreover, Ogasawara *et al.* [4] assumed the through-thickness electrical conductivity varied linearly with temperature between the epoxy matrix final decomposition temperature (600˚C) and the carbon fiber sublimation temperature (3,316˚C) [16]. Such an assumption may be unrealistic since early studies have not suggested such a linear relationship [7, 8]. Thus, their model may underpredict or overpredict thermal damage development and propagation in the thickness direction.

Later, Abdelal and Murphy [5] developed a lightning strike FE model to assess thermal damage development in carbon/epoxy composites with and without a 0.05 mm thickness copper mesh (CM) protection layer. Surface contact properties (thermal and electrical gap conductances) and temperature-dependent electrical and thermal properties were used to evaluate the temperature distribution in the composites. Their model predicted that use of a CM can successfully mitigate lightning-induced thermal damage development in the underlying laminates. They suggested that use of (1) a thinner CM that can be ablated more rapidly and (2) composites with relatively low thermal gap conductances can inhibit through-thickness electrical conduction from the CM and reduce thermal damage to the underlying laminates.

Dong *et al.* [6] also conducted coupled electrical-thermal-pyrolytic FE analyses of carbon/epoxy composites subjected to simulated lightning strikes. The time/temperature-dependent pyrolysis of an epoxy matrix was investigated using an Arrhenius kinetic decomposition equation using an estimated pre-exponential factor and activation energy measured at low heating rates ($\beta \leq 20^{\circ}$C/min [4]). However, such a relationship is likely inappropriate to characterize the very rapid heating encountered in a lightning strike, where the composite heating rate can exceed 1,000˚C/min [4] and locally much higher. The chemical kinetics and mechanisms of steady-state thermal decomposition are not the same as those for transient decomposition (*i.e.*, rapid localized heating). Furthermore, the *actual* time scales associated with structural changes and chemical reactions occurring in the rapidly heated matrix are not well known. Hence, estimating the extent of matrix pyrolysis in composites subjected to a lightning strike remains a significant challenge.

4.3.2 Lightning Strike Test Parameters

Idealized voltage and current waveforms under various lightning conditions are defined in SAE ARP 5412 [10]. Voltage waveforms are designed for the evaluation of lightning attachment and dielectric breakdown paths through non-conducting surfaces. Current waveforms are intended for evaluating the direct and indirect effects of lightning strike leading to aircraft physical damage to the aircraft's structure or avionics. It is highly desirable to determine and simulate the damage evolution mechanisms at and near an attachment point. Thus, idealized current waveforms have been commonly considered in recent artificial lightning strike tests [10]. The standard current lightning strike waveforms and their associated key characteristics (*i.e.*, peak current, time duration, electric charge transferred, and action integral) are shown in Figure 4.1 (adopted from [10]).

:

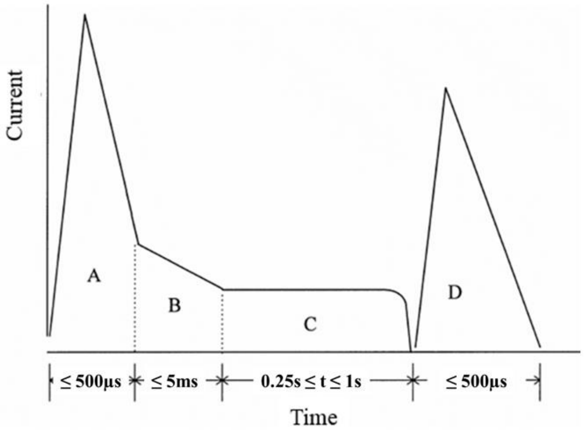

COMPONENT A (First Return Stroke)
  Peak Amplitude : 200kA (± 10%)
  Action Integral : 2×10^6 A^2s (± 20%) (in 500 μs)
  Time Duration : ≤ 500 μs
COMPONENT B (Intermediate Current)
  Max. Charge Transfer : 10 Coulombs (± 10%)
  Average Amplitude : 2 kA (± 20%)
  Time Duration : ≤ 5 ms

COMPONENT C (Continuing Current)
  Amplitude : 200 - 800 A
  Charge Transfer : 200 Coulombs (± 20%)
  Time Duration : 0.25 to 1 s
COMPONENT D (Subsequent Return Stroke)
  Peak Amplitude : 100kA (± 10%)
  Action Integral : 0.25×10^6 A^2s (± 20%) (in 500 μs)
  Time Duration : ≤ 500 μs

Figure 4.1 Standard current waveforms and their associated criteria (adopted from [10]).

In Fig. 4.1, components *A* through *D* present standard lightning current waveforms for the first return stroke, intermediate current, continuing current, and subsequent return stroke current, respectively [10]. Waveform *D* is used to certify the vast majority of airframe acreage [2]. Waveform *D* has a peak current amplitude of 100 kA (± 10%), a time duration of up to 500 μs, and an action integral of 2.5×10^5 A^2 s; waveform *D* is intended for full-scale or component lightning strike tests. Such high peak currents can produce intense heat that can instantly burn test coupons. Hence, prior laboratory-scale lightning strike tests [1-3] commonly injected current waveform *D* with peak currents of ≤ 50 kA (but with the same time duration). In this study, the current waveform *D* with the peak currents of 40 kA was applied over a 30 μs time duration to compare the shape and size of the matrix decomposition domains with experimentally measured results for a similar composite subjected to 40 kA peak lightning current [1, 2].

The lightning arc can be idealized as a cylindrical plasma channel with a radius that can be determined from the peak current and magnetic overpressure [17]. The size of a lightning arc channel directly influences composite mechanical and thermal damage development. Relatively large arc channel radii result in distributed damage development that is distinct from small arc radii, when all other factors are equal [17]. In addition, the heat fluxes and the magnetic overpressure due to a lightning strike are inversely proportional to the lightning arc radius [17]. Numerical estimates of the return stroke (waveform *D*) arc radius may exceed 5 cm for current peaks of ≥ 100 kA, while the typical radius of an arc attachment with continuing currents (waveform *C*) never exceeds 7 mm [7]. In previous lightning strike FE simulations [5, 6], the current waveforms with peak currents of ≤ 50 kA were centrally applied over 1-10 mm diameter attachment points on the outermost ply of composite laminates. In the current study, a 10 mm diameter arc channel was employed in all lightning strike simulations.

4.4 Theoretical Background

A conductor's electrical field is governed by Maxwell's law of conservation of electric charges [18]. While the total electrical charge can be determined by integrating the internal volumetric current source per unit volume, the *net* electric current can be obtained by integrating the electrical current density within a control volume. The lightning strike electrical charge transfer is a measure of the amount of the electrical energy dissipated by current flowing through a material. This is defined as the product of the electrical current density vector and the electric field intensity vector, *i.e.,* negative electrical potential gradient [11]. In ABAQUS FE simulations [19], electrical energy dissipated through a material is evaluated at the end of each time increment in steady-state analyses; a value averaged over each time increment is used in transient analyses. Thermal energy from Joule heating is proportional to the amount of electrical energy dissipated with an energy conversion factor (between 0 and 1). When an energy conversion factor is 1, all of the electrical energy is converted into thermal energy. A detailed description of the electrical charge conservation and the thermal energy balance is available in Ref. [19].

During a lightning strike to a composite, large electric current fluxes surging through the material are instantaneously converted into heat (Joule heating). For composites with CM protection systems, the lightning thermal energy can result in simultaneous melting and ablating, explosive boiling, and vaporizing of the Cu foil. High temperature mass transfer, transport properties of evaporating gas mixtures, and steep thermal gradients going from solid Cu to gases are unknown. Since typical metal alloy vaporization under rapid heating occurs much faster at high temperatures [20], CM vaporization was assumed to be the dominant ablation mechanism.

The Hertz-Knudsen (H-K) model [21] was used to predict the vaporization (ablation) rate of the CM and PCFP layers in this study. The ablation rate ($v(T)$) calculated in units of distance per unit time of an evaporating surface using the H-K model is:

$$v(T) = (1-\beta)\sqrt{\frac{m}{2\pi k_B T}}\frac{p_0}{\rho}\exp\left[\frac{L_V}{k_B}\left(\frac{1}{T_{BT}}-\frac{1}{T}\right)\right] \tag{4.1}$$

where β is the sticking coefficient (fraction of incident molecules that "stick" to an evaporating surface), k_B is the Boltzmann constant, ρ is the density of the material, L_V is the latent heat of vaporization of the material, T_{BT} is the boiling temperature of the material at the pressure p_0 = 1atm, and m is the mass of the material calculated by dividing the molecular weight (MW) by the Avogadro's number ($\sim 6.02\times10^{23}$) [21]. These properties for the CM and PCFP lightning protection layers are given in the next section.

In this study, the ablation mechanism for the PCFP protection layer was assumed to be vaporization only; formation of large-scale fragments of underlying lamina/PCFP due to mechanical loads was not considered. In practice, PCFP ablation involves bond rupture creating graphene-like fragment sheets from the fibers. Each fragment sheet requires proportionally more vaporization energy than single carbon atoms. However, far fewer graphene fragments are formed than the number of carbon atoms in the PCF because each fragment consists of many carbon atoms. A major limitation of the H-K model is that vaporization mechanisms are independent of mass, momentum, and energy transfer [22]. Hence, the model does not take into account the energy change required to break the chemical bonds in order to form the distribution of sheet-like fragments, which are then converted into vapor. Despite this limitation, the PCFP ablation was predicted using the H-K model as a simple approximation for comparison purposes. The details on how to develop the H-K model for the PCFP are addressed in the next section.

4.5 FE Model Development for Predicting Thermal Damage

Nonlinear transient ABAQUS FE simulations of lightning induced-thermal damage in a carbon/epoxy laminates performed in this study consisted of two sequential sub-analyses: (1) a fully coupled transient thermal-electrical analysis and (2) a transient heat transfer analysis. A coupled thermal-electrical analysis was employed to calculate the electrical potential and initial temperature distributions due to instantaneous Joule heating within the composite resulting from an applied electrical current. A transient nonlinear heat transfer analysis was then employed to characterize heat flow in the laminate. *A*utomatic time incrementation was used to achieve optimal convergence in these FE simulations.

4.5.1 Carbon/Epoxy Composite Material Properties

Mueller [15] measured the densities, specific heats, and thermal conductivities of carbon/epoxy composites, which were heated for less than 0.1 μs (by repetitively-pulsed laser irradiation) above the matrix decomposition temperature (~510 ˚*C*) and then cooled. The results were compared with those of pristine (undamaged) composites over the temperature range 10-3,316 ˚*C*. The resulting damaged composite properties were profoundly different from those of the undamaged composites due to the presence of matrix residues and chars. At sufficiently high temperatures, carbon/epoxy composites will be irreversibly damaged due to permanent matrix decomposition and fiber ablation and breakage. The length of time at each high temperature in the time/temperature profile will determine the chemistry and extent of matrix decomposition and fiber damage. All of these energy absorbing chemical decomposition reactions will follow Arrhenius kinetic equations. Following various extents of chemical decomposition, a decrease of matrix mass occurs via vapor generation and mass transfer.

The evolving composite properties are highly dependent on (1) the local temperature, and (2) the local time/temperature history. Below a certain temperature threshold, the composites may appear visually undamaged, but they still could exhibit material property changes. Rapid heating during lightning strike followed by cooling could change the properties of the fiber/matrix interface region, decreasing the degree of fiber/matrix adhesion. The spatial distribution of the time/temperature dependent damage could influence composite properties at significant and unknown distances from the lightning attachment point.

Table 4.1 Material properties of AS4/3506[a] carbon/epoxy plies [7, 8, 12, 15, 23]

Temp., T	Density [b], ρ	Specific Heat [b], C_p	Thermal Conductivity [b], k			Electrical Conductivity [c], σ		
			Longi.	Trans.	Thick.	Longi.	Trans.	Thick.
(˚C)	(Kg/mm^3)	(J/(kg·K))	(W/(mm·K))	(W/(mm·K))	(W/(mm·K))	(S/mm)	(S/mm)	(S/mm)
25	1.52E-06	1,065	4.66E-02	6.83E-04	6.83E-04	35.97	1.15E-03	3.9E-06
350	1.52E-06	2,100	2.47E-02	3.73E-04	3.73E-04	35.97	1.15E-03	3.9E-06
510	1.08E-06	2,100	1.46E-02	1.79E-04	1.79E-04	35.97	2	2
1,000	1.08E-06	5,750	1.17E-02	1.32E-04	1.32E-04	35.97	2	2
3,316	1.08E-06	5,875	1.00E-04	1.00E-04	1.00E-04	35.97	2	2
3,367	1.08E-06[d]	5,875[d]	1.00E-04[d]	1.00E-04[d]	1.00E-04[d]	1[d]	1[d]	1.0E+06[d]

[a] This composite typically has a fiber volume fraction of 0.60-0.66 [24, 25].

[b] Ref. [12, 15], [c] Ref. [7, 8].

[d] Properties determined by the extrapolation of the empirical data over the temperature range (25-3,316˚C).

Table 4.1 summarizes temperature-dependent material properties of AS4/3506 carbon/epoxy composites available in the literature [7, 8, 12, 15, 23]. In this study, a quasi-isotropic laminate, $[+45/0/-45/90]_{4s}$, comprised of AS4/3506 plies was simulated. Composites properties were updated based upon spatially- and temporally-varying temperature at each time increment during the FE simulations. The properties cited in Table 4.1 were measured up to the fiber sublimation temperature (3,316˚C) under steady-state conditions. Thus, these properties do not account for temporal variations. An additional set of properties were assumed at the critical sublimation temperature of pure solid carbon (3,367˚C) [23]. The density, specific heat, thermal conductivity, and electrical conductivity defined at this critical temperature (3,367˚C) were approximated by a quadratic extrapolation of the experimental data defined over the temperature range (25-3,316˚C). In the numerical simulation, the local temperature-dependent composite properties were updated by linearly interpolating the properties between the given temperatures shown in Table 4.1 Composite property degradation in the typical epoxy matrix decomposition temperature range of 300-500˚C was not considered in this study. It was assumed that the composites would start ablating when the local temperature exceeds the fiber sublimation temperature (3,316˚C) and be fully abated at the critical sublimation temperature (3,367˚C). Once the local temperature exceeded the critical sublimation temperature (3,367˚C), the local composite properties were assigned those at 3,367˚C for the rest of simulation. Once fiber sublimation begins to occur (3,316˚C), the composite conductivities were assumed to be isotropic as a consequence of irreversible char/residue formation. In addition to the subliming fibers, carbonaceous residues from the matrix that are still present were also assumed to sublime like the fibers. The composite latent heat of fusion (ΔH_f) was 4.8×10^3 kJ/kg from Ref. [5]. This latent heat was only absorbed between 300-500˚C, which is where the matrix is undergoing thermal damage, while the carbon fibers are only being heated and undergo no fusion change. The composite latent heat of vaporization (ΔH_V) was 4.3×10^4 kJ/kg from Ref. [5] absorbed between the fiber sublimation temperature (3,316˚C) and the critical sublimation temperature (3,367˚C). Note that the current lightning strike FE model was developed using a continuum-based approach, thus the composite latent heats were independent of the weight fractions of each constituent (*i.e.*, matrix and fibers). Note the specific heats (C_p) temperatures where phase change occurs (*i.e.*, between 300-500˚C and between 3,316-3,367˚C in this study) are associated with the sum of the total internal energy change (due to the effect of specific heat and the added effect of the latent heats). These specific heats are called *apparent* specific heats since they compensate for the latent heat changes over these specific temperature ranges. For example, the total energy per unit weight absorbed between the fiber sublimation temperature and the critical temperature (3,316-3,367˚C) is equal to the sum of $C_p \cdot \Delta T$ and ΔH_V, where the value of C_p was constant (5,875 J/(kg·K)) over this temperature range. The *apparent* specific heat C_p^* is greater than C_p by the amount needed to account for the total energy per unit weight absorbed over this temperature range (*i.e.*, $C_p^* \cdot \Delta T$= total energy per unit weight absorbed). The way we determined an *apparent* specific heat is addressed later in this work.

During a lightning strike, one or more of the outermost plies can be completely ablated in the vicinity of the attachment point. Once this occurs, the lightning arc channel and associated current are instantaneously transferred to the next intact inner ply. In this study, a special numerical procedure (akin to a moving boundary condition) was implemented to ensure physically realistic current flows occur as the composite locally ablates. Essentially, once the local temperature within a given element exceeds the critical sublimation temperature (3,367˚C), the in-plane electrical conductivities are set to negligible values (1 S/mm). This prevents in-plane conduction in the ablated region. In addition, the through-thickness conductivities in ablated elements are assumed to be very high (10^6 S/mm). This ensures that the through-thickness electrical currents flow instantaneously to the inner adjacent ply, consistent with physical observations.

Abdelal and Murphy [5] included constant thermal and electrical gap conductances to simulate and characterize heat transfer at the matrix-rich interfaces between carbon/epoxy laminas. In general, the contact properties vary with temperature, pressure, and surface roughness. Moreover, it is difficult to measure such contact properties at elevated temperatures once a phase change (*i.e.*, decomposition and vaporization) begins. Since the evolution of contact properties was not known, perfect bonding between lamina was assumed in this study. The effect of variable contact properties on predicted thermal damage development in composites will be considered as part of future investigations.

4.5.2 Copper Mesh (CM) Material Properties

Copper alloy meshes protect the underlying carbon/epoxy composites by quickly spreading the lightning-induced electrical charge across their highly conductive surface. Temperature-dependent CM properties were assumed to be those of pure isotropic copper (Table 4.2). Pure copper has a melting point of 1083˚C, a boiling temperature of 2567˚C, and a (thermodynamic) critical temperature of 8000˚C. The cited CM properties were measured up to 4500˚C. At temperatures between the boiling temperature (2567˚C) and the critical temperature (8000˚C), vaporized copper has certain transport properties describing the ability of gas molecules to transfer energy (*i.e.*, diffusion and electrical/thermal conductivity) in random directions. However, these transport properties are unknown. In our numerical simulations, the local CM properties defined up to 4500˚C were linearly interpolated between the tabulated values shown in Table 4.2. Furthermore, those defined above 4500˚C were simply approximated by a quadratic extrapolation of the experimental data defined over the temperature range (25-4500˚C). The isotropic CM electrical conductivity used in the simulation was about nine orders of magnitude higher than the composite's through-thickness electrical conductivity (*cf.,* Tables 4.1-2). However, the CM has the ability to continuously transfer heat that can cause extensive thermal damage in the underlying composite. In practice, a thin Cu layer will ablate before extensive through-thickness heat transfer and thermal damage becomes a serious concern [5]. The CM's latent heat of fusion was 2.05×10^{2} kJ/kg from Ref. [26]. It was absorbed between 1064˚C and 1083˚C. The latent heat of vaporization was 4.8×10^3 kJ/kg from Ref. [26] absorbed between the boiling temperature (2567˚C) and the critical temperature (8000˚C). As explained earlier, these CM's latent heats were independent of the rate of mass loss due to phase transitions.

The thermal conductivity of the CM (see Table 4.2) gradually decreases with increasing temperature above 1000˚C. In contrast, the electrical conductivity markedly decreases as temperature increases from 25 to 500˚C. Then a further significant drop in CM electrical conductivity occurs near 500-510˚C. This behavior is due to the dominant electron-phonon interactions. An electrical resistivity change in typical metals involves an electron interaction mechanism [27]. At low temperatures, the electrons interact with impurities (*i.e.*, lattice defects), thus the electrical resistance is less sensitive to temperature. However, at higher temperatures the electrons mainly interact with phonons. More phonons are thermally excited due to oscillation of crystal lattices as temperature increases. Simultaneously, however, electrons in a metal may collide with each other more often as temperature increases. Electron-electron collisions are more dominant than phonon excitations [27]. The rise in electron-electron collisions will increase electrical resistivity as temperature increases. Consequently, the electrical resistivity increases (therefore conductivity decreases) as temperature increases.

Table 4.2 Material properties of pure copper [26, 28, 29]

Temperature, *T* (˚C)	Density, [a] ρ (Kg/mm^3)	Specific Heat, [b] C_p (J/(kg·K))	Thermal Conductivity, [c] k (W/(mm·K))	Electrical Conductivity [b], σ (S/mm)
25	8.95E-06	385	0.40	58,140
500	8.95E-06	431	0.37	20,120
510	8.95E-06	491	0.34	4,651
1,000	8.95E-06	492	0.15	3,704
2,600	8.95E-06	493	0.18	2,227
3,227	8.95E-06	494	0.18	1,500
4,500	8.95E-06	495	0.18	1,470
7,000	8.95E-06[d]	499[d]	0.18[d]	1,421[d]
8,000	8.95E-06[d]	500[d]	0.18[d]	1,400[d]

[a] Ref. [26], [b] Ref. [28], [c] Ref. [29].
[d] Properties determined by the extrapolation of the empirical data over the temperature range (25-4500˚C).

Airframe manufacturers commonly apply metallic meshes on composite outer surfaces by resistance or induction welding techniques [30]. Imperfect bonding between the metallic meshes and underlying composites leads to significant thermal contact resistance. Both thermal and electrical contact (gap) resistances should be considered when characterizing lightning-induced thermal damage development in the composite. However, such contact properties are not available in the open literature. Hence, the thermal and electrical contact conductances of the CM protection layer were assumed to be the same as those of the PCFP protection layer. This issue is addressed in the next section.

4.5.3 Pitch-based Carbon Fiber Paper (PCFP) Material Properties

PCFP, containing two-dimensional, randomly oriented short or chopped PCFs, typically shows percolation behavior. Since the solid weight fraction of PCFP consists mainly of PCFs (> 99%) and a small amount (< 1%) binder, PCF properties are dominant. A complete set of PCFP properties are not available in the open literature. Thus, several major assumptions were made regarding PCFP properties in this study. Both the PCFP thermal and electrical conductivities were assumed to be isotropic. The bulk PCFP thermal conductivities were determined by averaging the fiber (axial) and radial thermal conductivities of a single PCF from Ref. [31]. The specific heats were assumed to be those of bulk graphite. The bulk electrical conductivity was motivated by the in-plane electrical conductivity of a commercial grade PCFP (DONACARBO S-259 [32], OSAKA Gas Chemicals) measured at room temperature (23˚C*)*. This electrical conductivity was assumed to be temperature-independent. Note that a PCFP typically shows much lower electrical conductivity in the thickness direction than in the in-plane direction. Thus, the assumption of an isotropic electrical conductivity of the PCFP may overestimate the thermal damage development in the underlying composite's top lamina. Table 4.3 summarizes PCFP bulk properties available in the literature [31-33].

Table 4.3 Material properties of a PCFP protection layer [31-33]

Temperature, T (˚C)	Density, [a] ρ (Kg/mm^3)	Specific Heat, [b] C_p (J/(kg·K))	Thermal Conductivity, [c] k (W/(mm·K))	Electrical Conductivity, [d] σ (S/mm)
25	1.60E-06	803	0.20	11.1
500	1.60E-06	1,598	0.19	11.1
1,000	1.60E-06	1,947	0.17	11.1
1,500	1.60E-06	2,096	0.16	11.1
2,000	1.60E-06	2,170	0.15	11.1
3,000	1.60E-06	2,234	0.12	11.1
3,316	1.60E-06	2,245	0.11	11.1
3,367	1.60E-06[e]	2,245[e]	0.10[e]	11.1[e]

[a] Ref. [32], [b] Ref. [33], [c] Ref. [31], [d] Ref. [32].
[e] Properties extrapolated of the empirical data over the temperature range (25-3,316˚C).

The PCFP latent heat of vaporization was assumed to be the same as AS4/3506 carbon/epoxy ply (4.3×10^4 kJ/kg) between the fiber sublimation temperature (3,316˚C) and the critical sublimation temperature (3,367˚C). Above 3,367˚C, the PCFP may exist partially in the vapor phase and subject to complex thermodynamics and mass transport mechanisms, which may be profoundly different from those for AS4/3506 or solid PCFP. Between 3,367˚C and a maximum temperature of 4000˚C, the *artificial* latent heat was assumed to be that of pure solid carbon (5.99×10^4 kJ/kg [23]). The previously described AS4/3506 carbon/epoxy composite electrical and thermal gap conductances [34, 35] were used to characterize the through-thickness electrical conduction and heat transfer at the PCFP/composite interface. Here, it was assumed that some of the epoxy resin from the AS4/3506 prepreg flowed into the interface region between the PCFP and the top ply during cure. The PCFP thermal conductance was 500 W/m^2 K [34] and the PCFP electrical contact conductance was 2.5×10^7 S/m^2 [35].

4.5.4 FE Model Discretization and Boundary Conditions

The simulated AS4/3506 carbon/epoxy laminates consisted of 32 plies (ply thickness of 0.125 mm) with a quasi-isotropic lay-up of $[+45/0/-45/90]_{4s}$. The composite had in-plane dimensions of 150×100 mm^2 (length × width). After performing a mesh-sensitivity study, these laminates were discretized using three-dimensional (3D) linear brick continuum elements with in-plane dimensions of 2.5×2.5 mm^2. Linear elements were selected since use of quadratic elements for nonlinear transient heat transfer analyses with a very small time increment can lead to convergence problems and spurious oscillations in the FE solutions. In previous FE simulations of lightning strikes to composites [4-6], the through-thickness temperature rises due to peak currents ≤ 50 kA were negligible upon reaching the 16th lamina. For this reason, the FE models of the 32-ply laminate in this study were discretized as follows: (1) the top 16 plies were each modeled using a single orthotropic continuum element through the thickness and (2) the remaining 16 plies were approximated using a single quasi-isotropic continuum element through the remaining stack up thickness.

In order to capture local composite temperature changes due to Joule heating, both the CM and PCFP were meshed using 3D linear brick elements and connected to the underlying composite using surface-to-surface contact. Thermal and electrical gap conductances of each protection layer were assigned at the interface between the protection layer and the underlying composite. The simulated CM possessed a diamond pattern with a unit-cell opening area of 2.3×1.15 mm^2 and a wire ribbon width of 0.1 mm. The CM thickness was 0.10 mm consistent with conventional metallic protection systems without adhesive resin [36]. The modeled PCFP was discretized using 3D linear brick continuum elements with in-plane dimensions of 2.5×2.5 mm^2. In general, commercially available PCFP layers are thicker than typical CMs and have thicknesses varying from 0.3 to 0.5 mm [32, 37]. The PCFP thickness was 0.5 mm in this study. Figure 4.2 shows a FE idealization of both the CM and PCFP lightning protection layers, each with a ~10 mm diameter lightning arc channel where the lightning waveforms were applied at the geometric centers of the protection layers. In Figure 4.2, the red regions correspond to lightning attachment regions where uniformly distributed surface currents were applied over the given lightning attachment locations. The black dotted lines refer to ~10 mm diameter lightning arc channels. In practice, the local current density will be higher near the outer radius of the lightning arc channel than in the interior. Since the actual gradient in the current density is not known, a uniform arc channel current was assumed in this study.

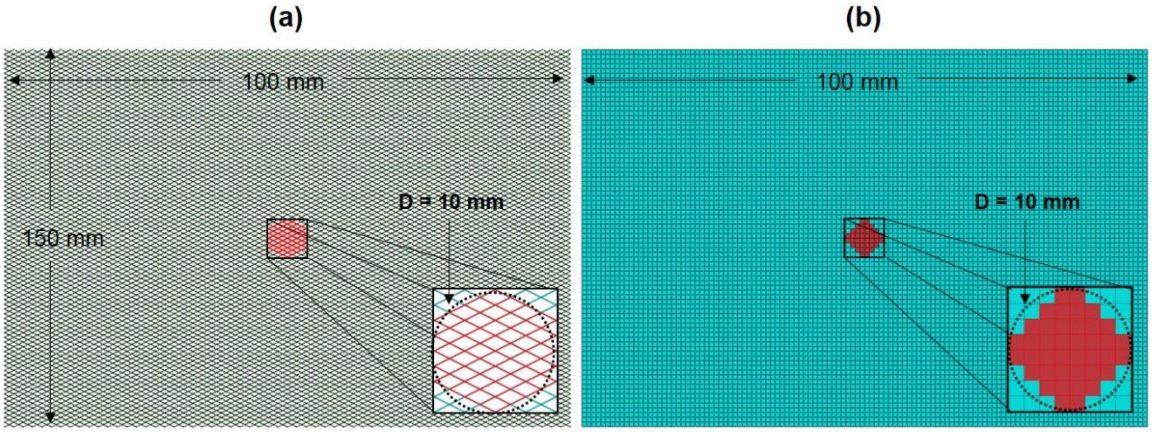

* Note: 1) The red regions correspond to lightning attachment regions.
2) The black dotted lines refer ~10 mm diameter lightning arc channels.

Figure 4.2 FE idealization of (a) the copper mesh (CM) and (b) the PCFP outer layers.

The electrical and thermal boundary conditions employed in this study were motivated by those used in laboratory-scale *artificial* lightning strike tests [1-3]. In these studies, the composite bottom surfaces were electrically grounded either by placing a copper plate underneath the laminate [1] or by connecting copper strips to the laminate edges [2, 3]. In the coupled thermal-electrical FE analyses performed in the this work, such grounding conditions can be represented by imposing zero electrical potentials on the bottom and lateral surfaces of the simulated unprotected and protected composites (Fig. 4.3a).

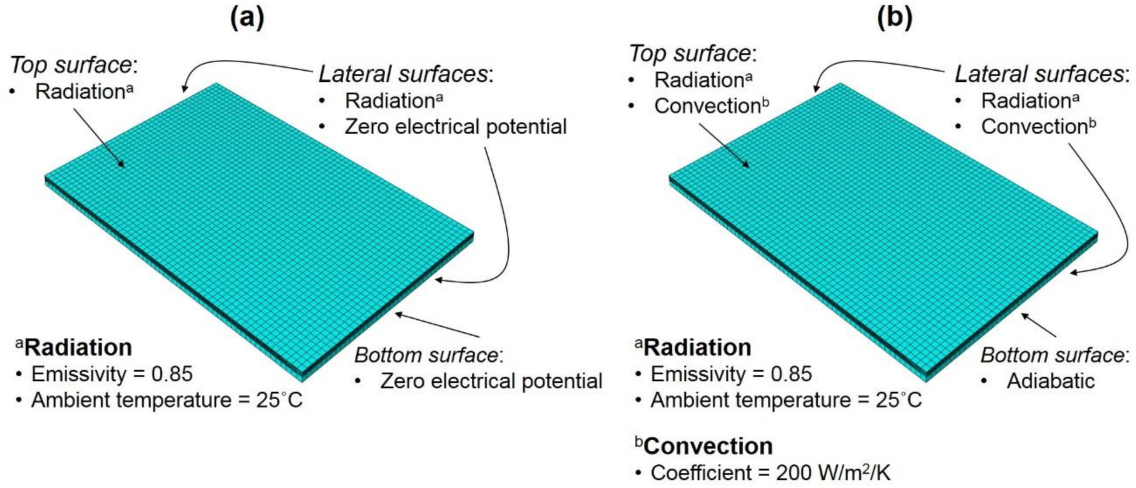

Figure 4.3 Electrical and thermal boundary conditions imposed in lightning strike FE simulations: (a) in coupled thermal-electrical analyses and (b) in subsequent heat transfer analyses.

The dominant heat transfer mechanisms during and immediately after lightning strike to composites are conduction and radiation [17]. Hence, a radiation boundary condition was imposed on the exposed top and lateral surfaces during coupled thermal-electrical analyses and subsequent heat transfer analyses. The composite and CM surface emissivities were assumed to be 0.85 [12] and 0.87 [29] with an ambient temperature of 25˚C, respectively. The surface emissivity of the PCFP was assumed to be same as that for the carbon/epoxy composite. In the subsequent longer duration nonlinear heat transfer analyses, convection boundary conditions were employed to account for simultaneous heat diffusion and advection. Convection may eventually reduce the through-thickness heat transfer and corresponding internal thermal damage development. In general, the convection coefficient strongly depends on the composition and the flow velocity of vaporized gas [38]. These are all unknown for the gas flow that results from matrix decomposition, carbon fiber ablations, and CM or PCFP ablations. Furthermore, the convection coefficient will also depend on solid or liquid fragments that are ejected into departing gases. Hence, the convection coefficient for each constituent was assumed to be that of carbon dioxide (CO_2, 200 $W/m^2/K$ [39]). Interestingly, Ogasawara *et al.* [4] reported the measured temperature increase at the composite's innermost surface (when subjected to simulated peak currents $\leq$ 40 kA) were nearly zero. Hence, these surfaces were considered to be adiabatic during the transient heat transfer analysis.

4.5.5 Simulated Ablation of Lightning Protection Layers

The ablation behavior of two lightning protection layers was predicted using the H-K model [21]. A sticking coefficient (corresponding to a probability that vaporized molecules are reflected back to a vaporizing surface) was assumed to be zero for both the CM and the PCFP, *i.e.*, when a sticking coefficient is zero, all molecules can be freely vaporized from the surface layers. The material properties used for determining the ablation rates of the lightning protection layers for the H-K model are presented in Table 4.4.

Table 4.4 Material properties used for developing the H-K model [26, 28, 29, 32, 33, 40]

Material	Boltzmann Constant, k_B (J/mol·K)	Molecular Weight, MW (g/mol)	Mass, m (kg)	Density, ρ (g/cm^3)	Latent Heat of Vaporization (kJ/kg)	Boiling Temperature, T_{BT} (K)
CM [a]	8.31	63.55	1.06×10^{-25}	8.95[a]	4.80×10^3	2,840
PCFP [b]	8.31	1,000[c]	1.66×10^{-24}	1.60	4.30×10^4	3,589

[a] CM properties are from Ref. [26, 28, 29], [b] PCFP properties are from Ref. [32, 33, 40].

[c] Assumed MW of an evaporating fragment used in this study. Pitch precursors originally used to synthesize fibers have molecular weights varying from 300-4000 g/mol [40].

The MW of a given constituent is a critical factor in developing the H-K model. The pitch used in making PCF consists of condensed aromatic hydrocarbons with and without alkyl branches; thus the MW of an individual pitch monomer unit fed into the fiber fabrication process varies widely from 300-4000 g/mol [40]. These are condensed into graphene layers that organize into various graphitic morphologies. When a PCFP outer layer is thermally ablated, it degrades into smaller fragments by rupturing numerous strong chemical bonds to give a distribution of fragment sizes with different MWs. The specific distribution of MWs produced from the vaporizing PCFPs is unknown. In the present study, a 1000 MW unit (g/mol) was simply assumed for all PCF fragments. The energy required to break all the chemical bonds required to form these fragments was not considered. Therefore, the neat transfer due to ablated PCFP estimated by the H-K model will underpredict the actual heat absorbed.

Using the material properties defined in Table 4.4, the ablation rates (in mm/s) of the CM ($v(T)_{\mathrm{CM}}$) and the PCFP ($v(T)_{\mathrm{PCFP}}$) are developed from Eq. 4.1 respectively as:

$$\begin{aligned} &\text{(a)} \qquad v(T)_{\mathrm{CM}} = \frac{0.395}{\sqrt{T}} \exp\left(3.669 \times 10^{4}\left(\frac{1}{2840} - \frac{1}{T}\right)\right) \\ &\text{(b)} \qquad v(T)_{\mathrm{PCFP}} = \frac{8.765}{\sqrt{T}} \exp\left(5.172 \times 10^{6}\left(\frac{1}{3859} - \frac{1}{T}\right)\right) \end{aligned} \tag{4.2}$$

4.5.6 Special-Purpose User Subroutines

Several special-purpose user subroutines were developed to predict lightning-induced thermal damage in both unprotected and protected composites.

A user-defined amplitude subroutine (UAMP) was developed to simulate lightning current waveforms. In this study, idealized current waveform *D* with a 40 kA peak current was applied over a 30 μs time duration. Uniformly distributed surface currents were injected over ~10 mm diameter lightning arc channels at the center in the outermost layers of each composite panel. The simulated double exponential current waveform, $I(t)$, is described as:

$$I(t) = I_0\left(e^{-\alpha t} - e^{-\beta t}\right) \tag{4.3}$$

where I_0 = 43,762 A, α = 22,708 1/s, and β = 1,294,530 1/s; these parameters were chosen from those defined in the current waveform D [10].

A user-defined heat generation subroutine (HETVAL) was defined to calculate the extent of matrix decomposition based on the spatially- and temporally-varying temperature. Matrix thermal decomposition was defined over a temperature range of 300-500˚C. The degree of matrix decomposition was simply defined between a normalized value of 0 (*undamaged*) and 1 (*fully damaged*) based on the highest temperature reached at that location. The length of time that the matrix was subjected to each temperature or remained in this 300-500˚C range was not considered. The extent of matrix decomposition was assumed to vary linearly throughout the given temperature range. This indicates, once the maximum local temperature reaches 400˚C, the composite is defined as 50% damaged at that location. Thus, the assigned matrix damage is independent of the length of time that the matrix spends at the highest temperature reached in the 300-500˚C range. Finally, this definition of damage should not be confused with matrix weight loss through gasification. Thus, at 400˚C most of the original matrix could still remain.

A user-defined field subroutine (USDFLD) was defined to update material properties based on the time-temperature history at each iteration of each time increment. This is primarily because the bulk properties of an undamaged composite are profoundly different from those of a fully *ablated* composite. In this subroutine, once the highest local temperature exceeds the critical fiber sublimation temperature (3,367˚C), the local composite properties were permanently updated with those defined at the critical temperature during analyses. As previously mentioned, composite property degradation in epoxy matrix decomposition temperature ranges (300-500˚C) was not considered.

A user-defined thermal material behavior subroutine (UMATHT) was developed to calculate the total internal energy change ($\Delta U_{\mathrm{Total}}$) and the ablation behavior of the two lightning protection layers associated with Joule heating ($\Delta U_{\mathrm{Joule}}$) and heat conduction ($\Delta U_{\mathrm{Cond}}$). The $\Delta U_{\mathrm{Joule}}$ is proportional to the electrical energy per unit volume (P_{ec}) dissipated by current flowing through the protection layer:

$$\Delta U_{Joule} = \eta_V P_{ec} \frac{1}{\rho} \tag{4.4}$$

where η_V is the energy conversion factor (between 0 and 1). When $\eta_V = 1$, all of the electrical energy is converted into heat. In this study, the value used was $\eta_V = 0.92$ representing highly efficient energy conversion [41]. P_{ec} is the electrical energy dissipated per unit volume by electric conduction and ρ is the density of the lightning protection layer. The ΔU_{Cond} depends on the specific heat (C_p) of the lightning protection layer associated with a given temperature change:

$$\Delta U_{cond} = C_P \Delta T \tag{4.5}$$

In the phase transition temperature ranges for a given protection layer, the apparent specific heats are employed which vary with latent heat [5]:

$$\begin{aligned} &\text{(a)} \qquad C_{P1}^{*} = C_P + \frac{H_1}{T_l - T_s} \\ &\text{(b)} \qquad C_{P2}^{*} = C_P + \frac{H_2}{T_c - T_g} \end{aligned} \tag{4.6}$$

where C_{P1}^{*} and C_{P2}^{*} are the *apparent* specific heats of a given protection layer that include the latent heat contributions. T_s, T_l, T_g, and T_c are a *solid* temperature, a *liquid* temperature, a *vaporization* temperature, and a *critical* temperature, respectively. H_1 is the latent heat of fusion and H_2 is the latent heat of vaporization.

Two criteria for lightning protection layer ablation to occur were defined: (1) once the highest local temperature exceeds the critical ablation temperature of each constituent (8000˚C for the CM, and 4000˚C for the PCFP) and (2) once the ablation has reached a depth where the lightning protection layer is fully removed. The total through-thickness ablation depth was obtained from the product of ablation rate, Eqs. 4.2 (a & b), summed over the current time increments. When this ablation depth is greater than protection layer's thickness, the lightning protection layer is gone.

4.6 Matrix Thermal Decomposition Prediction

4.6.1 Electrical Response of Unprotected and Protected Composites

The carbon/epoxy composites have temperature-dependent electrical conductivities. The amount of composite Joule heating depends upon the local electrical current density (ECD) and electrical potential (EPOT). The ECD (*i.e.,* electric current per unit cross-sectional area) is crucial to determine since the amount of Joule heating per unit volume is proportional to the square of the electric current. The EPOT (*i.e.,* electric potential difference or voltage) governs the total electrical energy stored and converted into heat between two arbitrary points. Both the ECD and EPOT of the protection layer and the underlying composite were calculated during the coupled thermal-electrical analyses.

Figure 4.4 shows the ECD and EPOT distributions in the top +45˚ lamina of unprotected, CM-protected, and PCFP-protected carbon/epoxy composites at the end of coupled thermal-electrical analyses (time, 30μs). For reference purposes, both the CM and PCFP lightning protection layers are not included. Both the ECD and EPOT distributions in the unprotected composite (Fig. 4a) are profoundly different from those in the protected composites (Figs. 4.4b-c). Not surprisingly, the resulting ECD and EPOT in the unprotected composite were primarily aligned along the top lamina's fiber direction (+45˚). Those obtained from the protected composites were less sensitive to the top lamina's fiber direction. This is primarily due to in-plane isotropic electrical current conduction in the CM and PCFP layers. Such isotropy will naturally lead to more diffuse

ECD and EPOT distributions in the underlying ply, along with lower peak ECD and EPOT magnitudes. The maximum ECD and EPOT in both the CM-protected and PCFP-protected composites were much smaller than the unprotected top lamina. This is reasonable because both the CM and PCFP outer layers can distribute electric current in-plane due to their high electrical conductivity.

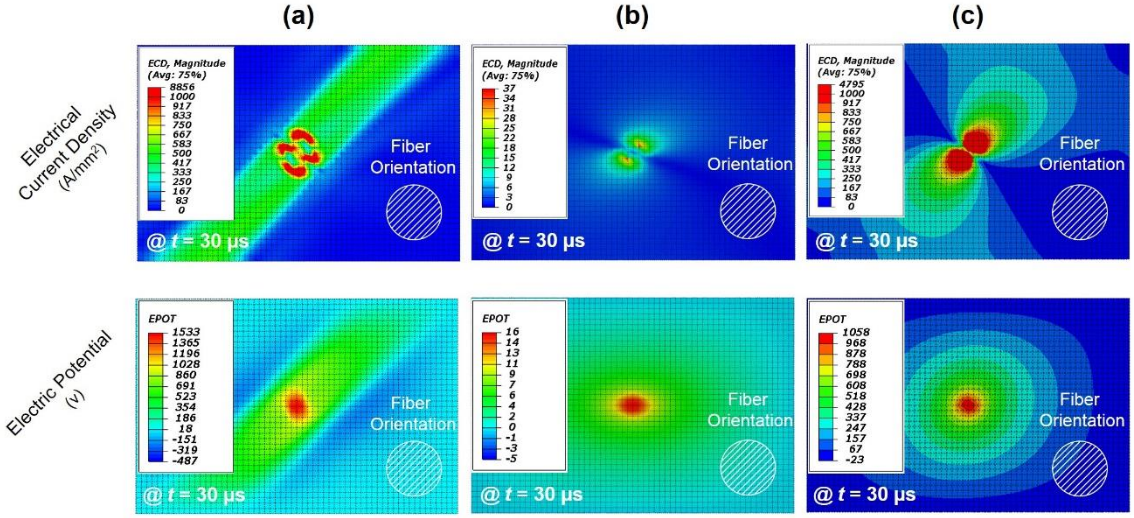

Figure 4.4 Electrical current density and electrical potential distributions in the top lamina of a) unprotected, b) CM-protected, and c) PCFP-protected 32-ply AS4/3506 carbon/epoxy laminates at the end of coupled thermal-electrical analyses ($t = 30\mu s$).

4.6.2 Matrix Thermal Decomposition in Unprotected and Protected Composites

Figure 4.5 shows the predicted matrix thermal decomposition in the top four AS4/3506 lamina of the unprotected, the CM-protected and the PCFP-protected composites after heat transfer analyses ($t = 10s$). The CM and PCFP outer protection layers are not shown. In the figure, domains with matrix decomposition levels greater than 0.01 were plotted. The red regions correspond to matrix decomposition in excess of

0.8 (*i.e.,* 80%). In the unprotected laminate (Fig. 4.5a), the decomposition area was elongated along the primary heat conduction path (*i.e.,* in the fiber direction). For successive inner plies, these domains were more elliptical with the semi-major axis aligned in the local fiber direction. In general, the extent of matrix decomposition decreases in the through-thickness direction. For the unprotected laminate, the elliptical domains with matrix decomposition in excess of 0.8 were approximately 18×15 mm^2, 14×13 mm^2, 13×12 mm^2, and 9×6 mm^2 in the top four plies, respectively. The shape and size of the matrix decomposition domains in the top +45˚ lamina of the unprotected composite agree fairly well with both experimentally measured results [1, 4] and a lightning strike FE simulation [42] for similar carbon/epoxy composites subjected to 40 kA peak lightning currents (Fig 4.6). A complete comparison of predicted matrix decomposition to an experimental result [1] will be addressed in Ref. [43].

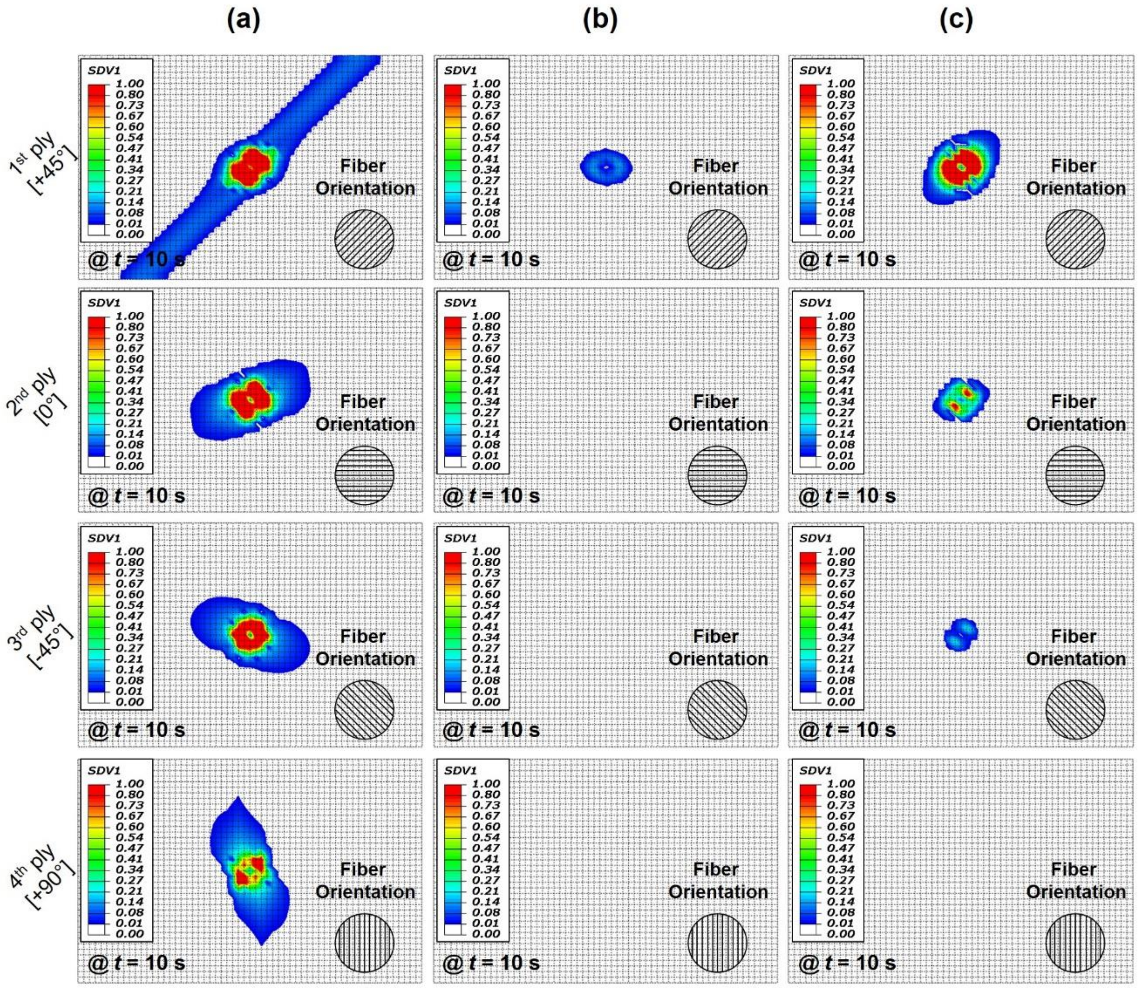

Figure 4.5 Matrix thermal decomposition in the top four lamina of the a) unprotected, b) CM-protected, and c) PCFP-protected 32-ply AS4/3506 carbon/epoxy laminates at the end of heat transfer analyses (*t* = 10 s).

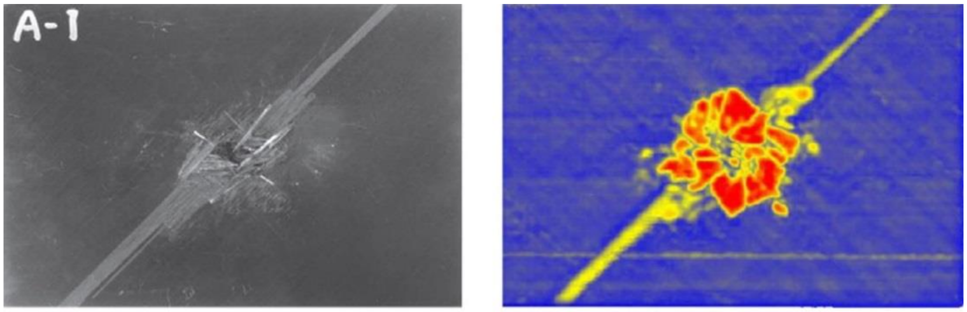

(a) Photograph
(40 kA from [56])

(b) Ultrasonic C-scan
(40 kA from [64])

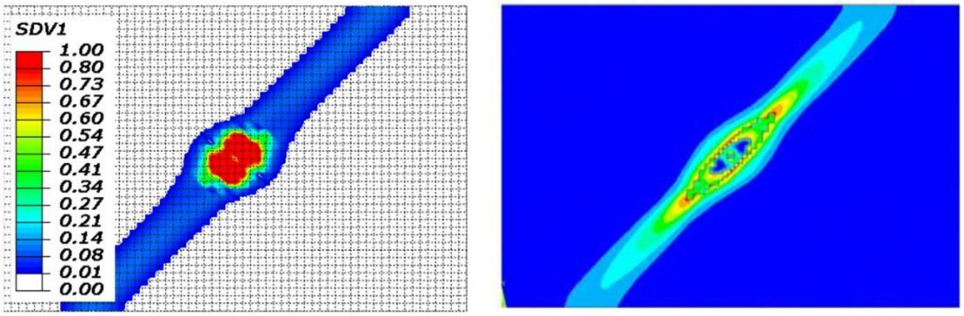

(c) Matrix Decomposition
(40 kA, this study)

(d) Temperature Distribution
(40kA from [30])

Figure 4.6 Lightning-induced thermal damage in typical carbon/epoxy laminate subjected to a simulated 40 kA peak lightning current: (a) photograph from Ref. [1], (b) ultrasonic C-scan from Ref. [4], (3) predicted matrix decomposition domain by the current FE model, and (d) temperature distribution after lightning strike from Ref. [42].

Since the CM and PCFP layers have isotropic in-plane electrical and thermal conductivities, the matrix decomposition occurring in the adjacent AS4/3506 plies will be somewhat more diffuse than for the unprotected laminate. For example, the predicted matrix decomposition area occurring in the outer +45˚ ply of the CM-protected laminate was fairly elliptical in shape and not elongated in the fiber direction (Fig. 4.5b). Moreover, the intensity of the predicted matrix decomposition was *drastically* lower than for the same ply in the unprotected laminate. In addition, no matrix decomposition was predicted in the underlying three plies. The maximum intensity of the predicted matrix decomposition in the top +45˚ lamina was 0.14 (*i.e.,* 14%); the total damaged area was approximately 28×19 mm^2. The carbon/epoxy plies adjacent to an arbitrary CM may be subjected to higher levels of heat transfer due to Joule heating and Cu vaporization to a hot gas. This is due to (1) the relatively high Cu boiling/critical temperatures (2567/8000˚C) and (2) the Cu electrical conductivity, which is nearly ten orders of magnitude greater than a composite's through-thickness conductivity (*cf.*, Tables 4.1 and 2). Abdelal and Murphy [5] suggested using a thinner CM that can be ablated more rapidly in order to reduce through-thickness heat transfer.

Similarly, the predicted matrix decomposition area occurring in the outer +45˚ ply of the PCFP-protected laminate was more concentrated in the vicinity of the lightning attachment point (Fig. 4.5c). Both the size and the intensity of matrix decomposition were reduced compared with the unprotected laminate's outer ply. The predicted damage in the next three plies were similarly reduced; no matrix decomposition was predicted in the fourth AS4/3506 ply. Hence, the PCFP outer layer also successfully reduced thermal damage in the underlying composite. The PCFP outer layer will be ablated more rapidly than the CM due to the PCFP's relatively low boiling/critical temperatures (3,316/3,367˚C). Moreover, the PCFP electrical conductivity is at least 100 times higher than the composite through-thickness electrical conductivity at high temperatures (≥ 510˚C). Therefore, the PCFP-protected composite is less susceptible to continuous heat transfer from the PCFP layer. The surface areas with the predicted matrix decomposition in excess of 0.80 in the top two AS4/3506 lamina of PCFP-protected composite were approximately 16×13 mm^2 and 7×6 mm^2, respectively. The maximum predicted matrix decomposition in the third AS4/3506 ply was 0.74 (*i.e.,* 74%); the total damaged area was approximately 6×6 mm^2. These predicted matrix decompositions (Fig. 4.5c) correspond to 23%, 77%, and 77% reductions compared to the unprotected composite (Fig. 4.5a). This suggests that a PCFP outer layer may be viable for a lightning protection layer.

The lightning strike FE models developed in this work suggested that no thermal ablation occurred in the top lamina of the unprotected, CM-protected, and PCFP-protected composites. In addition, no thermal ablation was predicted in the individual CM and PCFP lightning protection layers. Preliminary laboratory-scale lightning strike tests showed no evidence of thermal ablation in carbon/epoxy laminates with CM and PCFP protection layers. This will be addressed in Ref. [44].

Figures 4.7a-c shows the predicted through-thickness matrix decomposition in the unprotected, CM-protected, and PCFP-protected AS4/3506 carbon/epoxy laminates after heat transfer analyses (t = 10s), respectively. The CM and PCFP lightning protection layers are not shown in this figure. The region with predicted matrix decomposition of $\geq$ 0.01 is plotted. The dashed lines A-B in the upper images indicate the cutting plane used to define cross-sectional views shown in the lower images. For comparison, the top 16 plies of each composite are shown in the lower images, where the horizontal dashed lines define the maximum depth of thermal damage. Here, thermal damage penetration is defined as the maximum penetration depth. In the unprotected composite (Fig. 4.7a), predicted thermal damage penetrated to the fifth AS4/3506 ply. The predicted damaged area in each ply closely matched several previous lightning strike experiments [1, 4]. A complete comparison of thermal damage penetration is described in Ref. [43]. Both the CM (Fig. 4.7b) and the PCFP (Fig. 4.7c) mitigated thermal damage development in the underlying composites. The CM provided excellent protection from thermal damage, and predicted matrix decomposition only reached the first AS4/3506 ply (Fig. 4.7b). Similarly, the PCFP outer layer limited thermal damage to the top three composite plies. Both protection layers significantly lowered thermal damage verses the unprotected composite due to reduced through-thickness electrical current flow and heat conduction.

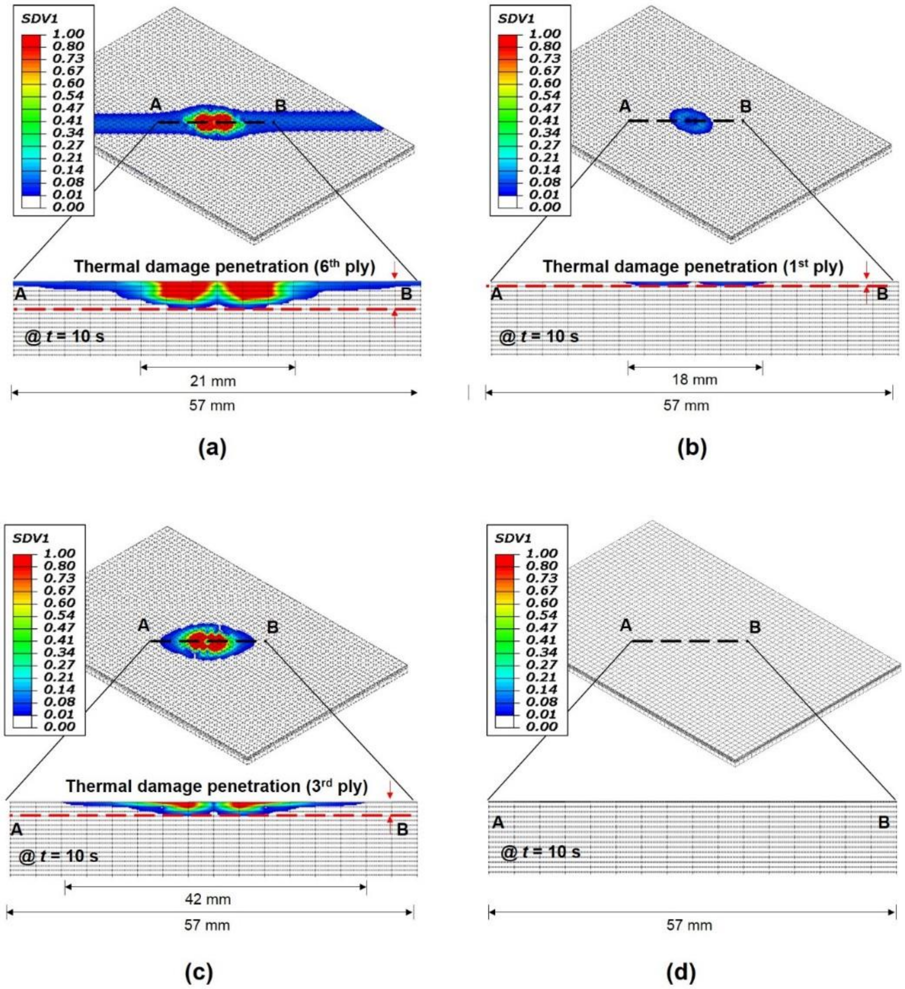

Figure 4.7 Thermal damage penetration from 40 kA peak current of a) unprotected and b) CM-protected, c) PCFP-protected, and d) PCFP-protected (with both the in-plane and through-thickness electrical conductivities 100 times greater the values defined in Table 3) 32-ply AS4/3506 carbon/epoxy composites at the end of heat transfer analyses (t = 10s).

Based upon parametric studies, the influence of the in-plane to through-thickness *thermal* conductivity ratio of a lightning protection layer plays a relatively small role thermal damage development in the underlying carbon/epoxy composite. In contrast, the in-plane to through-thickness *electrical* conductivity ratio has a profound impact on thermal damage development. This makes sense because lightning electric currents flowing through the carbon/epoxy composites are instantaneously converted into heat (Joule heating), which is proportional to the square of the currents. In addition, for a given level of current injection, a lower through-thickness electrical conductivity will lead higher electrical current densities, proportionally more Joule heating and more corresponding thermal damage. For instance, when the through-thickness electrical conductivity of a lightning protection layer is lowered, lightning thermal damage to the underlying (composite) plies *increases* since the total current density at a given instant in time increases (current can't flow as much in the thickness direction). This increased current raises the Joule heating created in the protection layer, thus creating more thermal damage in the underlying composite.

When the protection layer is designed to have a larger in-plane and smaller through-thickness electrical conductivity, the thermal damage to the underlying plies can be decreased. Figure 4.7d shows the predicted through-thickness matrix decomposition in the PCFP-protected AS4/3506 carbon/epoxy laminate with the in-plane electrical conductivity 100 times greater and the through-thickness electrical conductivity 100 times lower than those used in Fig. 4.7c. This PCFP outer layer limited thermal damage to the top two plies with fairly lower surface damage. This suggests how the PCFP can be tailored to give less thermal damage in the underlying composite, thus improve lightning strike protective capability. Furthermore, heat transfer at the interface between the protection layer and the underlying composite is governed by electrical and thermal gap conductances. Thus, the gap conductances will also have a significant effect on thermal damage development. The influences of lightning protection layer electrical/ thermal conductivities and the associated electrical/ thermal gap conductances with the first underlying ply on lightning thermal damage development in carbon/epoxy composite will be addressed in detail in a manuscript now in preparation [45].

4.7 Conclusions and Recommendations

Nonlinear transient coupled thermal-electrical and subsequent heat transfer FE analyses were performed to simulate the lightning-induced thermal damage development in AS4/3506 carbon/epoxy composites protected with copper mesh (CM) and pitch-based carbon fiber paper (PCFP) lightning protection layers. In this study, matrix thermal decomposition was considered as a primary form of lightning damage in the composites. Lightning-induced thermal damage development simulated in the protected composites were then compared with that in unprotected composites. The predicted matrix decomposition penetrated the top six plies in the unprotected AS4/3506 composite. The predicted domain with matrix decomposition closely matched results from the literature.

Both the CM and the PCFP protection layers successfully mitigated thermal damage development in the underlying composite. The intensity of the predicted matrix decomposition in both CM-protected and PCFP-protected composites was *drastically* lower than for the same ply in the unprotected laminate. In addition, no matrix decomposition in the CM-protected composite was predicted in the underlying second ply. Similarly, the PCFP outer layer limited thermal damage to the top three composite plies. For surface areas with the predicted matrix decomposition in excess of 0.80 (*i.e.*, 80%), the elliptical domains were approximately 16×13 mm^2 and 7×6 mm^2 in the top two plies of the PCFP-protected composite, while those were approximately 18×15 mm^2, 14×13 mm^2, 13×12 mm^2, and 9×6 mm^2 in the top four plies of the unprotected laminate. This suggests that the PCFP outer layer or similar conductive carbon-based layers may inhibit through-thickness electrical conduction, thus serving as an effective, lightweight lightning protection layer. Indeed, the PCFP protection layer in-plane, through-thickness, and gap electrical conductivities may be tailored to improve its lightning strike protective abilities. The pitch carbon fiber volume fraction and fiber orientation in the protective layer are variables that can be tailored.

The lightning strike FE models developed in this work may prove useful in preliminary assessments of lightning induced-thermal damage in both the unprotected and protected carbon/epoxy laminates. The current FE models, however, do not take into account possible interaction between individual carbon fibers and the epoxy matrix since each composite ply was idealized as a homogeneous continuum. The presence of local inhomogeneities (*i.e.*, fiber aggregates, voids, and resin rich regions) may exacerbate or mitigate lightning strike induced-damage development. For example, fiber aggregates or chars may accelerate thermal damage because of their relatively high electric/thermal conductivities. Resin rich domains may decrease thermal damage formation by providing electrically insulating regions in the through-thickness direction. In the future, the FE model will be revised to address such issues within a multiscale framework. In addition, inclusion of time- and temperature-dependent material properties and mechanical damage formation will be addressed.

Simulations to predict laminate mechanical damage, which results from both electromagnetic interactions and the magnetic overpressure during a lightning strike, would be a significant advance. The smaller the lightning attachment point/area, the greater such electromagnetic interactions can be [46]. This could enhance mechanical damage at/near the attachment point/area. Such grand challenges remain to be addressed.

Lightning strike tests are being conducted now to characterize thermal damage development in laminate test coupons (subjected to much higher current levels, up to 200 kA) at Mississippi State University High Voltage Laboratory (MSU-HVL). The lightning strike FE models developed in this study will be used to give preliminary assessments of lightning-induced thermal damage as a function of peak current level. The surface areas, depths, and volumes with predicted matrix decomposition will be then compared with experimental results at these higher current levels. Also, experimental strikes will be made on laminates protected by CM, PCFP, and graphene paper protection layers to assess their respective protective effects on the underlying laminates as a function of a peak current level. Moreover, Lee et. al. [47] recently characterized lightning-induced thermal damage development in stitched carbon/epoxy composite structures. They predicted that vertical through-thickness Vectran stitches may remain intact, effectively mitigating delamination initiation/growth emanating from the lightning damaged area. As part of future investigations, the current lightning strike FE model and experimental strike studies will be further developed to include the effect of stitching on thermal development in laminates and structural panels.

4.8 References

[1] Hirano, Y., S. Katsumata, Y. Iwahori, and A. Todoroki, "Artificial Lightning Testing on Graphite/Epoxy Composite Laminate," *Composites Part A: Applied Science and Manufacturing*, 2010, **41**(10): p. 1461-1470.

[2] Feraboli, P. and M. Miller, "Damage Resistance and Tolerance of Carbon/Epoxy Composite Coupons Subjected to Simulated Lightning Strike," *Composites Part A: Applied Science and Manufacturing*, 2009, **40**(6): p. 954-967.

[3] Kawakami, H. and P. Feraboli, "Lightning Strike Damage Resistance and Tolerance of Scarf-Repaired Mesh-protected Carbon Fiber Composites," *Composites Part A: Applied Science and Manufacturing*, 2011, **42**(9): p. 1247-1262.

[4] Ogasawara, T., Y. Hirano, and A. Yoshimura, "Coupled Thermal–Electrical Analysis for Carbon Fiber/Epoxy Composites Exposed to Simulated Lightning Current," *Composites Part A: Applied Science and Manufacturing*, 2010, **41**(8): p. 973-981.

[5] Abdelal, G. and A. Murphy, "Nonlinear Numerical Modelling of Lightning Strike Effect on Composite Panels with Temperature Dependent Material Properties," *Composite Structures*, 2014, **109**: p. 268-278.

[6] Dong, Q., Y. Guo, X. Sun, and Y. Jia, "Coupled Electrical-Thermal-Pyrolytic Analysis of Carbon Fiber/Epoxy Composites Subjected to Lightning Strike," *Polymer*, 2015, **56**: p. 385-394.

[7] Fanucci, J.P., "Thermal Response of Radiantly Heated Kevlar and Graphite/Epoxy Composites," *Journal of Composite Materials*, 1987, **21**(2): p. 129-139.

[8] Griffis, C., J. Nemes, F. Stonesifer, and C. Chang, "Degradation in Strength of Laminated Composites Subjected to Intense Heating and Mechanical Loading," *Journal of Composite Materials*, 1986, **20**(3): p. 216-235.

[9] SAE, "Aircraft Lightning Zoning," *Aerospace Recommended Practice ARP 5414*, 1999.

[10] SAE, "Aircraft Lightning Environment and Related Test Waveforms," *Aerospace Recommended Practice ARP 5412*, 1999.

[11] Ohm, G.S., Die galvanische Kette, Mathematisch Bearbeitet. 1827: Riemann.

[12] Menousek, J. and D. Monin, "Laser Thermal Modeling of Graphite Epoxy," *Naval Weapons Center Technical Memorandum*, 1979, **3834**.

[13] Mouritz, A.P. and A.G. Gibson, Fire Properties of Polymer Composite Materials. Vol. 143. 2007: Springer Science & Business Media.

[14] Matsumoto, T., "Mesophase pitch and its carbon fibers," *Pure and Applied Chemistry*, 1985, **57**(11): p. 1553-1562.

[15] Mueller, G., "Simulation of Repetitively-Pulsed Laser Irradiation of Graphite-Epoxy Composite." 1984, DTIC Document (NRL-MR-5467).

[16] Suzuki, Y., A. Todoroki, R. Matsuzaki, and Y. Mizutani, "Impact-damage Visualization in CFRP by Resistive Heating: Development of a New Detection Method for Indentations caused by Impact Loads," *Composites Part A: Applied Science and Manufacturing*, 2012, **43**(1): p. 53-64.

[17] Chemartin, L., P. Lalande, B. Peyrou, A. Chazottes, P. Elias, C. Delalondre, B. Cheron, and F. Lago, "Direct Effects of Lightning on Aircraft Structure: Analysis of the Thermal, Electrical and Mechanical Constraints," *AerospaceLab*, 2012, (5): p. 1-15.

[18] Maxwell, J.C., A Treatise on Electricity and Magnetism. Vol. 1. 1881: Clarendon press.

[19] ABAQUS, "ABAQUS Documentation," *Dassault Systémes Simulia Corp.*, 2014.

[20] Ahuja, S. and N. Jespersen, Modern Instrumental Analysis. Vol. 47. 2006: Elsevier.

[21] Oliveira, V. and R. Vilar, "Finite Element Simulation of Pulsed Laser Ablation of Titanium Carbide," *Applied Surface Science*, 2007, **253**(19): p. 7810-7814.

[22] Shklyaev, O.E. and E. Fried, "Stability of an Evaporating Thin Liquid Film," *Journal of Fluid Mechanics*, 2007, **584**: p. 157-183.

[23] Raffray, R., *Assessment of Dry Chamber Wall Configurations as Preliminary Step in Defining Key Processes for Chamber Clearing Code*, 2001 [cited 2015 17 Jun].

[24] Military-Handbook, "MIL-HDBK-17-2F: Composite Materials Handbook," *Polymer Matrix Composites: Materials Usage, Design, and Analysis*, 2002, **17**.

[25] Chen, J.-K. and F.A. Allahdadi, "Structural Composite Penetration Model Development." 1996, DTIC Document (PL-TR-96-1140).

[26] Zinkle, S. and S. Fabritsiev, "Copper alloys for High Heat Flux Structure Applications," *Atomic and Plasma-material Interaction Data for Fusion*, 1994, **5**: p. 163-191.

[27] Fultz, B., "Vibrational thermodynamics of materials," *Progress in Materials Science*, 2010, **55**(4): p. 247-352.

[28] Gathers, G., "Thermophysical Properties of Liquid Copper and Aluminum," *International Journal of Thermophysics*, 1983, **4**(3): p. 209-226.

[29] White, G. and M. Minges, "Thermophysical properties of some key solids: an update," *International Journal of Thermophysics*, 1997, **18**(5): p. 1269-1327.

[30] Xiao, X., S.V. Hoa, and K.N. Street, "Repair of Thermoplastic Resin Composites Using Fusion Bonding," *Composites Bonding, ASTM International*, 1994, **1227**: p. 30.

[31] Pradère, C., J.-C. Batsale, J.-M. Goyhénèche, R. Pailler, and S. Dilhaire, "Thermal properties of carbon fibers at very high temperature," *Carbon*, 2009, **47**(3): p. 737-743.

[32] Osaka Gas Chemicals, *DONACARBO Paper Data Sheet*, [cited 2015 17 Jun]; Available from: http://www.ogc.co.jp/e/products/carbon-f/donacarbo_paper.html.

[33] Potts, R.L., "Application of integral methods to ablation charring erosion-A review," *Journal of Spacecraft and Rockets*, 1995, **32**(2): p. 200-209.

[34] Mirmira, S., M. Jackson, and L. Fletcher, "Effective Thermal Conductivity and Thermal Contact Conductance of Graphite Fiber Composites," *Journal of Thermophysics and Heat transfer*, 2001, **15**(1): p. 18-26.

[35] Wang, S. and D. Chung, "Electrical Behavior of Carbon Fiber Polymer-Matrix Composites in the Through-Thickness Direction," *Journal of Materials Science*, 2000, **35**(1): p. 91-100.

[36] Dexmet Corporation, *Lightning Strike Protection for Carbon Fiber Aircraft (2007)*, [cited 2015 17 Jun]; Available from: http://www.dexmet.com/1_pdf/LSP%20for%20Carbon%20Fiber%20Aircraft.pdf.

[37] KRECA, *KRECA PAPER Paper Data Sheet*, [cited 2015 17 Jun]; Available from: http://www.kureha.com/pdfs/Kureha-KRECA-Carbon-Fiber.pdf.

[38] Njuguna, J. and K. Pielichowski, "Polymer Nanocomposites for Aerospace Applications: Properties," *Advanced Engineering Materials*, 2003, **5**(11): p. 769-778.

[39] Jiang, P., C. Zhao, J. Deng, and W. Zhang. "Experimental Investigation of Local Heat Transfer of Carbon Dioxide at Super-Critical Pressures in a Vertical Tube and Multi-Port Mini-Channels Under Cooling Conditions," in the *International Refrigeration and Air Conditioning Conference at West Lafayette, IN, July 14-17*, 2008.

[40] Lin, S.-S., "Current status of the carbon fiber industry in Japan." 1989, DTIC Document (MTL-TR-89-35).

[41] Kanoğlu, M., Y.A. Çengel, and İ. Dinçer, Energy Conversion Efficiencies, in *Efficiency Evaluation of Energy Systems*. 2012, Springer New York: New York, NY. p. 55-68.

[42] Wang, F., Y. Ji, X. Yu, H. Chen, and Z. Yue, "Ablation Damage Assessment of Aircraft Carbon Fiber/Epoxy Composite and its Protection Structures Suffered from Lightning Strike," *Composite Structures*, 2016, **145**: p. 226-241.

[43] Lee, J., T. E. Lacy, Jr., C. U. Pittman, Jr. and M. S. Mazzola, "Temperature-Dependent Thermal Decomposition of Carbon/Epoxy Laminates Subjected to Simulated Lightning Currents," *Polymer Composites, under revision*, 2017.

[44] Lee, J., Gharghabi, P., Brian, C., T. E. Lacy, Jr., C. U. Pittman, Jr. and M. S. Mazzola, "Experimental Validation of A Lightning Strike Finite Element Model of Carbon/Epoxy Laminates with Metallic and Non-Metallic Protection Layers," *manuscript in preparation*, 2017.

[45] Lee, J., T. E. Lacy, Jr., C. U. Pittman, Jr. and M. S. Mazzola, "The Influence of Material Properties on Lightning Strike Finite Element Simulation of Carbon/epoxy Composites," *manuscript in preparation*, 2017.

[46] Reid, G. "Mechanical Damage to Aircraft Structures from Lightning Strikes," in the *Proceedings of the Institution of Mechanical Engineers, Part G: Journal of Aerospace Engineering*, 1993.

[47] Lee, J., T. E. Lacy, Jr., C. U. Pittman, Jr. and M. S. Mazzola. "Thermal Response to Simulated Lightning Currents on Stitched Composite Aircraft Structures," in the *Proceedings of the American Society for Composites: Thirty-First Technical Conference, Williamsburg, VA, Sep 19-21*, 2016.

CHAPTER V

TEMPERATURE-DEPENDENT THERMAL DECOMPOSITION OF CARBON/EPOXY LAMINATES SUBJECTED TO HIGH IMPULSE CURRENTS

5.1 Abstract

A finite element (FE) parametric study was performed to characterize the temperature-dependence of thermal decomposition of AS4/3506 carbon/epoxy composites laminates subjected to simulated lightning currents of 40 kA or less during 30 μs. In this study, matrix thermal decomposition caused by simulated lightning currents was considered as a primary form of lightning damage. FE simulations were conducted to compare the size and the intensity of matrix thermal decomposition based on the fully coupled spatially- and temporally-varying temperature/material model that we developed and recently reported [1]. Two commonly used matrix decomposition temperature ranges of 300-500˚C and 300-600˚C were used to predict the extent of matrix decomposition. Matrix thermal decomposition was assumed to vary either *linearly* or *quadratically* within these given temperature ranges. The predicted size and intensity of matrix thermal decomposition around the lightning attachment point strongly depended on both the assumed thermal damage variation (*i.e.*, linear or quadratic) and matrix decomposition temperature ranges. The shape and size of the damaged matrix domains predicted using the linear damage variation between 300-500˚C agreed fairly well with experimentally

measured results available in the literature. Use of the linear damage variation between 300-600˚C and the quadratic damage variation of these temperature ranges somewhat underestimated thermal damage development compared to the few experimental lightning damage studies in the literature.

5.2 Introduction

Predicting lightning damage in carbon/epoxy composites is an ongoing focus of our laboratory [1]. A typical lightning strike occurs due to an electrical charge difference that ionizes surrounding air to a positive or negative charge [2]. The surrounding air acts as a good insulator, preventing electrical energy transfer from "electrically charged clouds" to the earth or adjacent clouds. In order to balance this difference in electrical charge, lightning occurs with local electrical breakdown of the air that makes it conductive. Hence, lightning follows an ionized conducting path. Numerical investigations of first and subsequent return strokes predicted that lightning arc radii continuously expand during the first 100 μs and these radii may reach more than 5 cm for peak currents ≥100 kA [3]. Lightning arc radii for relatively low peak currents (≤50 kA) are unknown.

Electrical current flow in continuous carbon fiber reinforced polymer (CFRP) composites depends on both the optimal conduction path (*i.e.*, fiber direction) and the grounding conditions [1]. CFRP plies exhibit orthotropic electrical properties; the electrical conductivity in the fiber direction can be significantly higher than for the in-plane transverse and the through-thickness directions. Since the amount of electrical energy dissipated as heat in CFRP composites by a transient lightning electric discharge is proportional to each constituent's electrical resistance [4], more Joule heating can occur in a relatively insulating polymer matrix per unit of current traversing that matrix region than for conductive fibers.

A lightning strike is a substantial transient electric discharge that can increase local temperatures to 30,000K at the lightning attachment point over 50-200 μs time scales [5, 6]. At such high temperatures, CFRP composites can be severely damaged in the vicinity of the lightning attachment point. In general, the lightning-induced damage in CFRP composites may be categorized into two main types: (1) thermal damage and (2) mechanical damage. Matrix damage (*i.e.*, thermal decomposition, local blistering, charring, and burning) and carbon fiber damage (*i.e.*, breakage and ablation) are often noticeable by visual inspection. Thermal damage underneath and beyond the lightning attachment location is difficult to detect and map, but can degrade mechanical properties. In addition, the mechanical damage resulting from the electromagnetic pulse and overpressure (magnetic pinch) can lead *to* fiber/matrix debonding and delamination failures [3]. In general, mechanical damage due to a lightning strike was considered less significant than thermal damage [7]. At higher electrical current magnitudes, the opposite may be true. In this study, lightning-induced mechanical damage was not considered, but will be investigated in the future.

The goal of the present study is to characterize the temperature-dependence of matrix thermal decomposition in AS4/3506 carbon/epoxy laminates subjected to simulated lightning currents ≤40 kA applied over 30 μs. Four unique matrix thermal decomposition profiles were considered and compared herein. These include linear and quadratic thermal damage variations occurring within two temperature ranges established in literature [8-11] (*i.e.*, 300-500˚C and 300-600˚C), which were utilized to predict the extent of matrix thermal decomposition in the laminates. For reference purposes, an Arrhenius kinetic equation was also approximated and employed in temperature ranges of 300-500˚C. The surface areas and depths associated with predicted degrees of matrix thermal decomposition were then compared with experimentally measured results for similar composites subjected to the same peak current levels. All simulations were carried out using ABAQUS 6.14 finite element (FE) code [12] employing special-purpose subroutines that we recently reported [1].

5.3 Literature Review

5.3.1 Lightning Strike Damage

Only a few laboratory-scale *artificial* lightning strike tests [13-17] have been reported that characterize damage development in typical carbon/epoxy composites. Hirano *et al.* [13] attempted to correlate the composite damage development with various lightning peak currents, electrical charges, and action integrals. They categorized lightning-induced damage into three distinct modes: (1) carbon fiber damage (*i.e.*, breakage and ablation), (2) matrix damage (*i.e.*, local burn/blistering), and (3) delamination damage. The peak current magnitude correlated with fiber damage and the through-thickness damage development. In contrast, the electrical charge and the action integral of applied lightning current waveforms governed both matrix and delamination damage.

Feraboli and Miller [14] performed damage tolerance analyses and residual strength tests on HTA/7714A carbon/epoxy composite laminates, with and without stainless steel fasteners, when subjected to simulated lightning strikes. The layup employed was $[+45/0/0/-45/0/0/90]_s$ with a nominal ply thickness of 0.18 mm. At the simulated lightning currents less than 50 kA, the resulting damage penetrated to the fourth lamina. In contrast, the damage completely penetrated through the fastener-containing composites, since a fastener serves as a through-thickness electrical conduction path. Composite specimens without fasteners subjected to a 50 kA current exhibited a ~20% reduction in tensile residual strength and a ~30% reduction in compressive residual strength. However, specimens with fasteners subjected to the same current exhibited negligible changes in tensile residual strength but a ~60% reduction in compressive residual strength. The tensile residual strength is governed by the stress concentration near an open hole [18]. In general, tensile residual strength increases as the stress concentration decreases [18, 19]. If a change in stress concentration due to damage caused by lightning strike is negligible, the tensile residual strength remains relatively unchanged. In contrast, the compressive residual strength is governed by global or local instabilities (fiber buckling, delamination growth/buckling, etc.) that can be exacerbated by local matrix damage, as well as the local stress concentration arising from an open hole. Extensive internal matrix decomposition associated with Joule heating induced by lightning currents may accelerate premature specimen failure.

Feraboli and Kawakami [15] compared the relative severity of lightning-induced damage and mechanical impact damage in similar (T700S/2510) carbon/epoxy laminates. The amount of electrical energy dissipated as heat in the composites during applied lightning currents was compared to the strain energy absorbed in the composites during low velocity impact tests. The amount of electrical energy dissipated during the lightning current application was *much greater* than the strain energy stored in the composites in low velocity impacts. However, these low velocity impacts caused greater damaged areas and more reduction in compressive residual strengths than the applied lightning currents. This indicates an energy-based comparison of two damage mechanisms is *inappropriate* as these energy inputs are absorbed differently.

Yin *et al.* [16] performed artificial lightning strike testing on AS4/8552 carbon/epoxy twill woven fabric composites after the application of 30, 50, and 80 kA nominal peak currents. The woven fabric composites were fabricated using 16 plies (ply thickness of 0.25 mm) with a $[0_W/90_F]_{16}$ layup: the subscripts ‘W’ and ‘F’ correspond to warp and fill directions, respectively. Surface examinations of actual lightning damage in the woven fabric composites were compared to a similar IM600/133 carbon/epoxy *laminated* composite [13]. The size of the regions with intense local damage (severe carbon fiber rupture/ablation, matrix decomposition, etc.) to the woven fabric composites increased as the peak current increased, since greater peak current leads to more Joule heating (*i.e.*, more thermal damage), consistent with those of the laminated composite. However, the regions of intense local damage were fairly circular in shape due to transversely isotropic electrical and thermal conductivities resulting from woven fabric architecture. This was not observed in a similar IM600/133 laminated composite (i.e., the damaged zones tended to elongate along the major fiber axis in the outermost ply). The size of the regions with both overall damage and matrix decomposition linearly varied with action integral of the applied current waveform. Furthermore, through-thickness damage penetration was somewhat proportional to the logarithm of the action integral.

Recently, Wolfrum et al. [17] characterized the lightning damage resistance of aerospace-grade carbon/epoxy laminated composites subjected to 260 kA nominal peak currents. Two representative carbon/epoxy composites were considered: (1) 20-ply (ply thickness of 0.135 mm) IM7/8552 carbon/epoxy composites with a $[45/90/45/0/45]_{2S}$ layup and (2) 20-ply (ply thickness of 0.130 mm) PAN-based HTA/HTS carbon fiber non-crimp fabrics (NCF) with a $[45/0/90/45/-45]_{2S}$ layup. The IM7/8552 laminates were fabricated in an autoclave and HTA/HTS NCFs were infused with 8552 epoxy resin using vacuum-assisted infusion technology. For both carbon/epoxy material systems, the lightning-damaged laminates exhibited intense local damage (severe fiber rupture/tow splitting/ablation, matrix decomposition, etc.) in the vicinity of the lightning attachment locations. Ultrasonic testing determined the through-thickness damage penetration in the five-six underlying plies. Furthermore, additional lightning strike tests were performed on scarf-repaired NCFs. Application of the scarf patch significantly reduced regions with intense local damage: the patch just outside the lightning attachment location remained intact after lightning strike tests. However, electrical flashovers in the tapered zone occurred between the patch and the underlying composite. These were prevented by enhancing adhesive's electrical conductivity.

Several lightning strike finite element (FE) models [1, 20-25] have been developed for characterizing thermal damage development in carbon/epoxy composites. Ogasawara *et al*. [20] first developed nonlinear transient lightning strike FE models for carbon/epoxy laminates using coupled thermal-electrical analyses and subsequent heat transfer analyses. Temperature-independent properties were employed to predict thermal damage development and the assumed through-thickness electrical conductivity varied linearly between the matrix decomposition temperature (600˚C) and the fiber sublimation temperature (3,316˚C). The surface areas reaching predicted temperature distributions in the range of 300-600˚C agreed roughly with experimentally measured results obtained by Hirano *et al.* [13].

Abdelal and Murphy [21] developed a multiphysics-based lightning strike FE model for carbon/epoxy laminates with and without a copper mesh (CM) protection layer. Their model predicted that a CM can successfully mitigate thermal damage penetration in the underlying laminates. Use of a thinner CM may reduce through-thickness electrical conduction and heat conduction from the CM. Recently, Lee *et al.* [1] predicted that a pitch-based carbon fiber (PCFP) and similar carbon-based layers may serve as efficient lightning protection layers. A detailed description on thermal performance of a PCFP protection layer is available in Ref. [1].

Guo *et al.* [24] developed lightning strike FE methodologies using the Scheil' superposition principle, which is commonly used for non-isothermal phase change. The time/temperature-dependent pyrolysis of IM600/133 carbon/epoxy system subjected to simulated lightning strikes was predicted using an Arrhenius kinetic equation with a selected pre-exponential factor and activation energy measured at low heating rates ($\beta \leq$ 20˚C/min [20]). The domains with predicted matrix decomposition and through-thickness thermal damage penetration were compared with the *actual* lightning damage morphologies of IM600/133 and TR50S15L/YPH-308 carbon/epoxy system. Although some relative errors were present, the FE results showed an acceptable agreement with the experimental data. Applications of an Arrhenius kinetic equation to matrix thermal decomposition require empirically determined parameters: a detailed description of these parameters is described in a forthcoming section. These are all unknown for cases involving the very rapid heating encountered in a lightning strike, where the composite heating rate in various locations can exceed 1,000˚C/s, 1,000˚C/min or 100˚C/min.

Matrix temperature decomposition ranges played an important role in previous lightning strike FE models [20-23] attempting to predict the extent of matrix thermal decomposition during lightning-induced damage to carbon/epoxy laminates. All the lightning strike FE models [20-23] assumed a linear variation of matrix decomposition over the given matrix decomposition temperature ranges. Such an assumption may be unrealistic since matrix decomposition occurs through a series of complex chemical reactions with different activation energies, leading to char formation and resin residues in the condensed state. Mass transfer at high temperatures and steep thermal gradients going from solid matrices to gases and residues and their effects on condensed state mechanisms are unknown. Thus, *actual* matrix thermal decomposition does not vary linearly with temperature. Moreover, at temperatures above the onset of epoxy decomposition (≥300˚C), carbon/epoxy composites can be progressively and irreversibly damaged due to permanent pyrolytic matrix decomposition as a function of time at these temperatures. Thus, thermal damage development should be determined based on the local time/temperature history, but this becomes enormously complicated. In this study, the highest local temperature was used as a parameter to represent irreversible damage at a given location.

Recently, Wang [25] developed the lightning strike FE methodologies for a composite wind turbine blade The model includes surface interaction between a lightning arc channel (as a function of standard impulse current waveform) and carbon fiber or glass fiber reinforced composites. The thermal response, fiber ablation, and matrix decomposition induced by lightning were predicted based upon the temporary and spatially varying (or non-uniform) heat flux and current density. In addition, using moving boundary concepts (i.e., varying lightning arc channel size and instantaneous material removal due to fiber ablation), a nonlinear transient heat transfer problem was formulated for AS4/3506 and IM600/133 carbon/epoxy material systems. The domains with fiber thermal ablation showed fairly good agreement with reported experimental results.

5.3.2 Lightning Strike Test Parameters

The lightning current waveform (Figure 5.1) used here was introduced and discussed in Ref. [1]. The high peak currents in components A and D of the current waveforms are used to perform research on lightning strikes and to certify the vast majority of airframe acreage [14]. Waveform A requires a peak current of 200 kA (± 10 %), an action integral of 2.0×10^6 $A^2 \cdot s$, and a time duration of ≤ 500 μs. Waveform D requires a peak current of 100 kA (± 10 %) and an action integral of 2.5×10^5 $A^2 \cdot s$ with the same time duration. The peak currents defined in SAE ARP 5412 [6] are intended for full-scale or component-level lightning strike tests. In prior laboratory-scale lightning strike tests [13, 14, 20, 22], such high peak currents can produce sudden intense heat that can instantly burn/destroy test coupons. Hence, typical laboratory-scale lightning strike tests employ peak currents ≤ 50 kA, while all other criteria remain unchanged.

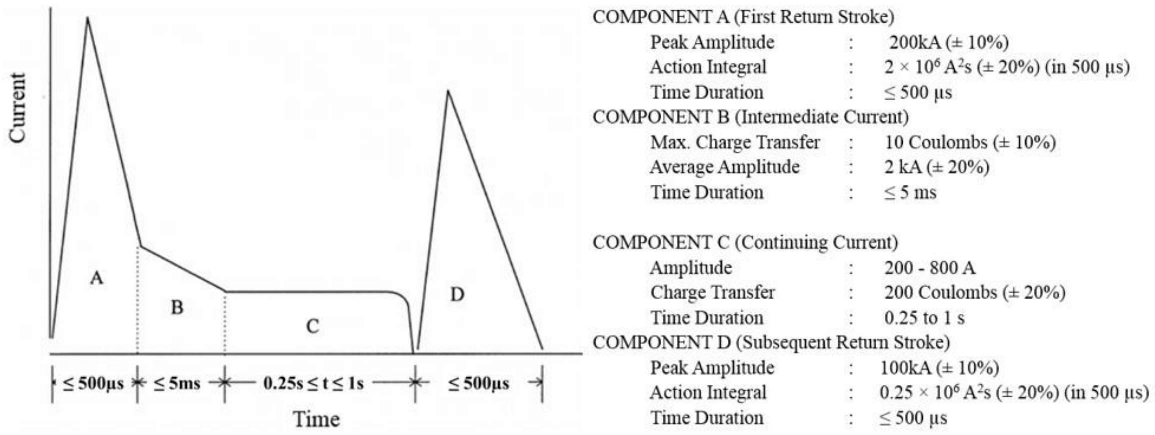

COMPONENT A (First Return Stroke)

Peak Amplitude	:	200kA (± 10%)
Action Integral	:	2×10^6 A^2s (± 20%) (in 500 μs)
Time Duration	:	≤ 500 μs

COMPONENT B (Intermediate Current)

Max. Charge Transfer	:	10 Coulombs (± 10%)
Average Amplitude	:	2 kA (± 20%)
Time Duration	:	≤ 5 ms

COMPONENT C (Continuing Current)

Amplitude	:	200 - 800 A
Charge Transfer	:	200 Coulombs (± 20%)
Time Duration	:	0.25 to 1 s

COMPONENT D (Subsequent Return Stroke)

Peak Amplitude	:	100kA (± 10%)
Action Integral	:	0.25×10^6 A^2s (± 20%) (in 500 μs)
Time Duration	:	≤ 500 μs

Figure 5.1 Standard current waveforms associated with peak current magnitudes, time durations, electrical charges and action integrals adopted from [6].

5.4 Theoretical Background

Epoxy matrices undergo thermal decomposition when exposed to elevated temperatures. Such matrix decomposition (due to pyrolysis) results in permanent irreversible damage. Char forms due to matrix decomposition are accompanied by out-gassing of H_2O, CO, CO_2, organic fragments, and increasing aromatization. Mouritz *et al.* [26] reported that the chars that form during thermal decomposition of thermosetting polymers are primarily carbon (85-98%) with higher aromatic contents; thus, these materials typically exhibit higher electrical and thermal conductivities than the initial (original) epoxy matrices. Above the epoxy matrix initial decomposition temperatures (≥300˚C), the composite properties are related to those of carbon fibers, undamaged remaining matrix, resin residues, and chars that underwent complex chemical reaction mechanisms. Hence, the extremely rapid temperature rise occurring during electrical conduction due to lightning and the subsequent heat transfer suggests that the "degree of matrix decomposition" is a function of time, temperature, and location [1].

One way to define the degree of thermal decomposition (*D*) is by the weight fraction lost:

$$D = \frac{m_i - m}{m_i - m_f} \tag{5.1}$$

where *m* is the material weight at any time and the subscripts *i* and *f* denote the initial and final states, respectively. Here, *D* = 0 and *D* = 1 correspond to no material decomposition and complete (100%) decomposition, respectively. The time rate change of *D* is proportional to the n^{th} power of the undecomposed portion of the decomposing mass, 1-*D* [27]:

$$\frac{dD}{dt} = k(1 - D)^n \tag{5.2}$$

where *k* is the rate constant of temperature-dependent chemical reaction that can be determined by an Arrhenius kinetic equation [28], *i.e.*,

$$k = A \exp\left(-\frac{E_a}{R\,T}\right) \tag{5.3}$$

Here *A* and E_a are the empirically determined pre-exponential factor (1/min) and activation energy (minimum amount of energy required to reach the transition state for a given reaction or, as defined here, simply fitted empirically to the entire complex decomposition process, J/mol). The parameters *R* and *T* are the ideal gas constant (J/mol/°C) and an absolute temperature, respectively. Substitution of Eq. 5.3 into Eq. 5.2 gives the rate of thermal decomposition change with increasing temperature:

$$\text{(a)} \qquad \frac{dD}{dT} = \frac{A}{\beta} \exp\left(-\frac{E_a}{R\,T}\right) (1 - D)^n$$

$$\text{(b)} \qquad D = \int \frac{A}{\beta} \exp\left(-\frac{E_a}{R\,T}\right) (1 - D)^n dT \tag{5.4}$$

where β denotes the heating rate (dT/dt, ˚C/min). Here the process is assumed to occur over a given matrix decomposition temperature range.

The degree of matrix decomposition may be expressed as a function of time and location using an Arrhenius kinetic equation and the temperature history of that location. However, an Arrhenius kinetic equation is likely to be inappropriate for use with the very rapid localized heating encountered in a lightning strike since the empirically determined parameters A and E_a (Eq. 5.3) can be only measured at much lower heating rates ($\beta \leq 20$˚C/min [20]). In contrast, the rate of temperature increase in the composite due to a lightning strike locally exceeds 1,000˚C/min [20]. Furthermore, the actual time scales associated with structural changes and chemical reactions in the condensed (solid) state are not well known. The activation energies for all of the reactions occurring will change as the local temperature increases because the chemical reactions that occur will change. Finally, the activation parameters for the plethora of chemical reactions occurring at elevated temperatures are unknown. Thus, application of an Arrhenius kinetic equation to the solid-state matrix thermal decomposition from a lightning strike can be used only as a simple approximation for reference purposes.

As a simple alternative to the use of an Arrhenius kinetic equation to predict the degree of matrix decomposition (D) in a carbon/epoxy composite, the amount of matrix decomposition can be assumed to instantly increase over the range of matrix decomposition temperatures (*i.e.*, 300-500˚C [8, 9] or 300-600˚C [10, 11]). This can be expressed mathematically as

$$D = \left(\frac{T - T_i}{T_F - T_i}\right)^m \qquad \text{for } T_i \leq T \leq T_F \qquad (5.5)$$

where T_i is the temperature defining the onset of matrix decomposition (300˚C in this study) and T_F is the temperature at which complete (100%) matrix decomposition occurs (500˚C or 600˚C). Here, matrix decomposition (damage) was assumed to vary linearly ($m = 1$) or quadratically ($m = 2$) over the matrix decomposition range. The degree of matrix thermal decomposition (Eq. 5.5) was simply defined between normalized values of zero and one (*i.e.*, $0 \leq D \leq 1$) based on the highest temperature reached at that location over either of the two matrix decomposition temperature ranges employed. Thus, the degree of matrix thermal decomposition below the *initial* matrix decomposition temperature was set to zero ($D = 0$ for $T \leq T_i$) and that above the *final* matrix decomposition temperature was set to one ($D = 0$ for $T \geq T_F$).

5.5 FE Model Development for Predicting Matrix Thermal Damage

The lightning strike FE simulation methodology [1] was previously developed to predict thermal damage development in AS4/3506 carbon/epoxy laminates. Using this methodology, the spatially- and temporally-varying local temperature and the corresponding matrix decomposition resulting from applied electrical currents simulating lightning strikes was predicted. This model includes the incorporation of material property changes as the temperature increases and decreases. Such an FE model is briefly summarized in the following sections.

5.5.1 Carbon/Epoxy Composite Material Properties

Typical epoxy matrices undergo thermal decomposition when exposed to elevated temperatures. The overall composite properties are highly dependent on matrix thermal decomposition, which is determined based on the time/temperature history at each location. Hence, it is necessary to employ matrix thermal decomposition associated with the time/temperature profile to characterize composite thermal damage development. The matrix undergoes irreversible thermal damage at much lower temperatures than the carbon fibers.

Table 5.1 Material properties of AS4/3506[a] carbon/epoxy plies [29-33]

Temp., T	Density [b], ρ	Specific Heat [b], C_p	Thermal Conductivity [b], k			Electrical Conductivity [c], σ		
			Longi.	Trans.	Thick.	Longi.	Trans.	Thick.
(˚C)	(Kg/mm^3)	(J/(kg·K))	(W/(mm·K))	(W/(mm·K))	(W/(mm·K))	(S/mm)	(S/mm)	(S/mm)
25	1.52E-06	1,065	4.66E-02	6.83E-04	6.83E-04	35.97	1.15E-03	3.9E-06
350	1.52E-06	2,100	2.47E-02	3.73E-04	3.73E-04	35.97	1.15E-03	3.9E-06
510	1.08E-06	2,100	1.46E-02	1.79E-04	1.79E-04	35.97	2	2
1,000	1.08E-06	5,750	1.17E-02	1.32E-04	1.32E-04	35.97	2	2
3,316	1.08E-06	5,875	1.00E-04	1.00E-04	1.00E-04	35.97	2	2
3,367	1.08E-06[d]	5,875[d]	1.00E-04[d]	1.00E-04[d]	1.00E-04[d]	1[d]	1[d]	1.0E+06[d]

[a] This composite typically has a fiber volume fraction of 0.60-0.66 [34, 35].

[b] Ref. [29, 30], [c] Ref. [31, 32].

[d] Properties determined by the extrapolation of the empirical data over the temperature range (25-3,316˚C).

Table 5.1 summarizes temperature-dependent material properties of AS4/3506 carbon/epoxy composites available in the literature [29-33]. These properties were experimentally measured up to the fiber sublimation temperature (3,316˚C). In our previous numerical simulations [1], the local composite properties were updated by linear interpolation of properties in the temperature range (25-3,316˚C). An additional set of properties were defined at the critical sublimation temperature of pure solid carbon (3,367˚C) [33]. Such properties were approximated by a quadratic extrapolation of the experimental results defined over the temperature range (25-3,316˚C). As described in Ref. [1] in more detail, several assumptions were made once the local temperature exceeded the critical sublimation temperature (3,367 ˚*C*): (1) the local composite properties were assigned those at 3,367 ˚*C* for the rest of simulation, (2) the thermal conductivities were assumed to be isotropic, and (3) the through-thickness conductivities are assumed to be very high (10^6 S/mm) when the composite ply has fully ablated to ensure electrical currents flow instantaneously to the inner adjacent ply. This special numerical procedure ensures realistic current flows to reach the next inner ply, akin to a moving boundary condition. The composite latent heat of fusion was 4.8×10^3 kJ/kg [21] absorbed in the matrix thermal decomposition temperature ranges (*i.e.*, 300-500˚C and 300-600˚C). The composite latent heat of vaporization was 4.3×10^4 kJ/kg [21], absorbed between the fiber sublimation temperature (3,316˚C) and the critical sublimation temperature (3,367˚C).

5.5.2 FE Model Discretization and Boundary Conditions

Consistent with previous work performed by several researchers [1, 20, 21], the simulated AS4/3506 carbon/epoxy laminate consisted of 32 plies (ply thickness of 0.125 mm) with a quasi-isotropic lay up of $[+45/0/-45/90]_{4s}$. The laminate was discretized using three-dimensional (3D) linear brick continuum elements with in-plane dimensions of 2.5×2.5 mm^2. A detailed description of the FE model discretization can be found in Ref. [1].

The electrical and thermal boundary conditions (see Fig. 5.2 from Ref. [1]) implemented in this study were motivated by those used in laboratory-scale artificial lightning strike tests [13, 14, 36]. In the coupled thermal-electrical FE analyses, zero electrical potentials representing electrical grounding conditions were imposed on the bottom and lateral surfaces of the simulated laminates. Thermal radiation is one of the dominant heat transfer mechanisms during and immediately after lightning strike to composites [3]. Thus, a radiation boundary condition was assigned on the exposed top and lateral surfaces during the entire simulation. The composite surface emissivity was 0.85 [29] with an ambient temperature of 25°C. In the subsequent longer duration nonlinear heat transfer analyses, a convection boundary condition was employed to account for simultaneous heat diffusion and advection. The composite convection coefficient for reasons described in Ref. [1] was assumed to be that of carbon dioxide (CO_2, 200 $W/m^2/K$ [37]).

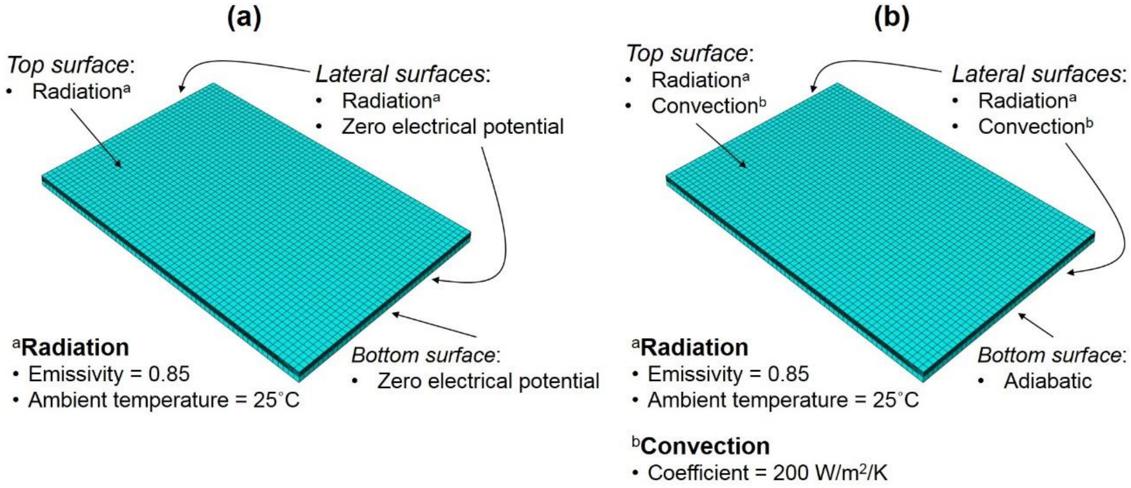

Figure 5.2 Electrical and thermal boundary conditions imposed in lightning strike FE simulations: (a) in coupled thermal-electrical analyses and (b) in subsequent heat transfer analyses [1].

5.5.3 Special-Purpose User Subroutines

In general, idealized lightning currents are typically defined as double exponential waveforms. The user-defined amplitude subroutine (UAMP) [1] was developed to simulate such double exponential current waveforms. In this study, uniformly distributed surface currents were injected over ~10 mm diameter lightning arc channels at the center in the outermost layer (top lamina). Three peak currents (20, 30, and 40 kA) were considered to compare FE model thermal damage predictions with experimental results for an analogous carbon/epoxy composite subjected to the same current levels. Figure 5.3 shows the lightning current waveform with a 40 kA peak current applied over a 30 μs time duration. For relatively low peak currents, the lightning current waveform parameters (*i.e.*, I_0, α, and β) are identical to those defined in Ref. [6] (see also, Fig. 5.3) with the exception that I_0 = 21,881 (for 20 kA) and 32,822 (for 30 kA).

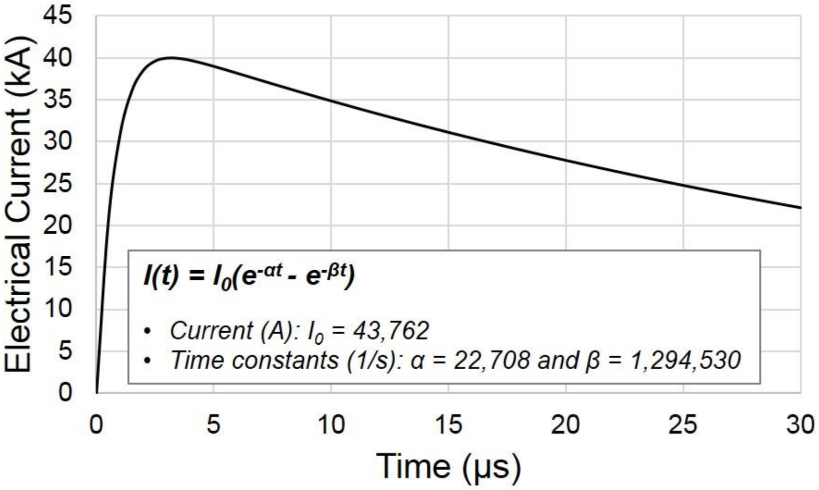

Figure 5.3 Lightning current waveform (I_0 = 43,762 A, α = 22,708 1/s, and β = 1,294,530 1/s) for a 40 kA peak current, these parameters were those defined in the current waveform D [6].

The user-defined heat generation subroutine (HETVAL) *[1]* was developed previously to calculate matrix thermal decomposition of AS4/3506 carbon/epoxy composites subjected to simulated lightning currents based on spatially- and temporally-varying temperature. In these temperature ranges, the degree of matrix thermal decomposition was defined between a normalized value of zero (*undamaged*) and one (*fully damaged*) based only on the highest temperature reached at that location (Eq. 5.5). The extent of matrix thermal damage was independent of the residence time at any temperature within the decomposition range in this simulation. The extent of matrix decomposition was assumed to vary either linearly ($m = 1$) or quadratically ($m = 2$) throughout both of these two given temperature ranges. For reference purposes, the Arrhenius kinetic equation (Eqs. 5.4a-5.4b) with the estimated parameters (*i.e.*, $n = 3.5$, $A = 5.0\times10^{13}$ 1/min, and $E_a = 180$ kJ/mol/K from Ref. [20]) was also developed to characterize matrix thermal decomposition in temperature ranges of 300-500˚C. These parameters were experimentally determined at a heating rate (≤ 20˚C/min), which is not related to the real heating rate of lightning strikes. Ogasawara et al. [20] estimated that the representative heating rate in the vicinity of the lightning attachment point was locally much higher than 1,000˚C/min. In order to reduce computational time, a quadratic approximation ($m = 2$, Eq. 5.5) was used to predict the degree of matrix decomposition over the range $T_i = 380$˚C and $T_F = 490$˚C. Such an approximation closely matches the predicted matrix damage obtained using the Arrhenius kinetic equation (Eqs. 5.4a-5.4b) with a heating rate of $\beta = 1{,}000$˚C/min. This use of a quadratic approximation for varying the degree of matrix thermal decomposition as temperature increases is one approach to account for the exponential dependence of decomposition reaction rates on increasing temperature.

Figure 5.4 plots the predicted extent of matrix thermal decomposition versus the highest temperature reached when determined using both linear ($m = 1$) and quadratic ($m = 2$) approximations (Eq. 5.5) in both temperature ranges of 300-500˚C and 300-

600˚C. The solid line with open triangles defined between 380-490˚C indicates the quadratic approximation of the matrix thermal decomposition profile that nearly overlaps the profile of the Arrhenius kinetic equation (Eqs. 5.4a-5.4b). Note that when using the quadratic approximation ($m = 2$) the rate of matrix decomposition increases with increasing temperature. All five of the approximations were used to predict the degree of matrix thermal decomposition.

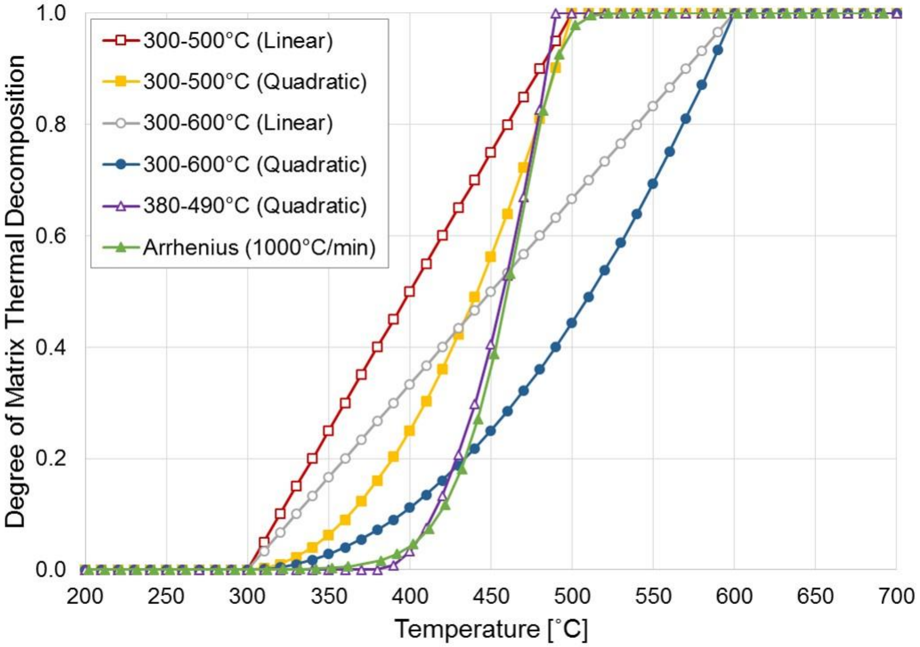

Figure 5.4 Predicted matrix thermal decomposition profiles defined by using a linear ($m = 1$) or quadratic ($m = 2$) approximation (Eq. 5.5) in the temperature ranges of 300-500˚C and 300-600˚C.

Predicted values obtained using the Arrhenius kinetic equation (β = 1,000˚C/min, Eqs. 5.4a-5.4b) and a nearly consistent quadratic approximation (solid line with open triangles) are plotted for reference purposes.

5.6 Predicted Matrix Thermal Decomposition

The predicted shape and size of the domains with matrix thermal decomposition for AS4/3506 laminates were compared with experimental and computational results for a similar IM600/133 carbon/epoxy composite subjected to a 40 kA peak lightning current [20]. Figures 5.5a-5.5b show a photograph and an ultrasonic C-scan image of fiber/matrix damage in a IM600/133 carbon/epoxy laminate subjected to 40 kA peak current [20]. In addition, Fig. 5.5c shows the predicted matrix damage obtained using room temperature material properties occurring over the temperature range 300-500˚C from Ref. [20]. The IM600/133 laminate [20] consisted of 32 plies (ply thickness of 0.147 mm) with a $[+45/0/-45/90]_{4s}$ layup. Lightning damage in composites depends on the material system and temperature history at each location. The room temperature IM600/133 ply properties and fiber volume fraction are similar to those for AS4/3506 plies. Since temperature dependent IM600/133 properties were not readily available in the literature, lightning damage predictions were obtained using properties for AS4/3506 laminate (Table 5.1). In the figures, fiber damage was largely localized in the vicinity of the lightning attachment point and aligned along the top lamina’s fiber direction (+45˚). In contrast, the matrix damage regions were somewhat distributed over the top lamina and typically included the fiber damaged regions. In Figs. 5.5a-5.5c, fiber damage was largely localized in the vicinity of the lightning attachment point and aligned along the top lamina’s fiber direction (+45˚). In contrast, the matrix damage regions were somewhat distributed over the top lamina and typically included the fiber damaged regions.

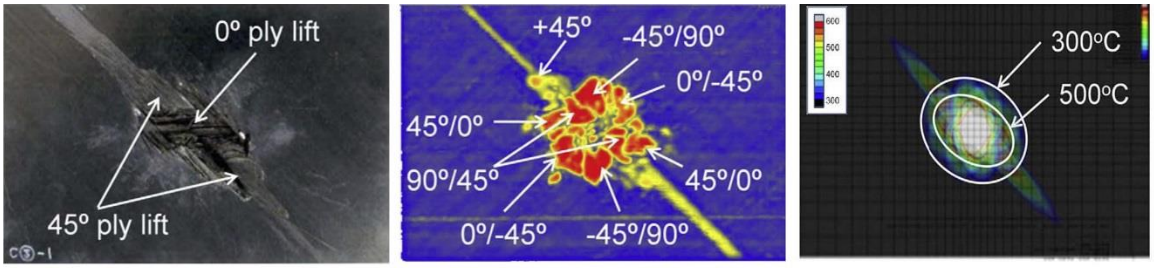

(a) Photograph (b) Ultrasonic C-scan (c) Predicted matrix damage

Figure 5.5 Lightning-induced damage in an IM600/133 carbon/epoxy composite subjected to a simulated 40 kA peak lightning current: (a) photograph, (b) ultrasonic C-scan, and (c) projected regions with predicted temperature distributions in the range of 300-500˚C (adopted from [20]).

A series of lightning strike FE simulations were performed to characterize matrix thermal decomposition in AS4/3506 carbon/epoxy laminates. Recall that the predicted extent of matrix decomposition caused by simulated lightning currents was determined using four sets of calculations involving either linear or quadratic approximations over the two temperature ranges of 300-500˚C and 300-600˚C (Fig. 5.4). The predicted size, shape, and extent of matrix thermal decomposition in the top AS4/3506 lamina subjected to a 40 kA peak current obtained using the four approximations are shown in Figs. 5.6a-5.6d. Also, a plot is included of the damage predicted over the 380-490˚C range using a quadratic approximation that correlated well with the Arrhenius kinetic equation (Fig. 5.6e). The red regions that correspond to matrix decomposition $D \geq 0.8$ (*i.e.*, ≥80%) are shown with their sizes (Table 5.2). All five of the approximations predicted roughly similar elliptical domains with matrix damage regions in excess of 0.8. The overall domains with predicted matrix thermal decomposition using the linear approximation in the temperature ranges between 300-500˚C (Fig. 5.6a) and between 300-600˚C (Fig. 5.6c) were much larger than those using the quadratic approximation (Figs. 5.7b and

5.7d-7e) in the same temperature ranges. This is expected since a linear approximation leads to more damage development at lower temperatures (Fig. 5.4) than for a quadratic approximation for the same temperature range; larger regions of the composite will experience such temperatures. The matrix decomposition domains using the linear damage approximation were elongated along the top lamina fiber direction (+45 ˚) (Figs. 5.6a and 5.6c). In contrast, those obtained by the quadratic damage approximation were more concentrated in the vicinity of the lightning attachment point (Figs. 5.6b and 5.6d).

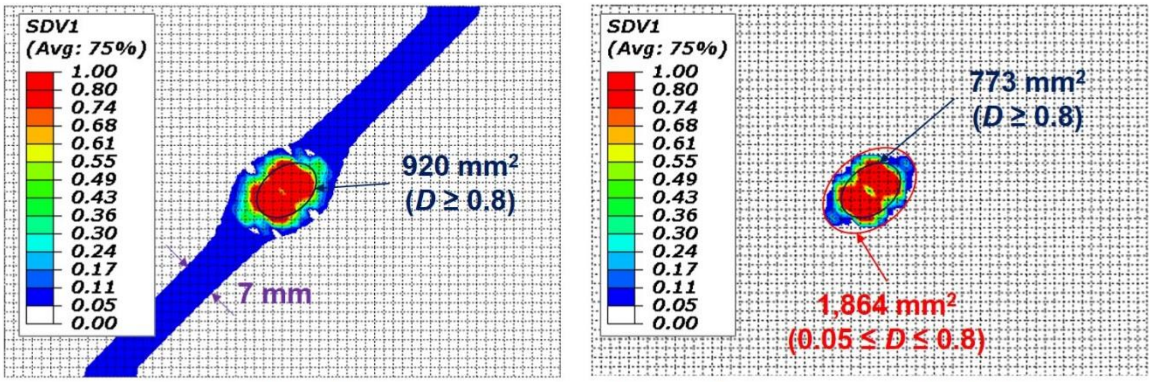

(a) Linear (*m* = 1, 300-500˚C) **(b) Quadratic (*m* = 2, 300-500˚C)**

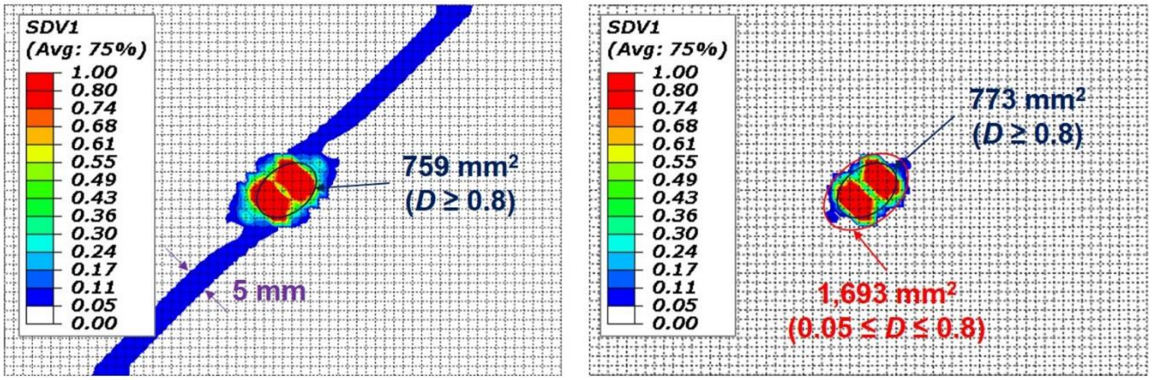

(c) Linear (*m* = 1, 300-600˚C) **(d) Quadratic (*m* = 2, 300-600˚C)**

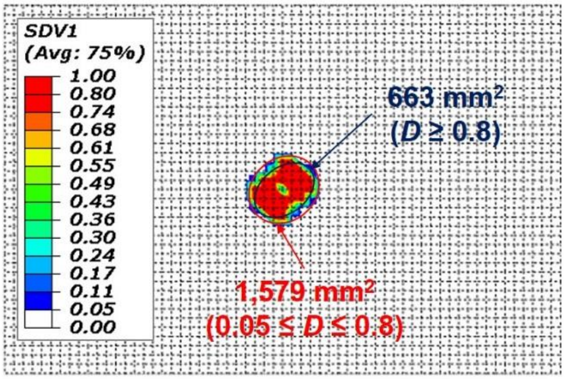

(e) Quadratic Arrhenius (*m* = 2, 380-490˚C)

Figure 5.6 Predicted extent of matrix thermal decomposition obtained using a linear (*m* = 1) or quadratic (*m* = 2) approximation (Eq. 5.5) in the top AS4/3506 lamina subjected to a 40 kA peak lightning current: (a) linear (*m* = 1, 300-500˚C), (b) quadratic (*m* = 2, 300-500˚C), (c) linear (*m* = 1, 300-600˚C), (d) quadratic (*m* = 2, 300-600˚C), and (e) quadratic Arrhenius (*m* = 2, 380-490˚C).

Table 5.2 Comparison of predicted matrix decomposition domains for 40 kA peak current with the experimental result [13]

FE Prediction				Experiment (mm^2)
Damage Variation	Epoxy Matrix Decomposition Temperatures (˚C)	Area of Predicted Matrix Decomposition (mm^2)		
		$0.05 \le D \le 1$	$D \ge 0.8$	
Linear ($m = 1$)	300-500	2,940	920	966*
Quadratic ($m = 2$)	300-500	1,864	773	
Linear ($m = 1$)	300-600	2,497	759	
Quadratic ($m = 2$)	300-600	1,693	683	
Quadratic ($m = 2$)	380-490	1,579	663	

[*] Roughly measured matrix damaged region surrounding severe fiber damage domain from.

Using the 300-500˚C temperature range to define the extent of damage led to a larger predicted domain with matrix thermal decomposition than using 300-600˚C. This makes sense since the rate of decomposition with increasing temperature is greater for the temperature range 300-500˚C (Fig. 5.4). The maximum predicted extent of matrix thermal decomposition was obtained using the linear approximation in the 300-500˚C range (Fig. 5.6a). The minimum extent of matrix decomposition was determined using the quadratic damage approximation based on a temperature range 380-490˚C (Fig. 5.6e) since decomposition does not initiate until $T > 380$˚C. Hence, the matrix decomposition determined using the linear approximation between 300-500˚C serves as an upper limit for our predictions of the extent of matrix decomposition. In contrast, predictions obtained using a quadratic variation from 380-490˚C, which nearly overlaps the profile of the Arrhenius kinetic equation with the heating rate of 1,000˚C/min, may be used as a lower limit for the matrix decomposition. The shape and size of the domain with predicted matrix thermal decomposition in the top +45˚ lamina of an AS4/3506 composite determined using a linear approximation in temperature ranges of 300-500˚C agree fairly well with surface examinations of actual lightning damage in a similar IM600/133 laminate (Figs. 5.5a-5.5b) from the literature [20]. Note that such experimental observations may include both thermal and mechanical damage. However, since the observed surface damage was mainly attributed to fiber and matrix thermal damage, mechanical damage (*i.e.*, delamination) in the experiment [20] may not be significant. Hence, our FE model for predicting matrix thermal decomposition based only upon the highest local temperature may prove useful in the future for preliminary assessments of lightning induced-thermal damage.

Figure 5.7 shows the predicted through-thickness thermal damage penetration into an AS4/3506 carbon/epoxy laminate subjected to a simulated 40 kA peak lightning current. Damage occurs over a 3D volume so surface examinations of the outermost ply alone do not provide a representative characterization of lightning damage. In the figure, the region with the predicted matrix thermal decomposition $D \geq 0.8$ is indicated in red. The lines (from points A1 to A2 and B1 to B2) in the images on the left indicate the cutting planes used to define cross-sectional views shown in the two right images. For comparison purposes, a 20×20 mm^2 planform area from the center of the top lamina was chosen for each cross-sectional view and the top 16 plies are only shown in the right images, since thermal damage never penetrates beyond this region. Each cross-sectional view is symmetric about the centerline of the lightning arc channel. Here, thermal damage penetration is defined as the maximum depth containing matrix decomposition. No thermal damage penetration was predicted in the underlying seventh ply using any of these five approximations (Figs. 5.7a-7e). The predicted thermal damage penetration depth was a minimum (*i.e.*, fifth ply) when using a linear damage approximation over the 300-500˚C temperature range and maximum (*i.e.*, sixth ply) from using a quadratic approximation of the Arrhenius kinetic equation in the 380-490˚C temperature range. All five approximations predicted fairly shallow thermal damage penetration resulting from 40 kA peak currents. This is consistent with observations from the literature [20]. Moreover, these approximations may be used to bound the range of expected matrix thermal damage. Thermal damage penetration at higher current levels may proceed through more plies and will be discussed in a subsequent publication.

(a) Linear (m = 1, 300-500˚C)

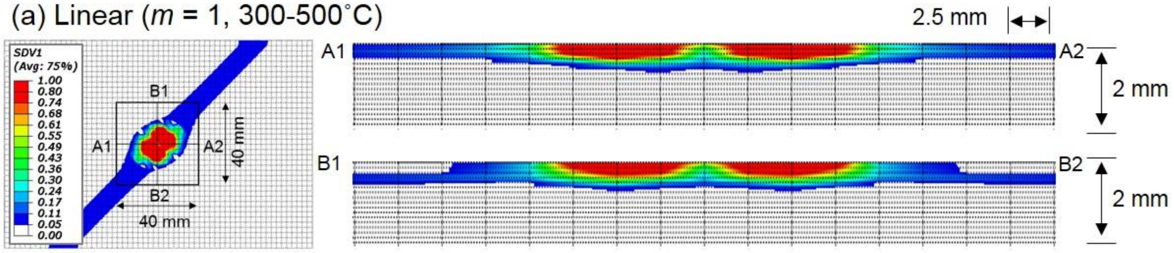

(b) Quadratic (m = 2, 300-500˚C)

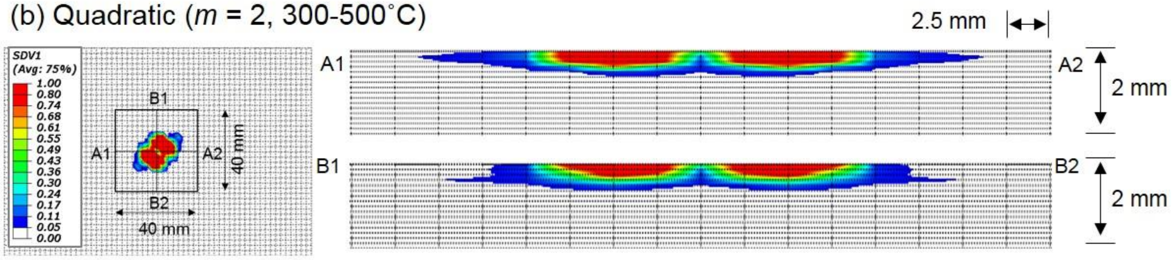

(c) Linear (m = 1, 300-600˚C)

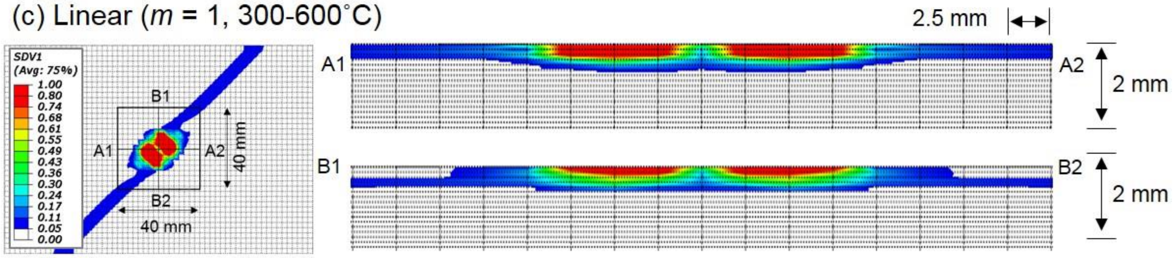

(d) Quadratic (m = 2, 300-600˚C)

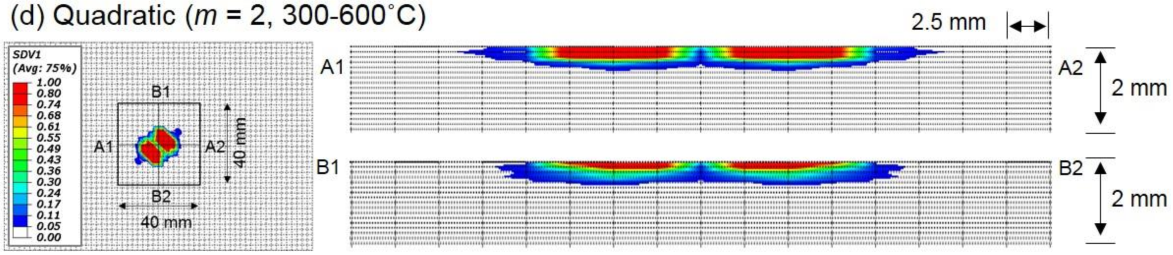

(e) Quadratic Arrhenius (m = 2, 380-490˚C)

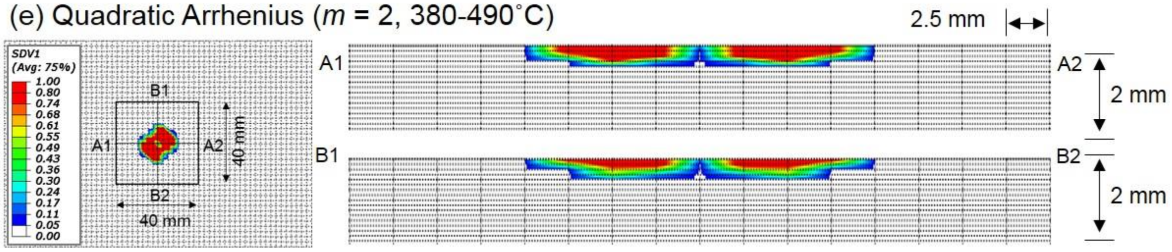

Figure 5.7 Predicted extent of thermal damage penetration using a linear (m = 1) or quadratic (m = 2) approximation (Eq. 5.5) in the top 16 AS4/3506 lamina subjected to a 40 kA peak lightning current: (a) linear (m = 1, 300-500˚C), (b) quadratic (m = 2, 300-500˚C), (c) linear (m = 1, 300-600˚C), (d) quadratic (m = 2, 300-600˚C), and (e) quadratic Arrhenius (m = 2, 380-490˚C).

Note that the predicted matrix thermal decomposition domains were compared earlier in this manuscript with surface observations of actual lightning damage in the IM600/133 carbon/epoxy laminates [13]. The lightning strike FE model [1] implemented in this study employed the temperature-dependent properties of a similar AS4/3506 carbon/epoxy laminate available in the literature, due to lack of available IM600/133 carbon/epoxy data. However, both of these carbon/epoxy laminates typically have a fiber volume fraction of 0.60-0.66 [34, 35, 38] and are commonly used for aircraft structural components. In addition, the predicted matrix decomposition domains [1] using AS4/3506 carbon/epoxy composite properties agreed well with surface examinations and damage penetration of actual lightning damage to similar IM600/133 carbon/epoxy laminates [13]. Thus, a difference in the lightning damage response of such laminate may be negligible.

In order to characterize the effect of the peak lightning current on the size of the matrix thermal decomposition domain, an additional series of lightning strike FE simulations were performed. Figures 5.8a-5.8f show photographs and ultrasonic C-scan images of IM600/133 carbon/epoxy laminates subjected to experimental 20, 30 and 40 kA peak lightning currents. The experimentally observed surface damage was compared with the matrix thermal decomposition domains predicted using the linear damage approximation between 300-500˚C for the top lamina subjected to 20, 30, and 40 kA peak lightning currents, as shown in Fig. 5.9. Recall that this approximation method showed fairly good agreement with surface examinations of actual lightning damage (Figs. 5.5a-5.5b) from the literature [20].

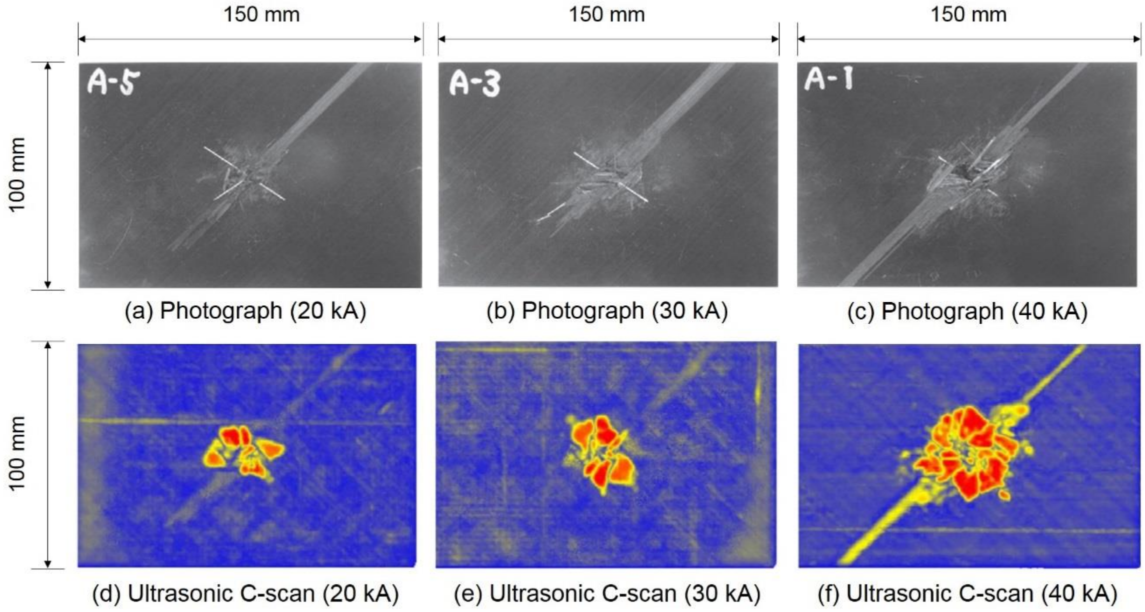

(a) Photograph (20 kA) (b) Photograph (30 kA) (c) Photograph (40 kA)

(d) Ultrasonic C-scan (20 kA) (e) Ultrasonic C-scan (30 kA) (f) Ultrasonic C-scan (40 kA)

Figure 5.8 Photographs and ultrasonic C-scan images of lightning-induced damage to IM600/133 carbon/epoxy laminates subjected to 20, 30, and 40 kA peak lightning currents (adopted from [13]).

Both the measured and predicted matrix thermal decomposition domains increased as the peak current increased. The domains with the predicted matrix decomposition $D \geq 0.8$ (Figs. 5.9d-5.9f) are superimposed on the on the photographs of the actual lightning damage morphologies (Figs. 5.9a-5.9c). The predicted matrix decomposition region exhibits better agreement with photographs (Figs. 5.8a-5.8c) of surface damage than the ultrasonic C-scan images (Figs. 5.8d-5.8f). The ultrasonic C-scan images by Hirano *et al.* [13] also will include any underlying delaminations; such delaminations were not accounted for in our model. The experimental shapes and sizes of the matrix thermal decomposition domains in the top lamina (Figs. 5.8a-5.8c) agree fairly well with predicted results (Figs. 5.9a-5.9c) at relatively low peak lightning currents (20-40 kA). This suggests that use of a linear damage approximation over the 300-500˚C temperature range may be used as one of the preliminary criteria to assess and predict lightning induced-thermal damage in carbon/epoxy composites. Simulations of thermal damage caused by peak lightning currents up to 200 kA are ongoing.

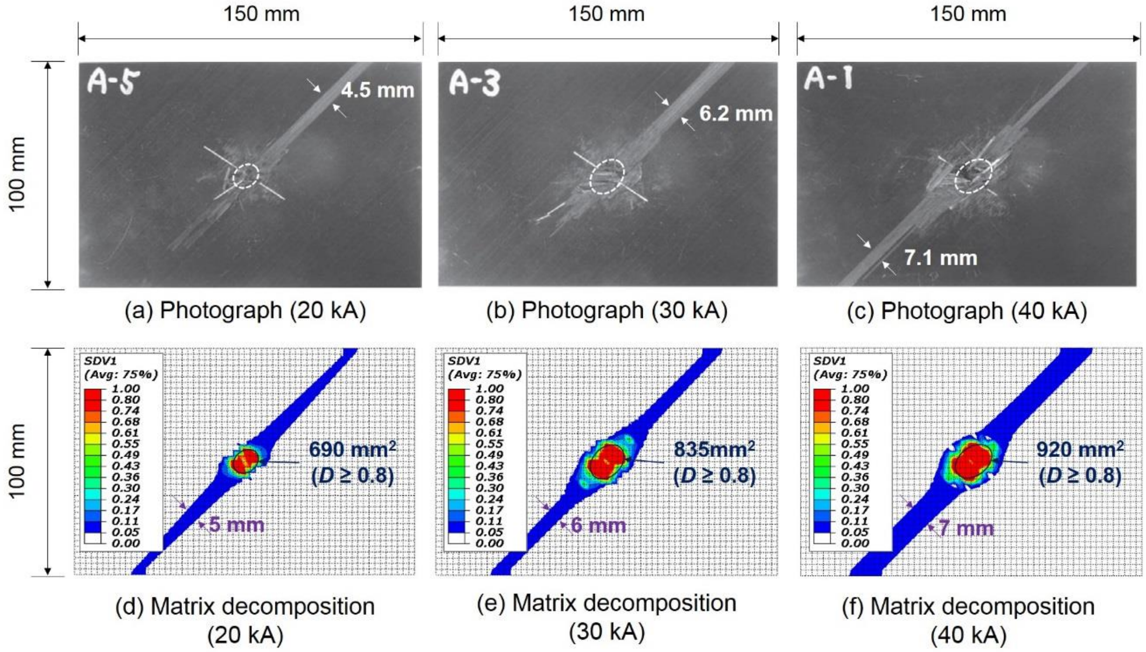

(a) Photograph (20 kA)
(b) Photograph (30 kA)
(c) Photograph (40 kA)
(d) Matrix decomposition (20 kA)
(e) Matrix decomposition (30 kA)
(f) Matrix decomposition (40 kA)

Figure 5.9 Comparison of (a-c) actual lightning damage morphology with (d-f) predicted extent of matrix thermal decomposition obtained using a linear ($m = 1$) approximation (Eq. 5.5) in the top AS4/3506 lamina subjected to 20, 30, and 40 kA peak lightning currents.

Additional AS4/8552 carbon/epoxy laminates were prepared to further validate the present lightning strike FE model. The 9-ply AS4/8552 laminates (60~65% fiber volume fraction) with in-plane dimensions of 200×200 mm^2 were fabricated using the manufacturer's recommended epoxy cure schedule [39]. All four edges of the laminates were smoothly sanded and then grounded using aluminum plates to permit evenly distributed electrical conduction throughout the laminates. Such laminates were subjected to 50 kA peak current and the visual observation of surface damage was compared to its simulated damage (outermost layer). Figure 5.10a shows surface inspection and a magnified picture of the typical lightning-damaged AS4/8552 laminate after application of 50 kA peak current. The predicted matrix decomposition domain (approximated by an ellipse in this study as shown in Fig. 10b) is superimposed on the photographs of the actual lightning damage. The region of predicted matrix decomposition closely matched with lightning damage morphology of the AS4/8552 carbon/epoxy material system, which validates the present FE simulation. Furthermore, the size of actual lightning damage to the 200×200 mm^2 AS4/8552 laminate which occurred at 50 kA peak current was much smaller than the damaged area of the 150×100 mm^2 IM600/133 panel (Fig. 5.8), although these were subjected to lower peak currents (≤40kA). Clearly, panel size and grounding condition influenced the distribution of electrical currents leading to damage. A detailed description on layup, configuration, and grounding condition associated with lightning damage morphology will be discussed in a future manuscript.

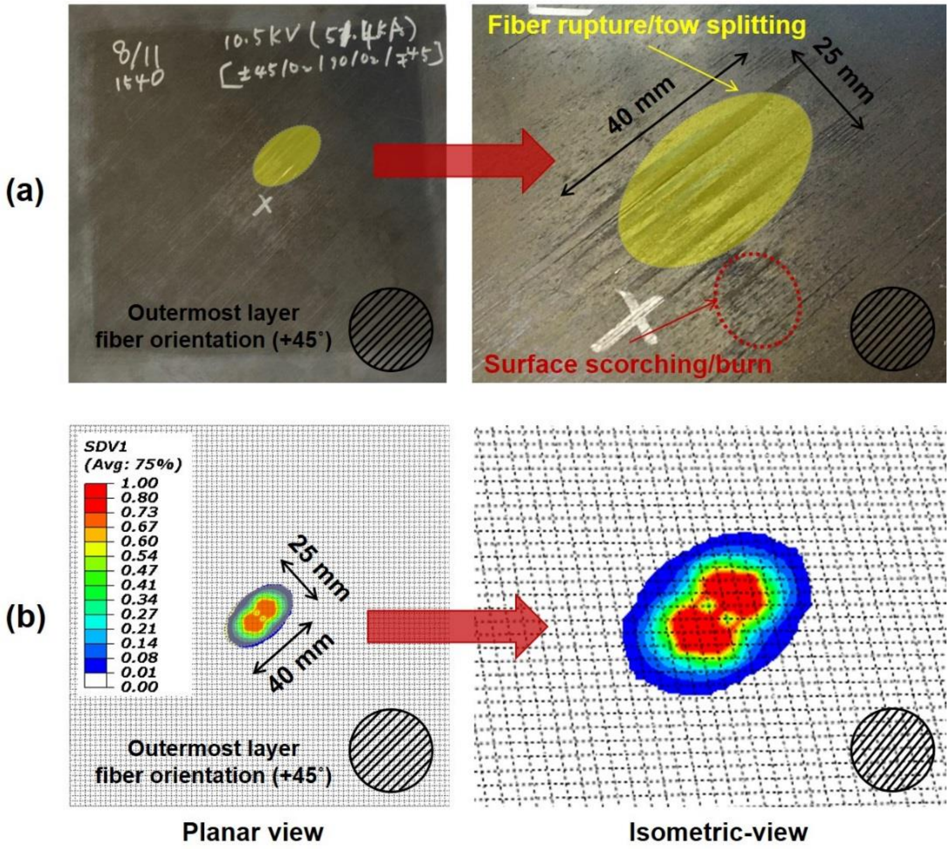

Figure 5.10 (a) Lightning damage morphology of the AS4/8552 carbon/epoxy composite subjected to 50 kA nominal peak current and (b) the predicted matrix thermal decomposition domain using the present lightning strike FE model.

The measured peak current (51.4 kA) is shown on the laminate and included for clarity.

5.7 Conclusions and Recommendations

The present study aimed to characterize matrix thermal decomposition induced by simulated lightning strikes on a typical 32-ply carbon/epoxy laminate subjected to simulated lightning peak currents of ≤50 kA. Using our previously published lightning strike finite element (FE) model [1] modified with user-defined heat generation subroutines, two commonly used epoxy matrix decomposition temperature ranges of 300-

500˚C and 300-600˚C were considered to predict the degree of the matrix thermal decomposition caused by simulated lightning strikes. Matrix thermal decomposition, which was defined in the normalized range $0 \leq D \leq 1$ based upon the highest local temperature reached during the simulations, was assumed to vary either linearly or quadratically in these given temperature ranges. A quadratic damage approximation using an Arrhenius kinetic equation approach with the heating rate of 1,000˚C/min over the range 380-490˚C was also developed in this study. The lightning strike FE model showed that the size, shape, depth, and intensity of predicted matrix thermal decomposition were strongly dependent on the order of the approximation, and somewhat dependent on the thermal decomposition temperature range selected. In general, use of a linear damage idealization led to more predicted matrix decomposition at lower local temperatures.

The shape and size of the two dimensional surface ply domains with matrix decomposition predicted assuming linearly varying damage between 300-500˚C agreed fairly well with surface examinations of actual lightning strike damage available in the open literature [13]. Assuming quadratically varying damage in the range 380-490˚C, the FE model somewhat underestimated the planar matrix thermal decomposition regions when compared with experimental results. The regions with predicted matrix thermal decomposition using a linear damage approximation in the temperature ranges between 300-500˚C and between 300-600˚C were much larger than those obtained using a quadratic approximation in these same temperature ranges. All of the calculations suggested that fairly shallow thermal damage penetration will occur during 40 kA peak currents. This is consistent with observations from the literature [13, 20]. Moreover, these damage approximations may be used to bound the range of expected matrix thermal decomposition for a given current level.

Using a linear damage approximation defined in the 300-500˚C range, the matrix thermal decomposition and thermal damage penetration in carbon/epoxy laminates subjected to 20, 30, and 40 kA peak lightning currents were predicted and compared with actual lightning-induced damage to similar laminates. The predicted matrix decomposition in the outermost ply showed fairly good agreement with experimental results obtained at the same peak lightning currents. This suggests that our FE model [1] for predicting matrix thermal decomposition based only upon the highest local temperature can be used for preliminary assessments or predictions of lightning induced-thermal damage. More investigation is required in order to better characterize the optimal matrix thermal decomposition temperature range for a given composite, as well the optimal damage-temperature relationship over that temperature range.

The peak lightning current was limited to 50 kA in this study because experimental results in the literature were only available below this peak current. Further simulations from 50 kA to 200 kA are ongoing. These will be compared with new experimental lightning strikes at these higher peak currents currently underway at Mississippi State University High-Voltage Laboratory (MSU-HVL), which span a variety of composite panels and structures [40].

5.8 References

[1] Lee, J., T. E. Lacy, Jr., C. U. Pittman, Jr. and M. S. Mazzola, "Thermal Response of Carbon Fiber Epoxy Composites with Metallic and Non-Metallic Protection Layers to Simulated Lightning Currents," *Polymer Composites, under revision*, 2017.

[2] Rakov, V.A. and M.A. Uman, Lightning: Physics and Effects. 2003: Cambridge University Press.

[3] Chemartin, L., P. Lalande, B. Peyrou, A. Chazottes, P. Elias, C. Delalondre, B. Cheron, and F. Lago, "Direct Effects of Lightning on Aircraft Structure: Analysis of the Thermal, Electrical and Mechanical Constraints," *AerospaceLab*, 2012, (5): p. 1-15.

[4] Ohm, G.S., Die galvanische Kette, Mathematisch Bearbeitet. 1827: Riemann.

[5] SAE, "Aircraft Lightning Zoning," *Aerospace Recommended Practice ARP 5414*, 1999.

[6] SAE, "Aircraft Lightning Environment and Related Test Waveforms," *Aerospace Recommended Practice ARP 5412*, 1999.

[7] Reid, G. "Mechanical Damage to Aircraft Structures from Lightning Strikes," in the *Proceedings of the Institution of Mechanical Engineers, Part G: Journal of Aerospace Engineering*, 1993.

[8] Kanapitsas, A., C. Tsonos, H. Zois, C.G. Delides, and G.C. Psarras, "Thermal and Mechanical Characterization of Epoxy Resin Nanocomposites," *Journal of Advanced Physics*, 2013, **2**(1): p. 25-28.

[9] Lampman, S., Characterization and Failure Analysis of Plastics. 2003: ASM International.

[10] Kiran, V. and B. Gaur, "Curing and Thermal Behavior of Epoxy Resins of Hexafluoro-Bisphenol–A and Bisphenol-A," *Polímeros*, 2016, **26**(1): p. 11-20.

[11] Azwa, Z. and B. Yousif. "Thermal Degredation Study of Kenaf Fibre/Epoxy Composites Using Thermo Gravimetric Analysis," in the *Proceedings of the 3rd Malaysian Postgraduate Conference (MPC 2013)*, 2013: Education Malaysia.

[12] ABAQUS, "ABAQUS Documentation," *Dassault Systémes Simulia Corp.*, 2014.

[13] Hirano, Y., S. Katsumata, Y. Iwahori, and A. Todoroki, "Artificial Lightning Testing on Graphite/Epoxy Composite Laminate," *Composites Part A: Applied Science and Manufacturing*, 2010, **41**(10): p. 1461-1470.

[14] Feraboli, P. and M. Miller, "Damage Resistance and Tolerance of Carbon/Epoxy Composite Coupons Subjected to Simulated Lightning Strike," *Composites Part A: Applied Science and Manufacturing*, 2009, **40**(6): p. 954-967.

[15] Feraboli, P. and H. Kawakami, "Damage of Carbon/Epoxy Composite Plates Subjected to Mechanical Impact and Simulated Lightning," *Journal of Aircraft*, 2010, **47**(3): p. 999-1012.

[16] Yin, J., F. Chang, S. Li, X. Yao, J. Sun, and Y. Xiao, "Experimental and Numerical Simulation Analysis of Typical Carbon Woven Fabric/Epoxy Laminates Subjected to Lightning Strike," *Applied Composite Materials*, 2017: p. 1-20.

[17] Wolfrum, J., T.J. Schuster, and T. Körwien, "Effects of heavy lightning strikes on pristine and repaired carbon composite structures," *Journal of Composite Materials*, 2017: p. 0021998317690445.

[18] Mallick, P., "Effects of hole stress concentration and its mitigation on the tensile strength of sheet moulding compound (SMC-R50) composites," *Composites*, 1988, **19**(4): p. 283-287.

[19] Heidlebaugh, D.L., W.B. Avery, and S.T. Uhrich, "Effect of Lightning Currents on Structural Performance of Composite Material." 2001, SAE Technical Paper.

[20] Ogasawara, T., Y. Hirano, and A. Yoshimura, "Coupled Thermal–Electrical Analysis for Carbon Fiber/Epoxy Composites Exposed to Simulated Lightning Current," *Composites Part A: Applied Science and Manufacturing*, 2010, **41**(8): p. 973-981.

[21] Abdelal, G. and A. Murphy, "Nonlinear Numerical Modelling of Lightning Strike Effect on Composite Panels with Temperature Dependent Material Properties," *Composite Structures*, 2014, **109**: p. 268-278.

[22] Dong, Q., Y. Guo, X. Sun, and Y. Jia, "Coupled Electrical-Thermal-Pyrolytic Analysis of Carbon Fiber/Epoxy Composites Subjected to Lightning Strike," *Polymer*, 2015, **56**: p. 385-394.

[23] Wang, F., Y. Ji, X. Yu, H. Chen, and Z. Yue, "Ablation Damage Assessment of Aircraft Carbon Fiber/Epoxy Composite and its Protection Structures Suffered from Lightning Strike," *Composite Structures*, 2016, **145**: p. 226-241.

[24] Guo, Y., Q. Dong, J. Chen, X. Yao, X. Yi, and Y. Jia, "Comparison between temperature and pyrolysis dependent models to evaluate the lightning strike damage of carbon fiber composite laminates," *Composites Part A: Applied Science and Manufacturing*, 2017, **97**: p. 10-18.

[25] Wang, Y., "Modeling of Lightning-Induced Thermal Ablation Damage in Anisotropic Composite Materials and its Application to Wind Turbine Blades," 2016.

[26] Mouritz, A.P. and A.G. Gibson, Fire Properties of Polymer Composite Materials. Vol. 143. 2007: Springer Science & Business Media.

[27] Henderson, J., M. Tant, G. Moore, and J. Wiebelt, "Determination of Kinetic Parameters for the Thermal Decomposition of Phenolic Ablative Materials by a Multiple Heating Rate Method," *Thermochimica Acta*, 1981, **44**(3): p. 253-264.

[28] Arrhenius, S., Recherches Sur La Conductibilité Galvanique Des Electrolytes. 1884: PA Norstedt & Söner.

[29] Menousek, J. and D. Monin, "Laser Thermal Modeling of Graphite Epoxy," *Naval Weapons Center Technical Memorandum*, 1979, **3834**.

[30] Mueller, G., "Simulation of Repetitively-Pulsed Laser Irradiation of Graphite-Epoxy Composite." 1984, DTIC Document (NRL-MR-5467).

[31] Fanucci, J.P., "Thermal Response of Radiantly Heated Kevlar and Graphite/Epoxy Composites," *Journal of Composite Materials*, 1987, **21**(2): p. 129-139.

[32] Griffis, C., J. Nemes, F. Stonesifer, and C. Chang, "Degradation in Strength of Laminated Composites Subjected to Intense Heating and Mechanical Loading," *Journal of Composite Materials*, 1986, **20**(3): p. 216-235.

[33] Raffray, R., *Assessment of Dry Chamber Wall Configurations as Preliminary Step in Defining Key Processes for Chamber Clearing Code*, 2001 [cited 2015 17 Jun].

[34] Military-Handbook, "MIL-HDBK-17-2F: Composite Materials Handbook," *Polymer Matrix Composites: Materials Usage, Design, and Analysis*, 2002, **17**.

[35] Chen, J.-K. and F.A. Allahdadi, "Structural Composite Penetration Model Development." 1996, DTIC Document (PL-TR-96-1140).

[36] Kawakami, H. and P. Feraboli, "Lightning Strike Damage Resistance and Tolerance of Scarf-Repaired Mesh-protected Carbon Fiber Composites," *Composites Part A: Applied Science and Manufacturing*, 2011, **42**(9): p. 1247-1262.

[37] Jiang, P., C. Zhao, J. Deng, and W. Zhang. "Experimental Investigation of Local Heat Transfer of Carbon Dioxide at Super-Critical Pressures in a Vertical Tube and Multi-Port Mini-Channels Under Cooling Conditions," in the *International Refrigeration and Air Conditioning Conference at West Lafayette, IN, July 14-17*, 2008.

[38] Suzuki, Y., A. Todoroki, R. Matsuzaki, and Y. Mizutani, "Indentation-Damage Visualization in CFRP by Resistive Heating: Analytical Verification of the Inspection of Aircraft Using its Lightning Protection Systems," *Journal of Solid Mechanics and Materials Engineering*, 2012, **6**(3): p. 213-226.

[39] Hexcel, *8552 Epoxy Matrix Product Data*, 2010; Available from: http://www.niar.wichita.edu/coe/ncamp_documents/Hexcel%208552/Hexcel8552-ProcessingCharacterizationV1-0.pdf.

[40] Lacy Jr., T.E., M.S. Mazzola, C.U. Pittman Jr., J. Lee, P. Gharghabi, D. Bousha, and B. Cerovsky, "Artificial Lightning Strike Tests on a PRSEUS Panel." 2017, Boeing Internal Report.

CHAPTER VI

LIGHTNING STRIKE TESTS ON A SANDED PRSEUS PANEL

6.1 Abstract

This study investigated the experimental lightning damage characterization of a Pultruded Rod Stitched Efficient Unitized Structure (PRSEUS) panel. A series of lightning strike tests with 50, 125, and 200 kA nominal peak currents were performed at four representative panel locations (*i.e.*, the mid-bay, stringer, frame, and frame/stringer intersection). The size of lightning-damaged regions increased as the peak current increased. Lightning damage to a PRSEUS panel was grouped into two types: (1) intense local damage occurring in the vicinity of the lightning attachment point (*i.e.*, severe fiber damage, matrix decomposition) and (2) surrounding surface damage (*i.e.*, smaller scale fiber damage, scorching/burning). The regions of both intense local damage and widespread less severe fiber damage were generally elliptical or semi-circular in shape and elongated along the top lamina's fiber direction. This is consistent with observations from unstitched carbon/epoxy laminates. The domains with small-scale fiber damage were consistent with the periodic distribution of polyester threads used to weave the warp-knit fabric skins of the PRSEUS panel. Furthermore, in the presence of through-thickness Vectran™ stitches, the regions of intense local damage at the stringer, frame, and frame/stringer intersection locations of the panel were mostly contained between the stitching lines. Those areas of intense local damage at the mid-bay (*i.e.*, a region without

through-thickness stitches) were not. Through-thickness Vectran™ stitches provide mechanical constraints that mitigate damage development. The PRSEUS panel made of warp-knit fabric skins and through-thickness Vectran™ stitches to connect skins, tear straps, stringers, and frames exhibited profoundly reduced lightning damage characteristics, compared to traditional laminated composites. This suggests that stitched composites have the potential to dramatically increase the lightning damage resistance and perhaps damage tolerance of integrated composite aircraft structures.

6.2 Introduction

The Pultruded Rod Stitched Efficient Unitized Structure (PRSEUS) concept [1-4] is an integrated composite structural panel developed by the Boeing Company for NASA Langley Research Center (LaRC) (Fig. 6.1). The PRSEUS concept uses through-thickness Vectran™ stitches to improve the composite structural integrity over traditional laminated composites. The out-of-plane delamination resistance is enhanced by the formation of stitch bridging zones [5, 6]. To validate the damage arresting capabilities, both flat and curved PRSEUS panels were subjected to axial tension, axial compression, internal pressure, and combined axial and internal pressure loadings [7-10]. Furthermore, the PRSEUS concept offers potential structural weight savings, while ensuring all performance requirements and safety criteria are satisfied. Lovejoy [11] reported that a PRSEUS wing design exhibited a 9% weight savings when compared to a stiffened composite wing. The results of these investigations suggest that the PRSEUS concept can be used for future aircraft structural applications.

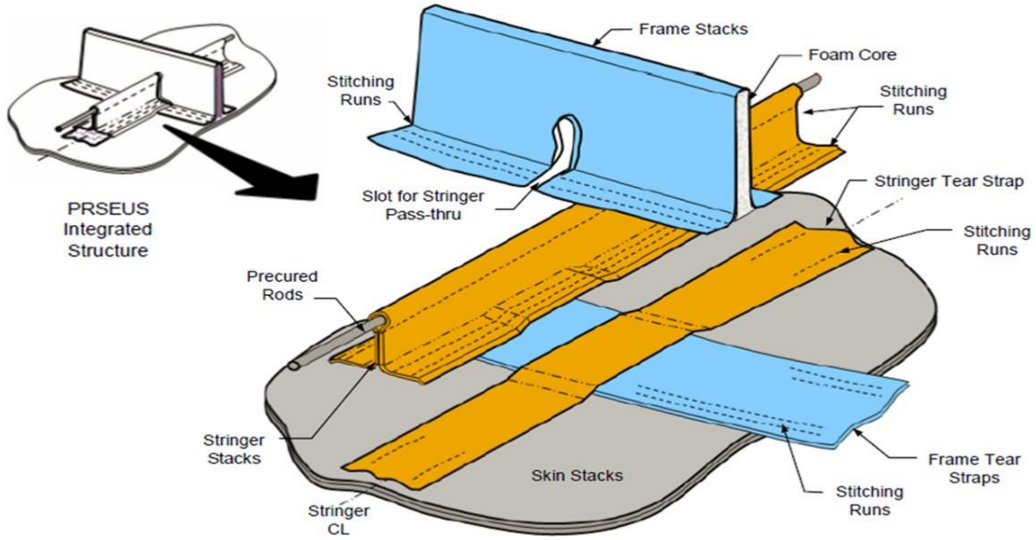

Figure 6.1 Schematic of PRSEUS concept [3].

Lightning strike protection is one major concern for composite aircraft structures. Since traditional carbon/epoxy composites have lower thermal and electrical conductivities compared to metallic materials, lightning strikes can cause a significant amount of damage to composite structures [12-15]. Matrix thermal decomposition, carbon fiber breakage/ablation, and delamination have been typically observed in laminated composite panels that have sustained lightning strikes.

Mississippi State University (MSU) received three PRSEUS panels from NASA LaRC and one PRSEUS panel from the Boeing Company to be used for simulated lightning strike experiments. The geometry, layup, and configuration of the PRSEUS panel will be described in a forthcoming section. The outer mold line (OML) skins of the LaRC PRSEUS panels were finished with white paint that may affect the size and shape of lightning strike surface damage. Two LaRC PRSEUS panels were subjected to standard Society of Automotive Engineers (SAE) impulse current waveforms [16] (consistent with actual lightning strikes) with 50, 125, and 200 kA nominal peak currents at a variety of panel locations. The type and extent of damage were characterized at each lightning attachment location. The OML skin of the PRSEUS panel used in this study was lightly sanded prior to lightning testing to remove the thin layer of white paint. The possible influence of white paint on lightning damage development in a PRSEUS panel was not considered here, but will be addressed in detail in a separate manuscript.

6.3 PRSEUS Structures

A fully integrated PRSEUS panel is typically comprised of the (skin) panel, stringers, frames, and tear straps. Each PRSEUS subcomponent is produced from three-dimensional (3D) preforms made of multiaxial warp-knitted fabrics (Fig. 6.2a; [17]), also known as Non-Crimp Fabrics (NCFs). Warp-knitted fabrics and their carbon fiber tows are held together by thermoplastic threads (preferably polyester [2, 3, 18]) in order to *i*) prevent crimping or two undulations and *ii*) enable easier handling when cutting [19]. The white lines in Fig. 6.2b correspond to polyester knitting threads [18]. The warp-knitted fabrics used in a PRSEUS panel (Fig. 6.2b) consist of multiple layers of oriented unidirectional Hexcel standard modulus AS4 carbon fiber tows.

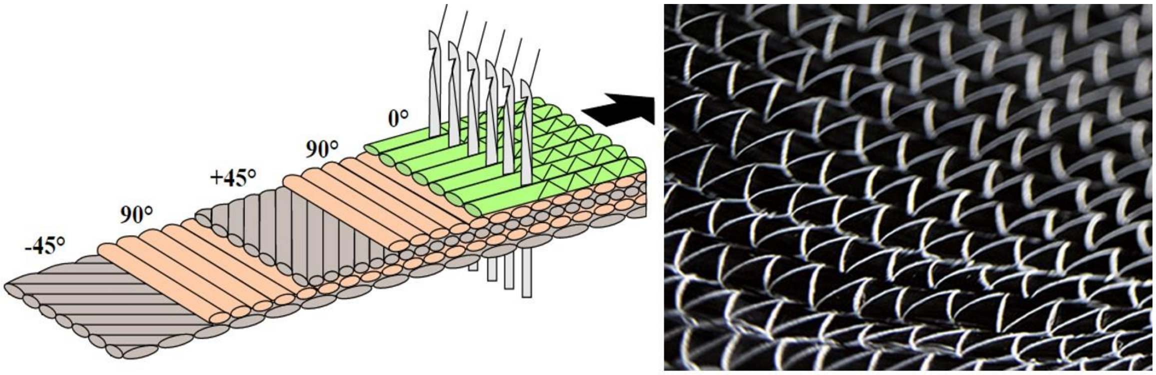

(a)

(b)

Figure 6.2 (a) Schematic of multiaxial warp-knitted fabric [17] and (b) photograph of SAERTEX multiaxial warp-knitted dry carbon fiber fabric [18].

Two additional reinforcement materials are commonly used in a PRSEUS panel construction. Rohacell 110WF closed-cell structural foam reinforces the frame webs and a pultruded unidirectional T800/3900-2B carbon/epoxy rod reinforces the stringer flanges (Fig. 6.1). High-performance thermoplastic threads made of the liquid crystal polymer, Vectran™, are used to stitch the pre-assembled dry 3D preforms of the skin panel, stringer, frames, and tear straps. These Vectran™ threads are typically made of three or four 400-denier Vectran™ threads twisted together for better strength and coated with nylon [2, 3] for thermal stability. A Hexcel Hexflow VRM-34 toughened epoxy resin is infused into a stitched pre-assembly of the skin panel, stringer, frames, and tear straps, and the composite is oven-cured using the Controlled Atmospheric Pressure Resin Infusion (CAPRI) process [20].

The materials, layups, and total stack up thicknesses of a PRSEUS panel including all sub-components are listed in Table 6.1. Stack A has a nominal thickness of 1.32 mm with a balanced symmetric stacking sequence, [+45/-45/0/0/90/0/0/-45/+45]. A detailed description of the ply stacking sequences implemented in the PRSEUS panel is available in references [2, 3].

Table 6.1 Material, thickness, and layup of LaRC PRSEUS sub-components [2, 21]

Part	Material	Layup [c]	Thickness (mm)
Exterior Skin	AS4/VRM-34 [a]	*Stack A/Stack A*	2.64
Tear Straps	AS4/VRM-34[a]	*Stack A*	1.32
Frame	AS4/VRM-34 [a]	*Stack A/Stack A*	2.64
Stringer	AS4/VRM-34[a]	*Stack A*	1.32
Foam Core	Rohacell 110WF	-	12.7
Rod	T800/3900-2B[b]	-	9.53 (dia.)

[a] AS4/VRM-34arp-knitted AS4 carbon fiber fabric and VRM-34 epoxy resin processed via resin infusion.
[b] Pre-cured unidirectional T800 fibers with a 3900-2B epoxy resin.
[c] *Stack A* = [+45/-45/0/0/90/0/0/-45/+45].

Two-needle single-sided stitching technologies [2, 3] are used to sew a stitching thread into the 3D preforms from the outer mold line (OML) side of the PRSEUS panel. The through-thickness Vectran ™ stitches dramatically increase the interlaminar fracture toughness. A locking thread holds the vertical stitch in place. Figures 6.3a-6.3b show schematics of a typical PRSEUS frame/stringer intersection and flange-to-skin stitches at that location. In Fig. 6.3b, two parameters can define a given stitch pattern: stitching spacing (S_s) and stitching pitch (S_p). For example, S_s = 25.4 mm and S_p = 5.1 mm for a prototype PRSEUS panel [21]. A single-sided 3D seam stitch introduces two rows of continuous stitching (Fig. 6.3c) and is used to attach stringer/frame flanges to the PRSEUS skin panel. Figure 6.3d shows a flat PRSEUS panel after single-sided 3D-seam stitching, prior to resin infusion. A detailed description of the single-sided stitching implemented in the PRSEUS concept is available [2-4]. In general, a continuous stitching line is used to attach a given stringer/tear strap or frame/tear strap combination to the overlapping PRSEUS skins. In regions where the upstanding web of a given frame intersects the upstanding web on an orthogonal stringer, no through-thickness stitching is possible. The lack of through-thickness reinforcement at the stringer/frame interconnections likely reduces the local damage resistance properties in these overlap areas. The PRSEUS panel used in this study consisted of nine rod-stiffened stringers and one foam core-reinforced frame (Fig. 6.4a). Figure 6.4a illustrates the inner mold line (IML) side view of a typical LaRC panel. Approximate nominal dimensions are shown for the panel, stringers, and frame in Figs. 6.4b-6.4d, respectively.

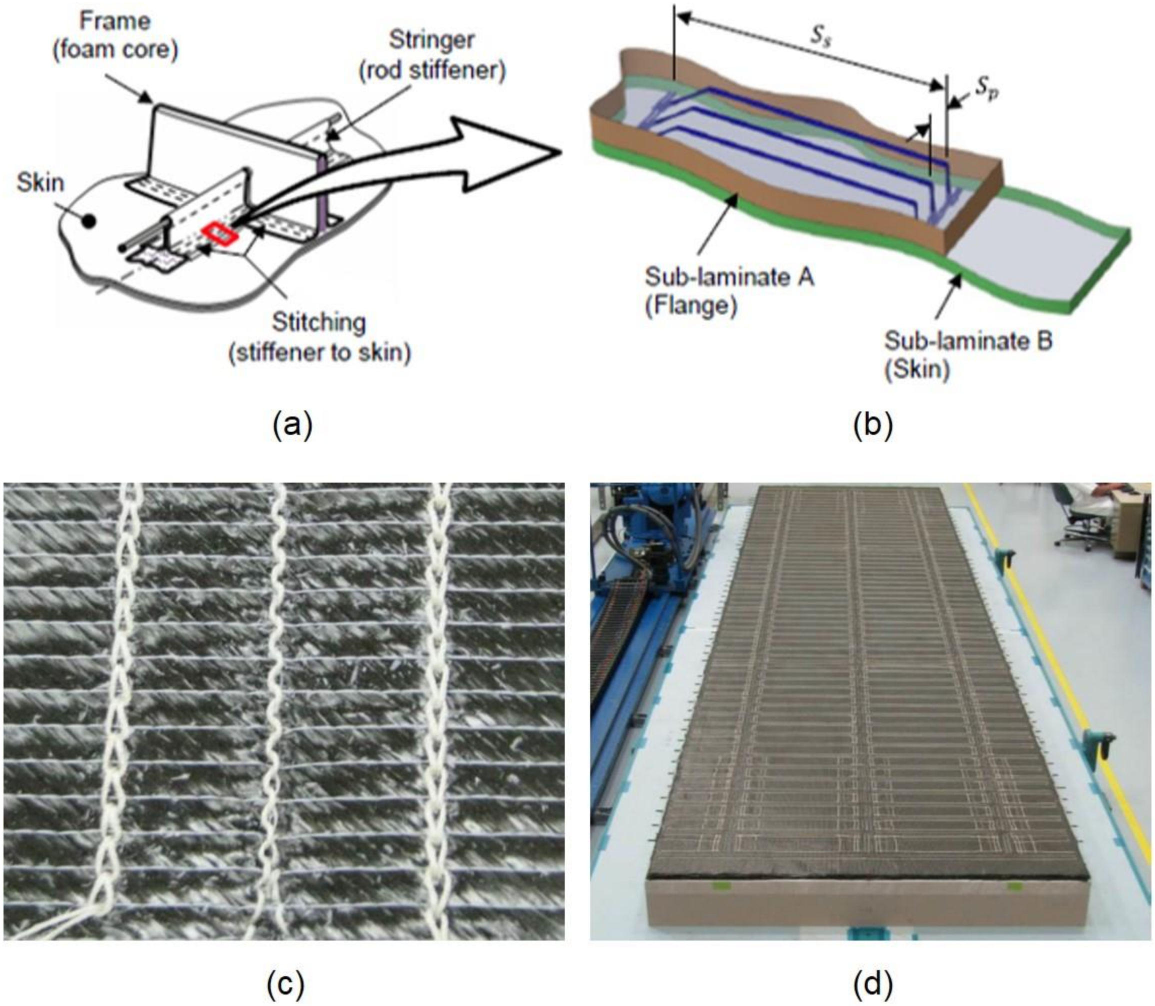

(a) (b)

(c) (d)

Figure 6.3 Single-sided stitching for the PRSEUS concept: (a) frame/stringer intersection (adapted from [21]), (b) flange-to-skin stiches [21], (c) single-sided stitch seam (adapted from [4]), and (d) a complete flat PRSEUS panel preform after stitching (adapted from [4]).

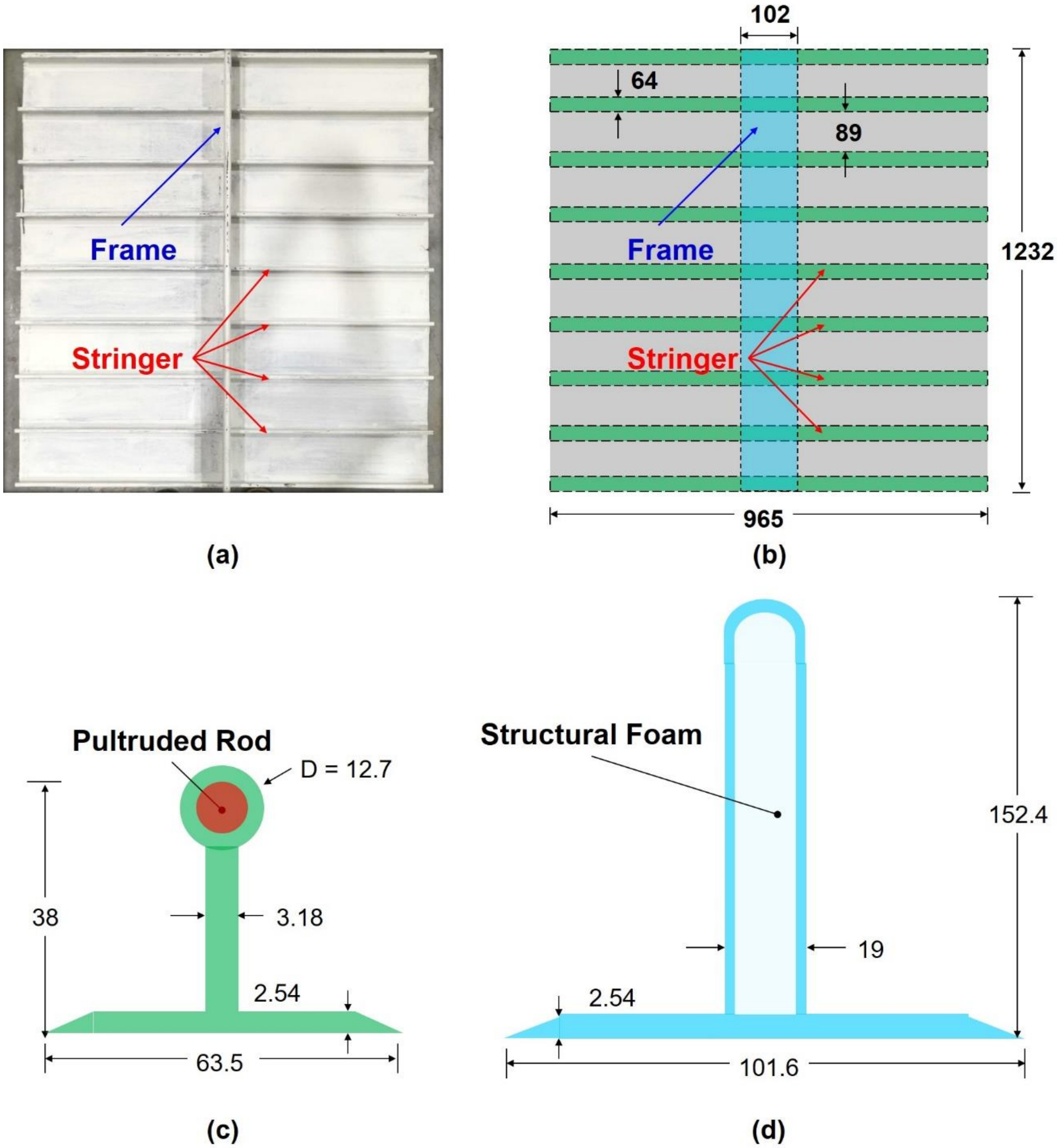

Figure 6.4 PRSEUS panel delivered to MSU: (a) photograph of IML surface, (b) schematics of IML surface, (c) rod-stiffened stringer, and (d) foam core-reinforced frame.

All nominal dimensions are in mm.

6.4 Laboratory-scale Lightning Strike Testing Conditions

6.4.1 High Impulse Current Generator

A one-stage impulse current generator was designed and assembled to produce standard impulse current waveforms consistent with actual lightning strikes [22]. The impulse current generator (Fig. 6.5) built at the Mississippi State University High-Voltage Lab (MSU-HVL) is able to produce double exponential current waveforms with up to 200 kA peak currents. The trigatron spark gap switch (Fig. 6.5a) was constructed to initiate an impulse current discharge. This spark gap switch consisted of two separated electrodes operating in air at atmospheric pressure: the upper electrode was connected to a set of capacitors (Fig 6.5a) and the lower electrode was grounded. Electrical current was discharged across the gap between the two electrodes. The gap spacing was optimized to achieve reliable control over the generated current. Preliminary test results showed that (1) the peak current depended on the gap spacing and (2) a minimum gap spacing existed below which un-triggered current discharges would occur. Table 6.2 contains the charging voltage and corresponding peak current with the optimized trigatron spark gap spacing. A more detailed description of the MSU-HVL impulse current generator is available [22].

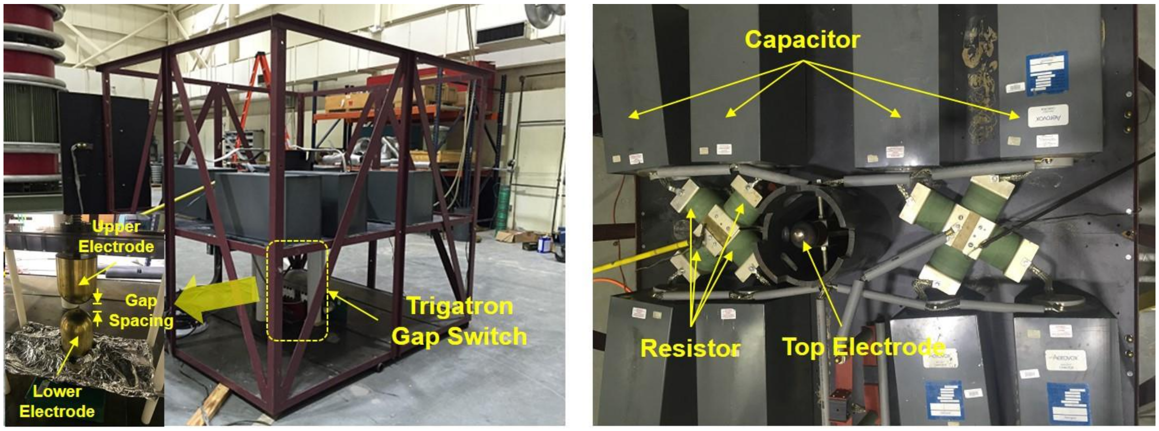

(a)

(b)

Figure 6.5 MSU-HVL impulse current generator: (a) edge view and (b) top View.

Table 6.2 Charging voltage and corresponding peak currents with the trigatron spark gap spacing

Nominal Charging Voltage (kV)	Nominal Peak Current (kA)	Nominal Spark Gap Spacing (mm)
10	50	9
24	125	15
38	200	25

6.4.2 Electrical Grounding Condition

Once lightning strikes a PRSEUS panel, a substantial amount of electrical current flows through the panel. Most composite aircraft panels are designed to distribute electrical current over their outer surfaces. This condition was ensured by connecting electrical grounding terminals along the four edges of the laboratory panel. Thus, the major electrical conduction path is from a lightning attachment location to the four edges of the PRSEUS' OML skin. Figure 6.6 shows the grounding connections on the PRSEUS panel prior to lightning strike tests. The four edges of the PRSEUS panel were smoothly sanded in order to provide sufficiently uniform electrical contact surfaces. Flexible, flat, and braided copper ground straps were then inserted between aluminum angle brackets and the PRSEUS panel. C-clamps were used to secure the aluminum angle brackets to the panel's OML side (Fig. 6.6b).

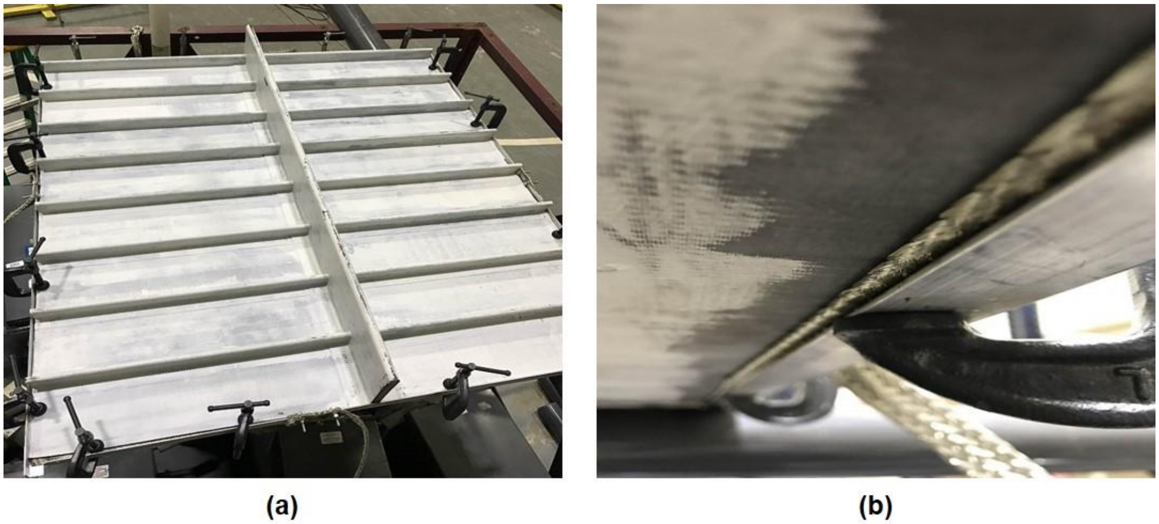
(a)

(b)

Figure 6.6 Electrical grounding condition along the edges PRSEUS panel: (a) IML view and (b) OML view.

6.4.3 Artificial Lightning Current Waveform

Figure 6.7 compares the standard impulse current waveform component A defined in SAE Aerospace Recommended Practice (ARP) 5412 [16] with the measured MSU-HVL 200 kA peak current impulse current waveform. The standard SAE waveform [16] has 200 kA peak current, a rise time of 6.4 μs, and a decay time of 69 μs with a ±20% tolerance level for repeatability. The MSU-HVL 200 kA peak current waveform was consistent with the standard SAE component A waveform. The rise and decay time determined from the MSU-HVL current waveforms were 18 μs and 75 μs (*cf*. Table 6.3). The MSU-HVL 200 kA current waveform had a rise time slightly longer than that of the SAE component A waveform; the decay time was consistent. The difference in the rise time between the MSU-HVL lightning waveform and the SAE component A waveform is not significant because the rise time is typically less important than decay time in determining the time response of an impulse current waveform [23]. A significant variation in rise time will not lead to noticeable changes in lightning-induced damage since lightning damage is governed by the amount of electrical energy, defined as the action integral, injected into the composite (integral of the square of the time-varying current over its time duration [24]). Similar action integrals were observed for both the MSU-HVL 200 kA current waveform and the SAE component A waveform (*cf*. Table 6.3).

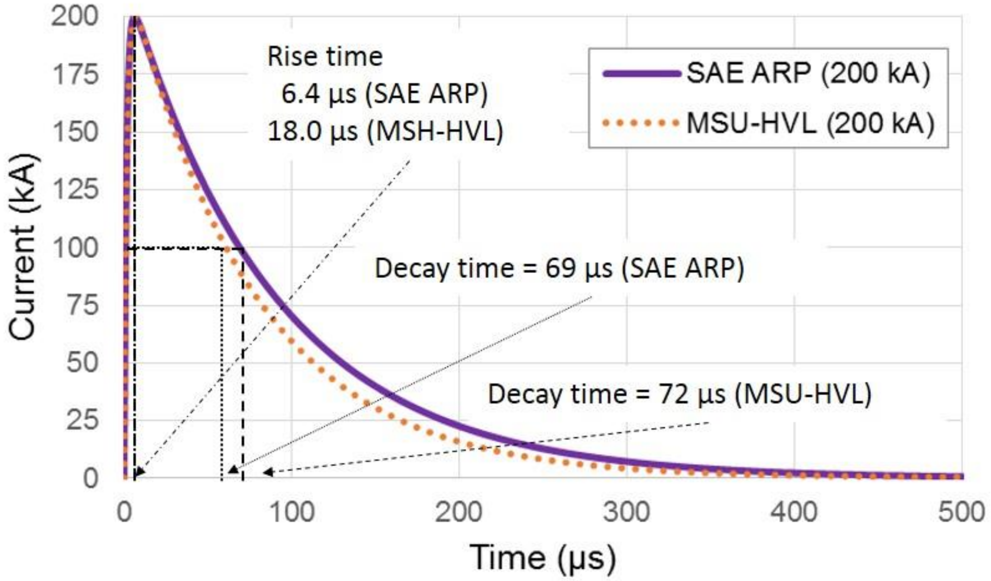

Figure 6.7 SAE component A [16] and MSU-HVL impulse current waveform (200 kA nominal peak current)

Table 6.3 Lightning waveform characteristics

Nominal Peak Current (kA)	Rise Time (µs)	Decay Time (µs)	Action Integral ($\times 10^5$ A^{2}s)	Source
50	18.0	75	1.3	MSU-HVL*
125	18.0	75	8.5	MSU-HVL*
200	18.0	75	21.5	MSU-HVL*
200	6.4 (±20%)	69 (±20%)	20.0 (±20%)	SAE ARP 5412 [16]

*Mississippi State University High Voltage Lab

Figure 6.8 shows the MSU-HVL impulse current waveforms with 50, 125, and 200 kA nominal peak currents. Note that rise and decay times of a current waveform strongly depend on the circuit parameters for the system (*i.e.*, resistance and inductance).

These are independent of the charging voltage, peak current, and test specimen. An impulse current generator typically has a constant resistance and inductance. Thus, the resulting rise and decay times of a current waveform are relatively constant, regardless of the magnitude of the peak current. For this reason, all MSU-HVL lightning waveforms showed identical rise and decay times. However, the action integrals of MSU-HVL lightning waveforms varied depending on the peak current, as would be expected.

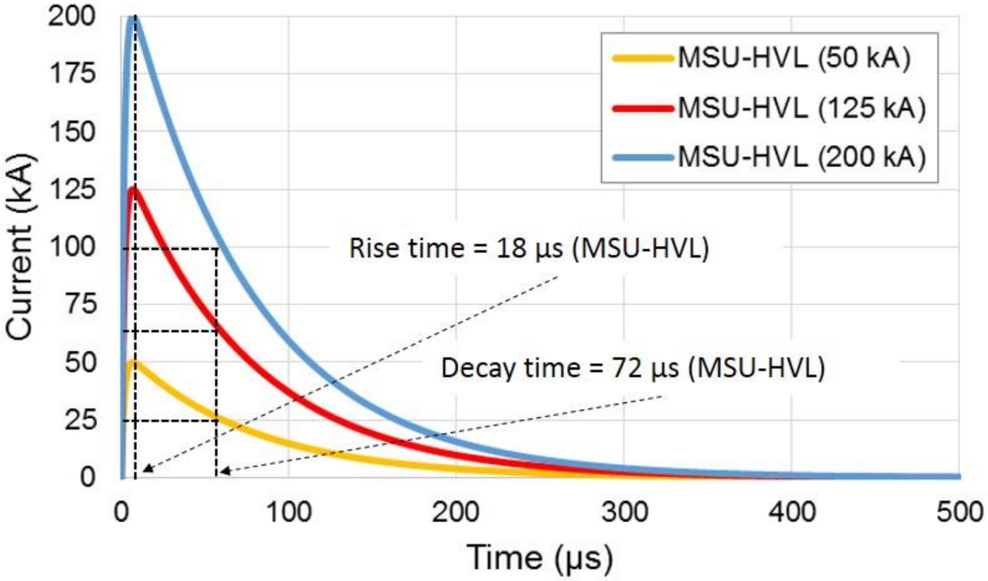

Figure 6.8 MSU-HVL impulse current waveforms with 50, 125, and 200 kA nominal peak currents.

6.4.4 Lightning Strike Locations on the PRSEUS Panel

Standard impulse current waveforms were applied at each of four representative lightning attachment locations on the OML skin of the sanded PRSEUS panel: (1) the mid-bay, (2) the stringer, (3) the frame, and (4) the frame/stringer intersection. Three peak current levels were considered in this work: (1) 50 kA (commonly used for laboratory-scale lightning strike tests [12, 13, 25-32]), (2) 125 kA (slightly higher than the *subsequent return stroke* defined in [16]), and (3) 200 kA (consistent with the *first return stroke* defined in [16]).

Twenty-four simulated lightning strike tests (including two calibration tests) were performed at a variety of key locations based on the size of the lightning damage zone after each representative lightning strike. Three 50 kA, three 125 kA, and two 200 kA nominal peak current tests were performed at both the mid-bay and stringer locations. Since the PRSEUS panel used in this study only had one frame, three 50 kA peak current tests were conducted at both the frame location and frame/stringer intersections. Figures 6.9a-6.9b show IML view of the simulated lightning attachment locations of the PRSEUS panel associated with the target and measured peak currents, respectively. Small differences between the target and measured peak currents were observed due to slight variations in the charging voltage between tests. Most measured peak currents were within 10% of the target peak currents, which proves the reliability of the MSU-HVL impulse current generator. Note that the standard SAE waveform [16] has ±10% peak current tolerance.

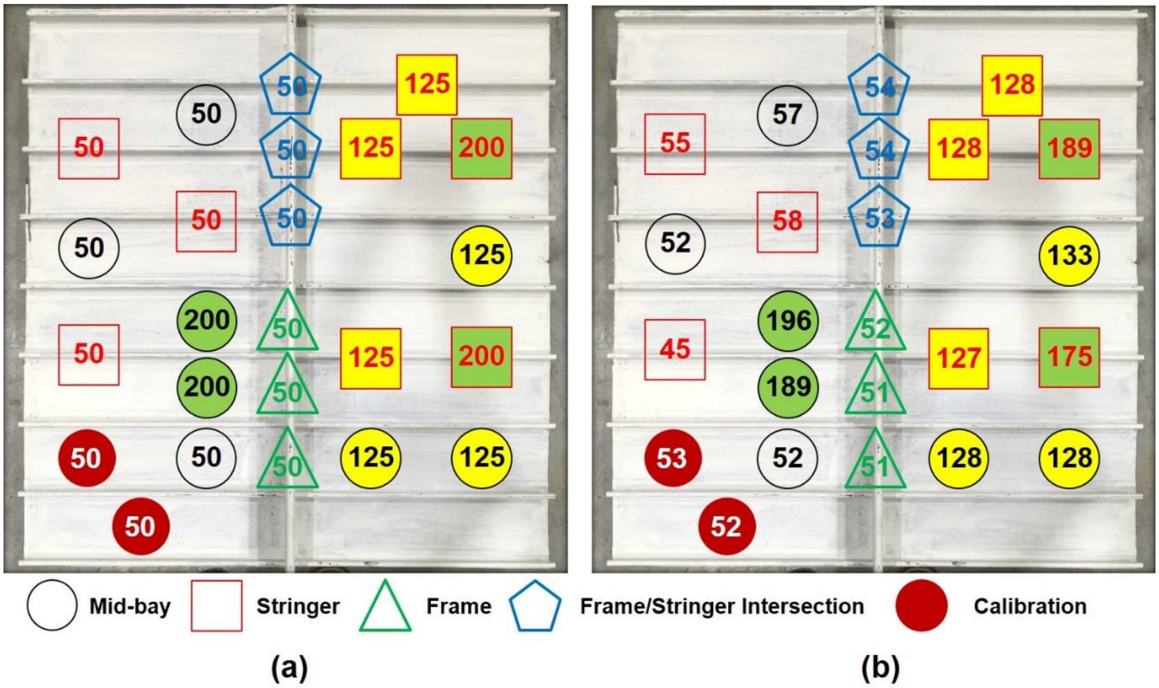

Figure 6.9 Simulated lightning strike locations on the PRSEUS panel that include the (a) target and (b) measured peak currents (in kA).

6.5 Results and Discussion

6.5.1 Lightning Damage Characterization

Figure 6.10 shows a photograph of the lightning-damaged PRSEUS panel after the application of the MSU-HVL impulse current waveforms. Measured peak currents are shown at each location for clarity. A magnified picture of lightning damage at the mid-bay location subjected to 200 kA nominal peak current is presented in Fig. 6.11. Based on surface observations of lightning damage, two primary damage types can be identified for the PRSEUS panel: (1) intense local damage near the attachment location and (2) surrounding widespread surface damage. The intense local damage includes severe fiber rupture, tow splitting, matrix decomposition, and underlying delamination. Regardless of damage severity, carbon fiber damage is associated with Joule heating resulting from an applied electrical current. This damage is oriented in the outermost lamina's fiber direction (+45˚). The regions of severe fiber rupture/delamination are surrounded by a large number of small clusters ("tufts") of broken fibers with a periodic arrangement consistent with the spacing between warp knit polyester threads (Fig. 6.1). There is also evidence of mild scorching (or burning) of the OML surface in this region. Such surface damage is caused by a combination of Joule heating and direct lightning heat fluxes (electronic or ionic recombination, convection flux, radiation flux, etc. [33]). As previously mentioned, rapid heating of the carbon fibers results in a severe contraction of the fiber/tows due to carbon fiber's negative coefficient of thermal expansion. This contraction leads to large-scale fiber rupture/tow splitting in the high thermal gradient region near the lightning attachment point. In addition, localized tufts of broken fibers arguably occur in the surrounding region where the fibers are relatively unconstrained between polyester warp knit threads. The regions with severe fiber rupture/tow splitting and underlying delamination were fairly elongated along the outermost lamina's fiber direction. In contrast, the scorched regions containing relatively small distributed tufts of broken fibers were roughly circular in shape. Lightning strikes create a narrow cylindrical plasma arc channel accompanied with radial heat fluxes [33-35]. Direct lightning heat fluxes are independent of an electrical conduction path (*i.e.*, outer ply fiber direction), but strongly depend on thermal boundary conditions (*i.e.*, convective/ radiative heat transfer coefficients and ambient temperature). Hence, the radial heat fluxes often create surface damage emanating from the center of the lightning attachment point [33]. For these reasons, the surface scorching and distributed broken fiber clusters likely result from direct lightning heat fluxes.

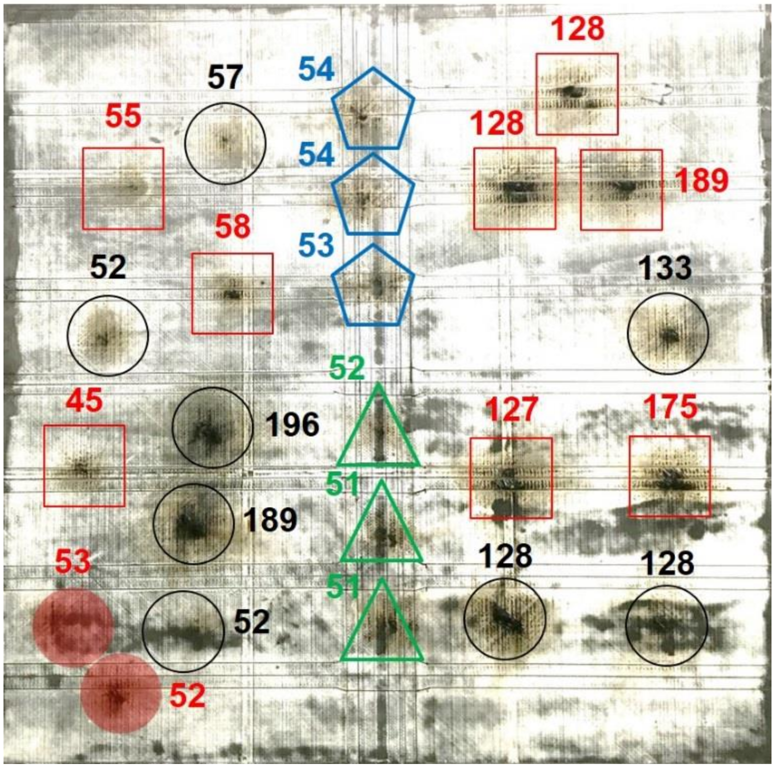

Figure 6.10 Damaged PRSEUS panel after being subjected to artificial lightning waveforms.

Measured peak currents (in kA) are shown at each strike location.

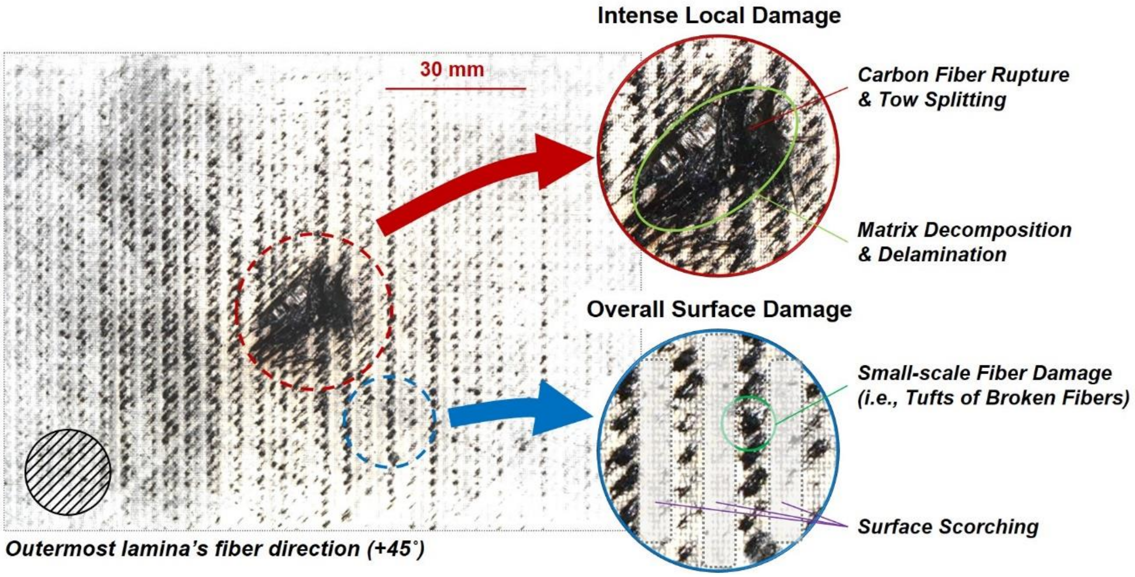

Figure 6.11 Two lightning damage categories observed at the PRSEUS mid-bay location subjected to 200 kA nominal peak current.

As mentioned previously, the periodic distribution of small broken fiber clusters in the vicinity of the lightning attachment location appears consistent with the spacing of warp-knitted fabric polyester threads. The PRSEUS skins considered in this study each consist of *two* nine-ply warp knit "stacks" (*i.e.*, stack A in Table 6.1). Each stack has a [+45/-45/0/0/90/0/0/-45/+45] layup where the nine plies are warp-knitted together with polyester thread to form an integrated preform (Fig. 6.2). The 18-ply PRSEUS skins were formed by layering two integrated stacks on top of one another. After lightning strike tests, the polyester knitting threads in regions away from the severe damage zone appeared to remain intact. Knitting threads provide through-thickness constraints that arguably affect mechanical or thermal wave propagation in the laminate. In addition, local contraction/densification of the fibers due to the presence of the warp knit threads may change the local thermal/electrical conductivities of the laminate. Such influences may explain the formation of small, periodically distributed clusters of broken fibers (Fig. 6.11). This unique lightning damage feature has not been observed in laminated composites [12, 13, 25-32]. Moreover, the influence of the warp knit thread architecture on delamination formation within a given stack remains to be fully explored. As an aside, in the absence of through-thickness Vectran™ stitches, delamination can form at the interface between two skin stacks since no warp knit threads span the interface.

6.5.2 Effect of Peak Current and Attachment Point on Lightning Damage Formation

Figure 6.12 shows typical lightning damage resulting at the mid-bay locations of the sanded PRSEUS panel subjected to MSU-HVL impulse current waveforms with 50, 125, and 200 kA nominal peak currents; the underlying PRSEUS panel corresponded to two warp-knitted skin stacks. The A^* in the figure indicates an approximate intense local damage area normalized by that associated with a 200 kA stringer strike. The horizontal solid lines shown in the figure correspond to through-thickness Vectran™ stitch lines where the skin stacks are sewn to the adjacent tear straps/stringers. The size of the regions with both intense local damage (solid ellipses) and widespread surface damage (dotted circles) increased as the peak current increased since greater peak current leads to more Joule heating (*i.e.*, more thermal damage). The areas with intense local damage increased dramatically with increasing current. Close inspection of these areas revealed substantial fiber ruptures in the outermost +45˚ ply, large-scale matrix decomposition, some fiber breakage, and tow splitting in the underlying -45˚ ply, as well as visible delamination between the top two plies. The degree of delamination, however, was far less pronounced than for prepreg laminates with no warp knitting. This suggests that the poly ester warp knit threads may play a significant role in delamination mitigation. The discrete lightning damage appeared to be most pronounced in the outermost lamina. While electrical current does penetrate into the underlying plies, the amount of current reaching these plies decreases with depth [36, 37]. Thus, the degree of instantaneous Joule heating should be greatest in the outermost ply and decrease for each successive inner ply; the observed damage appears to be consistent with this assumption. Since the primary electrical conduction path is along the carbon fiber direction, the regions of intense local damage were elliptical in character with the semi-major radius oriented in the outermost lamina’s fiber direction (+45˚), consistent with traditional (unstitched) carbon/epoxy laminates [12-14, 25-32].

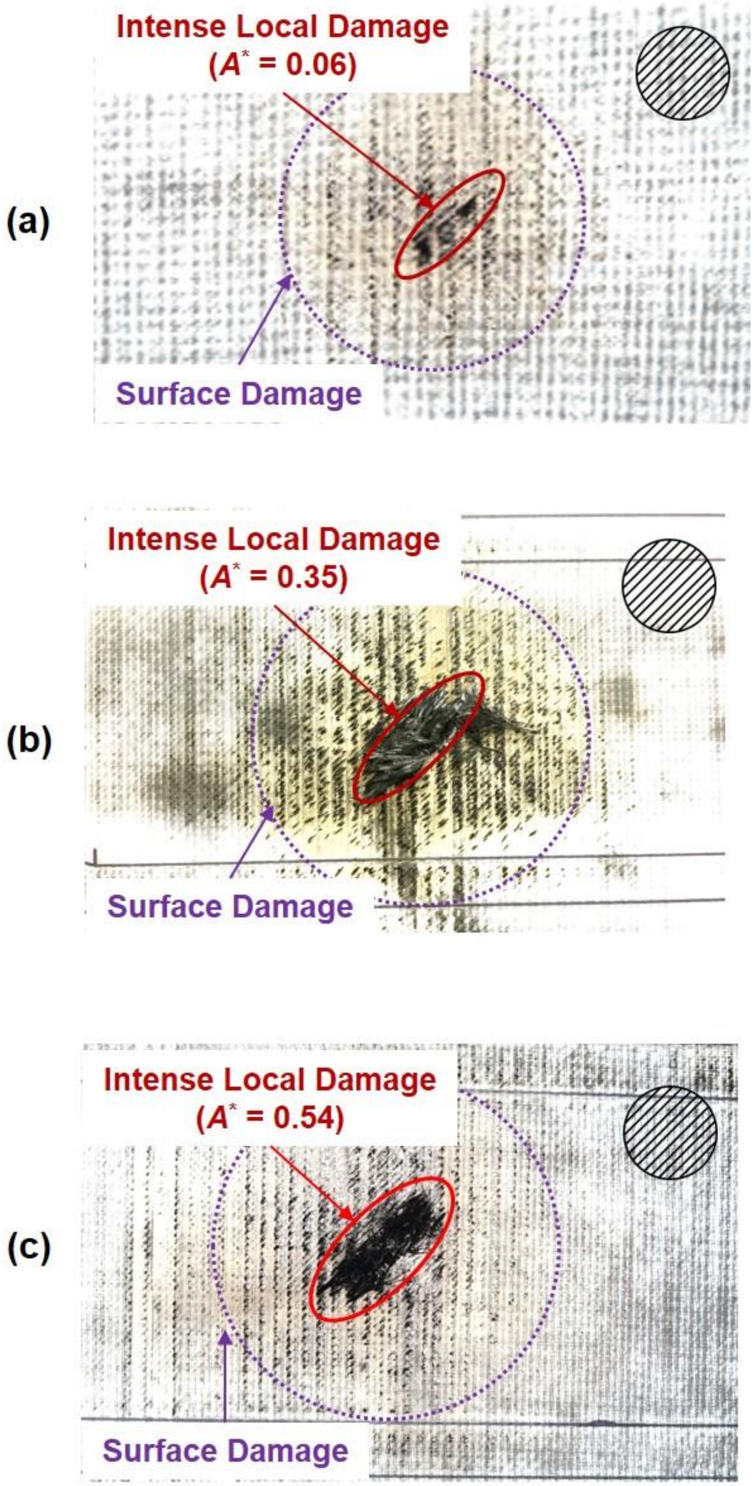

Figure 6.12 Typical lightning damage at the mid-bay locations subjected to (a) 50 kA, (b) 125 kA, and (c) 200 kA nominal peak currents.

Measured peak currents are included for clarity.

Figure 6.13 presents typical lightning damage at the stitched stringer locations of the PRSEUS panel subjected to 50, 125, and 200 kA nominal peak currents. The horizontal black lines indicate the Vectran™ stitch lines and the A^* corresponds to an approximate intense local damage area normalized by that associated with a 200 kA stringer strike. Similar to the mid-bay locations (Fig. 6.12), the lightning-damaged region increased as the peak current increased. In addition, lightning damage development was clearly constrained by the through-thickness Vectran™ stitches. For example, the regions with intense local damage at the stringer locations involved large-scale rupture of fiber tows in the outermost +45˚ ply (with corresponding tow splitting, matrix decomposition, etc. in the underlying adjacent plies). The spread of the domains with intense damage, however, was constrained between the Vectran™ stitch lines (*i.e.*, the damaged zones tended to elongate parallel to the stitching lines rather than along the major fiber axis in the outermost ply) (Fig. 6.13). Despite intense Joule heating and catastrophic damage to the warp knit skin stacks, the Vectran™ stitches remained essentially intact in the vicinity of the lightning attachment location. Vectran™ stiches, therefore, provide mechanical constraints that inhibit damage propagation across stitch lines. This is fairly remarkable, since Vectran™ stitches are decomposed at 400˚C [38], whereas the local lightning attachment temperature in the PRSEUS panel may drastically exceed this value. There appeared to be less visible delamination between plies in these locations relative to mid-bay strikes. Similar to the case for mechanical loading [5, 6], the stitch lines mitigated the formation of large-scale delamination based upon visual inspections. Similar to the mid-bay strikes, a periodic distribution of small carbon fiber tufts were observed surrounding the attachment point due to polyester warp knit thread confinement.

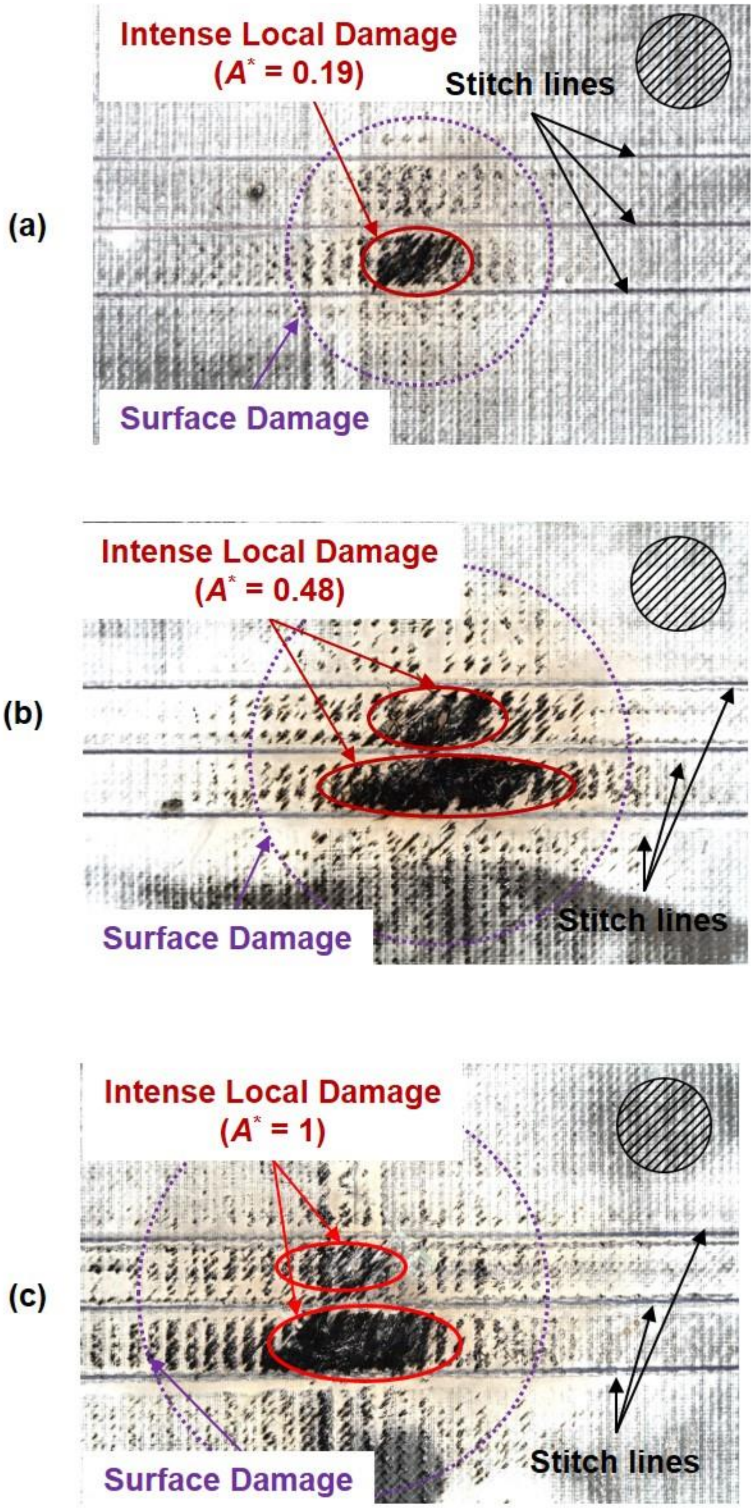

Figure 6.13 Typical lightning damage at the stringer locations subjected to (a) 50 kA, (b) 125 kA, and (c) 200 kA nominal peak currents.

Measured peak currents are included for clarity.

Typical lightning damage with approximate intense local damage areas (A^*) occurring due to a 50 kA peak current at the stitched frame location is shown in Fig. 6.14a. The vertical black/blue lines denote through-thickness Vectran™ stitches. Again, the region with intense local damage was confined between the stitching lines. While the presence of through-thickness Vectran™ stitches clearly plays a major role in mitigating lightning damage development, other factors may also contribute to the damage resistance characteristics of the PRSEUS panels. For example, the total composite thickness is different at the mid-bay (2.64 mm), stringer (5.28 mm), frame (5.28 mm), and frame/stringer interconnection (7.92 mm) locations. The local composite geometry and layup undoubtedly affects the dynamic behavior, mechanical and thermal strains, and other responses that influence lightning damage formation. The effect of panel thickness on damage formation remains to be fully explored. Figure 6.14b shows typical lightning damage occurring at a frame/stringer overlap due to a 50 kA peak current. At this location, the overlap region does not contain through-thickness stitching. As a consequence, the size of the region with intense local damage is larger than for the case of stringer (Fig. 6.13a) and frame (Fig. 6.14a) strikes. As an aside, the effect of higher peak currents (125, 200 kA) on damage development at the frame and frame/stringer interconnection is being addressed in a separate study [39].

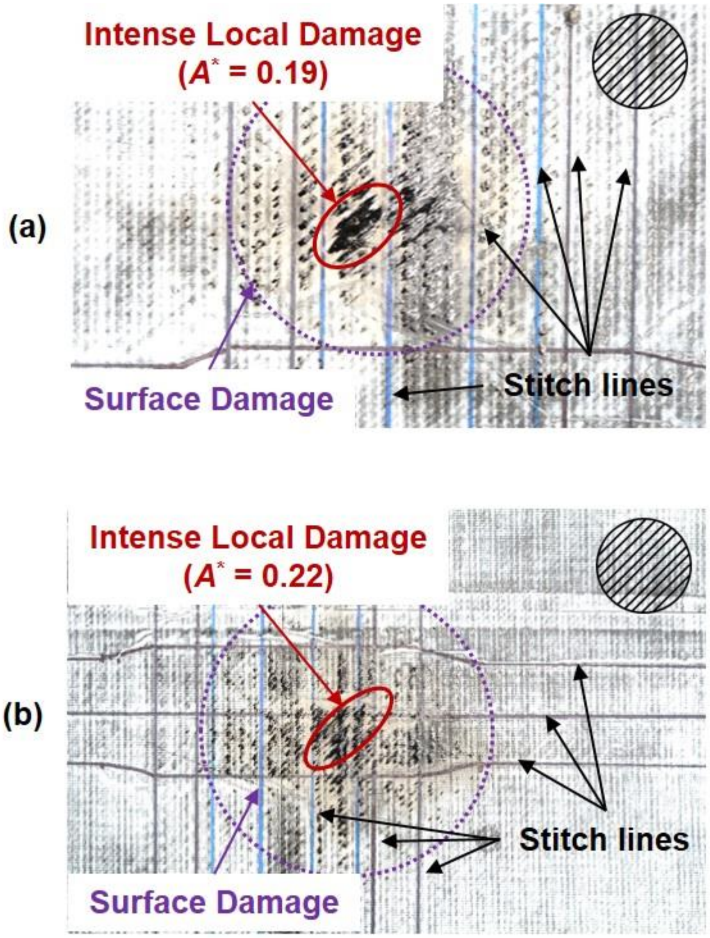

Figure 6.14 Typical lightning damage at the PRSEUS panel subjected to 50 kA nominal peak currents: (a) frame location (50.6 kA) and (b) frame/stringer intersection location (54.2 kA).

Measured peak currents are included for clarity.

Preliminary through-thickness ultrasonic (TTU) C-scan imaging was performed by Aurora Flight Sciences in Columbus, MS in order to assess the lightning-induced internal damage (*i.e.*, large-scale fiber ruptures, delamination, etc.) in the damaged PRSEUS panel. The sanded PRSEUS panel was inspected after lightning strike tests using a 5 MHz transducer with a 50.8 mm water path and 2.5 dB baseline scanning at

2.0 mm index (intersection point of the acoustic beam axis with the probe surface). High frequency ultrasonic waves were transmitted by a transducer from the OML side and captured by a receiver located on the IML side of the PRSEUS panel. If internal changes in the structure in an otherwise homogeneous part are significant, a large decrease in amplitude of the transmitted signal occurs. In this study, TTU C-scan results were obtained only at the mid-bay locations since the presence of underlying stringers, frames, and tear straps prohibited receiver access to the PRSEUS' IML side. Since the PRSEUS panels were delivered to MSU without establishment of viable C-scan standards, the following C-scan data are provided for reference purposes only; only a few reference standards [40, 41] exist for assessing internal mechanical damage for PRSEUS panels.

The extent of lightning-induced internal damage at the mid-bay locations increased as the peak current increased. Figure 6.15 contains identically scaled photographs and the corresponding TTU C-scan images of lightning damage at the mid-bay regions subjected to 50, 125 kA, and 200 kA nominal peak currents. The blue regions in the upper C-scan images correspond to significant signal attenuation indicative of internal damage; the size of such domain are approximated by the dashed blue lines in the C-scan images. These ellipses are superimposed on the photographs of the visual lightning damage. The regions of the internal damage detected by TTU C-scan were somewhat larger than those of the intense local damage determined by visual inspection. This suggests possible delamination between skin stacks (or other internal damage) not amenable to visual inspection was present. More comprehensive C-scan imaging and destructive sectioning of the entire PRSEUS panel will be performed as part of future work.

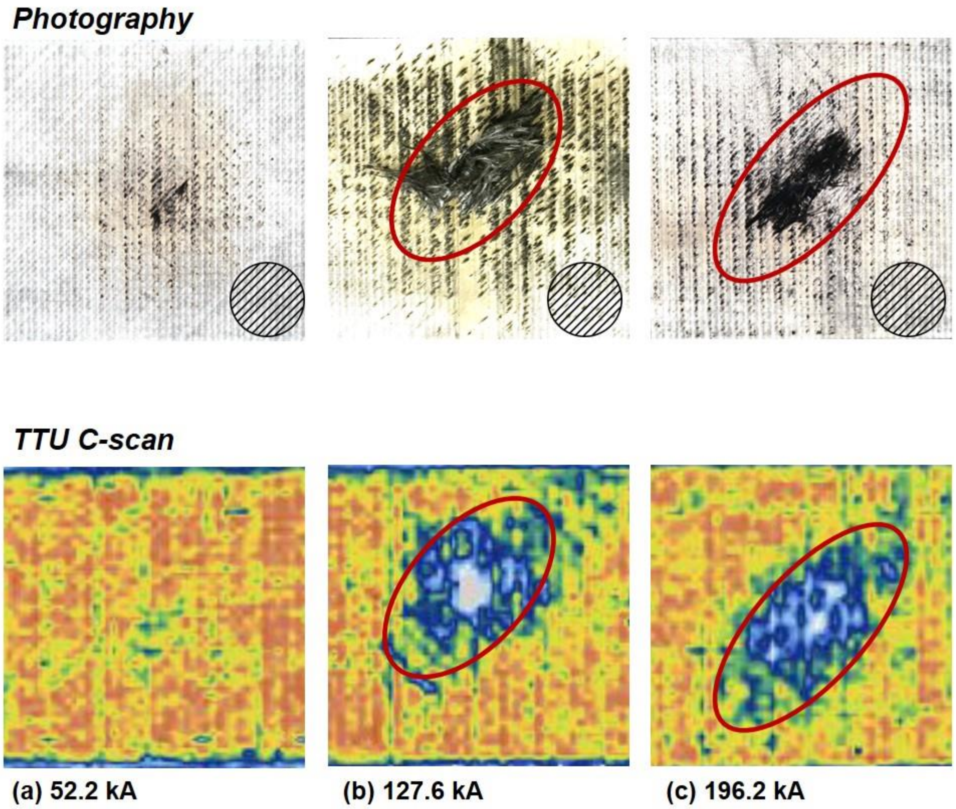

Figure 6.15 Photographs and TTU C-scan images of lightning damage at the mid-bay locations subjected to: (a) 50 kA, (b) 125 kA, and (c) 200 kA nominal peak currents.

Measured peak currents are included for clarity.

6.6 Conclusions and Recommendations

This work focused on lightning damage resistance characterization of a Pultruded Rod Stitched Efficient Unitized Structure (PRSEUS) panel subjected to standard impulse current waveforms, consistent with actual lightning strikes. A series of lightning strike tests with nominal 50, 125, and 200 kA peak currents were performed at four representative locations (*i.e.*, the mid-bay, stringer, frame, and frame/stringer intersection). The PRSEUS panel's outer mold line (OML) skin was lightly sanded prior to lightning strike tests to eliminate the influence of exterior surface paint on lightning damage development. Lightning damage was grouped into two types in this study: (1) intense local damage occurring in the vicinity of the lightning attachment point (*i.e.*, severe fiber rupture, tow splitting, matrix decomposition, and delamination) and (2) surrounding surface damage (*i.e.*, smaller scale fiber damage, scorching/burning).

Lightning strike testing to the sanded PRSEUS panel suggested that through-thickness Vectran™ stitches was highly effective in mitigating and constraining lightning damage. For OML lightning arc attachment locations with underlying stitched structural reinforcements (*i.e.*, stringers and frames), the ensuing visible lightning damage was constrained by the Vectran™ threads. Moreover, the Vectran™ stitches appeared relatively intact after all tests, even those conducted at high peak currents. In contrast, for attachment locations with no underlying stitching (*i.e.*, mid-bay and frame/stringer interconnections), both the size and severity of the resulting damage were greater than for analogous cases where through-thickness Vectran™ stitches were present. Preliminary through-transmission ultrasonic (TTU) C-scan imaging of both the sanded PRSEUS panels also suggests that the degree of internal damage (*i.e.*, delamination between skin stacks) is reduced due to the presence of stitches. Destructive sectioning of the panel will be performed in the future to correlate relevant aspects of internal damage morphologies with TTU C-scans of the damaged panels.

In addition, the polyester threads used in the warp-knitted skin stacks appear to influence lightning damage formation in regions just outside of the lightning attachment point (the area with severe fiber damage, matrix decomposition, etc.). Small clusters of broken fibers with a size and periodic spacing consistent with the polyester warp-knit thread architecture were formed in the vicinity of the attachment point. Such threads may also play a beneficial role in arresting delamination between plies in a given skin stack. Hence, use of through-thickness Vectran™ stitches, in combination with warp-knitted skin stacks may profoundly improve the lightning damage resistance of PRSEUS components relative to more traditional (non-reinforced) laminated composite structures.

Additional phased-array ultrasonic inspection of the sanded PRSEUS panels will be performed at Mississippi State University (MSU) using newly acquired non-destructive inspection (NDI) equipment. Such measurements will be coupled with destructive sectioning of both PRSEUS panels at each lightning strike zone to better characterize 1) the through-thickness integrity of Vectran™ stitches and polyester warp-knit threads and 2) internal damage morphologies, such as delamination between skin stacks and within plies in a single stack. Lastly, lightweight lightning protection layers (*i.e.*, copper mesh, pitch carbon fiber paper, graphene paper) will be integrated in the remaining PRSEUS panels to mitigate damage development.

6.7 References

[1] Velicki, A. and P. Thrash. "Advanced Structural Concept Development Using Stitched Composites," in the *Proceedings of the 49th AIAA/ASME/ASCE/ASC Structures, Structural Dynamics, and Materials Conference*, 2008, Schaumburg, IL.

[2] Velicki, A., N. Yovanof, J. Baraja, K. Linton, V. Li, A. Hawley, P. Thrash, S. DeCoux, and R. Pickell, "Damage Arresting Composites for Shaped Vehicles-Phase I Final Report." 2009, NASA/CR-2009-215932, NASA.

[3] Velicki, A., N. Yovanof, J. Baraja, K. Linton, V. Li, A. Hawley, P. Thrash, S. DeCoux, and R. Pickell, "Damage Arresting Composites for Shaped Vehicles-Phase II Final Report." 2011, NASA/CR-2011-216880, NASA.

[4] Velicki, A. and D. Jegley. "PRSEUS Development for the Hybrid Wing Body Aircraft," in the *Proceedings of the 11th AIAA Aviation Technology, Integration, and Operation*, 2011, Virginia Beach, VA.

[5] Jain, L.K. and Y.-W. Mai, "Mode I Delamination Toughness of Laminated Composites with Through-Thickness Reinforcement," *Applied Composite Materials*, 1994, **1**(1): p. 1-17.

[6] Dransfield, K.A., L.K. Jain, and Y.-W. Mai, "On the Effects of Stitching in CFRPs - I. Mode I Delamination Toughness," *Composites Science and Technology*, 1998, **58**(6): p. 815-827.

[7] Bergan, A., J. Bakuckas, J. Awerbuch, and T.-M. Tan, "Assessment of Damage Containment Features of a Full-Scale PRSEUS Fuselage Panel," *Composite Structures*, 2014, **113**: p. 174-185.

[8] Lovejoy, A.E., M. Rouse, K.A. Linton, and V.P. Li. "Pressure Testing of a Minimum Gauge PRSEUS Panel," in the *Proceedings of the 52nd AIAA Structures Dynamics and Materials Conference*, 2011, National Harbor, MD.

[9] Yovanof, N., A.E. Lovejoy, J. Baraja, and K. Gould. "Design, Analysis and Testing of a PRSEUS Pressure Cube to Investigate Assembly Joints," in the *Proceedings of the Aircraft Airworthiness and Sustainment Conference*, 2012, Baltimore, MD.

[10] Leone Jr, F.A. and D.C. Jegley. "Compressive Loading and Modeling of Stitched Composite Stiffeners," in the *Proceedings of the 57th AIAA/ASCE/AHS/ASC Structures, Structural Dynamics, and Materials Conference*, 2016, San Diego, CA.

[11] Lovejoy, A.E. "Preliminary Weight Savings Estimate for a Commercial Transport Wing Using Rod-stiffened Stitched Composite Technology," in the *Proceedings of the 56th AIAA/ASCE/AHS/ASC Structures, Structural Dynamics, and Materials Conference*, 2015, Kissimmee, FL.

[12] Hirano, Y., S. Katsumata, Y. Iwahori, and A. Todoroki, "Artificial Lightning Testing on Graphite/Epoxy Composite Laminate," *Composites Part A: Applied Science and Manufacturing*, 2010, **41**(10): p. 1461-1470.

[13] Feraboli, P. and H. Kawakami, "Damage of Carbon/Epoxy Composite Plates Subjected to Mechanical Impact and Simulated Lightning," *Journal of Aircraft*, 2010, **47**(3): p. 999-1012.

[14] Kawakami, H. and P. Feraboli, "Lightning Strike Damage Resistance and Tolerance of Scarf-Repaired Mesh-protected Carbon Fiber Composites," *Composites Part A: Applied Science and Manufacturing*, 2011, **42**(9): p. 1247-1262.

[15] Wang, F., Y. Ji, X. Yu, H. Chen, and Z. Yue, "Ablation Damage Assessment of Aircraft Carbon Fiber/Epoxy Composite and its Protection Structures Suffered from Lightning Strike," *Composite Structures*, 2016, **145**: p. 226-241.

[16] SAE, "Aircraft Lightning Environment and Related Test Waveforms," *Aerospace Recommended Practice ARP 5412*, 1999.

[17] Sugie, T., A. Nakai, and H. Hamada, "Effect of CF/GF Fibre Hybrid on Impact Properties of Multi-Axial Warp Knitted Fabric Composite Materials," *Composites Part A: Applied Science and Manufacturing*, 2009, **40**(12): p. 1982-1990.

[18] SAERTEX, *SAERTEX Thermoplastic Non-Crimp Carbon Fiber Fabrics* 2016.

[19] Karahan, M., S.V. Lomov, A.E. Bogdanovich, D. Mungalov, and I. Verpoest, "Internal Geometry Evaluation of Non-Crimp 3D Orthogonal Woven Carbon Fabric Composite," *Composites Part A: Applied Science and Manufacturing*, 2010, **41**(9): p. 1301-1311.

[20] Woods, J., A. Modin, R. Hawkins, and D. Hanks, "Controlled Atmospheric Pressure Infusion Process," *International Patent WO*, 2003, **3**(101708): p. A1.

[21] Bergan, A.C., "Test and Analysis of Stitched Composite Structures to Assess Damage Containment Capability." 2014, PhD Dissertation, Drexel University.

[22] Gharghabi, P., Lee, J., M. S. Mazzola, T. E. Lacy, Jr., C. U. Pittman, Jr., and James, G., "Carbon/Epoxy Laminates Protected with Copper Mesh and Pitch-Based Carbon Fiber Paper Subjected to Artificial Lightning Strikes " *manuscript in preparation*, 2016.

[23] Schon, K., Characterisation and Generation of High Impulse Voltages and Currents, in *High Impulse Voltage and Current Measurement Techniques*. 2013, Springer. p. 5-38.

[24] Heidler, F., W. Zischank, Z. Flisowski, C. Bouquegneau, and C. Mazzetti. "Parameters of Lightning Current Given in IEC 62305-Background, Experience and Outlook," in the *Proceedings of the 29th International Conference on Lightning Protection*, 2008.

[25] Feraboli, P. and M. Miller, "Damage Resistance and Tolerance of Carbon/Epoxy Composite Coupons Subjected to Simulated Lightning Strike," *Composites Part A: Applied Science and Manufacturing*, 2009, **40**(6): p. 954-967.

[26] Gou, J., Y. Tang, F. Liang, Z. Zhao, D. Firsich, and J. Fielding, "Carbon Nanofiber Paper for Lightning Strike Protection of Composite Materials," *Composites Part B: Engineering*, 2010, **41**(2): p. 192-198.

[27] Kawakami, H., "Lightning Strike Induced Damage Mechanisms of Carbon Fiber Composites." 2011, PhD Dissertation, University of Washington.

[28] Chen, X., G. Liu, and H. Wang. "The Residual Strength Test and Analysis of Composite Rudder After Lightning Strike," in the *Proceedings of the 18th International Conference on Composite Materials*, 2011, Jeju, South Korea.

[29] Szatkowski, G.N., K.L. Dudley, S.V. Koppen, J.J. Ely, T.X. Nguyen, L.A. Ticatch, J.J. Mielnik, and P.A. Mcneill. "Common Practice Lightning Strike Protection Characterization Technique to Quantify Damage Mechanisms on Composite Substrates," in the *Proceedings of the International Conference on Lightning and Static Electricity*, 2013, Seattle, WA.

[30] Yamashta, S., I. Ohsawa, and J. Takahashi. "Structural Integrity of Carbon Fiber Reinforced Polyprophylene After Lightning Strike," in the *Proceedings of the SAMPE Europe's 35th International Conference*, 2014, Paris, France.

[31] Li, Y., R. Li, L. Huang, K. Wang, and X. Huang, "Effect of Hygrothermal Aging on the Damage Characteristics of Carbon Woven Fabric/Epoxy Laminates subjected to Simulated Lightning Strike," *Materials & Design*, 2016, **99**: p. 477-489.

[32] Hirano, Y., T. Yokozeki, Y. Ishida, T. Goto, T. Takahashi, D. Qian, S. Ito, T. Ogasawara, and M. Ishibashi, "Lightning Damage Suppression in a Carbon Fiber-Reinforced Polymer with a Polyaniline-based Conductive Thermoset Matrix," *Composites Science and Technology*, 2016, **127**: p. 1-7.

[33] Chemartin, L., P. Lalande, B. Peyrou, A. Chazottes, P. Elias, C. Delalondre, B. Cheron, and F. Lago, "Direct Effects of Lightning on Aircraft Structure: Analysis of the Thermal, Electrical and Mechanical Constraints," *AerospaceLab*, 2012, (5): p. 1-15.

[34] Bazelyan, E.M. and Y.P. Raizer, Lightning Physics and Lightning Protection. 2000: CRC Press.

[35] Rakov, V.A. and M.A. Uman, Lightning: Physics and Effects. 2003: Cambridge University Press.

[36] Lee, J., T. E. Lacy, Jr., C. U. Pittman, Jr. and M. S. Mazzola, "Thermal Response of Carbon Fiber Epoxy Composites with Metallic and Non-Metallic Protection Layers to Simulated Lightning Currents," *Polymer Composites, under revision*, 2017.

[37] Lee, J., T. E. Lacy, Jr., C. U. Pittman, Jr. and M. S. Mazzola, "Temperature-Dependent Thermal Decomposition of Carbon/Epoxy Laminates Subjected to Simulated Lightning Currents," *Polymer Composites, under revision*, 2017.

[38] MatWeb, *Kuraray Vectran® HT 1500/300 LCP Fiber Material Property Data*, 2014 [cited 2017 Mar 28]; Available from: http://www.matweb.com/search/DataSheet.aspx?MatGUID=8552ae3f68e8401483d0641b8244792e.

[39] Boushab, D., "Artificial Lightning Strike Tests on a Painted PRSEUS Panel." 2017, MS Thesis, Mississippi State University.

[40] Johnston, P.H., "Ultrasonic Nondestructive Evaluation of PRSEUS Pressure Cube Article in Support of Load Test to Failure." 2013, NASA/TM-2013-217799, NASA.

[41] Johnston, P.H. and P.D. Juarez, "Ultrasonic Nondestructive Evaluation of Pultruded Rod Stitched Efficient Unitized Structure (PRSEUS) During Large-Scale Load Testing and Rod Push-Out Testing." 2016, NASA/TM-2016-218978, NASA.

CHAPTER VII

CONCLUDING REMARKS AND FUTURE WORK

7.1 Concluding Remarks

Lightning damage resistance of traditional aerospace carbon/epoxy laminates and Pultruded Rod Stitched Efficient Unitized Structure (PRSEUS) panel were characterized by laboratory-scale lightning strike tests and multiphysics-based lightning strike finite element (FE) models. This dissertation comprises three related research projects: (1) a three-dimensional (3D) heat transfer problem in an anisotropic composite heat spreader, (2) lightning damage resistance of the carbon/epoxy laminates, and (3) lightning damage resistance of a PRSEUS panel.

In the *first* project, an analytical solution for the steady-state temperature distribution in a thermally anisotropic heat spreader was presented as a solid foundation for future 3D heat transfer analyses. Lightning produces a plasma arc channel that injects heat into composites with a non-uniform heat flux that is a function of the electric current waveform. Thus, solutions to 3D heat conduction problems involving an anisotropic heat spreader subjected to a highly localized heat flux naturally leads to coupled thermal/electrical analyses of carbon/epoxy laminates subjected to lightning strike.

In the *second* project, lightning damage resistance of carbon/epoxy laminates were studied. AS4/8552 carbon/epoxy laminates were subjected to standard impulse current waveforms, consistent with actual lightning strikes, with 50, 125, and 200 kA nominal peak currents. Lightning surface damage and damage penetration increased as the peak current increased since greater peak current leads to more Joule heating (thus, more thermal damage). The regions of severe carbon fiber damage were aligned along the top lamina's fiber direction because electrical current occurs along the optimal conduction path (*i.e.*, in the fiber direction). In addition, carbon/epoxy laminates protected with either copper-mesh (CM) or pitch-based carbon fiber paper (PCFP) outer layers were also tested as part of this work to assess their potential effectiveness. Both the CM and the PCFP protection layers successfully mitigated lightning damage development in the underlying laminates.

The CM layer showed better lightning protection ability than the PCFP outer layer due to its relatively high in-plane electrical conductivity. The PCFP-protected laminates showed somewhat greater surface damage than the CM-protected laminates, but much smaller surface damage than the unprotected laminates. This suggests that the PCFP protection layer may serve as an efficient lightning protection layer.

Multiphysics-based lightning strike FE models were proposed that may prove useful in preliminary assessments of lightning damage to carbon/epoxy laminates. The FE models were developed for predicting matrix thermal decomposition in unprotected carbon/epoxy laminates as a function of spatially- and temporally-varying local temperatures. The predicted domains with matrix decomposition in the unprotected laminates showed good agreement with experimental results available in the literature, indicating that the present FE model is effective and reliable for predicting lightning damage. The FE models were further developed in order to predict matrix thermal decomposition of CM- and PCFP-protected carbon/epoxy laminates. FE results suggested that both the CM and the PCFP lightning protection layers successfully mitigated thermal damage development in the underlying composites, consistent with surface observations of lightning damage to the protected laminates. The extent of the predicted matrix decomposition in the CM-protected and the PCFP-protected laminates were much smaller than for an analogous ply in the unprotected laminate. The in-plane and through-thickness electrical conductivities of a PCFP layer can be tailored to improve its lightning strike protection abilities by controlling the pitch carbon fiber volume fraction, fiber orientation, and other factors. Thus, a PCFP protection layer or similar conductive carbon-based layers may be used to inhibit through-thickness lightning damage development, thus serving as an effective, lightweight lightning protection layer.

In the *third* project, the lightning damage resistance of a PRSEUS panel was characterized. Standard impulse current waveforms with nominal 50, 125, and 200 kA peak currents were applied at each of four representative locations (*i.e.*, the mid-bay, the stringer, the frame, and the frame/stringer intersection) on the outer mold line (OML) skin of a sanded PRSEUS panel. Similar to the laminate testing, lightning strike surface damage at the mid-bay and the stringer locations gradually increased as the peak current increased. Lightning damage was categorized into two types based on severity of damage: (1) intense local damage (*i.e.*, severe fiber rupture, tow splitting, matrix decomposition, and delamination) and (2) surface damage (*i.e.*, scorching/ burning as well periodically distributed clusters with small-scale fiber breaks). The regions with large-scale fiber-related damage were elongated along the outermost lamina’s fiber direction, indicating that the fiber damage is associated with Joule heating. This is consistent with surface observations of the lightning-damaged laminates. In contrast, the regions of widespread surface damage were roughly circular in shape, suggesting that the surface damage depends on direct heat fluxes which results from electronic or ionic recombination, convective or radiative fluxes.

The damaged PRSEUS panel exhibited unique lightning damage features due to use of warp-knitted fabrics and through-thickness Vectran™ stitches. Warp-knitted fabrics used in a PRSEUS panel are weaved with polyester knitting threads that hold individual carbon fiber tows together. The polyester knitting threads just outside the lightning attachment location appeared to remain intact after lightning strike tests. Such polyester knitting threads provide mechanical constraints to the fiber tows that lead to formation of a distribution of broken carbon fiber clusters surrounding the lightning attachment location. Through-thickness Vectran™ stitches provide a substantial similar mechanical constraint that inhibits lightning damage development. The Vectran™ stitches appeared to remain virtually undamaged near the lightning attachment location. The regions of intense local damage at the stringer and frame locations were mostly confined between adjacent through-thickness Vectran™ stitches.

7.2 Future Work

The lightning strike FE model developed in this work may be further developed 1) by including fiber/matrix interaction, 2) by considering mechanical loading, and 3) by applying much higher peak currents (≥ 40 kA). *First*, the current FE models do not take into account possible interaction between individual carbon fibers and the epoxy matrix since each composite ply was idealized as a homogeneous continuum. The presence of local inhomogeneities (fiber aggregates, chars, resin rich domains, etc.) may exacerbate or mitigate lightning thermal damage to carbon/epoxy laminates. The current FE models are being revised to address such issues within a multiscale framework. *Second*, lightning also produces electromagnetic forces and acoustic pressures that lead to mechanical damage (*i.e.*, fiber/matrix debonding and delamination). The present FE model is being modified to include coupled thermal, electrical, and mechanical loadings to better characterize lightning damage to carbon/epoxy laminates. A lightning strike FE model including surface electrical current and mechanical loading is being developed now. Lightning thermo-mechanical damage to carbon/epoxy laminates will be discussed in a manuscript now in preparation. *Lastly*, the peak lightning current was limited to 40 kA in the present FE model because experimental results in the literature were only available below this peak current. Recently laboratory-scale lightning strike tests with 50, 125, and 200 kA peak currents were performed on the unprotected, the CM-protected, and the PCFP-protected carbon/epoxy laminates. Further simulations from 50 kA to 200 kA are ongoing. Prediction of lightning damage to the laminates subjected to these high peak currents will be also addressed in detail in a separate manuscript.

APPENDIX A

FOURIER COEFFICIENTS

Table A.1 Fourier coefficients for Eq. 2.10

$$\mathrm{A}_{00}(Z) = 1 + \mathrm{Bi}\,(1 - Z) \tag{A1}$$

$$A_{\mathrm{m}0}(Z) = \frac{2\,\mathrm{Bi}\sin\left[\sqrt{A^*}m\pi\right]\left(\frac{\tau}{\kappa}m\pi\cosh\left[\frac{\tau}{\kappa}m\pi(Z-1)\right] - \mathrm{Bi}\sinh\left[\frac{\tau}{\kappa}m\pi(Z-1)\right]\right)}{\sqrt{A^*}m^2\pi^2\frac{\tau}{\kappa}\left(\mathrm{Bi}\cosh\left[\frac{\tau}{\kappa}m\pi\right] + \frac{\tau}{\kappa}m\pi\sinh\left[\frac{\tau}{\kappa}m\pi\right]\right)} \tag{A2}$$

$$A_{0\mathrm{n}}(Z) = \frac{2\,\mathrm{Bi}\sin\left[\sqrt{A^*}n\pi\right]\left(\frac{\tau}{\kappa}n\pi\cosh\left[\frac{\tau}{\kappa}n\pi(Z-1)\right] - \mathrm{Bi}\sinh\left[\frac{\tau}{\kappa}n\pi(Z-1)\right]\right)}{\sqrt{A^*}n^2\pi^2\frac{\tau}{\kappa}\left(\mathrm{Bi}\cosh\left[\frac{\tau}{\kappa}n\pi\right] + \frac{\tau}{\kappa}n\pi\sinh\left[\frac{\tau}{\kappa}n\pi\right]\right)} \tag{A3}$$

$$\zeta = \sqrt{m^2 + n^2} \tag{A4}$$

$$A_{\mathrm{mn}1}(Z) = -2\,\mathrm{Bi}\,\zeta^2\,\pi\frac{\tau}{\kappa}\,\cosh\left[\frac{\tau}{\kappa}\zeta\pi(Z-2)\right] \tag{A5}$$

$$A_{\mathrm{mn}2}(Z) = \left(\mathrm{Bi}^2 + \zeta^2\,\pi^2\frac{\tau^2}{\kappa^2}\right)\sinh\left[\zeta\pi\frac{\tau}{\kappa}(Z-2)\right] + \left(\mathrm{Bi}^2 - \zeta^2\,\pi^2\frac{\tau^2}{\kappa^2}\right)\sinh\left[\zeta\pi\frac{\tau}{\kappa}Z\right] \tag{A6}$$

$$\mathrm{A}_{\mathrm{mn}}(Z) = \frac{-2\,\mathrm{Bi}\sin\left[\sqrt{A^*}m\pi\right]\,\sin\left[\sqrt{A^*}n\pi\right]\left(A_{mn1}(Z) + \zeta\,A_{mn2}(Z)\right)}{A^*mn\zeta^2\pi^3\frac{\tau}{\kappa}\left(\mathrm{Bi}^2\cosh^2\left[\zeta\pi\frac{\tau}{\kappa}\right] + \zeta^2\pi^2\frac{\tau^2}{\kappa^2}\sinh^2\left[\zeta\pi\frac{\tau}{\kappa}\right] + \mathrm{Bi}\,\zeta\pi\frac{\tau}{\kappa}\,\sinh\left[2\,\zeta\pi\frac{\tau}{\kappa}\right]\right)} \tag{A7}$$

APPENDIX B

COMPARISON OF DIMENSIONLESS TEMPERATURES FROM ANALYTICAL AND FE SOLUTIONS

Table B.1 Dimensionless maximum temperatures for isotropic and TI heat spreaders with the dimensionless heat spreader thickness (τ) for various Biot numbers (Bi), source-to-spreader area ratios (A^*), and thermal conductivity ratios (κ^2)

Dimensionless Constant				Solution			Isotropy**
Bi	A^*	τ	κ^2	Analytical	FE	Relative Percent Difference*	
10^{-5}	10^{-4}	10^{-2}	1	0.8749	0.8750	0.004%	ISO (Fig. 2.6)
10^{-4}	10^{-4}	10^{-2}	1	0.3980	0.3981	0.009%	ISO (Fig. 2.6)
10^{-3}	10^{-4}	10^{-2}	1	0.0358	0.0358	0.002%	ISO (Fig. 2.6)
10^{-2}	10^{-4}	10^{-2}	1	0.0001	0.0001	0.000%	ISO (Fig. 2.6)
10^{-1}	10^{-4}	10^{-2}	1	0.0000	0.0000	0.000%	ISO (Fig. 2.6)
10^{-5}	10^{-3}	10^{-2}	1	0.8197	0.8199	0.028%	ISO (Fig. 2.7)
10^{-4}	10^{-3}	10^{-2}	1	0.2975	0.2979	0.039%	ISO (Fig. 2.7)
10^{-3}	10^{-3}	10^{-2}	1	0.0209	0.0209	0.003%	ISO (Fig. 2.7)
10^{-2}	10^{-3}	10^{-2}	1	0.0000	0.0000	0.002%	ISO (Fig. 2.7)
10^{-1}	10^{-3}	10^{-2}	1	0.0000	0.0000	0.004%	ISO (Fig. 2.7)
10^{-5}	10^{-2}	10^{-2}	1	0.7575	0.7547	0.286%	ISO (Fig. 2.8)
10^{-4}	10^{-2}	10^{-2}	1	0.2240	0.2212	0.274%	ISO (Fig. 2.8)
10^{-3}	10^{-2}	10^{-2}	1	0.0135	0.0133	0.023%	ISO (Fig. 2.8)
10^{-2}	10^{-2}	10^{-2}	1	0.0000	0.0000	0.001%	ISO (Fig. 2.8)
10^{-1}	10^{-2}	10^{-2}	1	0.0000	0.0000	0.000%	ISO (Fig. 2.8)
10^{-5}	10^{-4}	10^{-2}	0.1	0.9857	0.9858	0.008%	TI (Fig. 2.9)
10^{-4}	10^{-4}	10^{-2}	0.1	0.8726	0.8732	0.061%	TI (Fig. 2.9)
10^{-3}	10^{-4}	10^{-2}	0.1	0.3929	0.3942	0.135%	TI (Fig. 2.9)
10^{-2}	10^{-4}	10^{-2}	0.1	0.0350	0.0352	0.021%	TI (Fig. 2.9)
10^{-1}	10^{-4}	10^{-2}	0.1	0.0001	0.0001	0.000%	TI (Fig. 2.9)
10^{-5}	10^{-3}	10^{-2}	0.1	0.9759	0.9787	0.274%	TI (Fig. 2.10)
10^{-4}	10^{-3}	10^{-2}	0.1	0.8109	0.8199	0.901%	TI (Fig. 2.10)
10^{-3}	10^{-3}	10^{-2}	0.1	0.2921	0.2979	0.577%	TI (Fig. 2.10)
10^{-2}	10^{-3}	10^{-2}	0.1	0.0182	0.0209	0.272%	TI (Fig. 2.10)
10^{-1}	10^{-3}	10^{-2}	0.1	0.0001	0.0000	0.005%	TI (Fig. 2.10)
10^{-5}	10^{-2}	10^{-2}	0.1	0.9536	0.9592	0.556%	TI (Fig. 2.11)
10^{-4}	10^{-2}	10^{-2}	0.1	0.6910	0.6998	0.881%	TI (Fig. 2.11)
10^{-3}	10^{-2}	10^{-2}	0.1	0.1742	0.1766	0.239%	TI (Fig. 2.11)
10^{-2}	10^{-2}	10^{-2}	0.1	0.0084	0.0098	0.145%	TI (Fig. 2.11)
10^{-1}	10^{-2}	10^{-2}	0.1	0.0000	0.0000	0.001%	TI (Fig. 2.11)
10^{-5}	10^{-4}	10^{-2}	0.1	0.3985	0.3985	0.004%	TI (Fig. 2.12)
10^{-4}	10^{-4}	10^{-2}	10	0.0359	0.0359	0.000%	TI (Fig. 2.12)
10^{-3}	10^{-4}	10^{-2}	10	0.0001	0.0001	0.000%	TI (Fig. 2.12)
10^{-2}	10^{-4}	10^{-2}	10	0.0000	0.0000	0.000%	TI (Fig. 2.12)

Table B.1

Table B.1 (Continued)

10^{-1}	10^{-4}	10^{-2}	10	0.0000	0.0000	0.001%	TI (Fig. 2.12)
10^{-5}	10^{-3}	10^{-2}	10	0.3004	0.3001	0.031%	TI (Fig. 2.13)
10^{-4}	10^{-3}	10^{-2}	10	0.0212	0.0212	0.004%	TI (Fig. 2.13)
10^{-3}	10^{-3}	10^{-2}	10	0.0000	0.0000	0.001%	TI (Fig. 2.13)
10^{-2}	10^{-3}	10^{-2}	10	0.0000	0.0000	0.002%	TI (Fig. 2.13)
10^{-1}	10^{-3}	10^{-2}	10	0.0001	0.0000	0.007%	TI (Fig. 2.13)
10^{-5}	10^{-2}	10^{-2}	10	0.2398	0.2369	0.293%	TI (Fig. 2.14)
10^{-4}	10^{-2}	10^{-2}	10	0.0149	0.0146	0.027%	TI (Fig. 2.14)
10^{-3}	10^{-2}	10^{-2}	10	0.0000	0.0000	0.001%	TI (Fig. 2.14)
10^{-2}	10^{-2}	10^{-2}	10	0.0000	0.0000	0.000%	TI (Fig. 2.14)
10^{-1}	10^{-2}	10^{-2}	10	0.0000	0.0000	0.000%	TI (Fig. 2.14)

[*] Normalized, maximum temperatures at half length of the heat spreader ($X = 1$, $Y = 0$, and $Z = 1$): the maximum relatively percent difference is underlined for each figure.

[**] Isotropic (ISO) and transversely isotropic (TI).